The Evolution of Dusty Disks Around Low-Mass Pre-Main Sequence Stars

by

Catherine C. Espaillat

A dissertation submitted in partial fulfillment
of the requirements for the degree of
Doctor of Philosophy
(Astronomy and Astrophysics)
in The University of Michigan
2009

Doctoral Committee:

Professor Nuria P. Calvet, Chair
Professor Fred C. Adams
Professor Lee W. Hartmann
Associate Professor Edwin A. Bergin
Assistant Professor Jon M. Miller

Para mi familia.

Acknowledgements

This thesis is the product of three and a half years of support from generous colleagues and it is a pleasure for me to acknowledge their contributions to this work. First and foremost, I would like to express my gratitude to Nuria Calvet for being an insightful and supportive advisor and, more importantly, a mentor. Over these past few years, she has challenged and supported me to go beyond my expectations and to settle for nothing short of my best. Under her astute guidance and tutelage, I have learned a great deal about star formation and the field of astronomy. I am also indebted to Paola D'Alessio for sharing her disk codes with me. This thesis would not have been possible without her knowledge, support, and patience. My thesis committee members Fred Adams, Ted Bergin, Nuria Calvet, Lee Hartmann, and Jon Miller also provided invaluable feedback and direction for this work.

I would like to thank Ted Bergin, César Briceño, Nuria Calvet, Paola D'Alessio, William Forrest, Elise Furlan, Lee Hartmann, Jesús Hernández, Kevin Luhman, Melissa McClure, James Muzerolle, Joan Najita, Charlie Qi, Ben Sargent, and Dan Watson for providing comments on papers which have been incorporated into this thesis. Nuria Calvet, Elise Furlan, and Jesús Hernández also kindly provided figures.

Chapters 3, 4, 5, and 6 of this thesis are based on publications in the Astrophysical Journal Letters (Espaillat et al., 2007a,b, 2008a,b). Chapters 2 and 7 are

partially based on publications to appear in the Astrophysical Journal (Furlan et al. submitted, Espaillat et al. in preparation). This thesis was supported in part by the University of Michigan Rackham Merit Fellowship Program, the Woodrow Wilson National Fellowship Foundation, the Andrew W. Mellon Foundation, NASA Origins grant NNX08AH94G, Jet Propulsion Laboratory grants 1309768 and 1344183, Chandra Space Observatory grant GO8–9029X, and Hubble Space Telescope grant GO–11145.01–A.

Finally, I would like to thank my family and my friends for relentlessly cheering me on in the writing of this thesis. *¡Sí, se puede!*

Contents

List of Figures

Figure

List of Tables

Table

List of Abbreviations

2MASS	Two Micron All Sky Survey
ALMA	Atacama Large Millimeter Array
AOR	Astronomical Observation Request
ATCA	Australia Telescope Compact Array
BCD	Basic Calibrated Data
CARMA	Combined Array for Research in Millimeter Astronomy
CIDA	Centro de Investigaciones de Astronomía
CVSO	CIDA Variability Survey of Orion OB1
CTTS	Classical T Tauri Star
FAST	FAst Spectrograph for the Tillinghast Telescope
HR	Hertzsprung–Russell
IRAC	Infrared Array Camera
IRAF	Image Reduction and Analysis Facility
IRAS	Infrared Astronomical Satellite
IR	Infrared
IRS	Infrared Spectrograph
IRTF	Infrared Telescope Facility
ISM	Interstellar Medium

MIPS	Multiband Imaging Photometer for *Spitzer*
MMT	Multimirror Telescope
MOPEX	Mosaicker and Point source Extractor
MRI	Magnetorotational Instability
NASA	National Aeronautics and Space Administration
Ne	Neon
SED	Spectral Energy Distribution
SMA	Submillimeter Array
SMART	Spectral Modeling, Analysis, and Reduction Tool
SSC	*Spitzer* Science Center
TTS	T Tauri Star
ROSAT	Roentgen Satellite
USNO	United States Naval Observatory
UV	Ultraviolet
WTTS	Weak T Tauri Star
YSO	Young Stellar Object

Abstract

The evolution of protoplanetary disks is intricately tied to the origin of planets. The details of how these disks evolve from initially well-mixed distributions of gas and dust into systems composed mostly of rocky planets and gas giants like our own solar system is not well understood and is a fundamental question in astronomy. It is widely accepted that dust grain growth and settling to the disk midplane play an integral part in creating the planetesimals that amalgamate into planets. Newly formed planets will then interact with the disk, clearing the material around themselves and creating gaps. To get a more complete view of planet formation one should therefore study the observational signatures of dust growth, settling, and clearing in disks.

Here we present simulated spectral energy distributions of disks around low-mass classical T Tauri stars of various masses, accretion rates, inclinations, grain sizes, dust compositions, and amounts of settling. We find that the majority of observed disks lie within the parameter space probed by the models and are therefore "full disks." However, some disks have spectral energy distributions that cannot be explained by the full disk models. Some of these disks have a significant deficit of flux in the near- and mid-infrared but show substantial emission beyond 20 μm, similar to what is seen in full disks, indicating that the hot, inner regions of these "transitional disks"

have undergone significant dust clearing. Here we model the transitional disks of CS Cha and CVSO 224. CS Cha is located in the ∼2 Myr old Chamaeleon star–forming region. We show it has an optically thick circumstellar disk inwardly truncated at ∼43 AU with some small, optically thin dust within the innermost 1 AU of its inner disk hole. CS Cha also has large grains and a more settled outer disk suggesting that it is in an advanced state of dust evolution. CVSO 224 is the only transitional disk located within the ∼10 Myr old 25 Orionis group in Orion OB1a. We find a ∼7 AU inner disk hole that contains a small amount of optically thin dust and measure an accretion rate of 7×10^{-11} $M_\odot$ yr^{-1} in this object, making it one of the slowest accreting transitional disks detected so far.

We also present evidence for a new class of disk: the pre-transitional disks. These disks have significant near-infrared excesses (2 – 5 μm), similar to what is seen in full disks, which indicates the presence of an optically thick inner disk. However, these pre-transitional disks also have a deficit of flux in the mid-infrared (5 – 20 μm) and significant emission at longer wavelengths, similar to transitional disks. This points to a gap within the disk rather than an inner disk hole. The pre-transitional disks around UX Tau A and LkCa 15 have gaps of 56 and 46 AU respectively. UX Tau A's gap is devoid of small grains while LkCa 15 has some small optically thin dust within its gap. We analyze near-infrared spectra between 2–5 μm for LkCa 15 and UX Tau A and demonstrate that the near-IR excess of both can be fit with a single-temperature blackbody at the dust destruction temperature. This indicates that the near-infrared excesses of LkCa 15 and UX Tau A originate from the wall of an optically thick inner disk at the dust destruction radius, independently confirming

that these disks have gaps within their dust distributions.

This study of disks around pre-main sequence stars contributes new details on dust evolution. We report a range of grain sizes, settling, and inner disk hole radii in transitional disks as well as newly identified disks with gaps in their dust distributions. Our model grid of simulated disk SEDs also reveals that some observed disks in Taurus, Chamaeleon, and Ophiuchus cannot be explained by full disk models and are not known to be transitional or pre-transitional disks. We propose that these objects are pre-transitional disks with smaller gaps than previously observed, emphasizing that much still remains to be understood regarding the dust component of disks. A systematic study of disks around young stars is needed in order to provide needed insight and constraints to aid in theoretical modeling of dust evolution and planet formation.

Chapter 1

Introduction

We now know that planetary systems are relatively common around other stars (e.g. Butler et al., 2006). The origin of these extrasolar planets is intricately tied to the evolution of their primeval protoplanetary disks. These disks are composed of gas and dust and are formed in the collapse of high-density regions in molecular cores (Shu et al., 1987). As a result of angular momentum conservation, the collapse of a rotating molecular core will result in a protostar surrounded by a disk (Terebey et al., 1984), typically after $\sim 0.1 - 0.2$ Myr. The disk material will dissipate through accretion onto the star, accretion onto planets, and photoevaporation by ultraviolet radiation from the central star. Characteristic timescales for disk accretion and photoevaporation are about $1 - 10$ Myr and 10 Myr, respectively. Planet formation is thought to occur within $3 - 10$ Myr, while the disk material is still present and before the star reaches the main sequence (see Hartmann 2009 for a review). Therefore, to learn more about the origin of planets, we must understand the evolution of dusty disks around pre-main sequence stars.

Young stellar objects (YSOs; Strom, 1972) are those which have not yet reached the zero-age main sequence. YSOs include protostars, Herbig Ae/Be stars, T Tauri stars, and young brown dwarfs. Protostars are young stars which are still receiving

material from their infalling molecular cloud core. In Herbig Ae/BE stars, T Tauri stars, and brown dwarfs, the natal core is gone or has been exhausted and these objects have been observed with and without disks. Herbig Ae/Be stars have spectral types A – B and masses of 2 – 10 $M_\odot$. T Tauri stars have spectral types ranging from F – M and stellar masses of 0.08 – 2 $M_\odot$. Brown dwarfs by definition have masses less than 0.08 $M_\odot$.

In order to categorize these objects based on their spectral energy distributions (SEDs) Lada (1987) introduced a classification system based on the slope of the SED between 2.2 – 25 μm ($a = dlog(\lambda F_\lambda)/dlog(\lambda)$). Class I objects ($a > 0$) have SEDs with increasing infrared emission, as expected from protostars (Figure 1.1). Class II objects ($-2 < a < 0$) have relatively flat or negative slopes, corresponding to excess emission from dust in a disk around a pre-main sequence star (Figure 1.1). Class III objects ($a < -2$) have photospheric slopes and those Herbig Ae/BE stars, T Tauri stars, and brown dwarfs without disks fall into this category (Figure 1.1). In this thesis, we focus on Class II T Tauri objects.

T Tauri stars (TTS) can also be classified based on their accretion properties. In weak T Tauri stars (WTTS), material is no longer being accreted onto the star while classical T Tauri stars (CTTS) are still actively accreting material. The equivalent width of Hα is commonly used to identify the presence of accretion. Classical T Tauri stars have Hα equivalent widths greater than 3 Å for spectral types K0–K5, 10 Å for K7–M2.5, 20 Å for M3–M5.5, and 40 Å for M6–M7.5 (White & Basri, 2003). The present paradigm of mass transfer from the disk onto the star is magnetospheric accretion. In this model theory, the inner disk is truncated by the stellar magnetic

field and matter accretes from the disk onto the star via magnetic field lines (Hartmann et al., 1994; Muzerolle et al., 1998, 2001) forming an accretion shock at the stellar surface (Figures 1.2 and 1.3). The observed emission lines (e.g. Hα) form in the free-falling material within the accretion columns (Calvet & Hartmann, 1992; Hartmann et al., 1994; Muzerolle et al., 1998, 2001) while the excess continuum that dominates in the UV is formed in the accretion shock (Calvet & Gullbring, 1998). This excess continuum adds to the star's emission and "veils" stellar absorption lines in the optical, making them appear less deep (Hartigan et al., 1989). Measurements of the accretion luminosity based on this excess have been used to estimate mass accretion rates and typical values for classical TTS are $\sim 10^{-8}$ $M_\odot$ yr^{-1} (Hartmann et al., 1998; Gullbring et al., 1998). In this thesis, we will focus mainly Class II objects which are accreting.

The processes by which accreting disks around pre-main sequence stars evolve into planetary systems are a source of ongoing investigation. Dust growth and settling must play an important role in forming the planetesimals which will grow into planets that can clear the disk. To understand our origins, one should therefore study dust growth, settling, and clearing in disks. This thesis is an attempt to move us a few steps closer to this goal.

1.1 Dust Grain Growth and Settling in Dusty Accretion Disks

Accretion disks form around stars as a consequence of angular momentum conservation. Material from the infalling envelope cannot fall radially onto the star. Instead,

it will cross the equator at some distance from the star, where it encounters material falling from the opposite side of the envelope. This encounter results in a shock, where the vertical component of the material is dissipated. After some adjustment, material will remain in the midplane, rotating at near Keplerian velocities around the star (Terebey et al., 1984; Hartmann, 2009). Angular momentum is then conserved in the disk by transporting a small amount of disk material to very large radii while most of the disk material accretes onto the star.

Assuming that the accretion disk is steady and optically thick, it emits like a blackbody with $T \propto R^{-3/4}$ where T and R are the temperature and radius, respectively. However, observed SEDs of disks are less steep than the $\lambda F_\lambda \propto \lambda^{-4/3}$ expected from this temperature distribution (Kenyon & Hartmann, 1987). By taking into account stellar irradiation of the disk, Kenyon & Hartmann (1987) showed that disks which flare with radius can explain the observed SEDs. This is because flared disks can capture more radiation from the star and so the temperature falls less steeply with radius as $T \propto R^{-3/7}$ (if disks are vertically isothermal and the height is a fixed number of scale heights) and the resulting SED is less steep than a flat disk.

These flared, irradiated accretion disks are made up of gas and dust. While the gas dominates the mass of the disk, the dust controls most of what we see of the disk since the dust opacity dominates over the opacity of the gas. Thus the dust sets the heating and structure of the disk and hence its scattered and thermal emission. The dust also heats the gas in the disk through collisions (e.g. Glassgold et al., 2004). Small micron-sized dust grains have high opacities at optical and infrared wavelengths and thus are the main absorbers of stellar radiation when present and

contribute strongly to the disk's infrared emission and 10 μm silicate emission. Bigger grains have lower opacities at optical and infrared wavelengths and higher opacities at longer wavelengths and contribute strongly at millimeter wavelengths.

The evolution of the dust in the disk is significant, especially given that the first steps in making a planet are the growth of grains and subsequent settling to the midplane. Grains grow mainly by sticking to one another after they collide (Weidenschilling et al., 1997). These collisions occur due to relative velocities between grains of different sizes which are induced by the gas. The gas in the disk moves slightly slower than the Keplerian velocity due a radial pressure gradient which adds to the centrifugal force to counteract the star's gravity. Small grains ($<$ cm) are strongly coupled to the gas and move at the same angular velocity of the gas. However, grains are denser than gas and do not feel a radial pressure gradient and drift inward with velocities that increase with grain size. Large grains ($>$ m) are not coupled to the gas and move in Keplerian orbits. They drift inward with velocities that decrease with grain size due to friction with the slower moving gas which causes them to lose angular momentum. Concurrently, grains are also settling to the disk midplane due to the vertical component of the gravitational force of the star. Since the orbital period is shortest in the inner disk, grain growth and settling occur the fastest here, leading to inside-out dust evolution (Dullemond & Dominik, 2004, 2005).

There are major discrepancies between dust evolution theories and the observations. Weidenschilling et al. (1997) showed it is theoretically possible to form km-sized planetesimals from sub-micron sized grains within 10^5 years through collisional coagulation. However, grains with sizes up to 100 μm are severely depleted

within 10^4 yrs and so the observed spectral energy distributions should show no silicate emission and have weak infrared continuum emission by 1 Myr (Dullemond & Dominik, 2004, 2005). If turbulence is taken into account, the upper and lower layers of the disk will mix and the depletion of small grains will occur on even faster timescales since smaller grains from the upper layers will be accreted by larger grains in the midplane (Dullemond & Dominik, 2005). Yet disks with substantial infrared emission are observed in older clouds. About 65% of all T Tauri stars in the $\sim$1 Myr old Taurus cloud have substantial infrared excesses (Furlan et al., 2006). Most noticeably, the 10 μm silicate emission feature, which is indicative of small grains, is present in 90% of disk-bearing stars in Taurus (Figure 1.4; Furlan et al., 2006), but it is absent in the simulations which predict that small grains will be severely depleted by this age (Dullemond & Dominik, 2004, 2005). Dullemond & Dominik (2005) have proposed that ongoing destructive collisions between grains are needed to produce small grains to replenish the upper disk layers.

1.1.1 Linking Theory & Observations with Models

To compare the observations with theory in more detail, one must first develop sophisticated, self-consistent models of disks in order to quantify their properties. In this thesis we use the disk models of D'Alessio et al. (1998, 1999, 2001, 2005, 2006). The D'Alessio models are self-consistent models of irradiated accretion disks around T Tauri stars. The model assumes a steadily accreting disk and includes heating by viscous dissipation (using the α prescription of Shakura & Syunyaev, 1973), irradiation by the central star, radioactive decay, and cosmic rays; irradiation is the main

heating agent. The disk is a mixture of gas and dust, which are thermally coupled. Input parameters to the code are the stellar properties (luminosity, radius, effective temperature), the mass accretion rate ($\dot{M}$), the viscosity parameter α following Shakura & Syunyaev (1973), and the amount of settling.

The structure of the disk is solved iteratively since the height of the disk depends on the irradiation heating, which depends on the vertical structure of the disk. The solution of the structure equations indicates that the disk is not vertically isothermal. Stellar radiation enters the disk at an angle thus stellar radiation tends to be deposited in the uppermost layers of the disk (Calvet et al., 1991; Malbet & Bertout, 1991). In addition, the dust opacity is higher at the wavelengths where stellar radiation is absorbed than at the wavelengths where the disk is emitting. These two effects result in a "super heating" of the upper disk layers (Calvet et al., 1991, 1992; Chiang & Goldreich, 1997), making them hotter than the photospheric layers, if the disk is optically thick, or than the disk midplane, if the disk is optically thin. To illustrate these effects Figure 1.5 illustrates the temperature of the uppermost layers (T_0), the midplane temperature (T_m), and the photospheric temperature (T_{phot}), defined in the region where the disk is optically thick. The surface temperature of a viscous disk (T_{vis}) is shown for comparison. See Chapter 2.2.1 for a more detailed discussion of the vertical disk structure.

Grain growth is parameterized in the D'Alessio models by incorporating two populations of grains. The grain-size distribution follows a power-law of $a^{-3.5}$, where a is the grain radius, as is observed in the interstellar medium (ISM; Mathis et al., 1977). The minimum and maximum sizes of the dust grains in the upper layers

and midplane of the disk are adjustable. The initial steps of planet formation are coagulation of dust grains followed by settling to the midplane (Weidenschilling et al., 1997). Dust growth and settling are simulated by depleting the small dust in the upper layers of the disk. Assuming a constant dust-to-gas ratio at each radius, this decrease of small grains in the upper layers results in an increase of larger grains in the disk midplane. We define a settling parameter, $\epsilon = \zeta_{up}/\zeta_{st}$, which measures the mass fraction of the small grains in the upper layers relative to the standard dust-to-gas mass ratio. As the grains grow and sink downward to the midplane, the dust-to-gas mass ratio in the upper layers will decrease as the dust-to-gas mass ratio in the midplane increases. Since small grains have high opacities at the wavelengths of the stellar emission, this decrease in the number of small grains will lead to a decrease in the opacity of the upper disk layers and less stellar radiation will be absorbed and re-emitted by the dust. The resulting disk emission will decrease as settling increases (Figure 1.6).

The D'Alessio models have been used to confirm theoretical signatures of dust grain growth and settling in T Tauri disks. D'Alessio et al. (1999) showed that models of disks with uniformly mixed, small ISM-sized (0.005 – 0.25 μm) dust grains failed to explain observations of T Tauri disks (Figure 1.7). The models produced too much infrared emission and too little millimeter emission, pointing to an over-abundance of small grains, which have higher opacities at shorter wavelengths and therefore emit more strongly in the infrared, and not enough large grains, which emit strongly in the millimeter. D'Alessio et al. (2006) later incorporated grain growth and dust settling into their disk model and demonstrated that a disk which includes settling

and millimeter-sized grains in the midplane can reproduce the median observed SED of disks in the Taurus cloud (Figure 1.8; D'Alessio et al., 2006). The D'Alessio et al. studies were pivotal in illustrating that disks displayed signatures of grain growth and settling. Moreover, with the advent of the *Spitzer Space Telescope*, we can now see that there appears to be a large diversity of dust grain growth and settling in disks, even in those of a given age (Figure 1.9).

1.2 Clearing in Dusty Disks

Studies of disks in populations of various ages have yielded interesting clues to disk dissipation (e.g. Haisch et al., 2001; Gómez & Kenyon, 2001; Gutermuth et al., 2004; Hernández et al., 2005; Hartmann et al., 2005; Megeath et al., 2005; Carpenter et al., 2006; Lada et al., 2006; Sicilia-Aguilar et al., 2006). Hernández et al. (2007) studied stars located in star–forming regions of ages 1 – 10 Myr and showed that the percentage of TTS with excess near-infrared emission above photospheric levels, indicative of the presence of disks, decreases with age (Figure 1.10, left). At 1 Myr about 80% of TTS have disks, at 5 Myr 15% do so, and at 10 Myr the fraction is 10%. One can conclude that disks around TTS dissipate mostly within $\sim$ 10 Myr. Hernández et al. (2007) also found that the median near-infrared slope decreases with age (Figure 1.10, right). Near-infrared emission comes from hot dust in the inner regions of disks, and so a decrease of near-infrared emission indicates that the inner regions of these disks are clearing. Therefore, not only are disks disappearing with age, the amount of their near-infrared emission decreases with age. Near-infrared studies of gas in the inner disk also find that the amount of gas decreases with age

(Pascucci et al., 2006; Carmona et al., 2007). The overall picture is that, with a few exceptions, young $\sim$ 1 Myr old regions are dominated by TTS with disks displaying strong near-infrared excess while at $\sim$ 10 Myr most TTS have no disks, and the few that still have disks exhibit weak near-infrared excesses. Below we discuss a more dramatic form of disk clearing.

1.2.1 Transitional and Pre-transitional Disks

Over the past two decades, we have detected several disks with a significant deficit of flux in the near- and mid- infrared (2 – 20 μm) yet substantial excesses comparable to optically thick disks at longer wavelengths (>20 μm) (e.g. Strom et al., 1989; Skrutskie et al., 1990; Calvet et al., 2002, 2005b). The lack of near- and mid-infrared flux in these disks has been attributed to the removal of the hot dust close to the star which emits at shorter wavelengths, indicating the presence of inner disk holes. These "transitional disks" (Strom et al., 1989) have been proposed to be the link between Class II objects with full, accreting disks and Class III objects which show only photospheric emission. To date, studies of eight transitional disks with *Spitzer* IRS spectra have been published (Table 1.1). These objects have been modeled with optically thick disks containing inner holes where the frontally illuminated disk rim or "wall" of the inwardly truncated outer disk contributes to the rise in emission beyond 20 μm (Figures 1.11 and 1.12; D'Alessio et al., 2005; Calvet et al., 2005b; Hughes et al., 2009). Millimeter interferometric imaging has confirmed the presence inner disk holes in TW Hya (Hughes et al., 2007) and GM Aur (Figure 1.13; Hughes et al., 2009).

Transitional disks exhibit diverse properties. The estimated truncation radii of these disks cover a wide range, from 1 AU in Hen 3–600 (Uchida et al., 2004) to 43 AU in CS Cha (Chapter 3; Espaillat et al., 2007a). Some transitional disks have inner holes which are mostly cleared of small dust grains and exhibit no near-infrared excess (e.g. DM Tau, CoKu Tau/4). The rest have a small yet detectable near-infrared excess produced by some sub-micron and micron sized optically thin dust remaining within the inner disk hole (e.g. Calvet et al., 2005b, 2002; Espaillat et al., 2007a; Uchida et al., 2004).

Two years ago, we identified a new class of disk with inner disk clearing. These "pre-transitional disks" have gaps within their disks as opposed to the inner holes observed in transitional disks. Pre-transitional disks have a deficit of mid-infrared flux (5 – 20 μm) and substantial emission beyond 20 μm as is seen in transitional disks, but they have substantial emission in the near-infrared (2 – 5 μm), indicating the presence of an optically thick inner disk separated by a gap from an outer disk (Figure 1.14). UX Tau A and LkCa 15 are two such pre-transitional disks in the Taurus cloud (Chapter 5; Espaillat et al., 2007b). Their properties are listed in Table 1.1 and we will discuss them in greater detail in Chapter 5.

1.2.2 Disk Clearing Mechanisms

Several mechanisms have been proposed to create the inner disk holes seen in transitional disks. These mechanisms include dynamical clearing (i.e. planets, stellar companions), grain growth, photoevaporation, and the magnetorotational instability (MRI).

Planet formation theories predict that newly forming planets should interact with the surrounding disk, clearing the material around themselves through tidal disturbances (Goldreich & Tremaine, 1980; Ward, 1988; Rice et al., 2003; Paardekooper & Mellema, 2004; Quillen et al., 2004; Varnière et al., 2006). Planet clearing simulations have been able to reproduce the observed SEDs of transitional disks, particularly in the case of GM Aur (Rice et al., 2003). However, stellar companions can also dynamically clear the inner disk in a similar fashion (Mathieu et al., 1991; Artymowicz & Lubow, 1994). Aside from dynamical clearing, grain growth has been proposed as a disk clearing mechanism. Since dust evolves on faster timescales in the inner parts of the disk, eventually the small grains which contribute to the near-IR emission of the disk will grow causing a flux deficit in the SED (Dullemond & Dominik, 2004, 2005). It has also been proposed that X-rays from the star can activate the MRI in the ionized inner wall of the disk which will lead material to accrete from the wall onto the star, creating a hole in the disk that grows from the inside-out (Chiang & Murray-Clay, 2007). This MRI clearing mechanism predicts a correlation between the radius of the wall and the mass accretion rate and X-ray luminosity of the star. Radiation from the central star can also photoevaporate the surrounding disk (Hollenbach et al., 1994; Clarke et al., 2001). High energy photons from the star will heat the upper disk layers. The ionized gas will then attain a higher thermal energy than the gravitational potential energy and become unbound at the gravitational radius, $R_g \sim 7(M_*/M_\odot)$AU (Hollenbach et al., 1994). The typical value of the mass loss rate in this photoevaporative wind is $\sim 4\times10^{-10}$ $M_\odot$ yr^{-1} (Clarke et al., 2001). As the disk evolves viscously, the mass accretion rate decreases with time, eventually

reaching this value. When the disk accretion rate is this low, the outer disk mass is below $\sim$0.005 $M_\odot$ (Alexander & Armitage, 2007). At this point, the photoevaporative wind takes over and the disk is not resupplied within R_g (Clarke et al., 2001) and inward accretion onto the star will essentially stop. Once the isolated inner disk drains onto the star on the viscous timescale, the inner edge of the outer disk will be directly irradiated by the star and the hole will continue to grow outward as the disk continues to be photoevaporated (Alexander & Armitage, 2007). The timescale for the disk accretion rate to fall below the wind rate is a few Myr. The isolated inner disk will drain onto the star in $<10^5$ yr, and then the outer disk will be cleared within a few $<10^5$ yr (Alexander & Armitage, 2007).

Stellar mass companions have been confirmed within a few transitional disks. CoKu Tau4, HD98800B, and Hen 3–600 have stellar companions within their holes and their truncated disks are most likely due to clearing by the companion (Ireland & Kraus, 2008; Furlan et al., 2007; Uchida et al., 2004). Guenther et al. (2007) also found a companion in the inner hole of CS Cha although the separation of the stellar pair is less than 5 AU (Eike Guenther, private communication) which is too small to explain the truncation of the outer disk at $\sim$ 43 AU (Espaillat et al., 2007a) with existing models (Artymowicz & Lubow, 1994). Additional clearing mechanisms may be involved in clearing CS Cha's hole. TW Hya, GM Aur, DM Tau, LkCa 15, and UX Tau A are single stars down to about a few AU (White & Ghez, 2001; Ireland & Kraus, 2008) and no information exists on the multiplicity of CVSO 224.

Grain growth cannot explain the holes of the transitional disks around GM Aur, TW Hya, DM Tau, and CVSO 224 because they all have 10 μm silicate emission

features and the simulations predict there should be no small grains in the inner disk and hence no silicate emission (Dullemond & Dominik, 2005). The holes of GM Aur, TW Hya, DM Tau, and CVSO 224 can potentially be explained by the MRI. However, in order for this mechanism to work, an inner disk hole must already be present and so the MRI does not preclude planet formation nor is it an independent form of clearing. Photoevaporation cannot explain the holes of GM Aur, TW Hya, and DM Tau since their outer disks are massive ($M_{disk} > 0.05$ $M_{\odot}$; Calvet et al., 2002, 2005b) and their accretion rates are higher than the photoevaporative wind rate (Table 1.1). Photoevaporation could potentially explain the hole of CVSO 224 given its low mass accretion rate (Table 1.1; Chapter 4), however, its *Spitzer* IRS spectrum suggests it has a massive disk, contrary to what is expected in photoevaporative models (Alexander & Armitage, 2007). The exact mass of its outer disk cannot be currently estimated due to a lack of millimeter observations. The MRI, photoevaporation, and grain growth cannot explain the gaps seen in the pre-transitional disks around UX Tau A and LkCa 15 given that these inside-out clearing mechanisms cannot account for a remnant optically thick inner disk. According to current disk clearing theories, it seems that planet formation is most likely the dominant factor in clearing the inner disks of transitional and pre-transitional disks.

1.3 Overview of the Thesis

In this thesis, we will explore disks located within the Taurus, Chamaeleon, Ophiuchus, and Orion star–forming regions, with a particular emphasis on transitional and pre-transitional disks, in order to provide a fuller picture of dust evolution around

pre-main sequence stars. This will help refine theories of planet formation and develop timescales for the evolution of planetary systems.

The ∼1–3 Myr old Taurus cloud (Hartmann, 2003) is currently the most studied star–forming region. Its low levels of extinction (Kenyon & Hartmann, 1995) and nearby distance of 140 pc (Kenyon et al., 1994) make it an ideal test site. The Chamaeleon star–forming region is similar to Taurus in that it has relatively low levels of extinction, distributed star formation, and is close to the sun at a distance of 160 pc (Whittet et al., 1997). Chamaeleon has a median age of 2 Myr (Luhman, 2004), with objects ranging from 0.3 to 6 Myr in age (Luhman, 2007). The Ophiuchus region is the youngest studied here at an age of 0.1–1 Myr (Luhman & Rieke, 1999). It is located at 140 pc and its core is heavily embedded (Bontemps et al., 2001). We also study sources in the Ophiuchus off-core region which is less extincted and has an estimated age of 2 Myr (Wilking et al., 2005). Our last region, the Orion OB1 association, is a very large cloud complex located at ∼450 pc (Genzel & Stutzki, 1989). Within this region we look at the ∼10 Myr old 25 Orionis group (Briceño et al., 2007) located in the Orion OB1a sub-association of Orion OB1 (Briceño et al., 2005).

In Chapter 2, we explore the general characteristics of disks in Taurus, Chamaeleon, and Ophiuchus. In order to do this, we constructed a grid of ∼240 disks with the models of D'Alessio et al. (2006). This grid was calculated for different stellar masses, mass accretion rates, inclinations, grain sizes, dust compositions, and amounts of settling. We find that settled disks with low accretion rates and large grains will produce SEDs with a significant near-IR flux but substantially less emission at longer wave-

lengths and therefore may be mistakenly interpreted as disks undergoing clearing. We also use the grid to measure the slope of the SED between 13 μm and 31 μm versus the equivalent width of the 10 μm silicate feature for the disks in our sample and find that most disks can be explained by full disk models. However, there is a subset of disks that cannot be explained by the models. These $\sim$30 disks have more 10 μm silicate emission than is seen in full disks and we propose that these objects are pre-transitional disks with small gaps where the extra silicate emission arises from small optically thin dust located within the disk gap.

In Chapter 3, we model the transitional disk of CS Cha, located in the Chamaeleon cloud, and we detect a possible trend between grain growth and dust settling with age. The optically thin dust in the disk hole of the $\sim$2 Myr old CS Cha has grown to much larger sizes (2 μm; Espaillat et al., 2007a) than the dust in the inner holes of the $\sim$1 Myr old DM Tau and GM Aur (0.25 μm; Calvet et al., 2005b). Larger grains are also seen in the hole of the 10 Myr old TW Hya (Calvet et al., 2002). This may imply that there is some correlation between the process that creates the optically thin dust grains and dust evolution over time. CS Cha also needs a more settled outer disk to fit its millimeter emission indicating that its outer disk is in an advanced state of dust evolution. We also detect [Ne II] emission at 12.81 μm in CS Cha with *Spitzer* and find that there is no correlation between $L_{[NeII]}$ and L_X as would be expected if [Ne II] emission is due to X-ray heating (Glassgold et al., 2007). Given the variability of X-ray emission (Feigelson et al., 2007; Güdel et al., 2007), if any correlation was present, it may have been muted in these non-simultaneous data. We do find a correlation between $L_{[NeII]}$ and $\dot{M}$ which suggests that accretion

related EUV heating may be important in producing [Ne II] emission.

In Chapter 4, we model the transitional disk of CVSO 224 (Espaillat et al., 2008b), located in 25 Ori. It is one of the slowest accreting transitional disks found to date and provides a unique opportunity to explore the role of photoevaporation in transitional disks since its low $\dot{M}$ is in line with photoevaporative clearing theories. While it does have a low mass accretion rate, CVSO 224 has a significant infrared excess beyond 20 μm indicating that there is still a substantial outer disk in this object, contrary to what is expected from photoevaporative clearing models (Alexander & Armitage, 2007). Follow-up millimeter studies with the *SMA* or *CARMA* are needed to measure the mass of the outer disk in order to test if photoevaporation is the mechanism behind CVSO 224's clearing.

In Chapter 5, we identify a new class of "pre-transitional disks" around the stars UX Tau A and LkCa 15 in the Taurus cloud using broad-band *Spitzer* IRAC photometry and IRS spectra (Espaillat et al., 2007b). We model UX Tau A and LkCa 15 with gaps of $\sim$56 AU and $\sim$46 AU respectively. The location of LkCa 15's outer wall at $\sim$46 AU is in agreement with millimeter imaging (Piétu et al., 2006). In addition, we find that UX Tau A contains crystalline silicates in its outer disk ($\gtrsim$ 56 AU) while LkCa 15's silicates are amorphous and pristine.

In Chapter 6, we provide the first independent confirmation of a gap in the protoplanetary disk of LkCa 15 (Espaillat et al., 2008a). We previously showed that the substantial near-infrared excess of LkCa 15 could be explained by either optically thick primordial disk material or by optically thin dust (Espaillat et al., 2007b). In order to resolve this issue, we obtained a medium resolution near-infrared

SpeX spectrum spanning the wavelength range 2 – 5 μm (Espaillat et al., 2008a). We fit the near-IR excess of LkCa 15 with a single-temperature blackbody of 1600 K, within the range of dust sublimation temperatures found for a larger sample of disks by Monnier & Millan-Gabet (2002). This is firm evidence that the near-infrared excess of LkCa 15 originates from the wall of an optically thick inner disk at the dust destruction radius.

In Chapter 7, we present near-infrared Spex spectra of the pre-transitional disk UX Tau A as well as the transitional disks GM Aur and DM Tau. We demonstrate that the inner disk of UX Tau A is optically thick and confirm its membership in the pre-transitional disk class. We also show that the origin of the near-infrared excess in transitional and pre-transitional disks is different in nature.

In Chapter 8, we provide a summary of the thesis and propose directions for future work.

Table 1.1. Stellar and Disk Characteristics of Known Transitional and Pre-transitional Disk Sources

Target	R_{wall} (AU)	$\dot{M}$ ($M_\odot$ yr^{-1})	Spectral Type	M_* ($M_\odot$)	M_{disk} ($M_\odot$)	ϵ
TW Hya	$4^{(1)}$	$3.5^{(2)}\times 10^{-9}$	M1[12]	$0.5^{(2)}$	$0.02^{(13)}$	$0.1^{(13)}$
GM Aur	$20^{(4)}$	$7.2^{(2)}\times 10^{-9}$	K5[18]	$1.2^{(3)}$	$0.16^{(4)}$	$0.5^{(4)}$
DM Tau	$3^{(3)}$	$7.8^{(2)}\times 10^{-9}$	M1[9]	$0.65^{(3)}$	$0.05^{(3)}$	$0.1^{(3)}$
LkCa 15	$46^{(5,19)}$	$1.9^{(2)}\times 10^{-9}$	K5[9]	$1^{(5)}$	$0.1^{(5)}$	$0.001^{(5)}$
UX Tau A	$56^{(5,19)}$	$9.6^{(5)}\times 10^{-9}$	G6[18]	$1.5^{(5)}$	$0.01^{(5)}$	$0.01^{(5)}$
CVSO 224	$7^{(6)}$	$7^{(6)}\times 10^{-10}$	M3[10]	$0.3^{(6)}$	–	–
CS Cha[20]	$43^{(7)}$	$1.2^{(7)}\times 10^{-8}$	K6[11]	$0.91^{(7)}$	$0.04^{(7)}$	$0.01^{(7)}$
CoKu Tau/4[20]	$10^{(8)}$	$^{(8)}<<10^{-11}$	M1.5[9]	$0.5^{(8)}$	$0.0005^{(16)}$	–
HD98800B[20]	$6^{(14)}$	$^{(14)}<<10^{-11}$	K5[14]	–	–	–
Hen 3–600[20]	$1^{(15)}$	$5^{(17)}\times 10^{-11}$	M3[15]	$0.2^{(17)}$	–	–

[1]Calvet et al. (2002), [2]Ingleby & Calvet, submitted, [3]Calvet et al. (2005b), [4]Hughes et al. (2009), [5]Espaillat et al. (2007b), [6]Espaillat et al. (2008b), [7]Espaillat et al. (2007a), [8]D'Alessio et al. (2005), [9]Kenyon & Hartmann (1995), [10]Briceño et al. (2007), [11]Luhman (2004), [12]Batalha et al. (2002), [13]Espaillat et al. in preparation, [14]Furlan et al. (2007), [15]Uchida et al. (2004), [16]Andrews & Williams (2005), [17]Muzerolle et al. (2000), [18]Chapter 7

[19]For pre-transitional disks, we give the radius of the wall of the outer disk. The inner disk's wall is located at the dust destruction radius.

[20]CS Cha, CoKu Tau/4, HD98800B, and Hen 3–600 have known companions (Ireland & Kraus, 2008; Guenther et al., 2007; Furlan et al., 2007; Uchida et al., 2004).

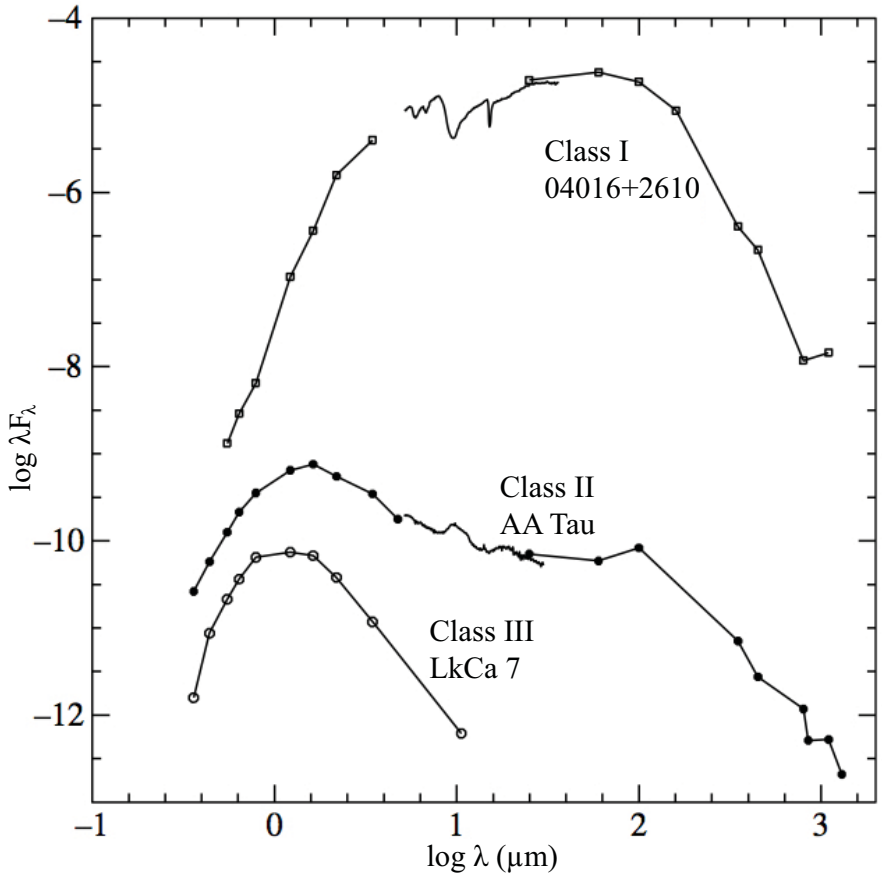

Figure 1.1 Spectral energy distributions of Class I, Class II, and Class III objects. 04016+2610 is a Class I object. These objects are still actively receiving mass from the molecular cloud core. The infalling envelope absorbs most of the radiation in the optical region. AA Tau is a Class II object. It is optically visible and also exhibits infrared emission originating from dust in a surrounding disk. LkCa 7 is a Class III object and has only photospheric emission. Figure adapted from Hartmann (2009). Optical and near-IR data points are from Kenyon & Hartmann (1995), IRS spectra are from Furlan et al. (2006), far-IR IRAS data are from Weaver & Jones (1992), and millimeter data are from Andrews & Williams (2005).

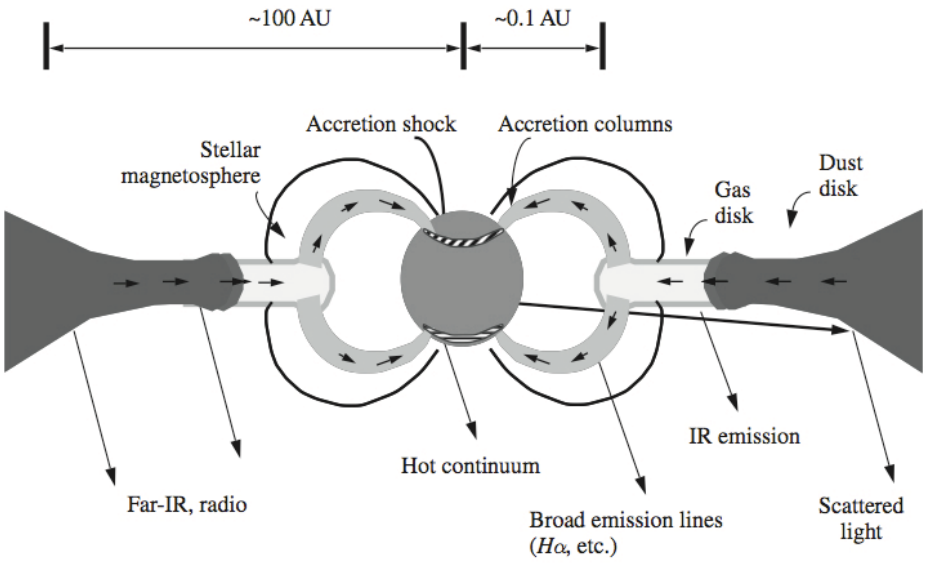

Figure 1.2 Inner disk of classical T Tauri stars. The dust disk is truncated at the dust sublimation radius, i.e. the radius at which the dust sublimation temperature is reached and dust can no longer exist. Within the dust sublimation radius there is only gas which is truncated at the magnetospheric radius and is channeled onto the star via magnetic field lines and impacts the star at the accretion shock. The hot continuum from the accretion shock veils the absorption lines in the optical and is conspicuous in the ultraviolet. The inner disk emits primarily in the infrared and at larger radii the disk emits in the far-infrared and radio. Scattered light from the disk surface is observed mainly at optical wavelengths. Figure taken from Hartmann (2009).

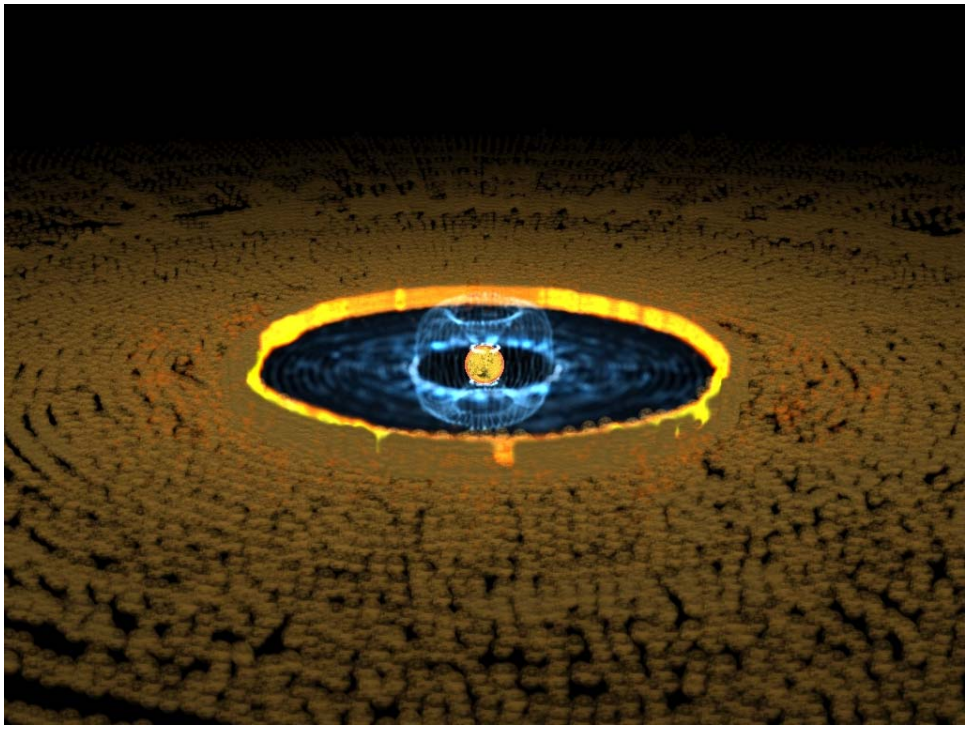

Figure 1.3 Artist's conception of the innermost disk region of classical T Tauri stars. The bright ring corresponds to the wall of the truncated dust disk located at the dust sublimation temperature. The inner gaseous disk is truncated by the stellar magnetic field. Art by L. Belerique. Figure taken from Calvet & D'Alessio (in press).

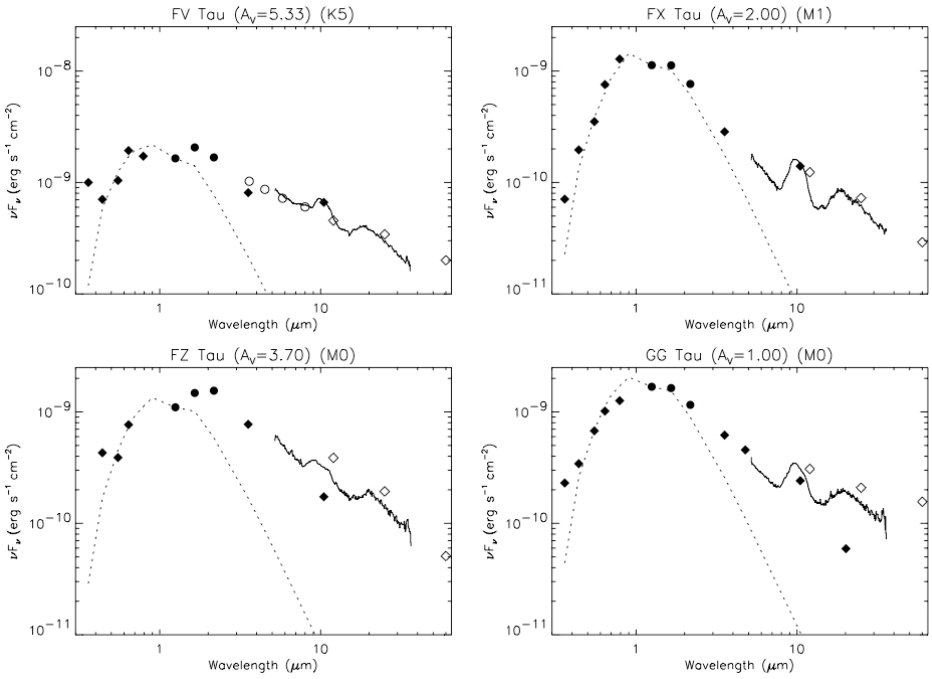

Figure 1.4 Spectral energy distributions of T Tauri stars with disks in Taurus. Most of the Taurus objects with disks display 10 μm silicate emission of varying strength. Dotted lines correspond to the stellar photosphere. Plotted symbols are data obtained with ground-based photometry, *Spitzer* IRAC, *Spitzer* MIPS, and IRAS. The solid spectra were taken with the *Spitzer* IRS instrument. Data are dereddened with the Mathis (1990) reddening law. Figure from Furlan et al. (2006).

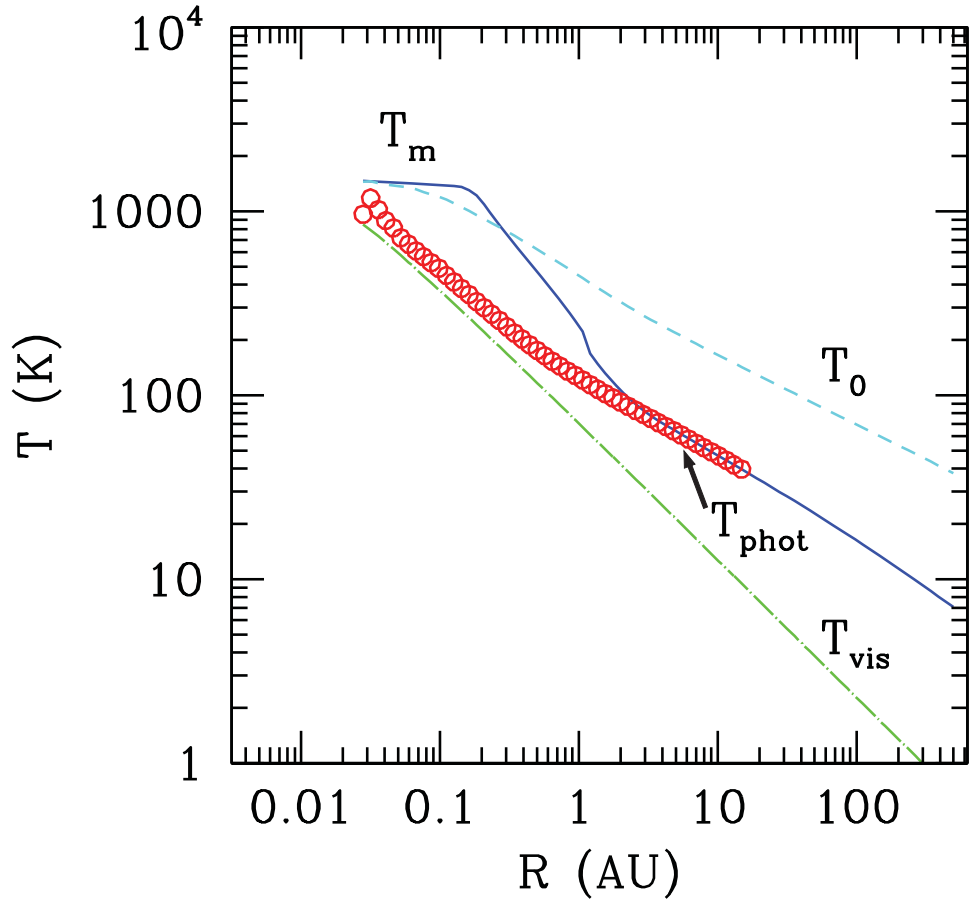

Figure 1.5 Characteristic temperatures of a disk model with well-mixed ISM-sized dust. Shown here are the surface temperature expected from a simple viscous disk (T_{vis}, green), the disk surface (T_0, cyan), the disk midplane (T_m, dark blue), and the disk photosphere (T_{phot}, red), defined in the regions where the disk is optically thick to its own radiation. The model shown here has $M_* = 0.5$ $M_\odot$, $R_* = 2$ $R_\odot$, $T_* = 4000$ K, and $\dot{M} = 10^{-8}$ $M_\odot$ yr^{-1}. Figure from Calvet & D'Alessio (in press).

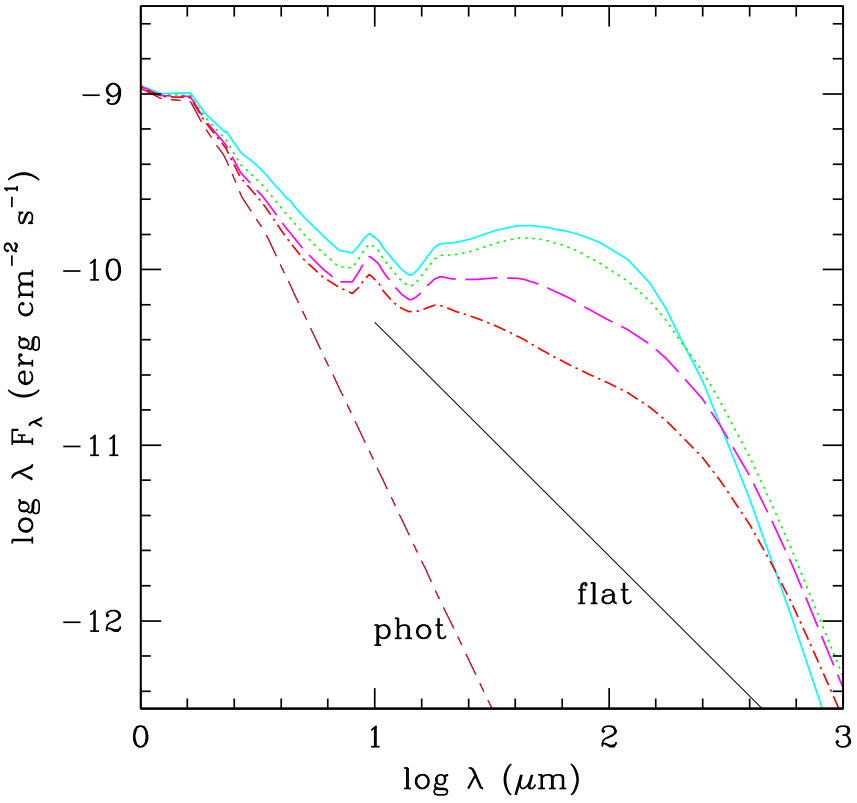

Figure 1.6 SEDs of disks with varying amounts of dust settling. Disks with settling parameters of ϵ=0.1 (green dotted line), 0.01 (magenta dashed line), and 0.001 (red dot-dashed line) are shown. For comparison the stellar photosphere (red short-long dashed line), the expected emission from a flat disk (heavy solid black line), and the emission from a well-mixed disk (light cyan solid line) are shown. Figure from Calvet & D'Alessio (in press).

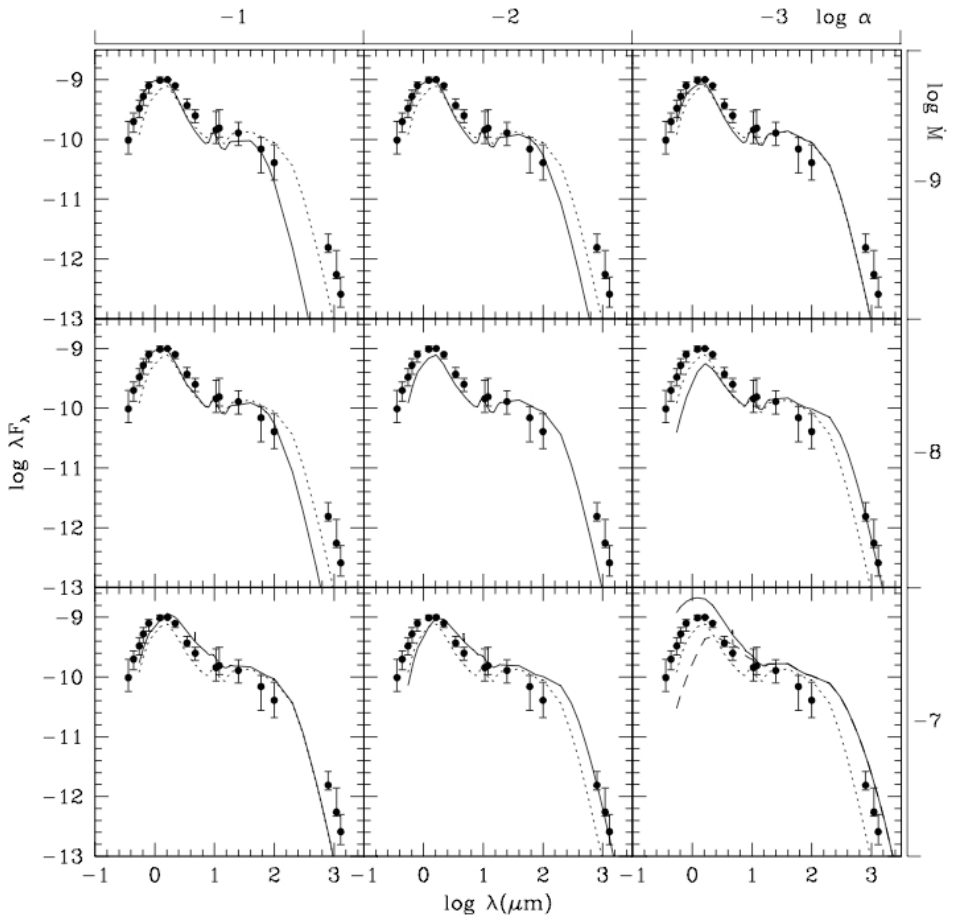

Figure 1.7 Models of disks with well-mixed ISM-sized grains compared to the observed median Taurus SED. Circles and bars correspond to the median Taurus SED and quartiles, respectively. The middle panel corresponds to the fiducial model which is repeated as the dotted line in the other panels. The models cannot simultaneously fit the infrared and millimeter emission. They tend to over-predict the infrared emission and under-predict the millimeter emission. In the model with α= 0.001 and a mass accretion rate of 10^{-7} $M_\odot$ yr^{-1}, the dashed line corresponds to a model with an inner radius of 4 R_* instead of the 3 R_* that is used in all the other panels. Figure taken from D'Alessio et al. (1999).

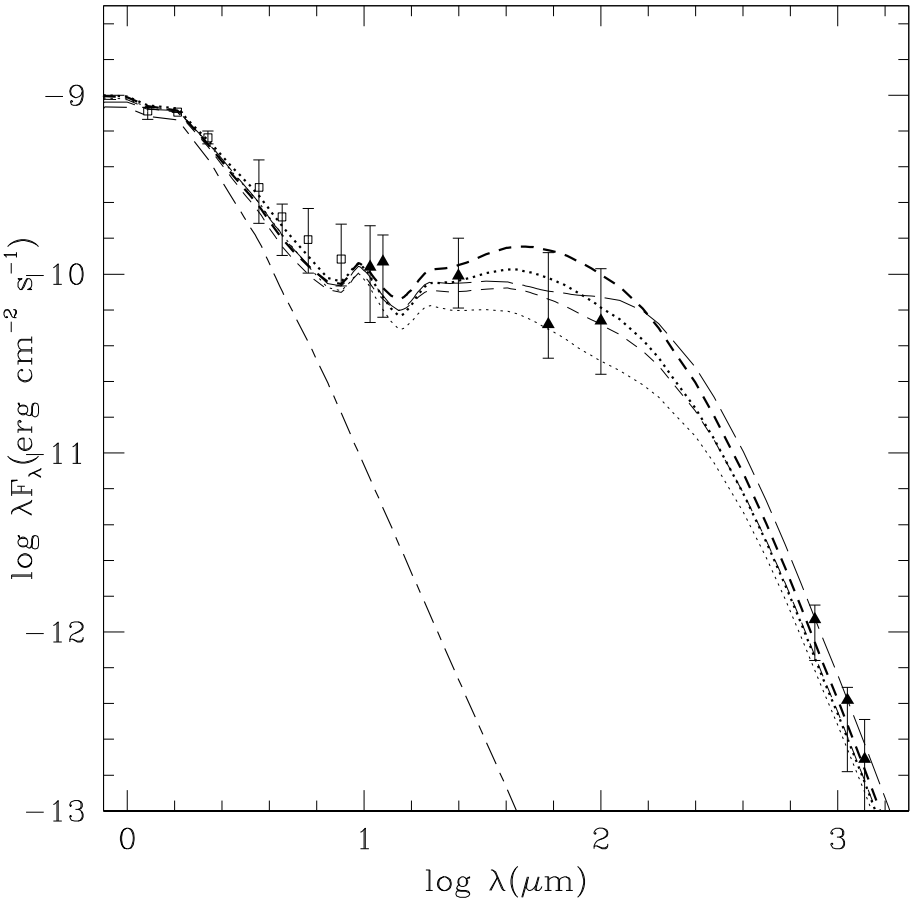

Figure 1.8 Models of disks with grain growth and dust settling compared to the observed median Taurus SED. Open squares and closed triangles are the median observations. Bars denote the quartiles of the observations. The short-dash-long-dashed line corresponds to the stellar photosphere. Other broken lines correspond to different disk models incorporating various amounts of settling (ϵ of 0.1, heavy lines; ϵ of 0.01, light lines) and inclinations (30°, dashed lines; 60°, dotted lines). The long-dashed line corresponds to a model with radially dependent settling. Figure from D'Alessio et al. (2006).

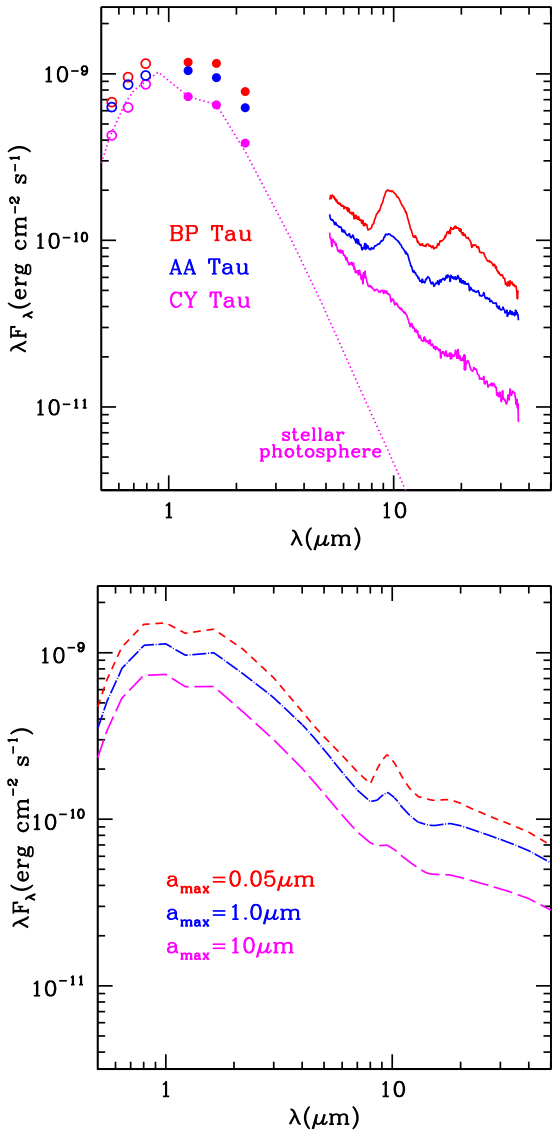

Figure 1.9 Grain growth in T Tauri disks. Top: Observed SEDs of the T Tauri stars BP Tau, AA Tau, and CY Tau located within the 1 Myr old Taurus cloud. All three disks exhibit advanced settling and varying degrees of grain growth. Ground-based optical (open circles) and J-, H-, and K- band data (closed circles) are shown along with *Spitzer* IRS data (solid lines). Bottom: Models of a typical $0.01 M_{\odot}$ T Tauri disk with maximum grain sizes of 0.05 μm (short dashed line), 1.0 μm (dot dashed), and 10 μm (long dashed) in the upper layers of the disk. As the size of the grains increases, the 10 μm silicate feature becomes wider and flatter and the ratio between the strengths of the 10 μm and 20 μm emission becomes smaller. These models assume a stellar mass of 0.5 $M_{\odot}$, a mass accretion rate of 10^{-8} $M_{\odot}$ yr^{-1}, an α of 0.01, and an ϵ of 0.001 which corresponds to a depletion of 1000 times the standard dust-to-gas mass ratio in the upper disk layers. Note that the models have been scaled arbitrarily in order to be displayed more clearly. The upper panel is based on data from Furlan et al. (2006) and the bottom panel is based on models presented in Chapter 2.

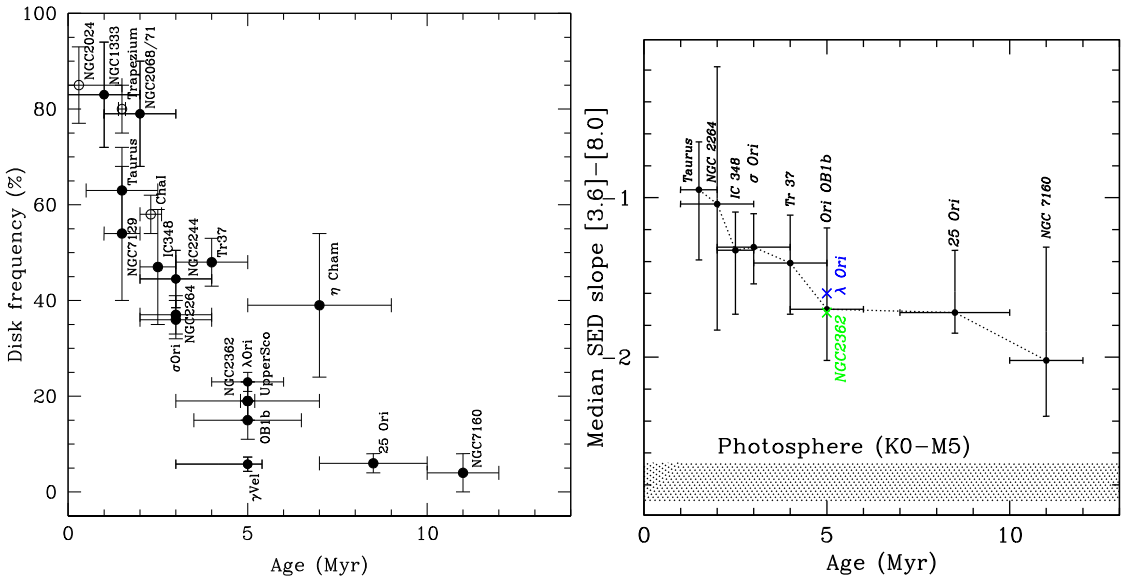

Figure 1.10 Indications of dust evolution in disks around TTS. Left: Fraction of objects with near-infrared emission measured in star–forming regions of various ages. The solid circles are clusters with *Spitzer* data and the open circles represent clusters whose disk frequency is measured with ground-based J-,H-, K-, and L-band photometry. Right: Median near-infrared slope measured with *Spitzer* IRAC as a function of age. The bars are quartiles and the hatched region corresponds to photospheric slope. Figures from J. Hernández, modified from Hernández et al. (2007).

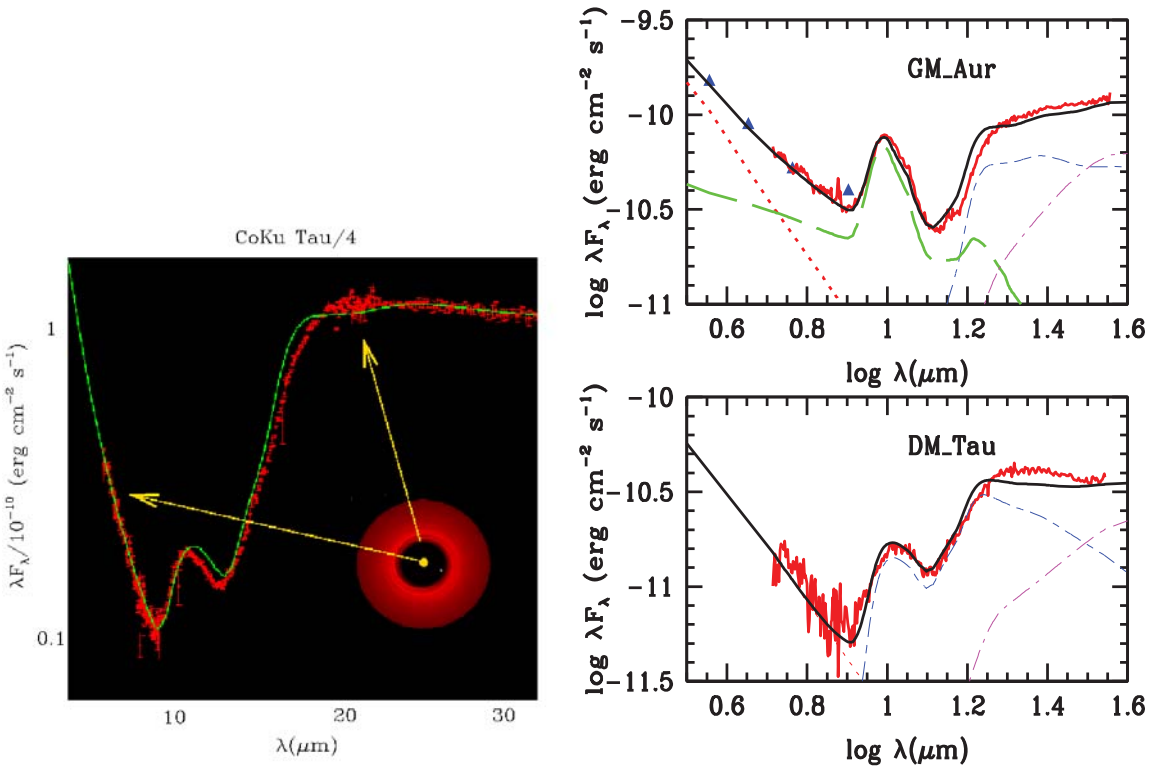

Figure 1.11 Spectral energy distributions of transitional disks in Taurus. Here we show CoKu Tau/4 (D'Alessio et al., 2005), GM Aur and DM Tau (Calvet et al., 2005b), centered on the *Spitzer* mid-IR spectra (red). The flux is essentially photospheric at shorter wavelengths, due to the absence of optically thick material in the inner disk. The long wavelength flux ($\lambda > 20$ μm) arises from the frontally illuminated wall of a truncated optically thick outer disk, as depicted in the accompanying drawing. Detailed models (solid lines) find that the hole sizes in these disks are 10 AU, 24 AU and 3 AU for CoKu Tau/4, GM Aur and DM Tau respectively. GM Aur has a non-negligible near-IR excess from a small amount of dust remaining in the inner hole. This small amount of dust produces the 10 μm silicate feature in GM Aur, whereas in CoKu Tau/4 and DM Tau this silicate feature comes from small grains in the wall atmosphere. Broken lines in the right panels correspond to different components of the model: stellar photosphere (dotted magenta line), optically thin inner region (long dashed green line), wall (short- long- dashed blue line), outer disk (short- long- dashed magenta line). Figure on left from P. D'Alessio, modified from D'Alessio et al. (2005). Figure on right from Calvet et al. (2005b).

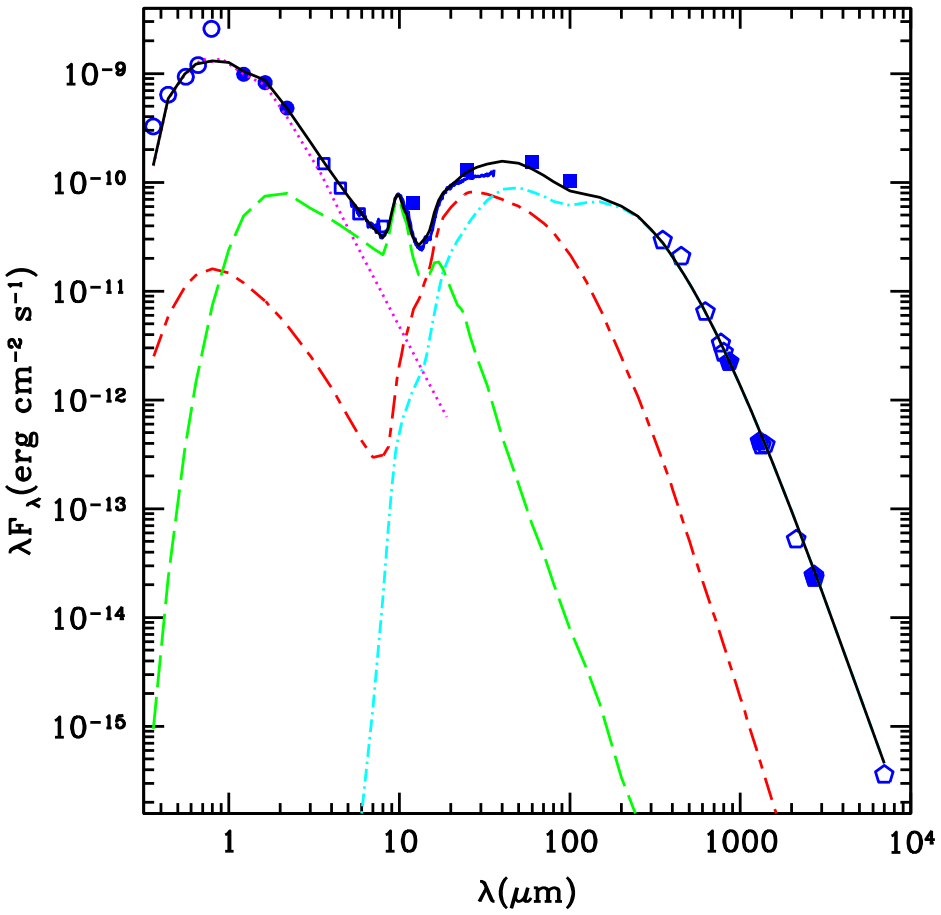

Figure 1.12 Model fit to the broad-band SED of GM Aur. The model fit to the SED has an inner disk hole of 20 AU. We show optical (open circles), 2MASS (closed circles), IRAC (open squares), and IRAS (closed squares) data, a *Spitzer* IRS spectrum (Calvet et al., 2005b), and millimeter data (open pentagons). The best-fit model (solid line) includes the following components: stellar photosphere (dotted line), optically thin dust region (long-dashed line), disk wall (short-long dashed line), outer disk (dot-dashed line). Figure from Hughes et al. (2009).

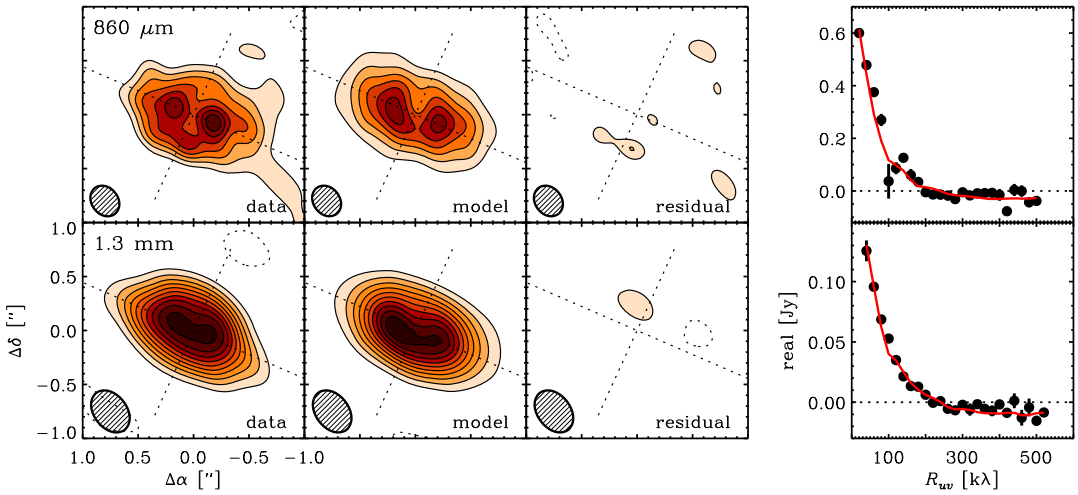

Figure 1.13 Continuum millimeter emission for GM Aur. Observations were taken with the *SMA* and are compared to model images with ϵ=0.5 from Figure 1.12. At the far right, observed visibilities (points) are compared to calculated visibilities based on model spatial brightness distributions (solid). Figure taken from Hughes et al. (2009).

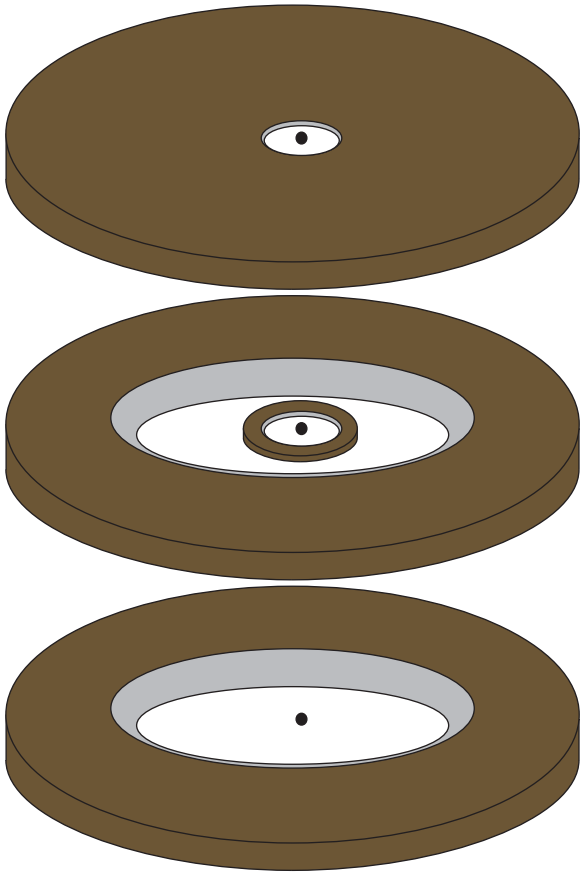

Figure 1.14 Schematic of the disk structure of full, pre-transitional, and transitional disks. Full disks (top) have dust throughout the disk, up to the dust destruction radius. Transitional disks (bottom) have inner holes in their distribution of dust and pre-transitional disks (middle) have gaps.

Chapter 2

Modeling Irradiated Accretion Disks Around T Tauri Stars

Abstract: In order to make a first attempt at describing the overall qualities of disks in Taurus, Chamaeleon, and Ophiuchus we created a grid of ∼240 disk models with the codes of D'Alessio et al. We present the physical properties and simulated SEDs of disks around 0.5 $M_\odot$ and 0.2 $M_\odot$ stars with mass accretion rates between 10^{-7} and 10^{-10} $M_\odot$ yr^{-1}, various amounts of dust settling, and different maximum grain sizes in the upper disk layers. We find that slowly accreting, settled disks with large grains in the upper layers will have SEDs that display a significant near-IR flux, as is seen in full disks, but substantially less emission at longer wavelengths. Such disks may be mistakenly interpreted as undergoing clearing. We explore the effects of incorporating different silicates in the disk and compare the resulting spectral energy distributions to the median SEDs of Taurus and Chamaeleon. We also use the grid to measure the slope of the SED between 13 μm and 31 μm versus the equivalent width of the 10 μm silicate feature. Aside from the well-known transitional and pre-transitional disks, most of the disks can be explained by typical "full" disk models. However, there is a subset of ∼30 disks which show stronger silicate emission than can be explained by the full disk models. We propose that these objects are pre-

transitional disks with small gaps (< 20 AU) where the extra silicate emission comes from optically thin small dust located within these disk gaps. Detailed modeling in conjunction with millimeter interferometric images are needed to confirm this.

2.1 Introduction

The Taurus, Chamaeleon, and Ophiuchus star–forming regions are young clouds located within 160 pc of the Sun (Kenyon et al., 1994; Whittet et al., 1997; Bontemps et al., 2001). Taurus and Chamaeleon are distributed populations of low-mass pre-main sequence stars (Kenyon & Hartmann, 1995; Luhman, 2004) while Ophiuchus consists of a densely populated core region and a distributed off-core region (Bontemps et al., 2001; Wilking et al., 2005).

Currently, the Taurus cloud is the most studied star–forming region. With *Spitzer* IRS spectra, Furlan et al. (2006) showed that disks in Taurus are not uniform in their mid-IR SEDs. They are experiencing grain growth and dust settling as evidenced by the strength of their 10 μm silicate features and varying mid-infrared slopes. Furlan et al. (2006) confirmed this by comparing the data to a grid of D'Alessio et al. disk models spanning different amounts of settling. In fact, most of the disks seemed to have undergone substantial settling, with ϵ of 0.01 and 0.001 corresponding to depletions of 100–1000 times the standard dust-to-gas mass ratio in their upper layers.

Here we do a more extensive grid and compare it to disks in Taurus, Chamaeleon, and Ophiuchus. This sample contains over 240 disks and given that individual, detailed modeling is time-intensive, we leave SED fits to future works. However,

with a grid of models we can test the general effects of dust composition, settling, inclination, mass accretion rate, and stellar mass on the SEDs. We find that ∼70% of the sample can be explained by full disk models. About ∼10% of the sample cannot be accounted for by full disk models and are known to be transitional and pre-transitional disks (see Section 1.2.1). However, ∼20% of the sample cannot be explained by the full disk models and they are also not known to be transitional or pre-transitional disks. We propose that these "outliers" are pre-transitional disks.

The recently identified pre-transitional disks have an optically thick inner disk separated from an optically thick outer disk by an optically thin gap (Espaillat et al., 2007b, 2008a). These disks with gaps provide a unique insight into the relationship between dust clearing and planets since their structure is most likely due to planet formation in its early stages, before the inner disk has drained onto the star. To date, we have only detected large gaps of ∼50 AU and the smaller gaps expected during the initial stages of planet formation have yet to be found. We propose that the "outliers" in Taurus, Chamaeleon, and Ophiuchus are pre-transitional disks with small gaps (<10 AU).

2.2 Overview of the D'Alessio Code

The D'Alessio code assumes that disks are steady (i.e. the mass accretion rate is constant), geometrically thin, and in vertical hydrostatic equilibrium. The mass accretion rate is constant throughout the disk and the viscosity is parameterized by α as per the viscosity prescription of Shakura & Syunyaev (1973). The disk is heated by viscous dissipation, radioactive decay, cosmic rays, and stellar irradiation. In most

cases, viscous dissipation dominates the heating at the midplane at small radii (< 1 AU) and irradiation dominates at all other radii. The code assumes that dust and gas are thermally coupled, which is unlikely in the uppermost disk layers.

The next section summarizes the work of Calvet et al. (1991, 1992), D'Alessio et al. (1998, 1999, 2001, 2005, 2006), and Calvet & D'Alessio (in press). See those works for a more detailed treatment of the following.

2.2.1 Vertical Disk Structure

Calvet et al. (1991) showed that disks are not vertically isothermal. As stellar radiation enters the disk, it does so at an angle to the normal of the disk surface ($\theta_0 = cos^{-1}\mu_0$). A fraction of the stellar radiation is scattered and the stellar radiation captured by the disk is $\sim (\sigma T_*^4/\pi)(R_*/R)^2\mu_0$. The star emits its energy mostly at shorter wavelengths and it is at these short wavelengths that the opacity of the dust in the disk is high. The stellar energy is absorbed by the dust at short wavelengths and gets re-emitted at longer wavelengths, corresponding to the local temperature of the disk, where the opacity of the dust is lower. Disks around hotter stars will capture more energy, and therefore have higher temperatures, than disks around cooler stars. The incident stellar radiation decreases with height in the disk since only a fraction of the stellar radiation ($d\tau_s/\mu_0$) reaches each height (z). The subscript s refers to the "stellar" range.

From the equation of conservation of energy, the vertical temperature profile can be written as

$$\kappa_P(T)\frac{\sigma T^4(z)}{\pi} = \kappa_P(T)J_d(z) + \kappa_P(T_*)\frac{\sigma T_*^4}{\pi}\left(\frac{R_*}{R}\right)^2 e^{-\tau_s/\mu_0} \tag{2.1}$$

where κ_P is the Planck mean opacity and J_d is the mean intensity (Calvet et al., 1991; D'Alessio et al., 1998, 1999). The subscript d refers to the "disk" range (i.e. the local disk temperature and emissivity). In the uppermost layers, the disk is optically thin and so $\tau_s/\mu_0 \ll 1$ and $e^{-\tau_s/\mu_0} = 1$. As the stellar radiation penetrates deeper into the disk, less of it is absorbed because the optical depth increases, and therefore the temperature decreases. The temperature also depends on μ_0 and the more the disk is flared, the hotter the disk will be at a given z.

D'Alessio et al. (1998) give the full set of differential equations that describe the disk vertical structure and solve them in detail. Figure 2.1 shows the characteristic heights in the disk. z_s is the height of the disk surface defined where $\tau_s \sim 1$ along the radial direction from the star, which is where most of the stellar radiation is absorbed; H_m is the gas scale height evaluated at the midplane temperature; z_{phot} is the photospheric height where $\tau_{Ross} \sim 1$, i.e. where the disk is optically thick to its own radiation. Note that the disk stays optically thick to the stellar radiation out to very large radii, even if the disk becomes thin to its own radiation.

Figure 2.2 shows that in the inner disk (< 1 AU), the temperatures in the midplane of the disk (T_{mid}) are higher than the temperatures in the upper layers of the disk (T_0) for typical conditions. Note that the plateau occurs at the dust sublimation temperature. Here the disk is very optically thick to its own radiation and effectively captures the energy, which is provided dominantly by viscous heating at these small radii. This can also be seen in the fact that the surface temperature of a viscous disk (T_{vis}) is similar to the photospheric temperature (T_{phot}), defined in the region where the disk is optically thick. At larger radii, irradiation heating dominates.

Further out, the disk surface temperature is greater than the midplane temperature ($T_0 > T_{mid}$) and the disk becomes optically thin beyond $\sim$ 50 AU to its own radiation; here the temperature is nearly isothermal in the midplane. At all radii, the surface temperature is higher than the photospheric temperature ($T_0 > T_{phot}$) and the upper layers of the disk are hotter than the deeper layers where $\tau_R \sim 1$ and the continuum forms. This "chromospheric effect" (Calvet et al., 1991, 1992) in the disk atmosphere leads to emission features, most notably the 10 μm silicate feature.

2.2.2 Disk Surface Density and Mass

Unlike most other disk models, the disk surface density of the D'Alessio models can be self-consistently calculated from the irradiated disk equations. From the conservation of angular momentum, the surface density is

$$\Sigma = \frac{\dot{M}}{4\pi\nu}\left[1 - \left(\frac{R_*}{R}\right)^{1/2}\right], \tag{2.2}$$

where $\dot{M}$ is the mass accretion rate, R_* is the stellar radius, and ν is the viscosity. With $\nu = \alpha c_s H = \alpha c_s^2/\Omega_K$ (Shakura & Syunyaev, 1973)

$$\Sigma = \frac{\dot{M}}{4\pi\alpha}\frac{\Omega\mu m_H}{k < T >}\left[1 - \left(\frac{R_*}{R}\right)^{1/2}\right], \tag{2.3}$$

where Ω is the Keplerian angular velocity and $< T >$ is the vertically averaged temperature. The disk mass is given by

$$M_d = \int_{R_i}^{R_d} \Sigma 2\pi R dR \tag{2.4}$$

where R_d and R_i are the outer and inner radii of the disk, respectively. Figure 2.3 illustrates the surface density and mass of the disk as a function of radius. While

the surface density decreases with radius, the surface area of the disk increases with radius and so the mass of the entire disk is mostly in the outer disk. As is seen in Figure 2.3, $\Sigma \propto R^{-1}$ given that $T \propto R^{-1/2}$ (Equation 2.1).

2.2.3 The Effect of Dust Opacity on Disk Structure

The opacity of the disk, and hence the temperature structure, is controlled by dust. The dust opacity depends on changes in the dust due to grain growth and settling. Grains grow through collisional coagulation and settle to the disk midplane due to gravity (Weidenschilling et al., 1997; Dullemond & Dominik, 2004, 2005).

Smaller grains have higher opacities at shorter wavelengths than at longer wavelengths. Bigger grains have higher opacities than small grains at longer wavelengths and less at shorter wavelengths. The models assume spherical grains with a distribution of a^{-p} where a is the grain radius between a_{min} and a_{max}. Figure 2.4 shows how the opacity varies with wavelength for dust distributions of $p = 2.5$ and 3.5 for different maximum sizes and temperatures for mixtures with silicates, troilite, ice, and organics (Pollack et al., 1994). One can see that a mixture with a smaller a_{max} has a larger opacities at shorter wavelengths than mixtures with a larger a_{max}. As the maximum grain size increases, the opacity of the dust mixture becomes higher at longer wavelengths.

The dust opacity sets the location of the disk surface, z_s. Since z_s is defined by the height where $\tau_s \sim 1$, small grains will reach this limit higher in the disk relative to big grains. Smaller grains result in a higher z_s at each radius, and hence lead to more disk flaring. Therefore, μ_0 is larger and more stellar irradiation will be intercepted

by the disk and the disks will be hotter. Bigger grains have lower opacities in the near-IR and as a result will have less flaring and lower temperatures.

Increased settling will also lower z_s. The code assumes settling does not vary with radius, which is likely untrue given that evolutionary timescales are more rapid closer to the star, but we leave an exploration of this to future work. The settling is parameterized by $\epsilon = \zeta_{small}/\zeta_{standard}$ where ϵ is equal to the dust-to-gas mass ratio in the upper layers of the disk relative to the standard dust-to-gas mass ratio. Settling lowers z_s since it decreases the dust-to-gas mass ratio of the upper disk; as a result, there are less grains overall and fewer small grains, with a corresponding decrease in the opacity and flaring. The resulting decrease in infrared emission is similar to what one would see if we increased the grain size in the upper disk layers. However, one difference between increasing the settling and increasing the grain size is that with settling, small grains remain in the upper disk layers and so we still see silicate emission. With grain growth, the silicate emission disappears since larger grains do not have this feature in their opacity.

2.2.4 Inner Disk Wall

According to the magnetospheric accretion model, the inner disk is truncated by the stellar magnetic field. However, the stellar radiation will destroy the dust out to a radius where the it is at the dust sublimation temperature. This will create an inner edge or "wall" of the dust disk which is frontally illuminated by the star (Natta et al., 2001). Here we review D'Alessio et al. (2005)'s treatment of the inner disk wall. This treatment assumes the gas between the magnetospheric truncation radius and the

dust destruction radius is optically thin and does not contribute to the heating of the wall.

The wall's optical depth increases radially and is optically thin closest to the star. The stellar radiation impinges directly onto the wall, with an angle of 0° to the normal of the wall's surface. The wall is also assumed to be vertical and flat with evenly distributed dust. In addition, light is isotropically scattered.

Following Calvet et al. (1991, 1992), the radial distribution of temperature for the wall atmosphere is

$$T_d(\tau_d)^4 = \frac{F_0}{4\sigma_R}[(2+\frac{3}{q}) + (\frac{\kappa_s}{\kappa_d} - \frac{3}{q})e^{-q\tau_d})] \tag{2.5}$$

where $F_0 = L_* + L_{acc}/4\pi R_{wall}^2$, σ_R is the Stefan-Boltzmann constant, τ_d is the total mean optical depth in the disk, and κ_s and κ_d are the mean opacities at the stellar and disk temperatures. The wall atmosphere has an inversion in the temperature with radius (T(τ_d=0)>T(τ_d ~1)) and so emission features can also originate in the wall. To get the location of the wall, one sets $\tau_d = 0$ and

$$R_{wall} = [\frac{(L_* + L_{acc})}{16\pi\sigma_R}(2 + q\frac{\kappa_s}{\kappa_d})]^{1/2}\frac{1}{T_0^2}. \tag{2.6}$$

At the dust sublimation radius $T_0 = T_{sub}$, which is usually taken to be 1400 K. L_* is the stellar luminosity and L_{acc} ($\sim GM_*\dot{M}/R_*$) is the luminosity of the accretion shock onto the stellar surface, which also heats the inner wall. The opacity in the wall (κ_s/κ_d) is due to silicates and smaller dust grains will have a larger opacity ratio and hence a larger R_{wall}.

2.3 Grid of Disk Models

We created a grid of ∼240 disks with the models of D'Alessio et al. for comparison with disks in Taurus, Chamaeleon, and Ophiuchus. This grid was calculated for stellar masses of 0.5 $M_\odot$ and 0.2 $M_\odot$, corresponding to spectral types of about K7 and M5 respectively. We obtained stellar parameters by using the pre-main-sequence tracks of Baraffe et al. (2002). For the 0.5 $M_\odot$ star, we adopted a R_* of 2 $R_\odot$, a temperature of 4000 K, and a L_* of 0.9 $L_\odot$ (Table 2.1). For the 0.2 $M_\odot$ star, we adopted a R_* of 1.4 $R_\odot$, a temperature of 3240 K, and a L_* of 0.2 $L_\odot$ (Table 2.1). To plot the simulated SEDs in Section 2.4.2, we used photospheric colors from Kenyon & Hartmann (1995) scaled to the flux of the adopted stellar parameters in the J-band assuming a distance of 140 pc (Table 2.1).

For the dust opacity, we use amorphous silicates with a standard dust-to-gas mass ratio of 0.004 and graphite with a standard dust-to-gas mass ratio of 0.0025 (Draine & Lee, 1984), both with ISM-sized dust with a_{min} of 0.005 μm and a_{max} of 0.25 μm (Mathis et al., 1977) in the upper layers and a_{min} of 0.005 μm and a_{max} of 1000 μm in the disk midplane with a p of 3.5 (see Section 2.2.3). Graphite opacities are taken from Draine & Lee (1984). Given the difference in opacity between different silicate compositions (Figure 2.5), we test the effect of incorporating different silicates on the simulated SED by comparing SEDs with astronomical silicates from Draine & Lee (1984) to those with olivine silicates from Dorschner et al. (1995). We note that the peak of the opacity at ∼10 μm is about the same for both dust compositions, however, the olivine silicates have more flux above the continuum in the ∼10 μm feature. The astronomical silicates have higher opacities at ∼2–7 μm. We also explore the effects

of changing a_{max} in the upper disk layers for both silicate compositions.

In each grid we use mass accretion rates of 10^{-7}, 10^{-8}, 10^{-9}, and 10^{-10} $M_\odot$ yr^{-1}, inclinations of 20°, 40°, 60°, and 80°, an α parameter of 0.01, and settling parameters (ϵ) of 1, 0.1, 0.01, and 0.001. The outer disk radius is taken to be 300 AU in all cases and we adopt a distance of 140 pc to the star. Tables 2.2 and 2.3 list the sublimation radii, wall heights, and disk masses for grids using astronomical silicates in disks around stars with stellar masses of 0.5 $M_\odot$ and 0.2 $M_\odot$, respectively. Tables 2.4 and 2.5 list the same information for grids using olivines in disks around stars with stellar masses of 0.5 $M_\odot$ and 0.2 $M_\odot$. The dust sublimation radius is obtained following Equation 2.6 and the disk mass is calculated with Equation 2.4. The height of the wall (h_{wall}) is typically taken to be a free parameter whose value is set by fitting to the observations (Calvet et al., 2005b; D'Alessio et al., 2005), however, here we assume that the wall is the same height as the disk behind it at the dust sublimation radius (R_{sub}). In Tables 2.2 through 2.5 we present the height of the wall in terms of both AU and the gas scale height. In some cases, the value of the Toomre parameter ($Q = c_s(T_c)\Omega/\pi G\Sigma$) is greater than or equal to 1 at radii greater than ∼100 AU in disks with mass accretion rates of 10^{-7} $M_\odot$ yr^{-1}, indicating that these disks are are gravitationally unstable. Since the model approximations are no longer valid in these cases, we do not present those disks in this work.

Several of the following figures have been presented in D'Alessio et al. (2006) for the case of a disk using astronomical silicates around a 0.5 $M_\odot$ star (Table 2.2), however, here we present these cases again in order to facilitate comparison with our other grids.

2.4 Results

2.4.1 Disk Properties

Here we explore the basic effects of stellar mass, mass accretion rate, and settling on the structure and properties of disks with astronomical silicates. Using a different silicate composition will not significantly alter the main conclusions of this section and so we do not present results using olivine silicates.

The disk is optically thick to its own radiation when the Rosseland mean optical depth (τ_R) is greater than 1. This sets the height (z_{phot}) above which the disk is optically thin and it is from this "disk atmosphere" that silicate features originate. In Figures 2.6 and 2.7 we present τ_R as a function of radial distance in the disk, integrated from the disk midplane to the surface. For disks with a mass accretion rate of 10^{-10} $M_\odot$ yr^{-1}, the disk is optically thick to its own radiation within $\sim$1 AU; for disks accreting at 10^{-9} $M_\odot$ yr^{-1} the transition from optically thick to optically thin occurs at $\sim$5 AU; for disks accreting at 10^{-8} $M_\odot$ yr^{-1} this occurs at $\sim$30 AU, and for disks accreting at 10^{-7} $M_\odot$ yr^{-1} this happens at $\sim$100 AU.

The range over which $\tau_R > 1$ sets the radii where the photospheric temperature (T_{phot}) is defined in Figures 2.8 through 2.14. For each stellar mass, accretion rate, and settling parameter explored in this chapter, the photospheric temperature is lower than that of the disk surface ($T_{phot} < T_0$), resulting in a "chromospheric effect" (Calvet et al., 1991, 1992) which causes the silicate emission feature to always be in emission in our model grid, unless the feature is extinguished by the disk itself.

By comparing the viscous temperature (T_{vis}) with the photospheric temperature,

one can see that in some cases viscous heating is important in the midplane of the inner disk. Viscous heating dominates when the midplane temperature is higher than the photospheric temperature ($T_c > T_{phot}$). This occurs in disks with mass accretion rates of 10^{-9} $M_\odot$ yr^{-1} (Figures 2.9 and 2.13), 10^{-8} $M_\odot$ yr^{-1} (Figures 2.10 and 2.14), and 10^{-7} $M_\odot$ yr^{-1} (Figure 2.11). In these disks, the inner regions are very optically thick to their own radiation($\tau_R \gg 1$; Figures 2.6 and 2.7) and are more efficient at trapping their own energy. Note that the plateau in T_c seen in disks accreting at 10^{-8} $M_\odot$ yr^{-1} and 10^{-7} $M_\odot$ yr^{-1} occurs at the dust destruction temperature (1400 K). In disks with low mass accretion rates (Figures 2.8 and 2.12), the photospheric temperature is similar to the midplane temperature ($T_c \sim T_{phot}$). This indicates that the disk becomes optically thick to its own radiation at the midplane. We will explore the implications of this new result in Sections 2.4.2 and 2.5.

Figures 2.15 through 2.21 present the cumulative emergent flux as a function of disk radius at wavelengths of 7 μm, 10 μm, 16 μm, 25 μm, 40 μm, 100 μm, and 1000 μm for mass accretion rates, settling parameters, and stellar masses used in our model grid. The emission is calculated for disks which are face-on with a negligible contribution from the wall, which is assumed to be flat and vertical. We find that all of the 10 μm silicate emission originates within the inner 20 AU of disks around $0.5M_\odot$ stars and from within 10 AU for 0.2 $M_\odot$ stars. For disks with mass accretion rates of 10^{-10} $M_\odot$ yr^{-1}, around 0.5 $M_\odot$ stars, 80% of the emission shortwards of 10 μm comes from within .5 AU for ϵ=0.001 and 2AU for ϵ=1.0; around 0.2 $M_\odot$ stars, 80% of this emission is from within 0.15 AU for ϵ=0.001 and .5 AU for ϵ=1.0. For disks with $\dot{M}$ of 10^{-9} $M_\odot$ yr^{-1}, around 0.5 $M_\odot$ stars, 80% of the emission shortwards

of 10 μm comes from within .7 AU for ϵ=0.001 and 2AU for ϵ=1.0; around 0.2 $M_\odot$ stars, 80% of this emission is from within 0.2 AU for ϵ=0.001 and .5 AU for ϵ=1.0. For disks with mass accretion rates of 10^{-8} $M_\odot$ yr^{-1}, around 0.5 $M_\odot$ stars, 80% of the emission shortwards of 10 μm comes from within 1 AU for ϵ=0.001 and 2AU for ϵ=1.0; around 0.2 $M_\odot$ stars, 80% of this emission is from within 0.2 AU for ϵ=0.001 and .25 AU for ϵ=1.0. For disks with $\dot{M}$ of 10^{-7} $M_\odot$ yr^{-1}, 80% of the emission shortwards of 10 μm comes from within 0.6 AU for ϵ=0.001 around 0.5 $M_\odot$ stars. These results show that the 10 μm silicate emission feature and the emission from shorter wavelengths is a good tracer of the innermost disk.

Overall, 50% of the millimeter emission comes from within 70 AU in disks around 0.5 $M_\odot$ stars and from within 60 AU in disks around 0.2 $M_\odot$ stars. For disks with mass accretion rates of 10^{-10} $M_\odot$ yr^{-1}, around 0.5 $M_\odot$ stars, 50% of the millimeter emission is from within 20 AU for ϵ of 0.001 and 70 AU for ϵ of 1; around 0.2 $M_\odot$ stars, 50% of the millimeter emission is from within 15 AU for ϵ of 0.001 and 60 AU for ϵ of 1. For mass accretion rates of 10^{-9} $M_\odot$ yr^{-1}, around 0.5 $M_\odot$ stars, 50% of the millimeter emission is from within 20 AU for ϵ of 0.001 and 60 AU for ϵ of 1; around 0.2 $M_\odot$ stars, 50% of the millimeter emission is from within 15 AU for ϵ of 0.001 and 40 AU for ϵ of 1. For mass accretion rates of 10^{-8} $M_\odot$ yr^{-1}, around 0.5 $M_\odot$ stars, 50% of the millimeter emission is from within 40 AU for ϵ of 0.001 and 50 AU for ϵ of 1; around 0.2 $M_\odot$ stars, 50% of the millimeter emission is from within 20 AU for ϵ of 0.001 and 35 AU for ϵ of 1. For mass accretion rates of 10^{-7} $M_\odot$ yr^{-1}, 50% of the millimeter emission is from within 60 AU for ϵ of 0.001 around 0.5 $M_\odot$ stars. In summary, about 25% of the millimeter emission comes from within the

inner optically thick regions of the disk (see Figures 2.6 and 2.7).

2.4.2 SED Simulations

In Figures 2.22 and 2.23 we present simulated SEDs for disks using astronomical silicates around 0.5 $M_\odot$ and 0.2 $M_\odot$ stars for various mass accretion rates and settling parameters at an inclination of 60°. Extinction of the star by the disk is included and it is significant in those disks with less settling, and hence a higher disk surface which leads to greater extinction of the star by the outer disk. For a 0.2 $M_\odot$ star with a mass accretion rate of 10^{-8} $M_\odot$ yr^{-1} and a settling parameter of 1.0, the silicate emission feature is strongly extincted by the outer disk and appears to be in absorption. Extinction of the star by the disk becomes even more apparent at higher inclinations. Figures 2.24 and 2.25 illustrate the effect of inclination on the resultant disk emission. While inclination effects can cause significant flux deficits in the infrared, the stellar emission will be extinguished as well and so inclined disks will not have SEDs which resemble those of transitional disks.

In Figure 2.26 we illustrate the effect of increasing the grain size in the upper layers of the disk. The emission from wavelengths of $\sim$10 μm out to a few hundred microns tends to decrease with increasing grain size because the opacity in the upper layers decreases as the grain size increases. The millimeter emission remains about the same since most of this emission comes from the midplane at larger radii. The 10 μm feature is also "washed out" as the maximum grain size increases (Figure 2.27). In Figure 2.28, we show the contributions to the SED from the wall emission and the thermal disk emission. The wall dominates the emission in the near-IR and the disk

emission dominates at longer wavelengths. When compared to the disks around 0.5 $M_\odot$ stars, the disks around 0.2 $M_\odot$ stars have less silicate emission relative to the continuum for each a_{max} in grid (Figures 2.29, 2.30, and 2.31). This is because the disks in the 0.2 $M_\odot$ grid have lower disk surface temperatures overall relative to the disks in the 0.5 $M_\odot$ grid.

The strength of the silicate emission also changes for different adopted silicate compositions. Figures 2.32 and 2.33 compare disks with astronomical and olivine silicates with ϵ of 0.1 and 0.001 around 0.5 $M_\odot$ and 0.2 $M_\odot$ stars, respectively. The results are reflective of the silicate opacities shown in Figure 2.5. Around both stars, the disks in the olivine grid have more silicate emission above the continuum at 10 μm and 20 μm and the disks with astronomical silicates have slightly more near-IR emission. In Figures 2.34 and 2.35 we present simulated SEDs for disks around 0.5 $M_\odot$ and 0.2 $M_\odot$ stars with olivine silicates. When compared to Figures 2.22 and 2.23, it is apparent that the disks with olivine silicates have more prominent 10 μm and 20 μm silicate features.

In Figure 2.36 we illustrate the effect of increasing the grain size in the upper layers of the disk when adopting olivine silicates. The 10 μm feature is also "washed out" as the maximum grain size increases (Figure 2.37) as was seen in the case of astronomical silicates. In contrast, there is a difference in the near-IR emission: grain size distributions with $a_{max} > 1$ μm have stronger near-IR emission than distributions with smaller a_{max}. The contribution to the 10 μm silicate emission from the wall is larger for smaller grain sizes in the case of olivine silicates (Figure 2.38) than was seen for astronomical silicates. For disks around 0.2 $M_\odot$ stars with olivine silicates,

increasing the maximum grain size leads to weaker silicate emission features as well (Figures 2.39). However, there is no significant difference in the near-IR emission as was seen in the disks around 0.5 $M_\odot$ stars with olivine silicates (Figure 2.40) and the contribution of the wall to the silicate emission is even higher (Figure 2.41). We note that if we varied the height of the wall these relative differences in the near-IR emission and the wall's contribution to the silicate feature could be adjusted.

In Section 2.4.1 we found that in disks with low mass accretion rates, the photospheric temperature was similar to the midplane temperature, indicating that the disk becomes optically thick to its own radiation at the midplane and that we are seeing down to the midplane of the disk. In Figure 2.42 we illustrate the effect of using a large a_{max} (10 μm) in the upper disk layers in a very settled disk (ϵ=0.001) with a mass accretion rate of 10^{-10} $M_\odot$ yr^{-1} around a 0.5 $M_\odot$ star. We find that relative to disks with higher accretion rates, even those with larger grains, the very low opacities due to using large grains in a slowly accreting, settled disk results in a SED with a significant deficit of flux at longer wavelengths, even in the millimeter. When taken in conjunction with the relatively "normal" near-IR excess, the observed SEDs of such disks may be mistaken as disks with clearing or as small, outwardly truncated disks.

2.4.3 Comparison to Observations

In Figures 2.43, 2.44, and 2.45 we compare the models using astronomical silicates to the median observed SEDs of K5–M2 stars in Taurus as well as K5–M2 and M3–M8 stars in Chamaeleon, respectively. For the higher mass stars in Taurus and

Chamaeleon, the models which provide the best fit to the medians have mass accretion rates of 10^{-8} $M_\odot$ yr^{-1} and 10^{-7} $M_\odot$ yr^{-1} (Figures 2.43 and 2.44). For the lower mass stars in Chamaeleon, the models with higher mass accretion rates of 10^{-9} $M_\odot$ yr^{-1} and 10^{-8} $M_\odot$ yr^{-1} also fit the median observed SED better (Figure 2.45). Using olivine silicates improves the fits to the medians at $\sim$20 μm and beyond, however, it is still difficult to account for the upper quartile of the median (Figures 2.46 , 2.47, and 2.48). We discuss possible explanations for this discrepancy in Section 2.5.

In order to compare the models to the observations with a diagnostic which is less dependent on the resultant disk flux, we measure the slope of the SED between 13–31μm versus the equivalent width of the 10 μm silicate feature. Figure 2.49 shows that the grid covers a large parameter space with 10 μm silicate equivalent widths ranging from $\sim$0.2–3.5 and slopes between 13–31 μm of $\sim$-0.5–1. When comparing the parameter space covered by the grid (polygon, Figure 2.50) with the observations (points, Figure 2.50) we find that the full disk models can account for $\sim$70% of the disks in Taurus, Chamaeleon, and Ophiuchus. The vast majority of the most extreme outliers with the steepest slopes and the most silicate emission, are well-known transitional and pre-transitional disks (labeled points, Figure 2.50) and account for $\sim$10% of the observations. However, $\sim$20% of the disks cannot be explained by full disk models and are not known to be transitional or pre-transitional disks.

2.5 Discussion & Conclusions

We expand the previous grid done by D'Alessio et al. (2006) to stellar masses of 0.2 $M_\odot$ and 0.5 $M_\odot$, mass accretion rates of 10^{-7} to 10^{-10} $M_\odot$ yr^{-1}, inclinations spanning ~ 0 to $\sim 90°$, settling parameters of 1, 0.1, 0.01, and 0.001, maximum grain sizes of 0.05 μm–1000 μm in the upper disk layers, and dust compositions including astronomical and olivine silicates. We find that the disk is optically thick to its own radiation ($\tau_R > 1$) within 1 AU for disks with accretion rates of 10^{-10} $M_\odot$ yr^{-1}, 5 AU for disks accreting at 10^{-9} $M_\odot$ yr^{-1}, 30 AU for disks accreting at 10^{-8} $M_\odot$ yr^{-1}, and 100 AU for disks accreting at 10^{-7} $M_\odot$ yr^{-1}. For all of the disks in our grids, the disk surface temperature is higher than the temperature at the disk photosphere, defined as where $\tau_R > 1$, leading to a "chromospheric effect" which causes silicate features to appear in emission (Calvet et al., 1991, 1992).

We find differences between disks around 0.5 $M_\odot$ stars and 0.2 $M_\odot$ stars. All emission at wavelengths of 10 μm and shorter arises from the inner 20 AU of disks around 0.5 $M_\odot$ stars and 10 AU for 0.2 $M_\odot$ stars. About 50% of millimeter emission originates in the inner 70 AU of disks around 0.5 $M_\odot$ stars and 60 AU for 0.2 $M_\odot$ stars. In each, an increase in a_{max} in the upper layers of the disk leads to a decrease in the disk emission between wavelengths of 10 μm to a few 100 μm, but the millimeter emission remains the same. The biggest difference between adopting astronomical or olivine silicates in the disk is the strength of the silicate emission; for olivines, this emission is much stronger.

In disks with low mass accretion rates, we find that the photospheric temperature is similar to the midplane temperature, indicating that the disk becomes optically

thick to its own radiation at the midplane. In essence, we are peering down to the midplane of the disk, past the upper layers. This has important implications on disk studies of slowly accreting disks. Previously, we had no good tracers of the midplane in the innermost disk of TTS. These results indicate that *Spitzer* IRS spectra are a powerful tool in accessing not only the upper layers of the disk but also the midplane of the disk. This finding encourages further study of disks with low mass accretion rates in order to probe the dust in the inner disk midplane.

Our disk grid demonstrates that full disks can produce SEDs with a very wide variety of appearances, particularly in their slopes and their amount of infrared emission. In attempting to identify additional transitional disks in Taurus, Najita et al. (2007b) selected objects with infrared emission which was weaker than the median SED of observed disks in Taurus and showed that their "transitional disks" have systematically lower mass accretion rates than other disks in Taurus. However, here we show that settled disks will have the steep slopes and weak excesses which Najita et al. (2007b) interpreted as indicators of inner disk holes. As a result, many of the disks in Najita et al. (2007b) which were classified as transitional disks are most likely disks which have undergone significant settling. We also explored the effect of incorporating large grains in slowly accreting, settled disks and found that such disks will have a significant near-IR flux, as is seen in full disks, but substantially less emission at longer wavelengths. The observed SEDs of such disks may be mistakenly interpreted as undergoing clearing in the inner disk or as being outwardly truncated to small radii. This highlights the importance of detailed modeling in ascertaining disk structure.

In order to make a general comparison to disks in Taurus and Chamaeleon, we attempted to fit the disk models to the median observed SEDs in these star–forming regions. We find that models with mass accretion rates between $\sim 10^{-8}$ $M_{\odot}$ yr^{-1} and $\sim 10^{-7}$ $M_{\odot}$ yr^{-1} are in better agreement with the observed medians. These mass accretion rates are higher than the average value of $\sim 10^{-8}$ $M_{\odot}$ yr^{-1} that has been measured for CTTS (Hartmann et al., 1998; Gullbring et al., 1998). This discrepancy between the slowly accreting disk models and the medians may indicate that mass accretion rates in TTS are actually higher than the average measured TTS mass accretion rate. These mass accretion rate measurements are based on measurements of the excess luminosity above the photosphere in the ultraviolet and at optical wavelengths (0.32–0.54 μm). However, measurements at 0.84 and 1 μm indicate that there is excess emission at these redder wavelengths (White & Hillenbrand, 2004; Edwards et al., 2006). Fitting this excess at redder wavelengths with an accretion shock model which incorporates multiple accretion columns carrying different energy fluxes (thereby resulting in a range of temperatures in the regions of the photosphere heated by the accretion shock) Ingleby & Calvet (submitted) get up to a factor of 2 increase in the mass accretion rate relative to previous measurements. Therefore, it is possible that the accretion rates of TTS are higher than previously measured and that the fit of the higher accretion rate models to the median SED is a reflection of this. Some of the discrepancy between the models and the median SEDs may also reflect that we are trying to fit a median observed SED that encompasses several stellar luminosities with a model which uses a single stellar luminosity. It is also possible that there is some discrepancy in the dust opacity. If there were some other

unknown contributor to the opacity at 1 μm where the stellar radiation is absorbed, the disks would be hotter and produce more near-IR emission. Alternatively, in constructing the median it is assumed that each object is a full disk, however, some objects which have been assumed to be full disks might actually have gaps. If this is the case, it would be inappropriate to fit full disk models to a median that is not truly representative of a full disk.

In fact, further comparison of the models with the observations indicates that some disks which have previously been thought to be full disks may actually have gaps. About $\sim$20% of disks in Taurus, Chamaeleon, and Ophiuchus are "outliers" which cannot be explained by full disk models when comparing the slope of our simulated SEDs between 13 μm – 31 μm versus the equivalent width of the 10 μm silicate feature to that of observed disks. This subset of objects has significantly more 10 μm silicate emission than can be explained by a full disk. One possible explanation is that the optically thick disks of these outliers have optically thin gaps that are filled with small optically thin dust from which the extra 10 μm silicate emission arises. This has been seen in the case of the pre-transitional disk of LkCa 15 (Espaillat et al., 2007b). LkCa 15's $\sim$46 AU gap contains 4×10^{-11} $M_{\odot}$ of optically thin dust within the inner 5 AU of the gap which accounts for most of its strong 10 μm silicate emission. The gap detected in LkCa 15 is quite large, reflecting an observational bias toward picking out pre-transitional disks with large gaps since their mid-infrared deficits will be more obvious in *Spitzer* spectra. Smaller gaps will not have as obvious of a deficit and will be difficult to detect. These "outliers" in 10 μm silicate emission may be pre-transitional disks in the incipient stages of disk

gap opening with smaller gaps than previously observed, filled with small dust.

Given that the majority of the 10 μm silicate emission traces traces the dust within the inner 1 AU of the disk (see Figures 2.15 through 2.21), the *Spitzer* IRS instrument will be most sensitive to clearings in which some of the dust located at radii <1 AU has been removed. Because of this, the IRS cannot easily detect gaps whose inner boundary is outside of 1 AU. As is seen in Figure 2.51, a disk with a gap ranging from 5 – 10 AU will be difficult to distinguish from a full disk and it will be up to *ALMA* to detect gaps in disks a radii greater than 1 AU. One can speculate that as the gap grows with time, it will be more easily detected by the IRS instrument. As the inner disk accretes onto the star and the gap grows, we will begin to see part of the outer wall, which had been previously obscured by the inner disk (see Figure 2.51). When this happens, the SED begins to differ from that of a full disk beyond 20 μm. When the inner disk is quite small we will see significant departures from a full disk SED assuming that the outer wall is now fully illuminated and that there is some optically thin dust in the inner disk (see Figure 2.51). Such a disk will have very strong 10 μm silicate emission, as is observed in the outliers, supporting our proposal that the outliers could be pre-transitional disks (see Section 1.2.1 for a review). Given that the outliers have not been previously identified as pre-transitional disks from visual inspection of their SEDs, it is likely that the outliers have gaps less than 10 AU since Figure 2.51 indicates that a gap spanning radii of $\sim$0.2–10 AU in the disk should lead to an obvious deficit in the SED. We note that this disk structure is similar to that of the pre-transitional disk of LkCa 15 (Section 5.3.3), which may indicate that LkCa 15 is representative of the last stages of gap opening, before the inner disk

completely accretes onto star and becomes a transitional disk.

Our disk model grid has revealed that several disks cannot be explained by typical full disk models. Detailed modeling of individual disks and millimeter imaging with the *SMA* and *ALMA* is needed to explore the disk structure producing these SEDs.

Table 2.1. Stellar Properties Adopted for Disk Model Grids

M_* ($M_\odot$)	R_* ($R_\odot$)	T_* (K)	L_* ($L_\odot$)	F_J (ergs cm^{-2} s^{-1} Hz^{-1})
0.5	2.0	4000	0.9	3.6×10^{-24}
0.2	1.4	3240	0.2	1.1×10^{-24}

Table 2.2. Disk Model Properties for Grid using Astronomical Silicates & $M_*=0.5M_\odot$

$\dot{M}$($M_\odot$ yr^{-1})[1]	ϵ	R^2_{sub} (AU)	h_{wall}(AU)	h_{wall}(H)	$M_d(M_\odot)$
10^{-10}	0.001	0.08	4.74×10^{-3}	2.37	1.45×10^{-4}
	0.01	0.08	5.44×10^{-2}	2.72	1.48×10^{-4}
	0.1	0.08	6.22×10^{-3}	3.11	1.36×10^{-4}
	1.0	0.08	6.96×10^{-3}	3.48	1.63×10^{-4}
10^{-9}	0.001	0.08	5.91×10^{-3}	2.96	1.46×10^{-3}
	0.01	0.08	6.26×10^{-3}	3.13	1.39×10^{-3}
	0.1	0.08	7.01×10^{-3}	3.51	1.53×10^{-3}
	1.0	0.08	7.85×10^{-3}	3.93	2.09×10^{-3}
10^{-8}	0.001	0.08	6.58×10^{-3}	3.29	1.47×10^{-2}
	0.01	0.08	7.32×10^{-3}	3.66	1.57×10^{-2}
	0.1	0.08	8.45×10^{-3}	4.23	2.10×10^{-2}
	1.0	0.08	9.83×10^{-3}	4.92	3.34×10^{-2}
10^{-7}	0.001	0.09	1.10×10^{-2}	2.75	1.68×10^{-1}
	0.01	0.09	1.29×10^{-2}	3.23	2.12×10^{-1}

[1]For disks with $\dot{M}$ of 10^{-7} $M_\odot$ yr^{-1} and ϵ of 0.1 and 1.0, the Toomre stability criterion is not satisfied and these disks are gravitationally unstable. Therefore, the model assumptions are no longer valid and we do not present these models.

[2]We adopt an inner disk radius corresponding to a dust sublimation temperature of 1400 K and an outer radius of 300 AU. We use α=0.01 for all cases.

Table 2.3. Disk Model Properties for Grid using Astronomical Silicates & $M_*=0.2M_\odot$

$\dot{M}$($M_\odot$ yr^{-1})[1]	ϵ	R^2_{sub} (AU)	h_{wall}(AU)	h_{wall}(H)	$M_d(M_\odot)$
10^{-10}	0.001	0.04	2.41×10^{-3}	2.41	1.34×10^{-4}
	0.01	0.04	3.02×10^{-3}	3.02	1.42×10^{-4}
	0.1	0.04	3.54×10^{-3}	3.54	1.20×10^{-4}
	1.0	0.04	3.99×10^{-3}	3.99	1.30×10^{-4}
10^{-9}	0.001	0.04	3.03×10^{-3}	3.03	1.30×10^{-3}
	0.01	0.04	3.57×10^{-3}	3.57	1.16×10^{-3}
	0.1	0.04	4.06×10^{-3}	4.06	1.23×10^{-3}
	1.0	0.04	4.68×10^{-3}	4.68	1.65×10^{-3}
10^{-8}	0.001	0.04	3.72×10^{-3}	3.72	1.24×10^{-2}
	0.01	0.04	4.35×10^{-3}	4.35	1.27×10^{-2}
	0.1	0.04	5.11×10^{-3}	5.11	1.66×10^{-2}
	1.0	0.04	5.89×10^{-3}	5.89	2.90×10^{-2}

[1]For disks with $\dot{M}$ of 10^{-7} $M_\odot$ yr^{-1}, the Toomre stability criterion is not satisfied and these disks are gravitationally unstable. Therefore, the model assumptions are no longer valid and we do not present these models.

[2]We adopt an inner disk radius corresponding to a dust sublimation temperature of 1400 K and an outer radius of 300 AU. We use α=0.01 for all cases.

Table 2.4. Disk Model Properties for Grid using Olivine Silicates & M_*=0.5$M_\odot$

$\dot{M}$($M_\odot$ yr^{-1})[1]	ϵ	R^2_{sub} (AU)	h_{wall}(AU)	h_{wall}(H)	M_d($M_\odot$)
10^{-10}	0.001	0.13	8.45×10^{-3}	2.11	1.38×10^{-4}
	0.01	0.13	9.88×10^{-2}	2.47	1.41×10^{-4}
	0.1	0.13	1.14×10^{-2}	2.85	1.29×10^{-4}
	1.0	0.13	1.28×10^{-2}	3.20	1.58×10^{-4}
10^{-9}	0.001	0.13	1.03×10^{-2}	2.58	1.39×10^{-3}
	0.01	0.13	1.14×10^{-2}	2.85	1.32×10^{-3}
	0.1	0.13	1.28×10^{-2}	3.20	1.47×10^{-3}
	1.0	0.13	1.42×10^{-2}	3.55	2.05×10^{-3}
10^{-8}	0.001	0.15	1.37×10^{-2}	2.74	1.40×10^{-2}
	0.01	0.15	1.54×10^{-2}	3.08	1.51×10^{-2}
	0.1	0.15	1.74×10^{-2}	3.48	2.06×10^{-2}
	1.0	0.15	2.03×10^{-2}	4.06	3.32×10^{-2}
10^{-7}	0.001	0.25	2.99×10^{-2}	3.32	1.61×10^{-1}
	0.01	0.25	3.46×10^{-2}	3.84	2.08×10^{-1}

[1]For disks with $\dot{M}$ of 10^{-7} $M_\odot$ yr^{-1} and ϵ of 0.1 and 1.0, the Toomre stability criterion is not satisfied and these disks are gravitationally unstable. Therefore, the model assumptions are no longer valid and we do not present these models.

[2]We adopt an inner disk radius corresponding to a dust sublimation temperature of 1400 K and an outer radius of 300 AU. We use α=0.01 for all cases.

Table 2.5. Disk Model Properties for Grid using Olivine Silicates & M_*=0.2$M_\odot$

$\dot{M}$($M_\odot$ yr^{-1})[1]	ϵ	R^2_{sub} (AU)	h_{wall}(AU)	h_{wall}(H)	M_d($M_\odot$)
10^{-10}	0.001	0.05	3.22×10^{-3}	1.61	1.29×10^{-4}
	0.01	0.05	4.11×10^{-3}	2.06	1.37×10^{-4}
	0.1	0.05	4.76×10^{-3}	2.38	1.16×10^{-4}
	1.0	0.05	5.39×10^{-3}	2.69	1.25×10^{-4}
10^{-9}	0.001	0.05	4.19×10^{-3}	2.09	1.24×10^{-3}
	0.01	0.05	4.83×10^{-3}	2.42	1.10×10^{-3}
	0.1	0.05	5.47×10^{-3}	2.74	1.18×10^{-3}
	1.0	0.05	6.18×10^{-3}	3.09	1.61×10^{-3}
10^{-8}	0.001	0.07	6.96×10^{-3}	2.32	1.19×10^{-2}
	0.01	0.07	7.99×10^{-3}	2.66	1.22×10^{-2}
	0.1	0.07	9.24×10^{-3}	3.08	1.62×10^{-2}
	1.0	0.07	1.09×10^{-2}	3.63	2.90×10^{-2}

[1]For disks with $\dot{M}$ of 10^{-7} $M_\odot$ yr^{-1}, the Toomre stability criterion is not satisfied and these disks are gravitationally unstable. Therefore, the model assumptions are no longer valid and we do not present these models.

[2]We adopt an inner disk radius corresponding to a dust sublimation temperature of 1400 K and an outer radius of 300 AU. We use α=0.01 for all cases.

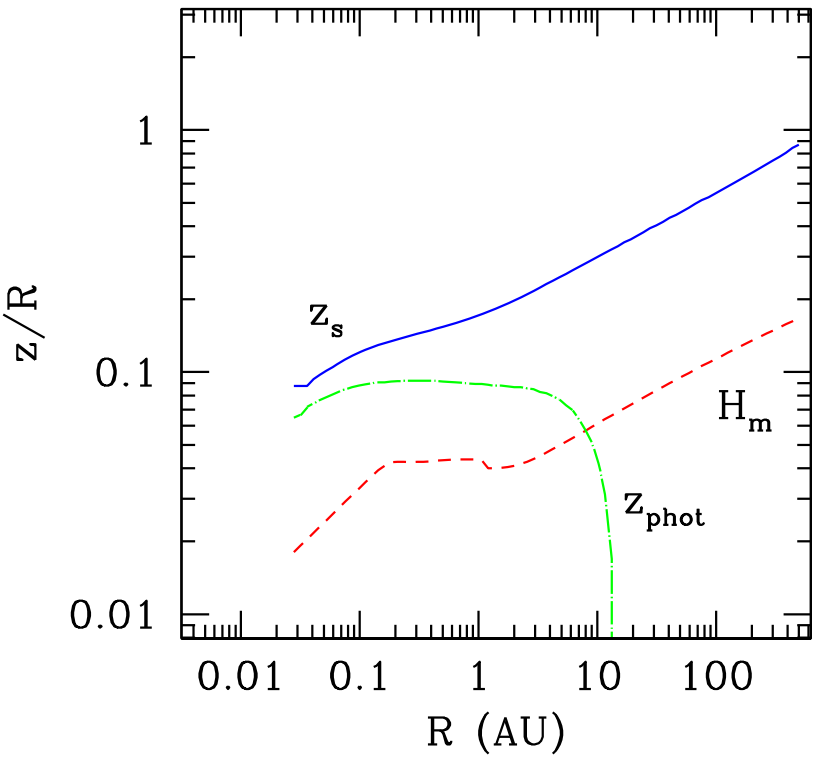

Figure 2.1 Characteristic disk heights. Shown here are the height where the stellar radiation is absorbed (z_s; dark blue), the "photospheric" height where the disk is optically thick to its own radiation (z_{phot}; green), and the gas scale height (H_m; red). Figure from Calvet & D'Alessio (in press).

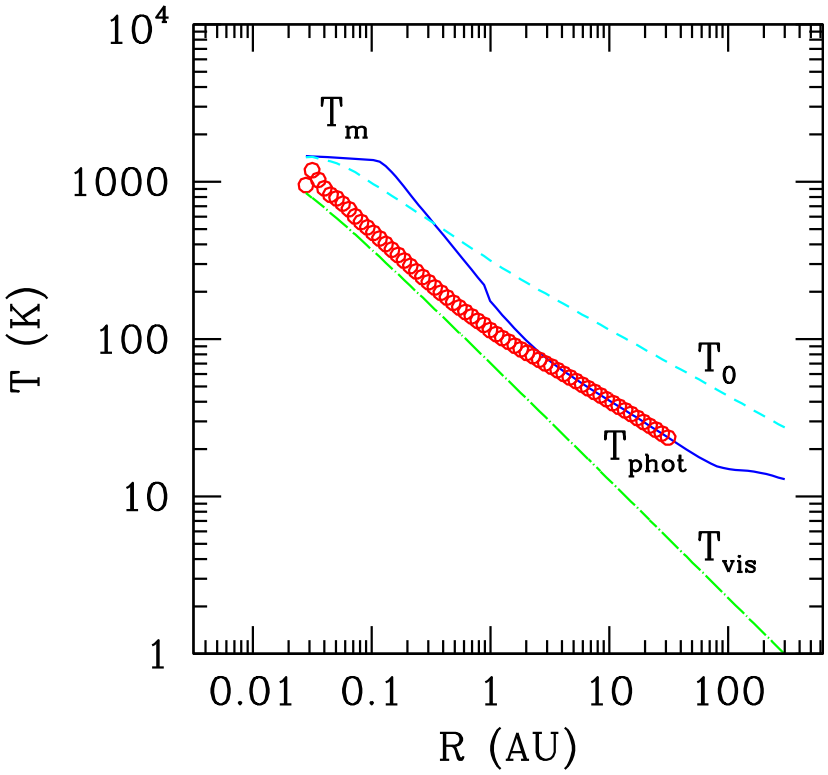

Figure 2.2 Characteristic temperatures of a disk model with well-mixed dust and a_{max}=1 mm. Shown here are the temperatures expected from a simple viscous disk (T_{vis}; green), the disk surface (T_0; cyan), the disk midplane (T_m; dark blue), and the disk photosphere (T_{phot}; red), defined as where the disk is optically thick to its own radiation. The model shown here has M_* of 0.5 $M_\odot$, R_* of 2 $R_\odot$, T_* of 4000 K, and $\dot{M}$ of 10^{-8} $M_\odot$ yr^{-1}. Figure from Calvet & D'Alessio (in press).

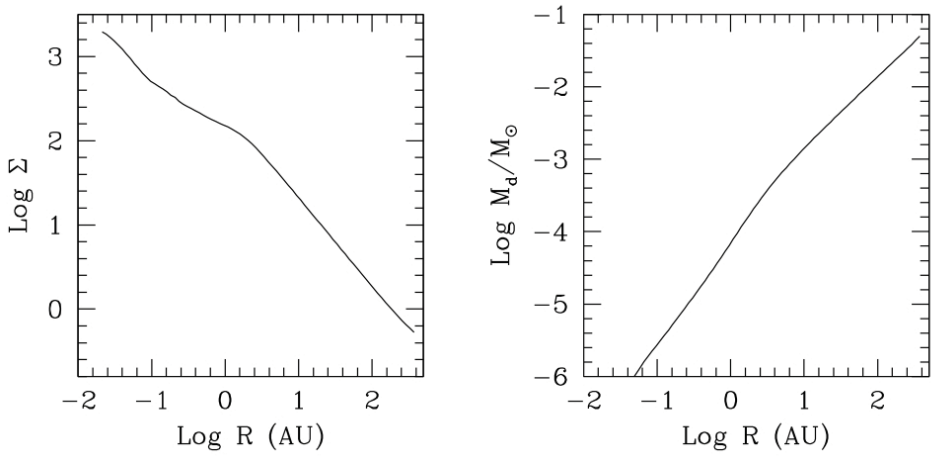

Figure 2.3 Disk surface density and mass. Both are shown as a function of distance from the central star. Figure from D'Alessio et al. (1999).

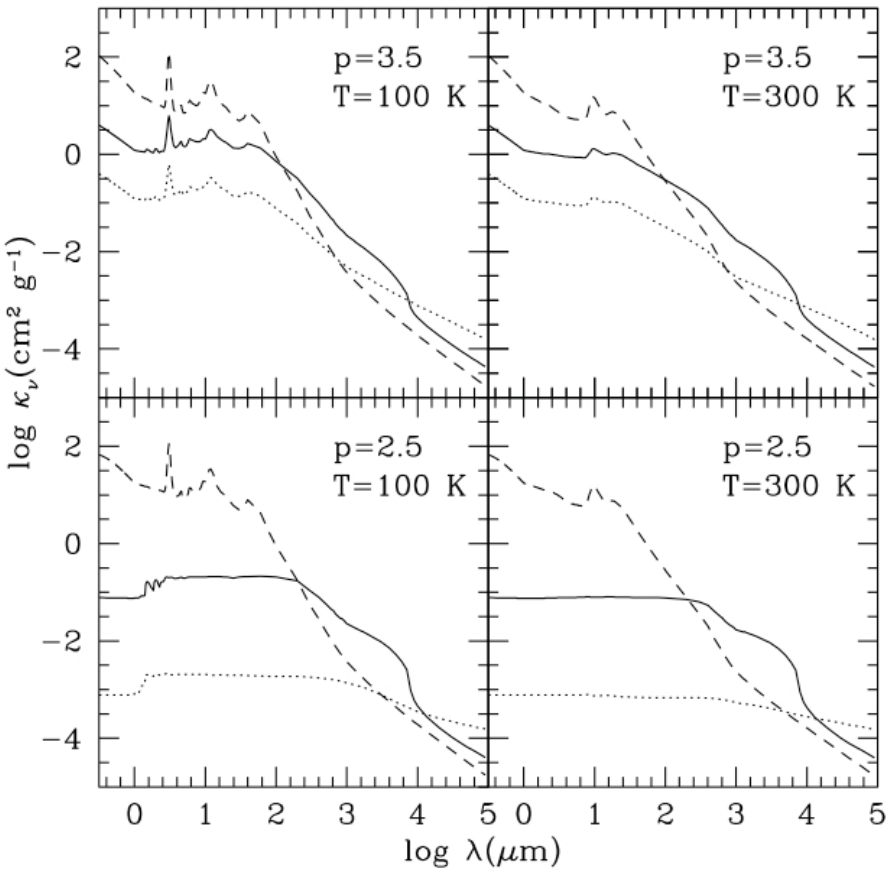

Figure 2.4 Relationship between dust opacity, grain size, and wavelength. Top panels correspond to a grain size distribution with $p = 3.5$ and bottom panels have $p = 2.5$. Grains with $a_{max} = 1$ μm (dashed line), 1 mm (solid line), and 10 cm (dotted line) are shown. In the left panels, the dust is at a temperature of 100 K and consists of silicates, troilite, water ice, and organics (Pollack et al., 1994). In the right panels, the dust is at a temperature of 300 K and ice has been sublimated. The emission at 10 μm is dominated by silicates and it decreases as the maximum grain size increases. Figure from D'Alessio et al. (2001).

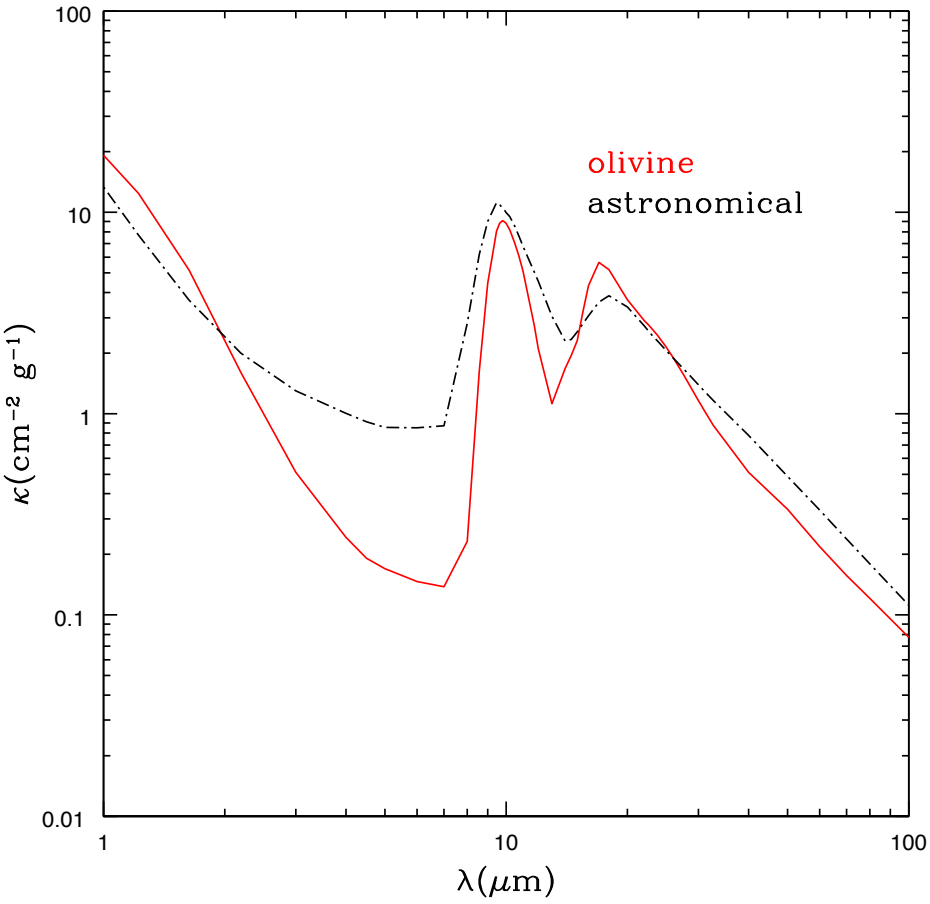

Figure 2.5 Dust opacity for silicate grains. We show dust opacities for astronomical silicates (broken black line) from Draine & Lee (1984) and olivine silicates (solid red line) from Dorschner et al. (1995).

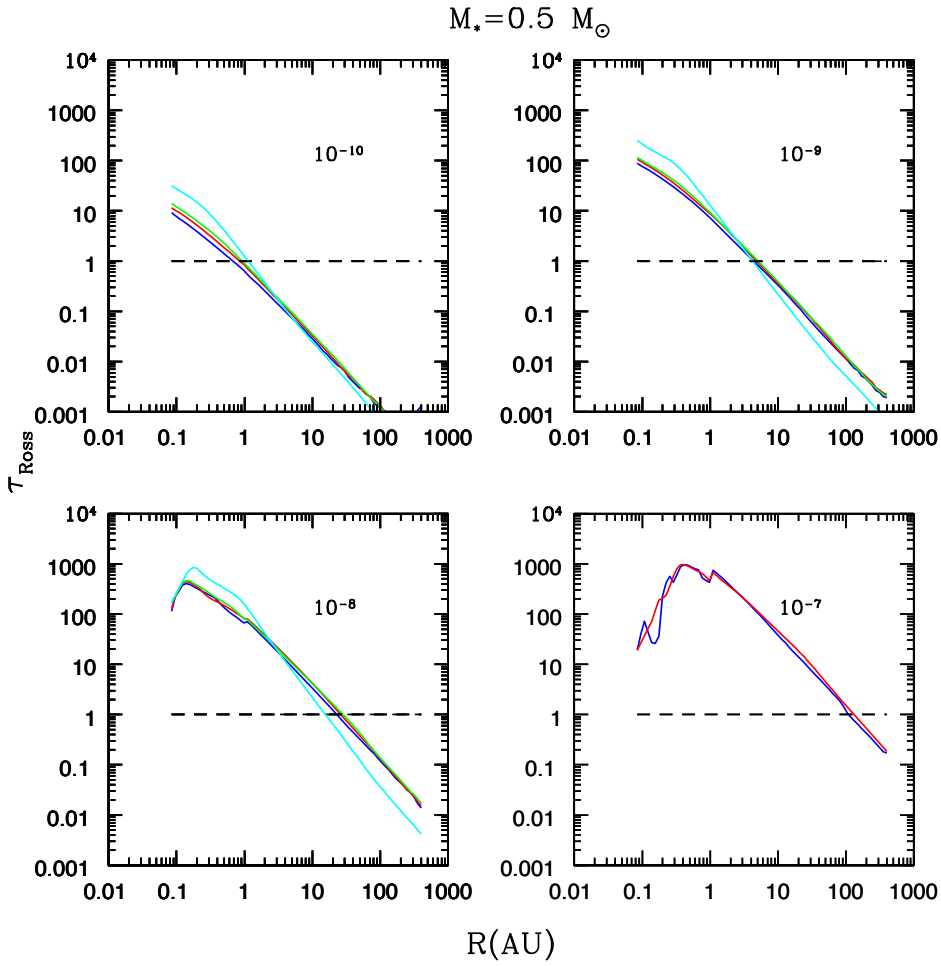

Figure 2.6 Rosseland mean optical depth of disk models with M_*=0.5 $M_\odot$. τ_R was integrated vertically from the midplane to the disk surface and is shown as a function of radial location in the disk. The disk is optically thick to its own radiation when $\tau_R > 1$. Clockwise from top left, panels correspond to disks with mass accretion rates of 10^{-10}, 10^{-9}, 10^{-7}, and 10^{-8} $M_\odot$ yr^{-1}. We show τ_R for $\epsilon = 0.001$ (dark blue), 0.01 (red), 0.1 (green), and 1.0 (cyan).

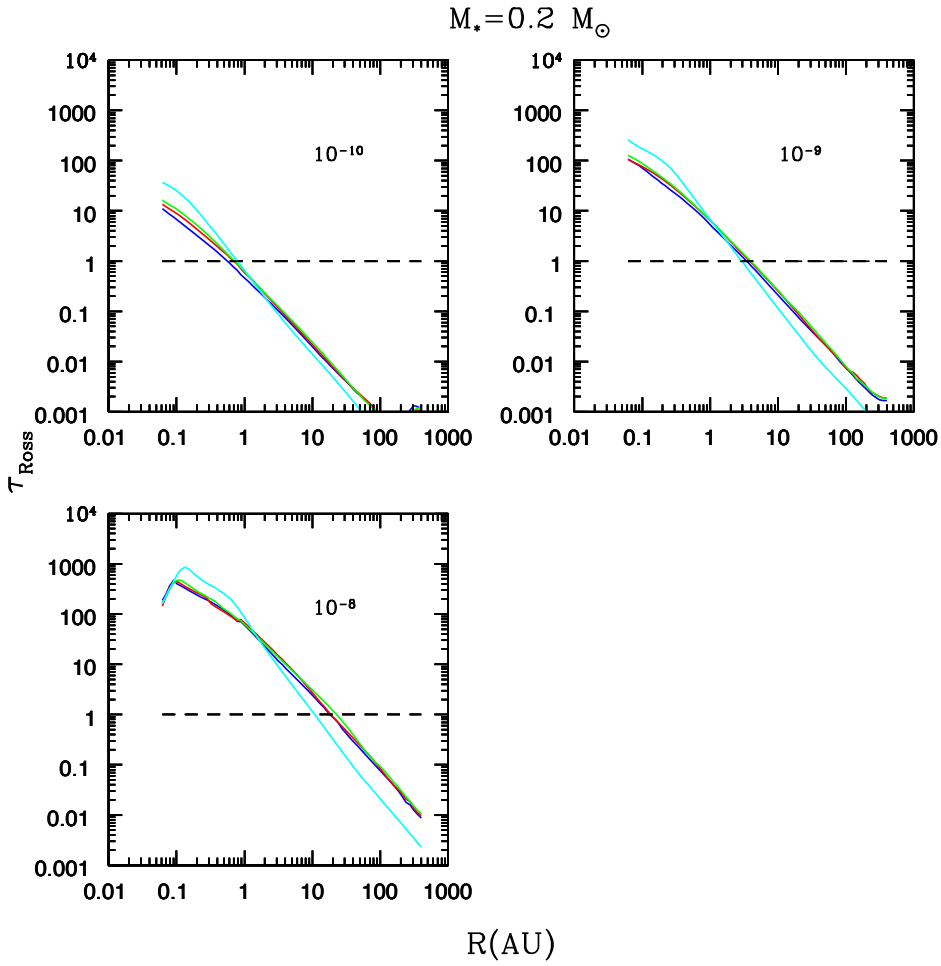

Figure 2.7 Rosseland mean optical depth of disk models with M_*=0.2 $M_\odot$. τ_R was integrated vertically from the midplane to the disk surface and is shown as a function of radial location in the disk. The disk is optically thick to its own radiation when $\tau_R > 1$. Clockwise from top left, panels correspond to disks with mass accretion rates of 10^{-10}, 10^{-9}, and 10^{-8} $M_\odot$ yr^{-1}. We show τ_R for $\epsilon = 0.001$ (dark blue), 0.01 (red), 0.1 (green), and 1.0 (cyan).

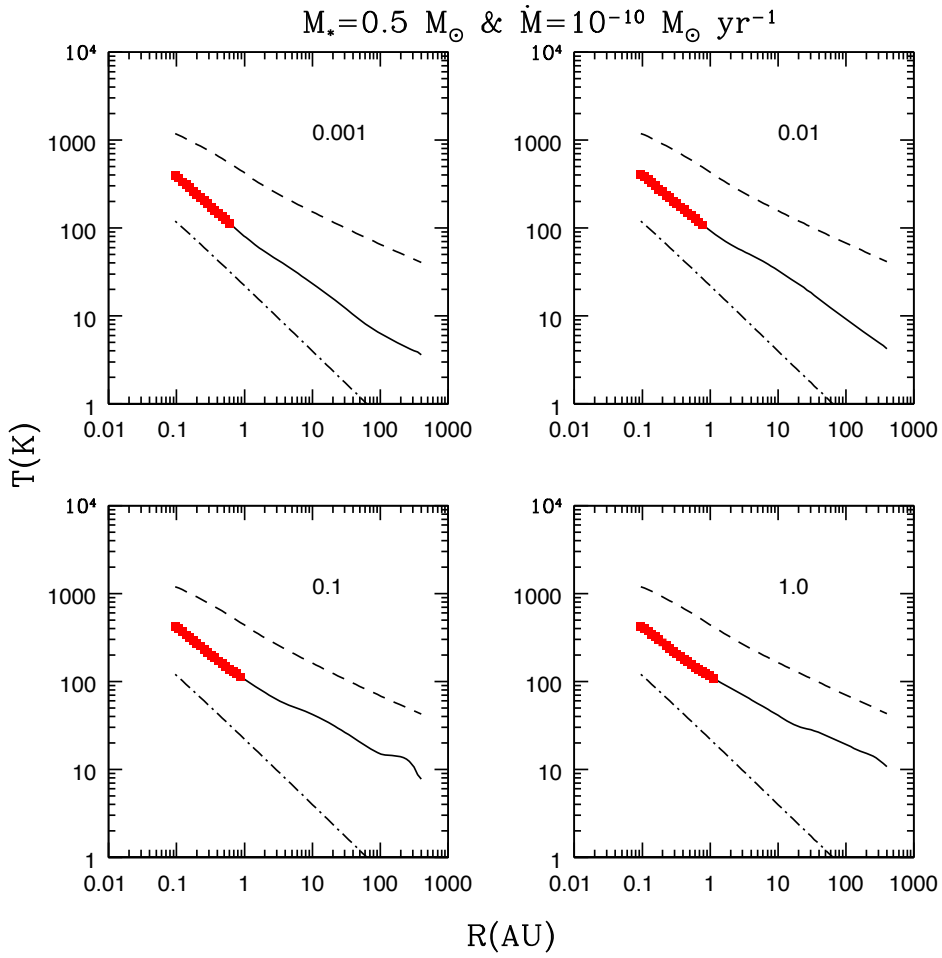

Figure 2.8 Temperature structure of disk models with M_*=0.5 $M_\odot$ and $\dot{M}$ =10^{-10} $M_\odot$ yr^{-1}. Clockwise from top left, panels correspond to disks with ϵ of 0.001, 0.01, 1.0, and 0.1. We show T_0 (dashed line), T_{phot} (red squares), T_c (solid line), and T_{vis} (dot dashed line).

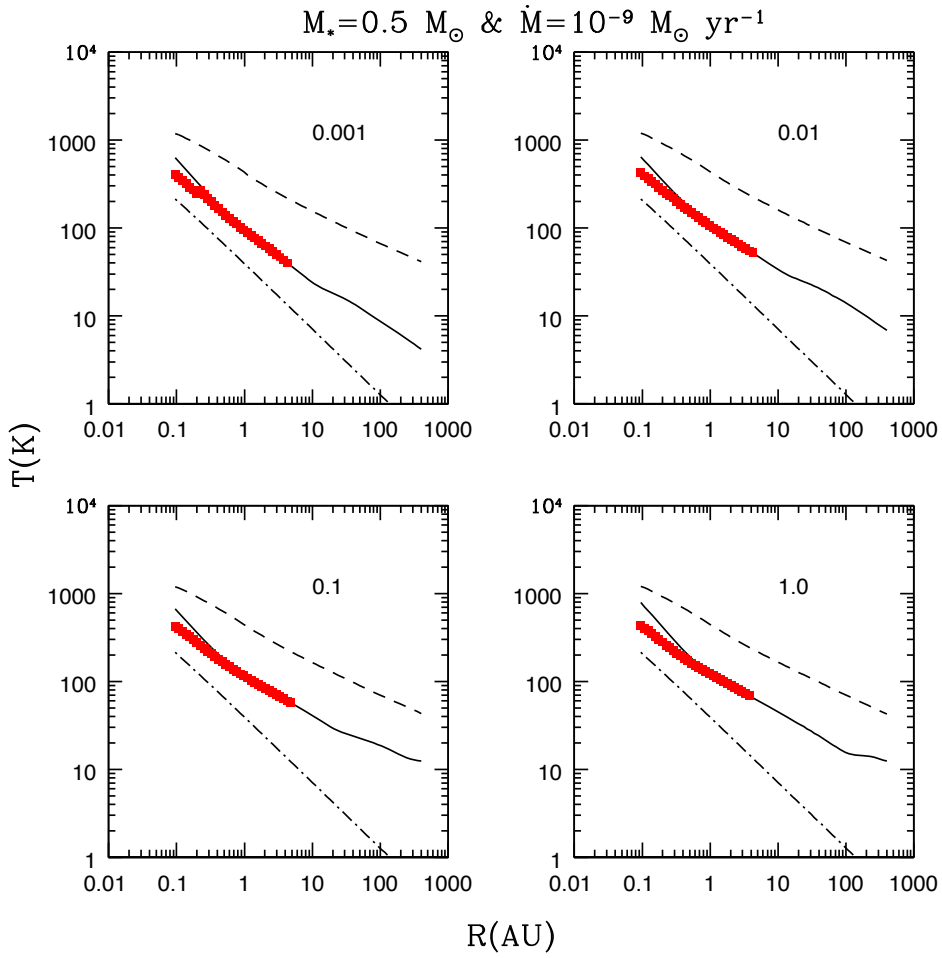

Figure 2.9 Temperature structure of disk models with M_*=0.5 $M_\odot$ and $\dot{M}$ =10^{-9} $M_\odot$ yr^{-1}. Clockwise from top left, panels correspond to disks with ϵ of 0.001, 0.01, 1.0, and 0.1. We show T_0 (dashed line), T_{phot} (red squares), T_c (solid line), and T_{vis} (dot dashed line).

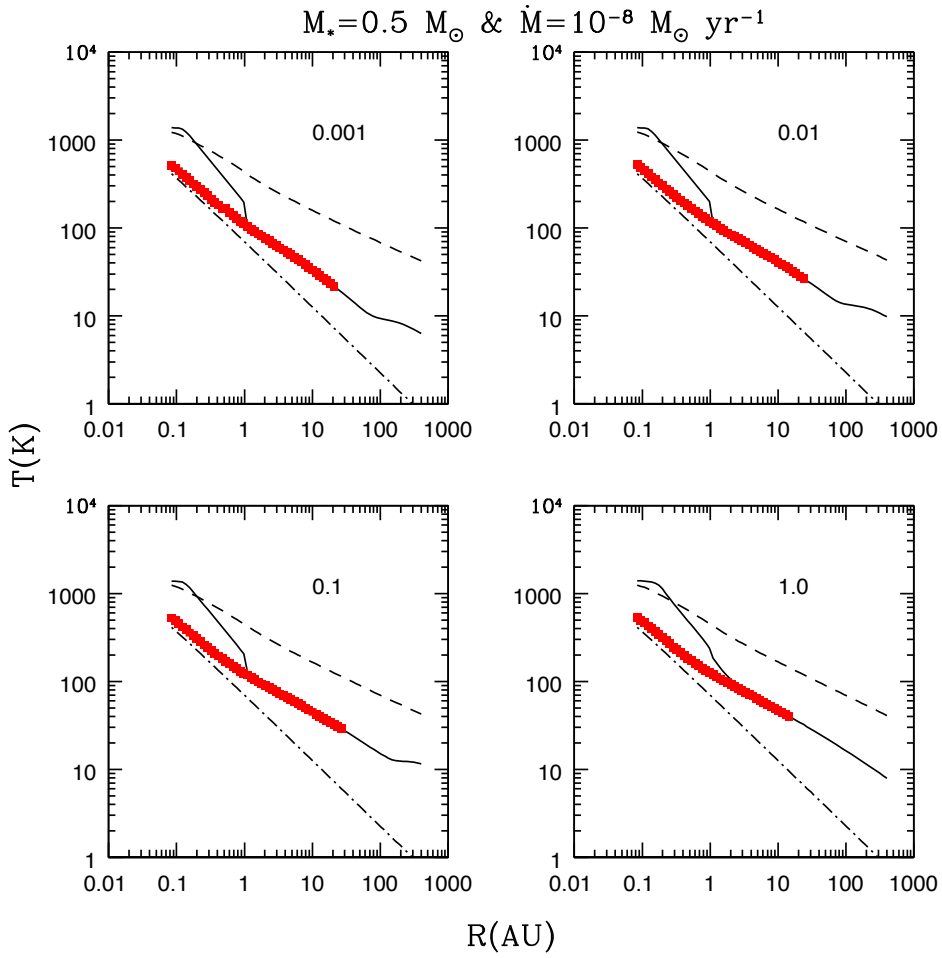

Figure 2.10 Temperature structure of disk models with M_*=0.5 $M_\odot$ and $\dot{M}$ =10^{-8} $M_\odot$ yr^{-1}. Clockwise from top left, panels correspond to disks with ϵ of 0.001, 0.01, 1.0, and 0.1. We show T_0 (dashed line), T_{phot} (red squares), T_c (solid line), and T_{vis} (dot dashed line).

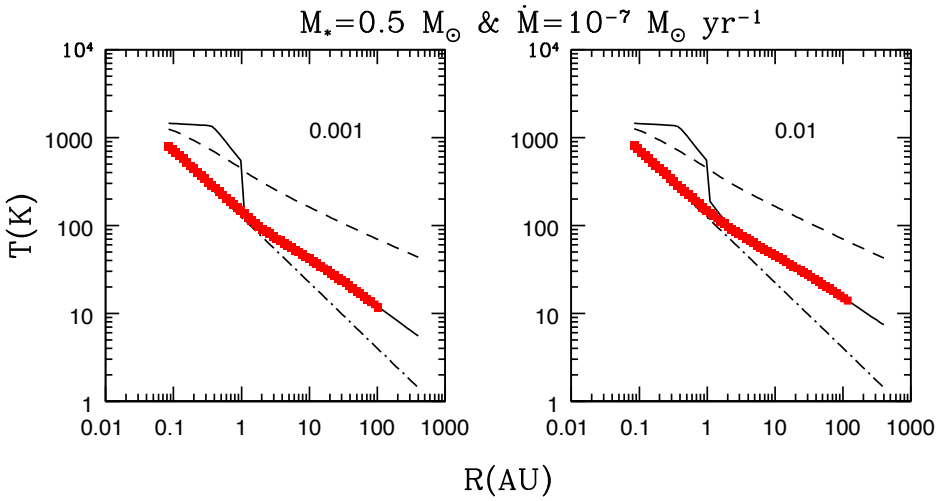

Figure 2.11 Temperature structure of disk models with M_*=0.5 $M_\odot$ and $\dot{M}$ =10^{-7} $M_\odot$ yr^{-1}. Left and right panels correspond to disks with ϵ of 0.001 and 0.01, respectively. We show T_0 (dashed line), T_{phot} (red squares), T_c (solid line), and T_{vis} (dot dashed line).

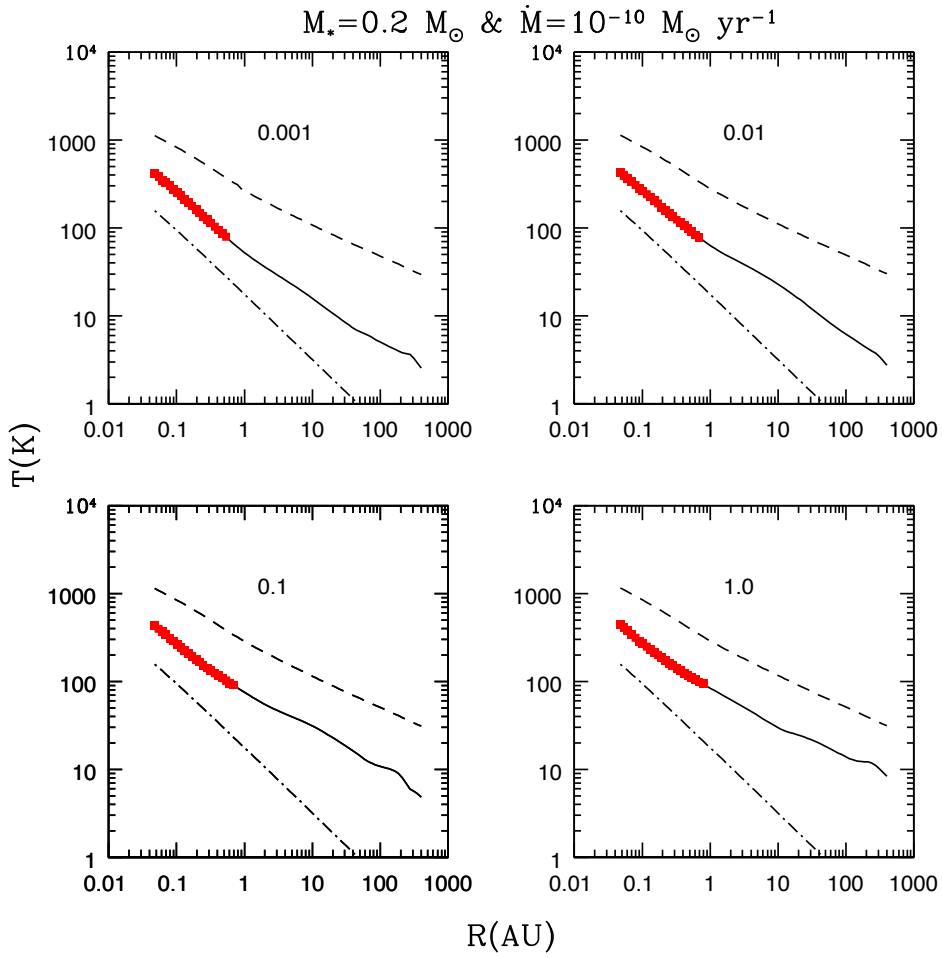

Figure 2.12 Temperature structure of disk models with M_*=0.2 $M_\odot$ and $\dot{M}$ =10^{-10} $M_\odot$ yr^{-1}. Clockwise from top left, panels correspond to disks with ϵ of 0.001, 0.01, 1.0, and 0.1. We show T_0 (dashed line), T_{phot} (red squares), T_c (solid line), and T_{vis} (dot dashed line).

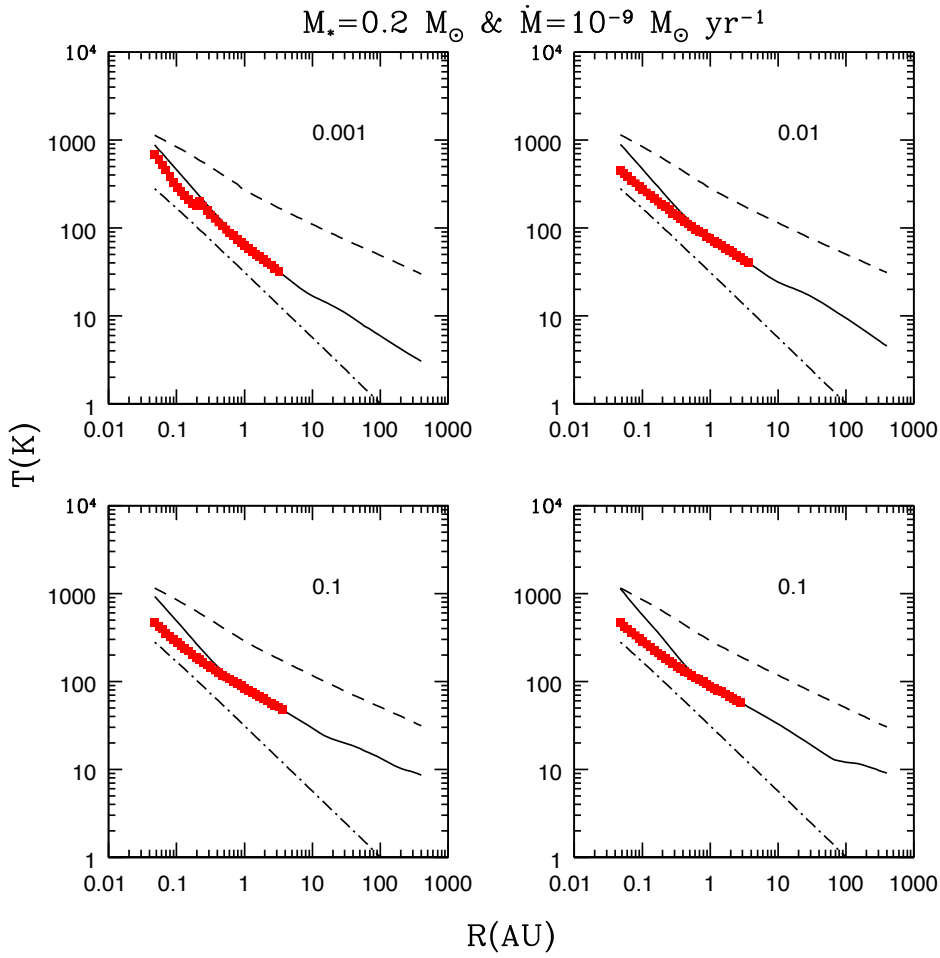

Figure 2.13 Temperature structure of disk models with M_*=0.2 $M_\odot$ and $\dot{M}$ =10^{-9} $M_\odot$ yr^{-1}. Clockwise from top left, panels correspond to disks with ϵ of 0.001, 0.01, 1.0, and 0.1. We show T_0 (dashed line), T_{phot} (red squares), T_c (solid line), and T_{vis} (dot dashed line).

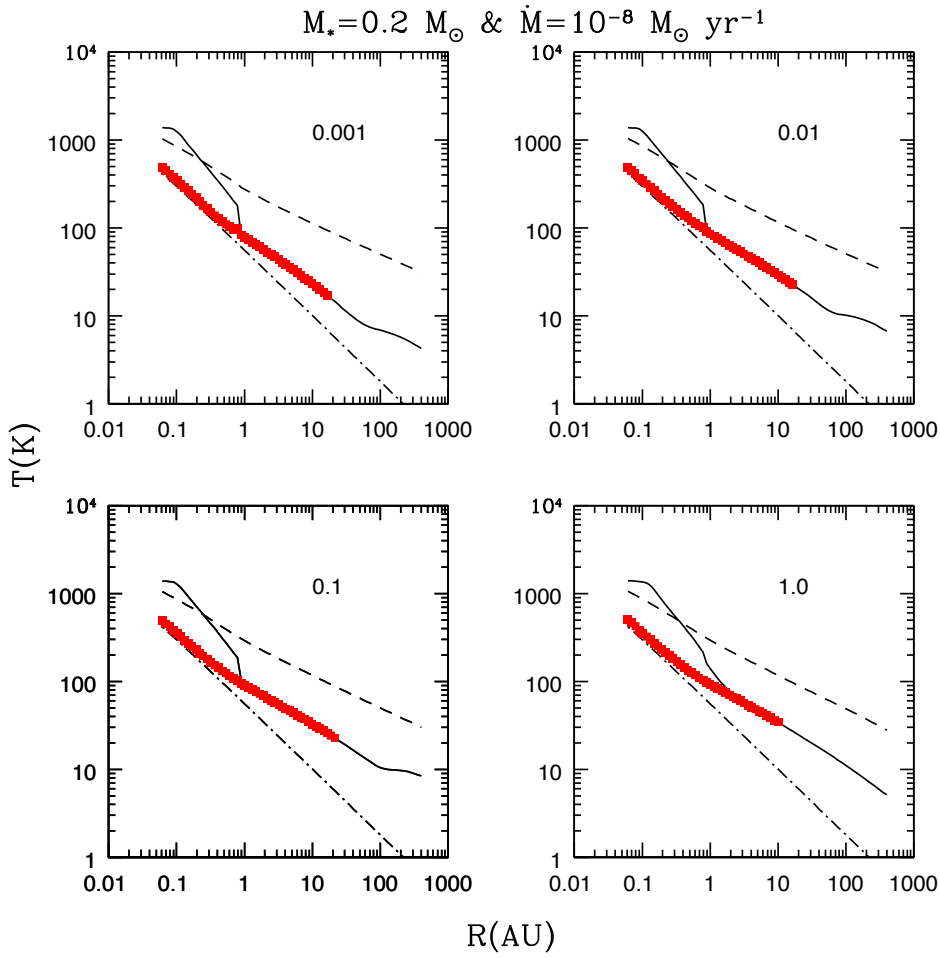

Figure 2.14 Temperature structure of disk models with M_*=0.2 $M_\odot$ and $\dot{M}$ =10^{-8} $M_\odot$ yr^{-1}. Clockwise from top left, panels correspond to disks with ϵ of 0.001, 0.01, 1.0, and 0.1. We show T_0 (dashed line), T_{phot} (red squares), T_c (solid line), and T_{vis} (dot dashed line).

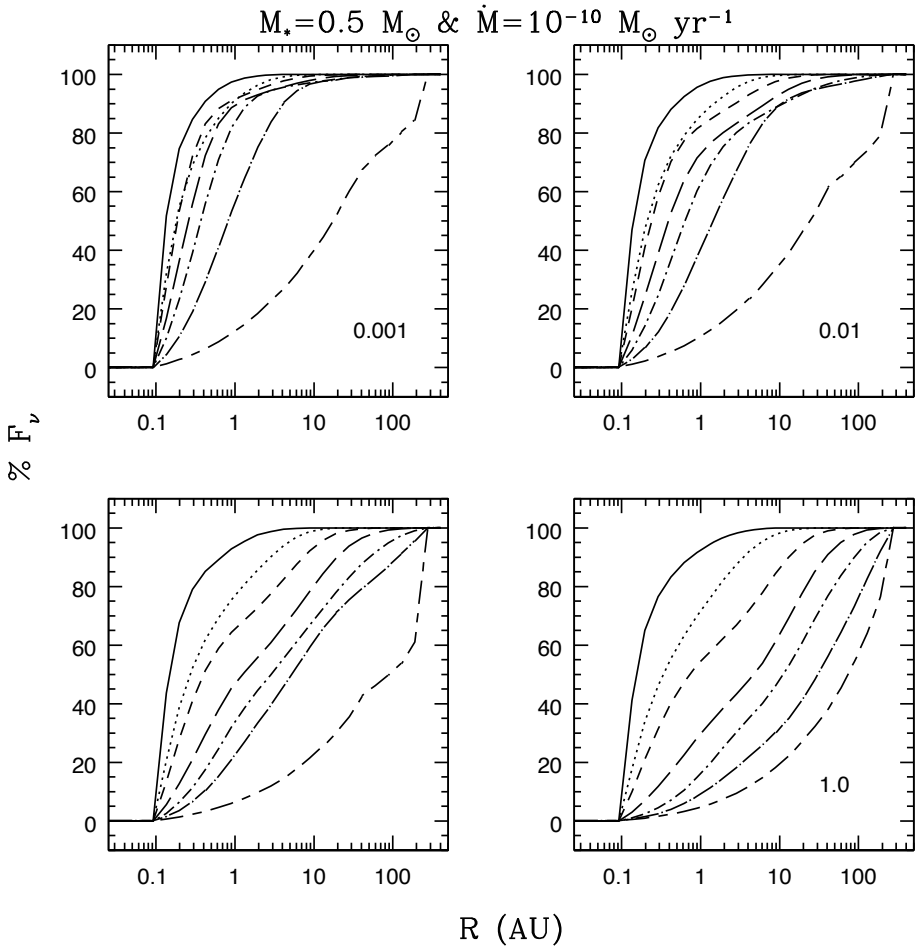

Figure 2.15 Cumulative flux to radius R settled disk models with M_*=0.5 $M_\odot$ and $\dot{M}$ =10^{-10} $M_\odot$ yr^{-1}. Clockwise from top left, panels correspond to disks with ϵ of 0.001, 0.01, 1.0, and 0.1. Curves correspond to 7 μm (solid), 10 μm (dotted), 16 μm (short dashed), 25 μm (long dashed), 40 μm (dot short dashed), 100 μm (dot long dashed), and 1000 μm (short long dashed).

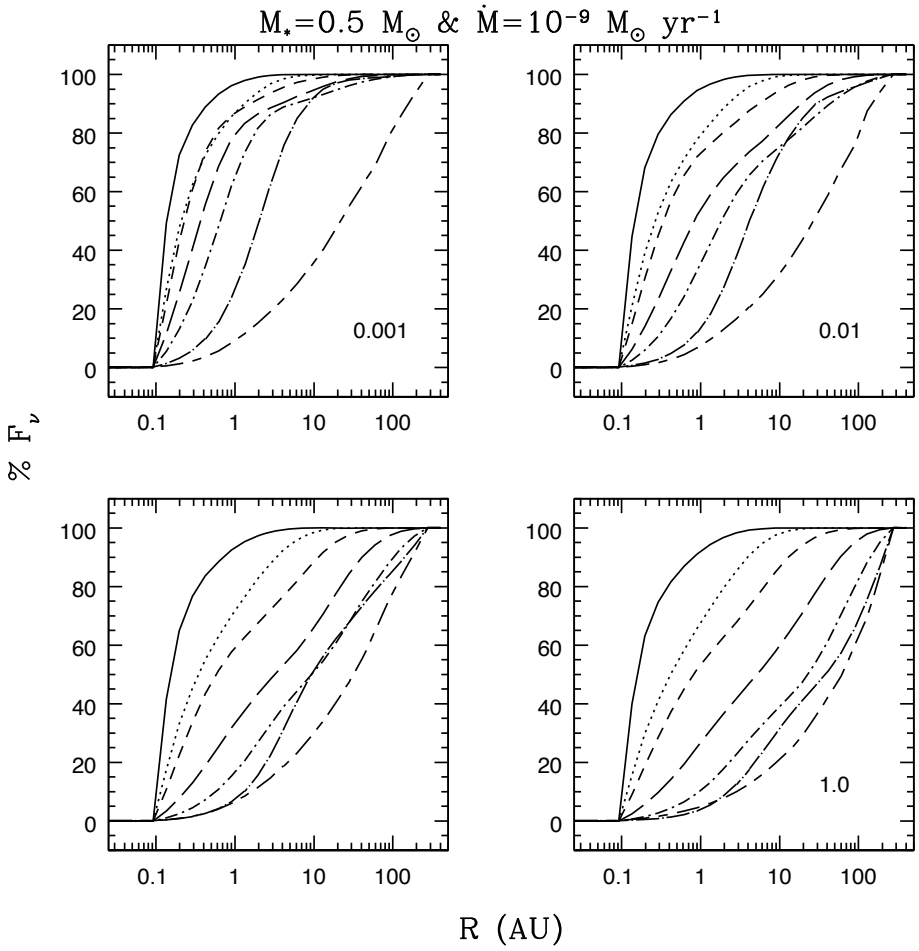

Figure 2.16 Cumulative flux to radius R settled disk models with M_*=0.5 $M_\odot$ and $\dot{M}$ =10^{-9} $M_\odot$ yr^{-1}. Clockwise from top left, panels correspond to disks with ϵ of 0.001, 0.01, 1.0, and 0.1. Curves correspond to 7 μm (solid), 10 μm (dotted), 16 μm (short dashed), 25 μm (long dashed), 40 μm (dot short dashed), 100 μm (dot long dashed), and 1000 μm (short long dashed).

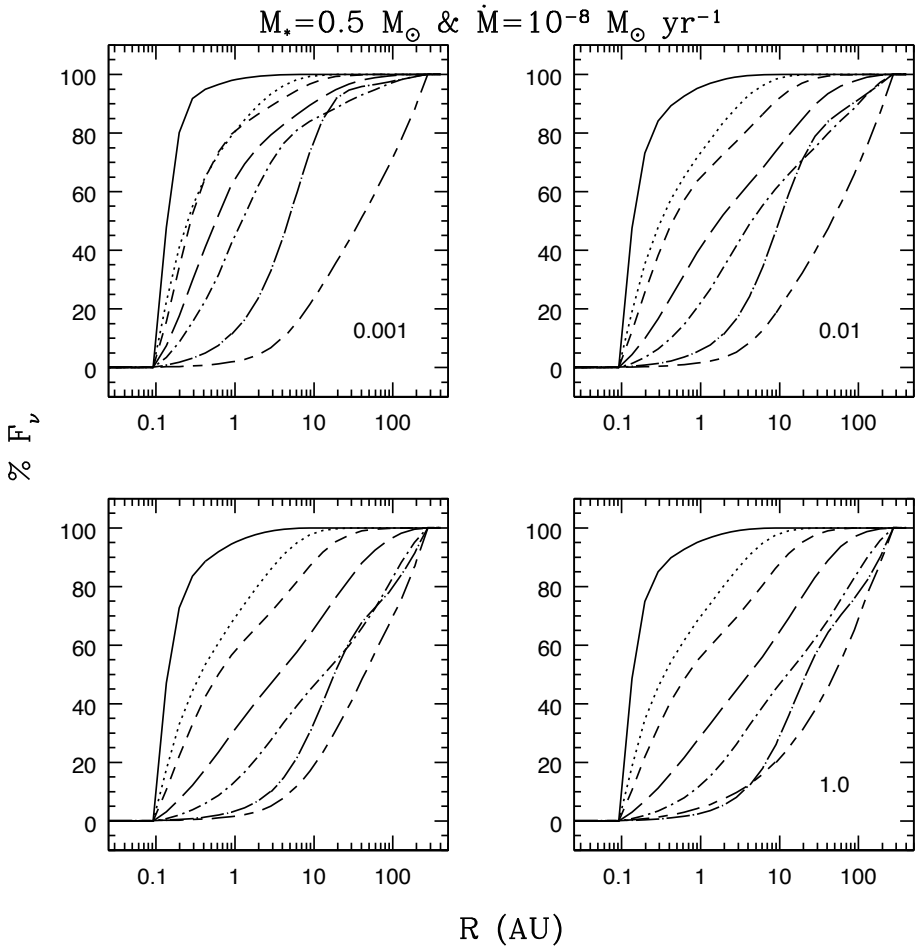

Figure 2.17 Cumulative flux to radius R settled disk models with M_*=0.5 $M_\odot$ and $\dot{M}$ =10^{-8} $M_\odot$ yr^{-1}. Clockwise from top left, panels correspond to disks with ϵ of 0.001, 0.01, 1.0, and 0.1. Curves correspond to 7 μm (solid), 10 μm (dotted), 16 μm (short dashed), 25 μm (long dashed), 40 μm (dot short dashed), 100 μm (dot long dashed), and 1000 μm (short long dashed).

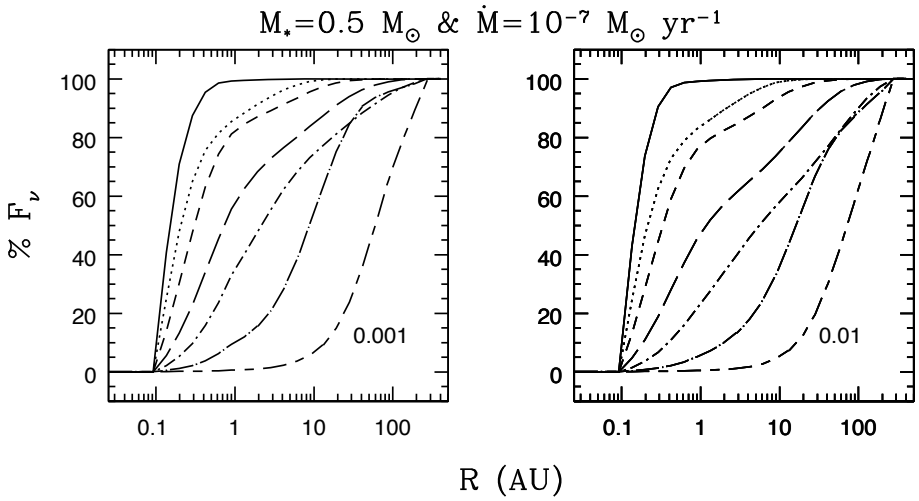

Figure 2.18 Cumulative flux to radius R settled disk models with M_*=0.5 $M_\odot$ and $\dot{M}$ =10^{-7} $M_\odot$ yr^{-1}. Panels correspond to disks with ϵ of 0.001 and 0.01. Curves correspond to 7 μm (solid), 10 μm (dotted), 16 μm (short dashed), 25 μm (long dashed), 40 μm (dot short dashed), 100 μm (dot long dashed), and 1000 μm (short long dashed).

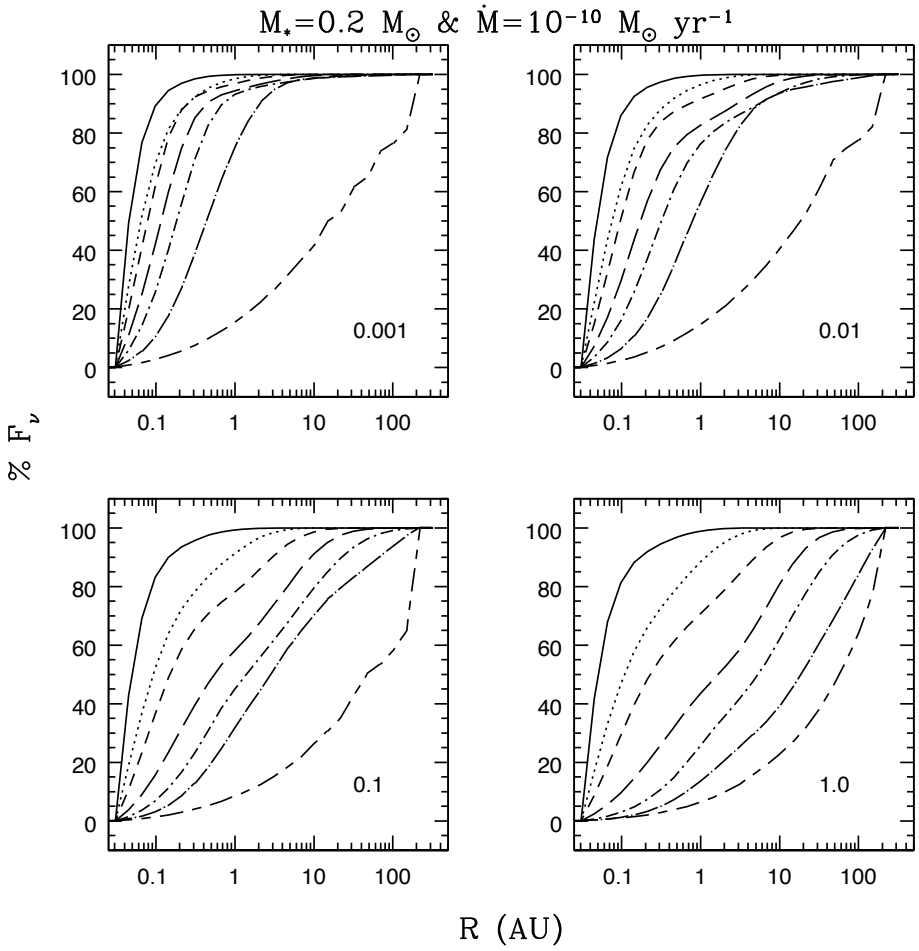

Figure 2.19 Cumulative flux to radius R settled disk models with M_*=0.2 $M_\odot$ and $\dot{M}$ =10^{-10} $M_\odot$ yr^{-1}. Clockwise from top left, panels correspond to disks with ϵ of 0.001, 0.01, 1.0, and 0.1. Curves correspond to 7 μm (solid), 10 μm (dotted), 16 μm (short dashed), 25 μm (long dashed), 40 μm (dot short dashed), 100 μm (dot long dashed), and 1000 μm (short long dashed).

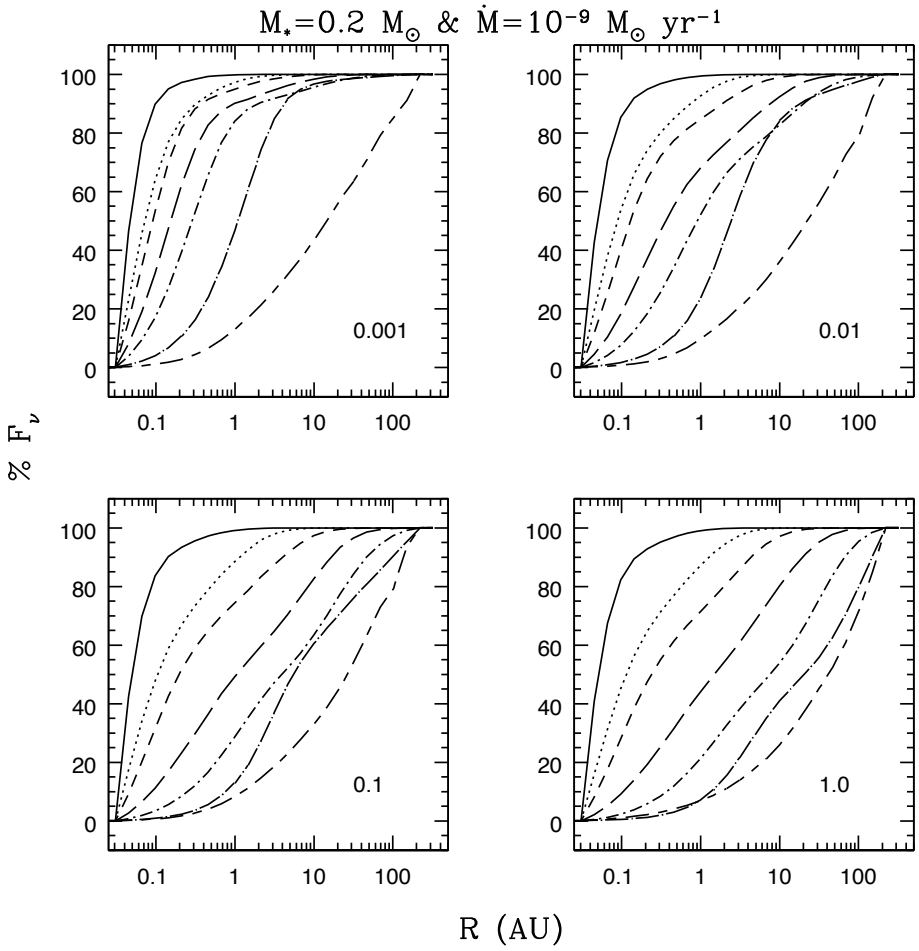

Figure 2.20 Cumulative flux to radius R settled disk models with M_*=0.2 $M_\odot$ and $\dot{M}$ =10^{-9} $M_\odot$ yr^{-1}. Clockwise from top left, panels correspond to disks with ϵ of 0.001, 0.01, 1.0, and 0.1. Curves correspond to 7 μm (solid), 10 μm (dotted), 16 μm (short dashed), 25 μm (long dashed), 40 μm (dot short dashed), 100 μm (dot long dashed), and 1000 μm (short long dashed).

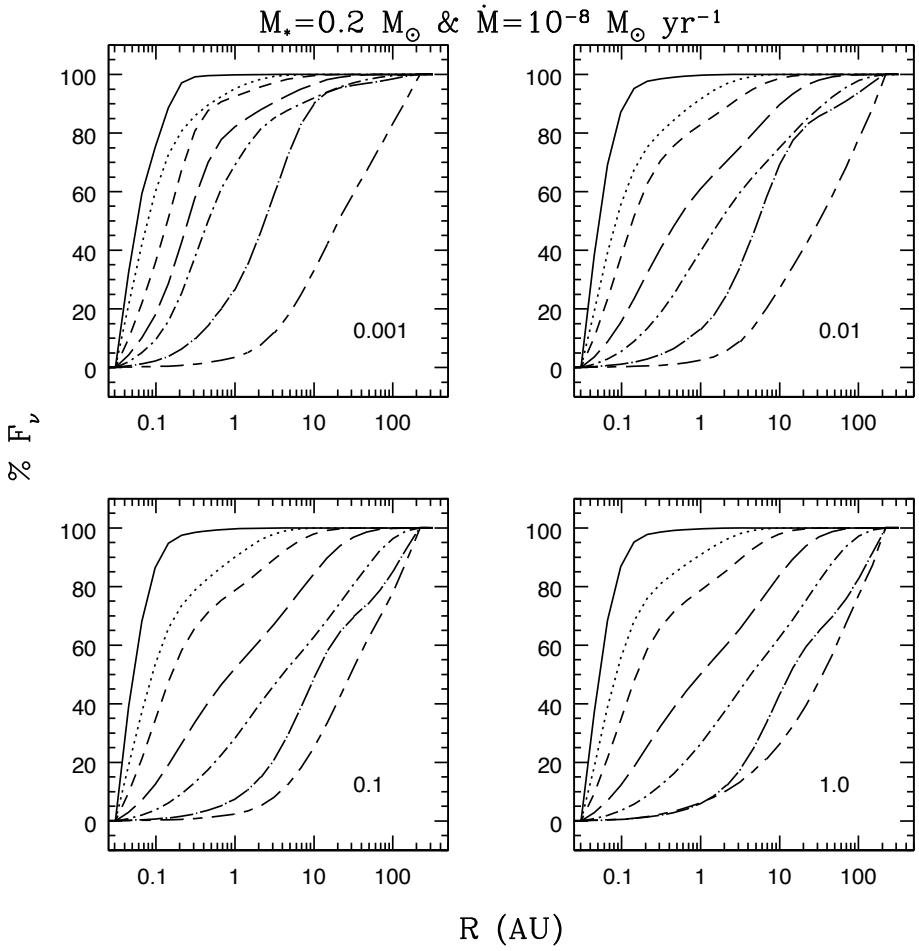

Figure 2.21 Cumulative flux to radius R settled disk models with M_*=0.2 $M_\odot$ and $\dot{M}$ =10^{-8} $M_\odot$ yr^{-1}. Clockwise from top left, panels correspond to disks with ϵ of 0.001, 0.01, 1.0, and 0.1. Curves correspond to 7 μm (solid), 10 μm (dotted), 16 μm (short dashed), 25 μm (long dashed), 40 μm (dot short dashed), 100 μm (dot long dashed), and 1000 μm (short long dashed).

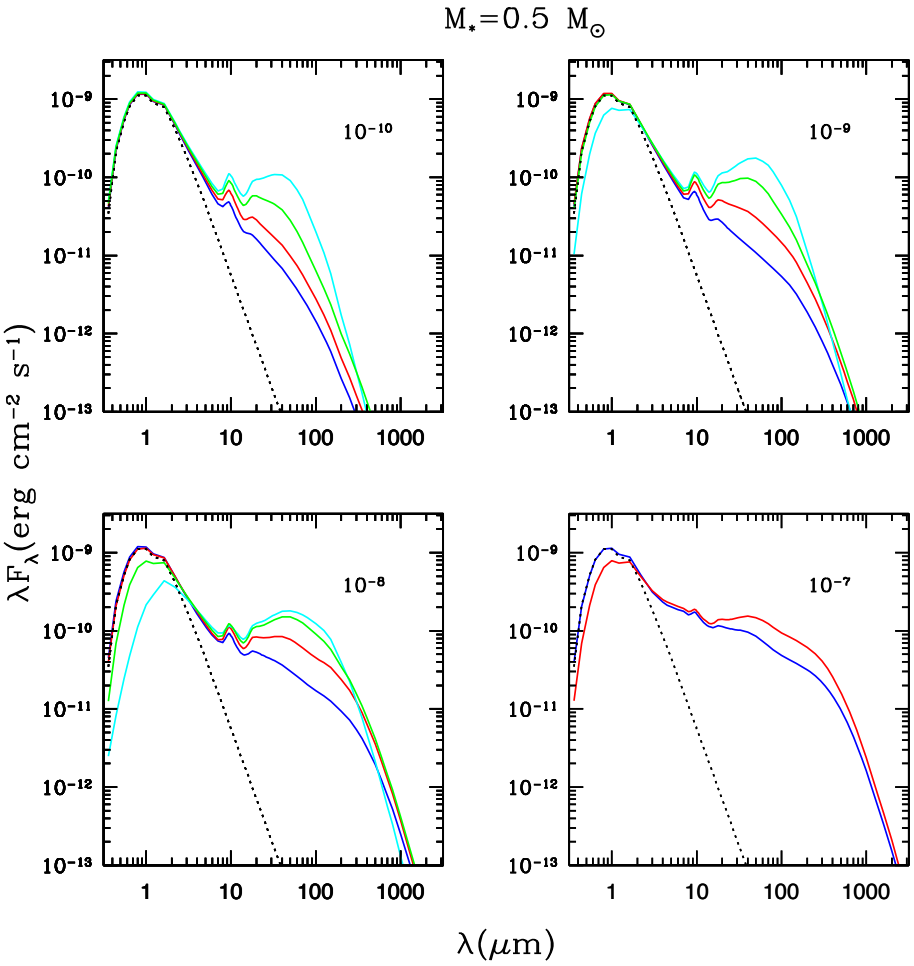

Figure 2.22 SEDs for disk models with M_*=0.5 $M_\odot$ and astronomical silicates. We show SEDs for mass accretion rates of 10^{-10}, 10^{-9}, 10^{-8}, and 10^{-7} $M_\odot$ yr^{-1} and ϵ = 0.001 (dark blue), 0.01 (red), 0.1 (green), and 1.0 (cyan) at an inclination of 60°. We include extinction of the star by the disk. The broken line corresponds to the unextincted stellar emission.

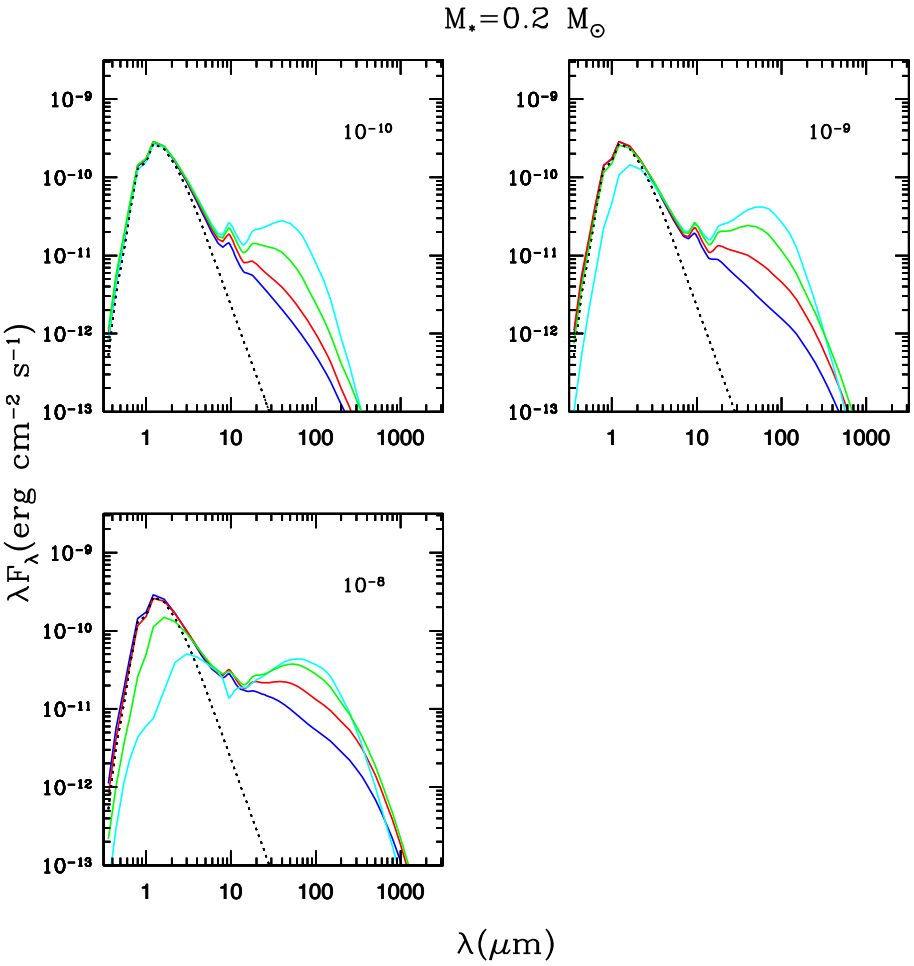

Figure 2.23 SEDs for disk models with M_*=0.2 $M_\odot$ and astronomical silicates. We show SEDs for mass accretion rates of 10^{-10}, 10^{-9}, 10^{-8}, and 10^{-7} $M_\odot$ yr^{-1} and ϵ = 0.001 (dark blue), 0.01 (red), 0.1 (green), and 1.0 (cyan) at an inclination of 60°. We include extinction of the star by the disk. The broken line corresponds to the unextincted stellar emission.

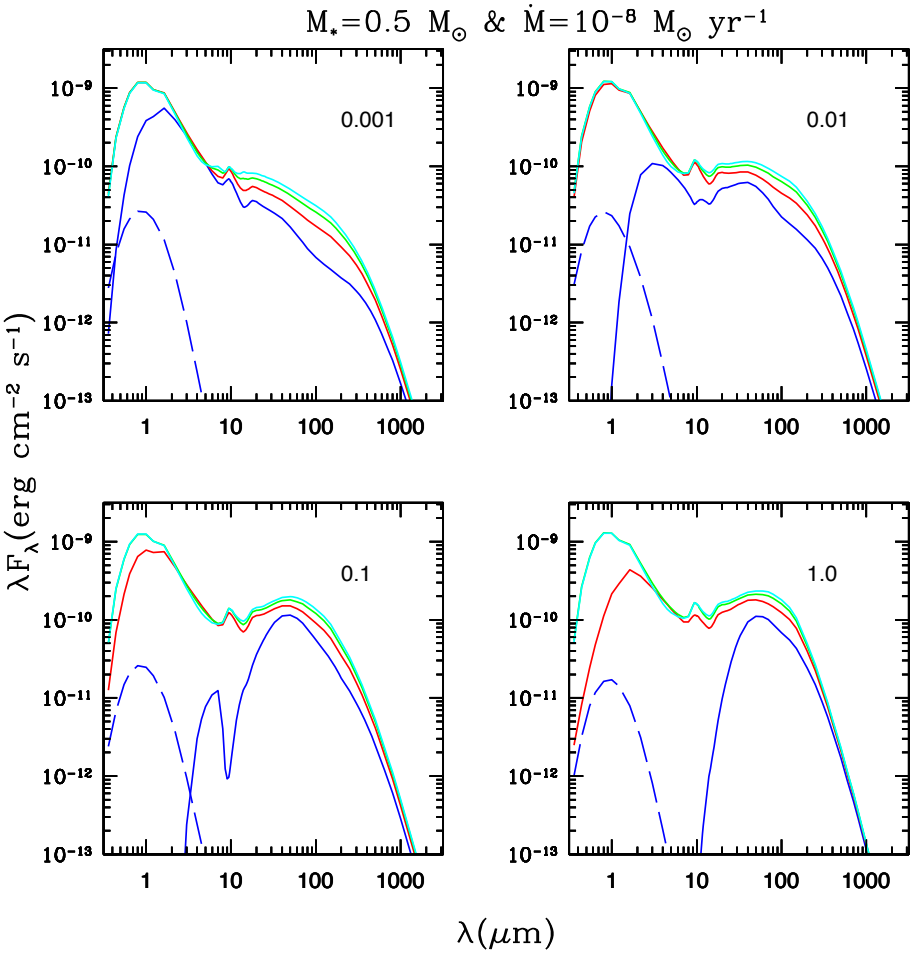

Figure 2.24 SEDs for disk models at different inclinations with M_*=0.5 $M_\odot$ and astronomical silicates. We show SEDs with a mass accretion rate of 10^{-8} $M_\odot$ yr^{-1} and $\epsilon = 0.001$, 0.01, 0.1, and 1.0 for inclinations of 20° (cyan), 40° (green), 60° (red), and 80° (dark blue). In the cases where $i = 80°$, we plot the scattered emission (broken dark blue line) and the thermal emission (solid dark blue line) separately.

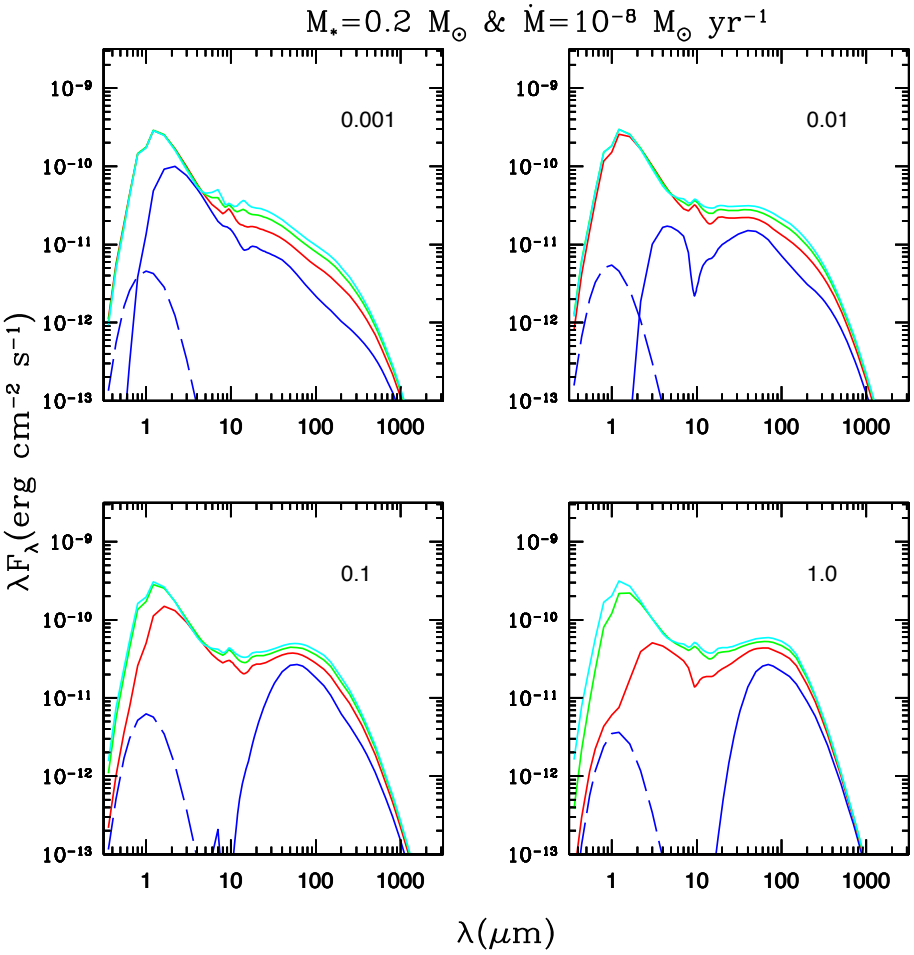

Figure 2.25 SEDs for disk models at different inclinations with M_*=0.2 $M_\odot$ and astronomical silicates. We show SEDs with a mass accretion rate of 10^{-8} $M_\odot$ yr^{-1} and for ϵ = 0.001, 0.01, 0.1, and 1.0 for inclinations of 20° (cyan), 40° (green), 60° (red), and 80° (dark blue). In the cases where $i = 80°$, we plot the scattered emission (broken blue line) and the thermal emission (solid blue line) separately.

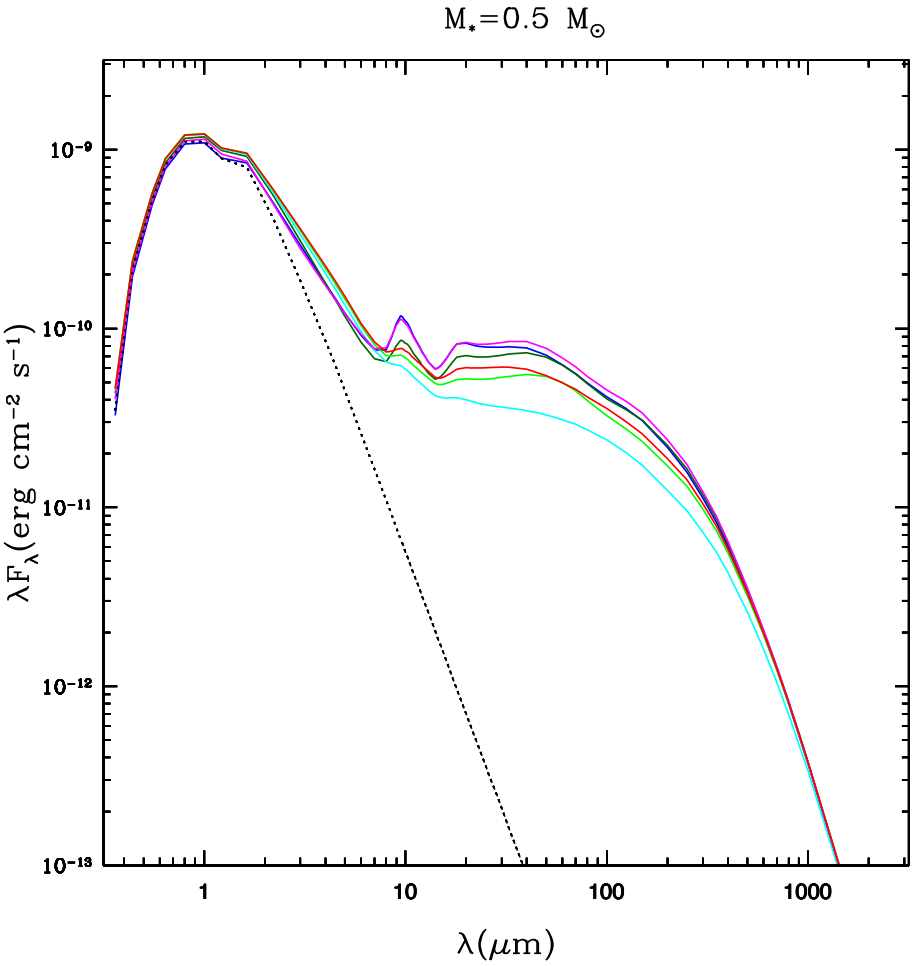

Figure 2.26 Dependence of disk emission on grain size for a disk model of M_*=0.5 $M_\odot$ and astronomical silicates. Here we vary the maximum size of grains in the upper layers of the disk for a model with $\dot{M}$=10^{-8} $M_\odot$ yr^{-1}, ϵ=0.01, and i=60°. We show disk models with a_{max}=0.05 μm (dark blue), 0.25 μm (magenta), 1 μm (dark green), 5 μm (red), 10 μm (light green), and 100 μm (cyan). The broken line corresponds to the stellar photosphere.

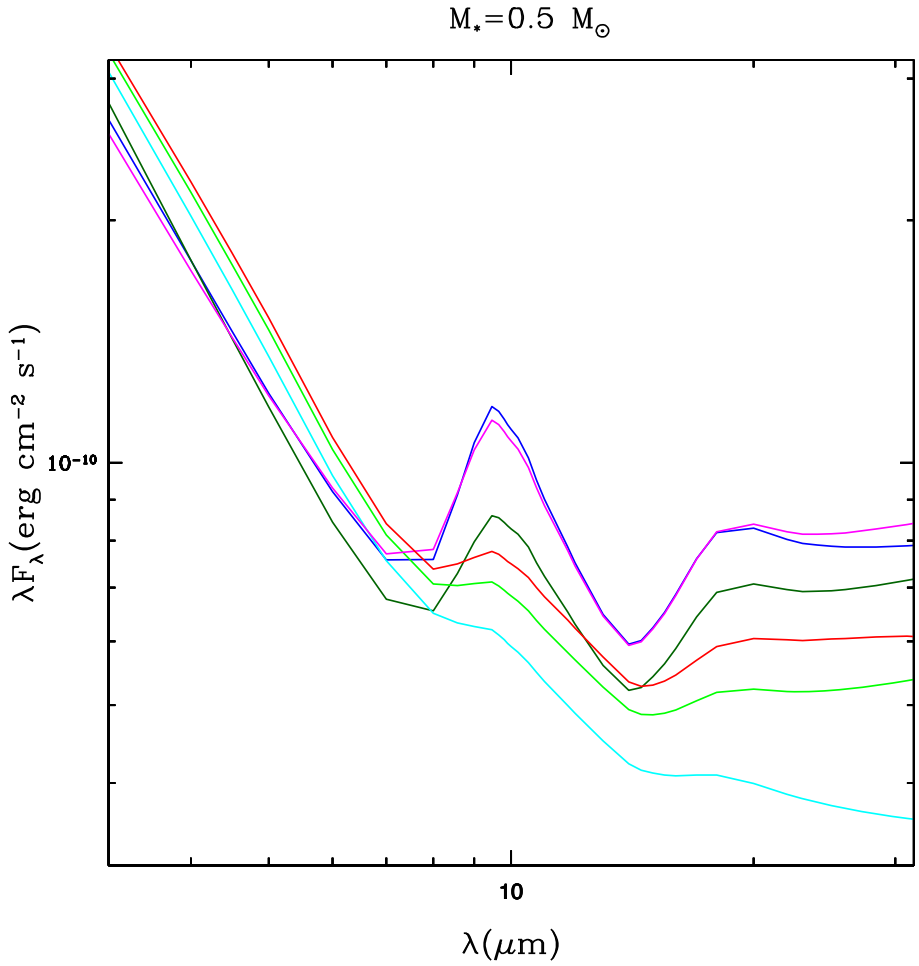

Figure 2.27 Dependence of silicate emission on grain size for a disk model of M_*=0.5 $M_\odot$ and astronomical silicates. Here we vary the maximum size of grains in the upper layers of the disk for a model with $\dot{M}$=10^{-8} $M_\odot$ yr^{-1}, ϵ=0.01, and i=60°. We show disk models with a_{max}=0.05 μm (dark blue), 0.25 μm (magenta), 1 μm (dark green), 5 μm (red), 10 μm (light green), and 100 μm (cyan).

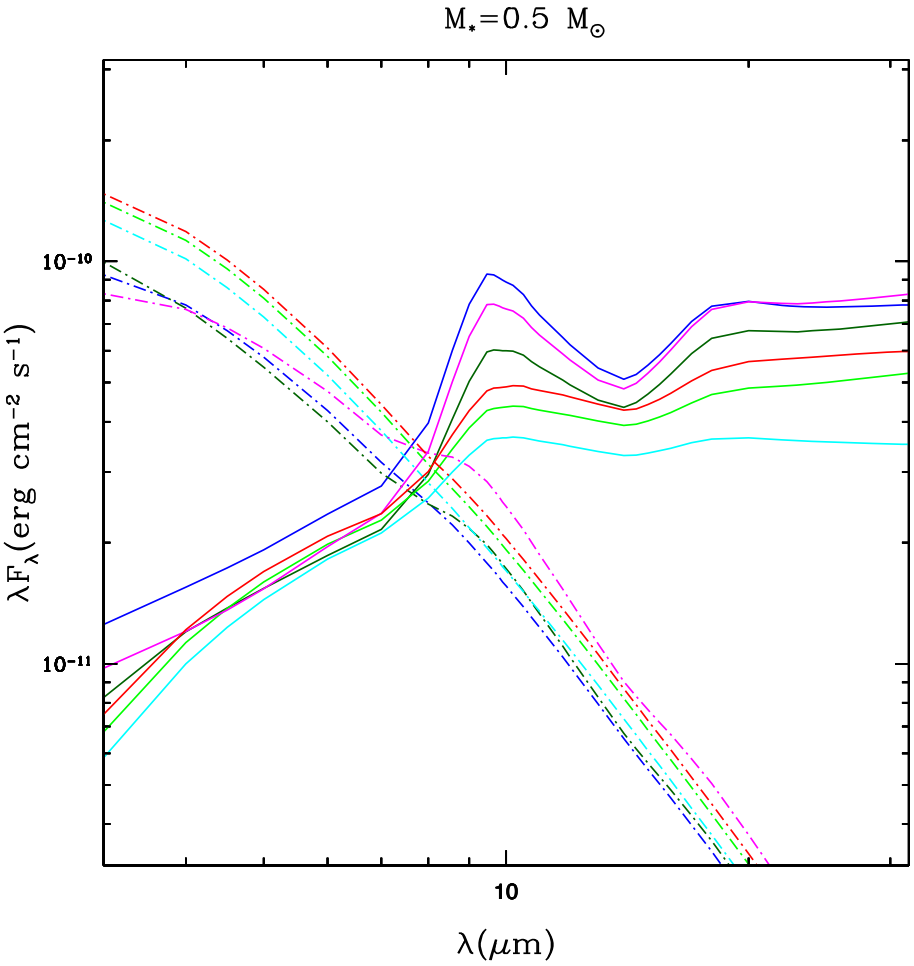

Figure 2.28 Dependence of wall (broken lines) and outer disk (solid lines) emission on grain size for a disk model of M_*=0.5 $M_\odot$ and astronomical silicates. Here vary the maximum size of grains in the upper layers of the disk for a model with $\dot{M}$=10^{-8} $M_\odot$ yr^{-1}, ϵ=0.01, and i=60°. We show disk models with a_{max}=0.05 μm (dark blue), 0.25 μm (magenta), 1 μm (dark green), 5 μm (red), 10 μm (light green), and 100 μm (cyan).

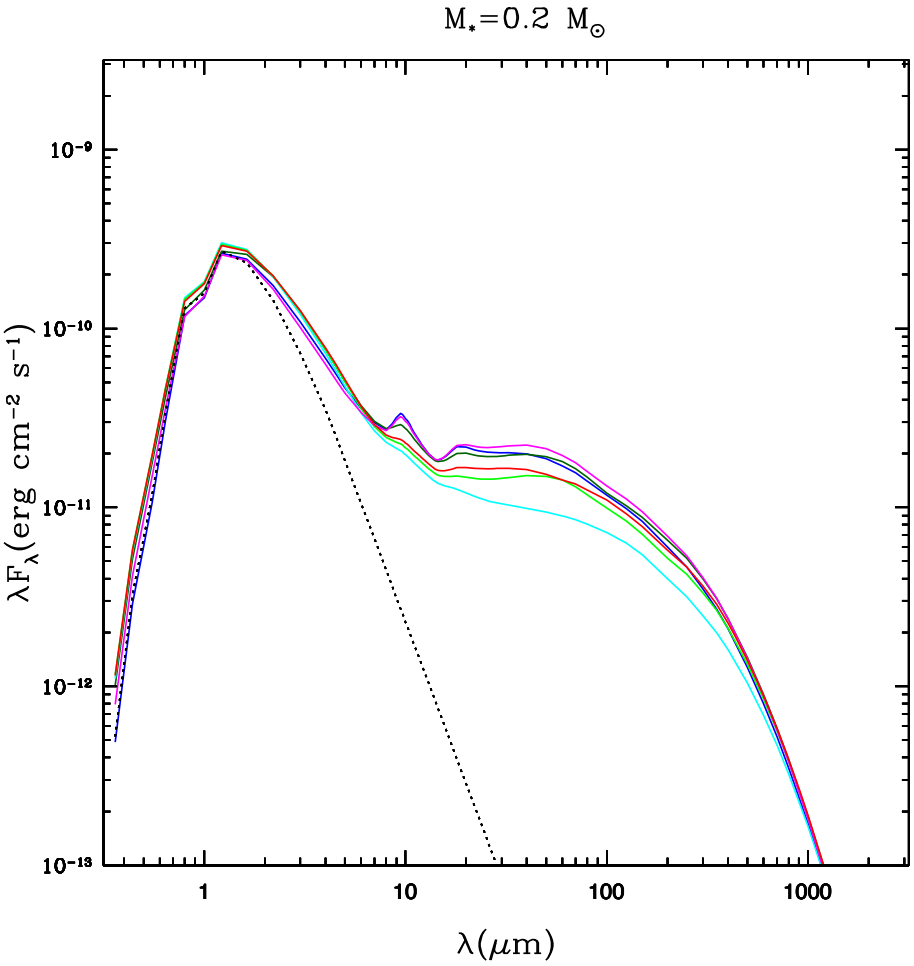

Figure 2.29 Dependence of disk emission on grain size for a disk model of M_*=0.2 $M_\odot$ and astronomical silicates. Here we vary the maximum size of grains in the upper layers of the disk for a model with $\dot{M}$=10^{-8} $M_\odot$ yr^{-1}, ϵ=0.01, and i=60°. We show disk models with a_{max}=0.05 μm (dark blue), 0.25 μm (magenta), 1 μm (dark green), 5 μm (red), 10 μm (light green), and 100 μm (cyan). The broken line corresponds to the stellar photosphere.

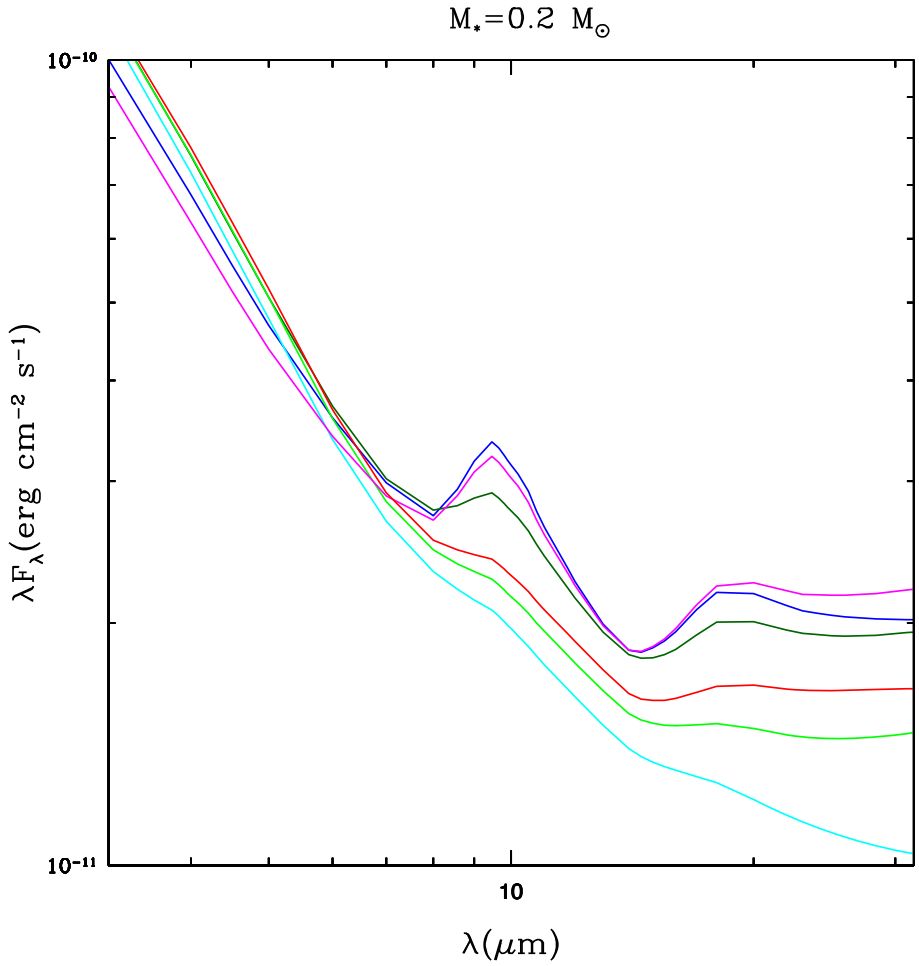

Figure 2.30 Dependence of silicate emission on grain size for a disk model of M_*=0.2 $M_\odot$ and astronomical silicates. Here we vary the maximum size of grains in the upper layers of the disk for a model with $\dot{M}$=10^{-8} $M_\odot$ yr^{-1}, ϵ=0.01, and i=60°. We show disk models with a_{max}=0.05 μm (dark blue), 0.25 μm (magenta), 1 μm (dark green), 5 μm (red), 10 μm (light green), and 100 μm (cyan).

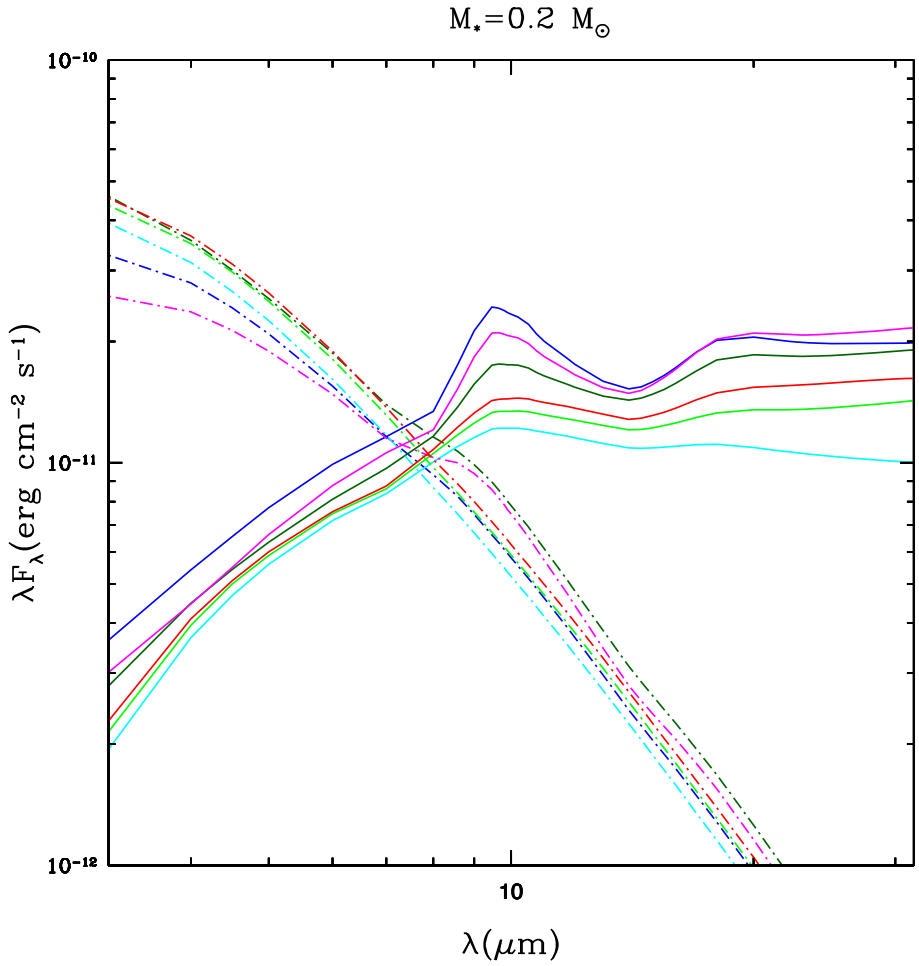

Figure 2.31 Dependence of wall (broken lines) and outer disk (solid lines) emission on grain size for a disk model of M_*=0.2 $M_\odot$ and astronomical silicates. Here vary the maximum size of grains in the upper layers of the disk for a model with $\dot{M}$=10^{-8} $M_\odot$ yr^{-1}, ϵ=0.01, and i=60°. We show disk models with a_{max}=0.05 μm (dark blue), 0.25 μm (magenta), 1 μm (dark green), 5 μm (red), 10 μm (light green), and 100 μm (cyan).

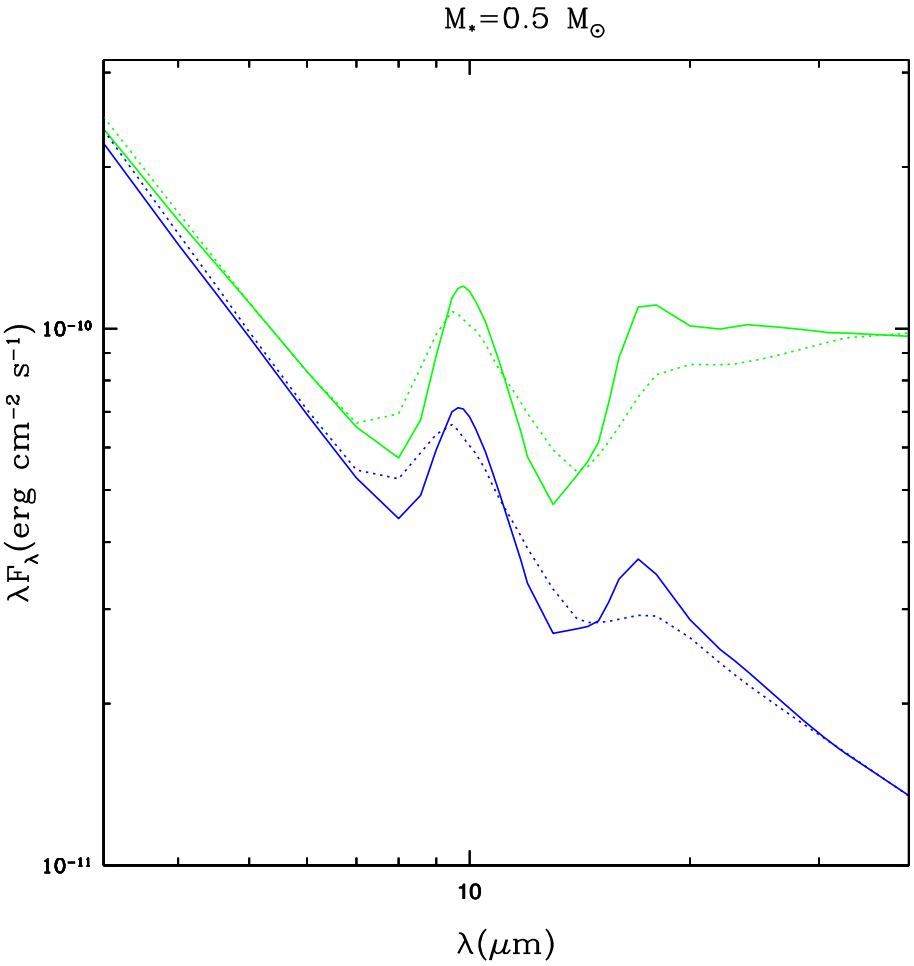

Figure 2.32 Comparison of SEDs for disk models with M_*=0.5 $M_\odot$ and different silicate compositions. We show disks with dust opacities for astronomical silicates (broken lines) from Draine & Lee (1984) and olivine silicates (solid lines) from Dorschner et al. (1995). The disks presented here have mass accretion rates of 10^{-9} $M_\odot$ yr^{-1} and $\epsilon = 0.001$ (dark blue) and 0.1 (green) and are at an inclination of 60°.

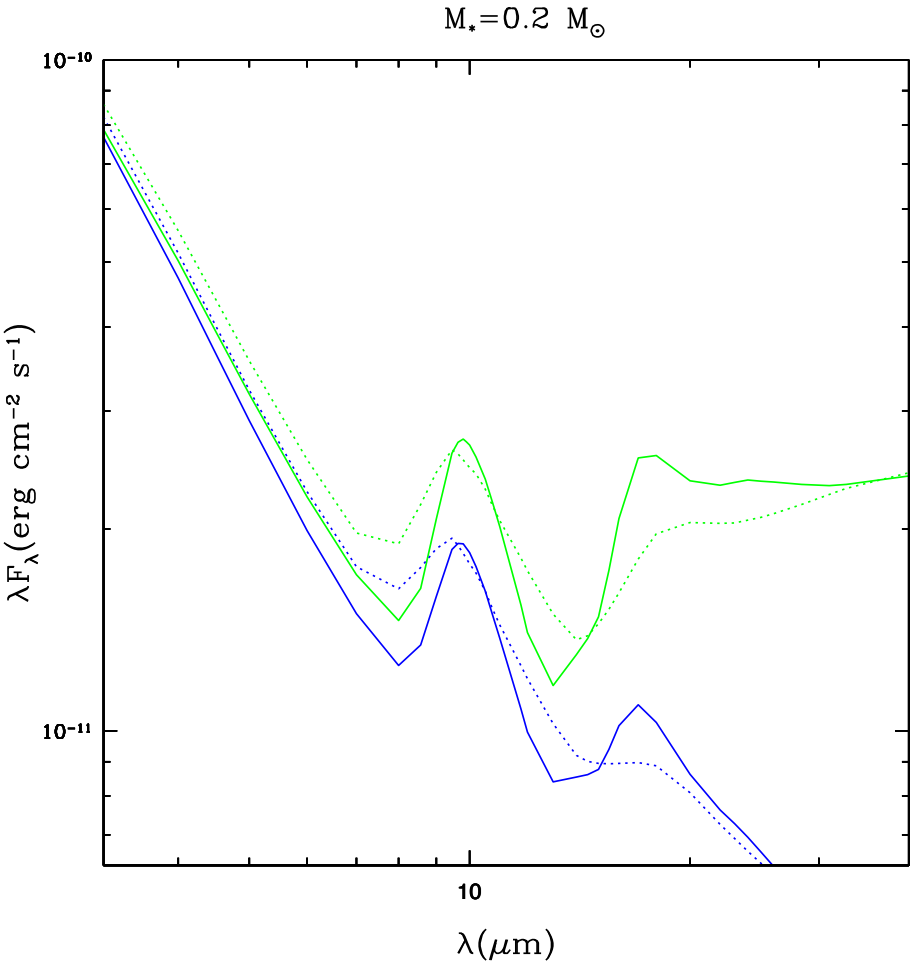

Figure 2.33 Comparison of SEDs for disk models with M_*=0.2 $M_\odot$ and different silicate compositions. We show disks with dust opacities for astronomical silicates (broken lines) from Draine & Lee (1984) and olivine silicates (solid lines) from Dorschner et al. (1995). The disks presented here have mass accretion rates of 10^{-9} $M_\odot$ yr^{-1} and $\epsilon = 0.001$ (dark blue) and 0.1 (green) and are at an inclination of 60°.

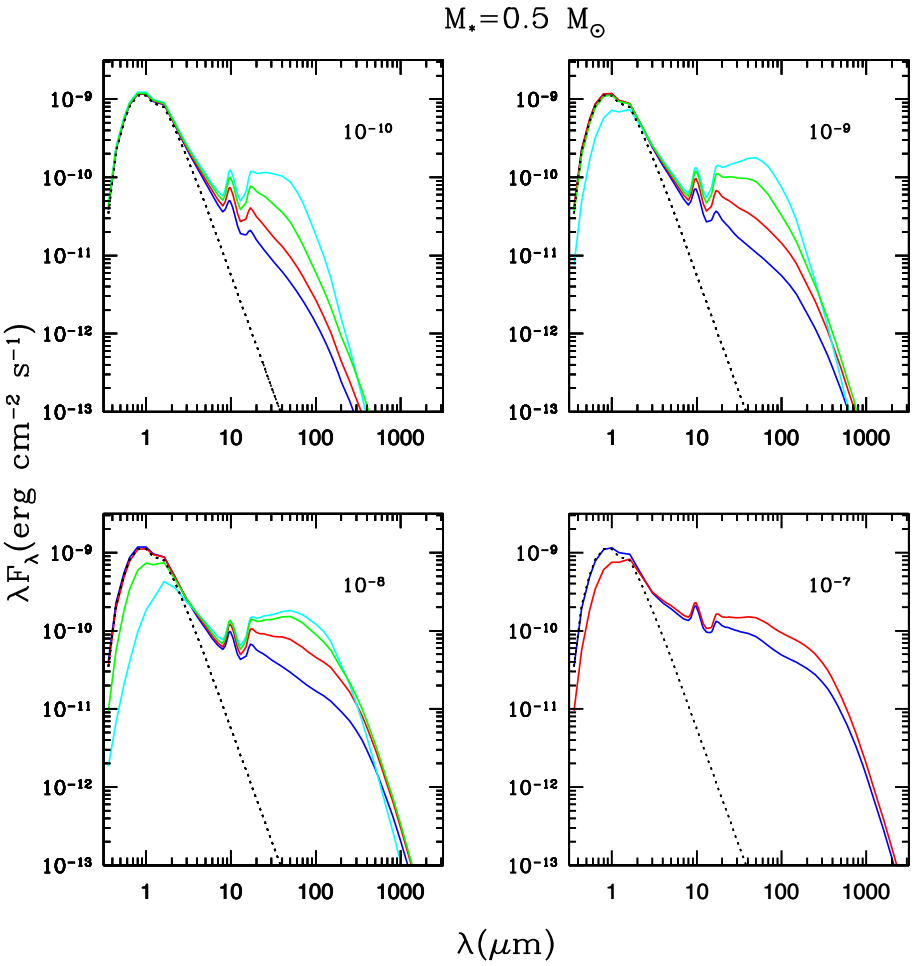

Figure 2.34 SEDs for disk models with M_*=0.5 $M_\odot$ and olivine silicates. We show SEDs for mass accretion rates of 10^{-10}, 10^{-9}, 10^{-8}, and 10^{-7} $M_\odot$ yr^{-1} and ϵ = 0.001 (dark blue), 0.01 (red), 0.1 (green), and 1.0 (cyan) at an inclination of 60°. We include extinction of the star by the disk. The broken line corresponds to the unextincted stellar emission.

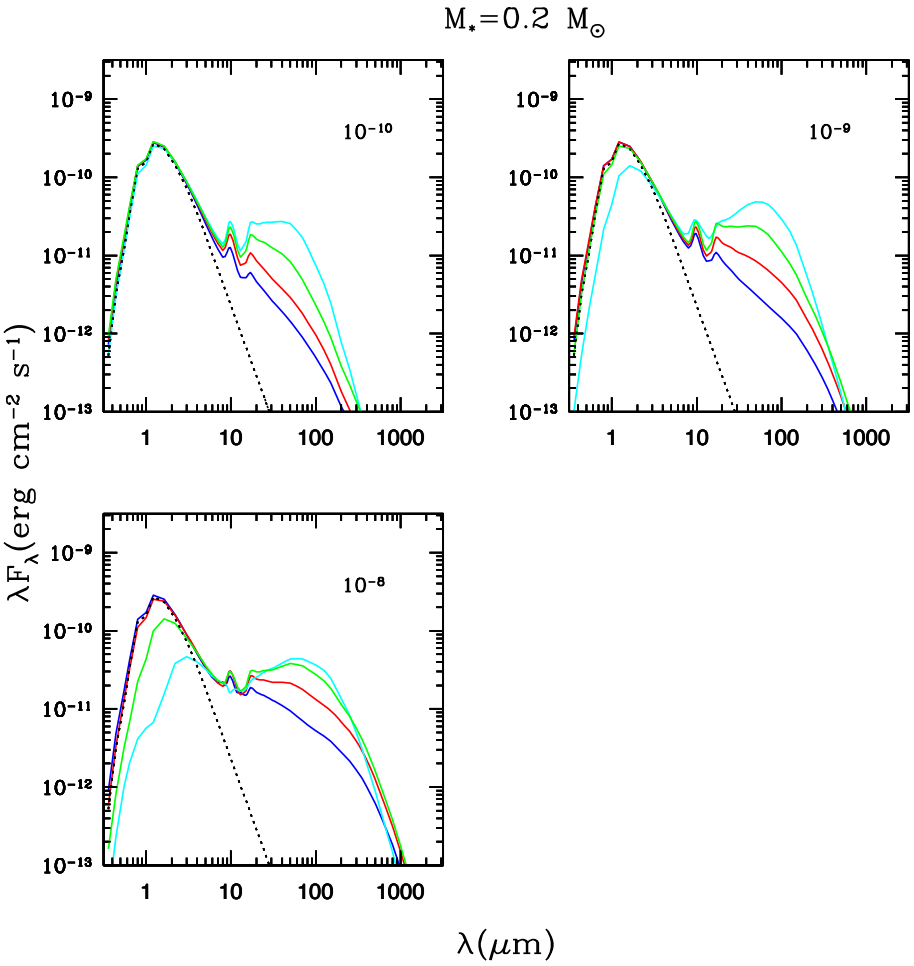

Figure 2.35 SEDs for disk models with M_*=0.2 $M_\odot$ and olivine silicates. We show SEDs for mass accretion rates of 10^{-10}, 10^{-9}, and 10^{-8} $M_\odot$ yr^{-1} and $\epsilon = 0.001$ (dark blue), 0.01 (red), 0.1 (green), and 1.0 (cyan) at an inclination of 60°. We include extinction of the star by the disk. The broken line corresponds to the unextincted stellar emission.

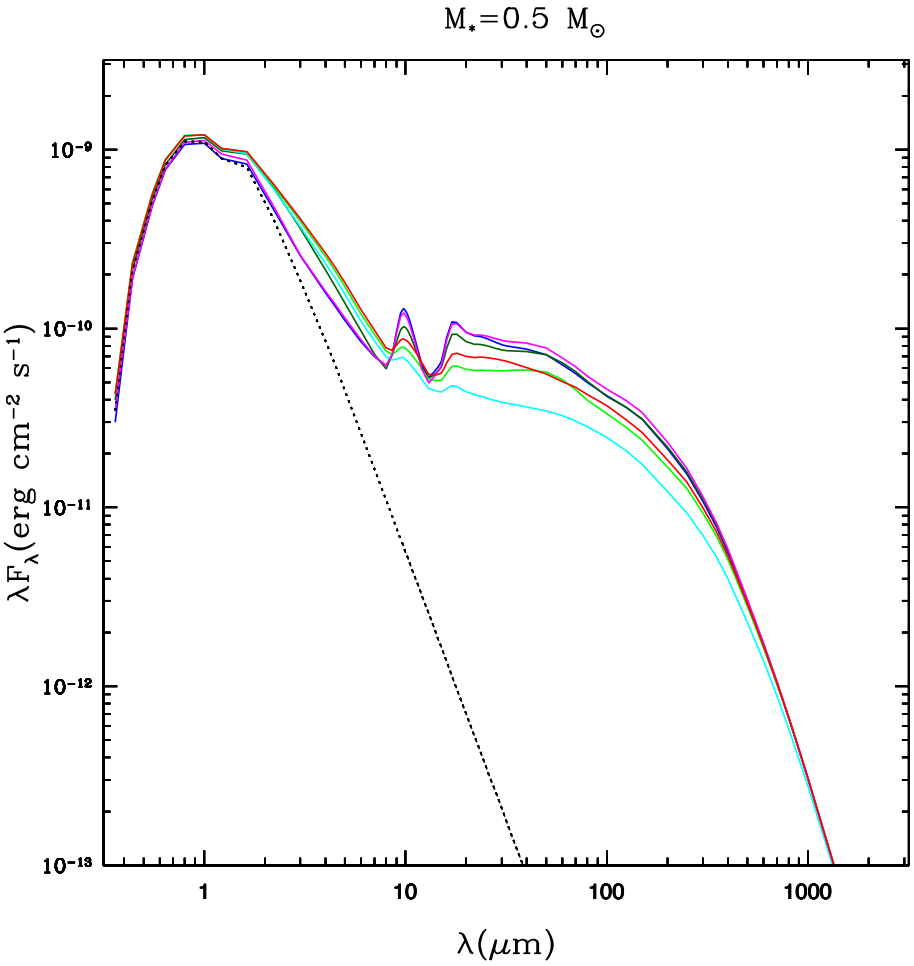

Figure 2.36 Dependence of disk emission on grain size for a disk model of M_*=0.5 $M_\odot$ with olivine silicates. Here we vary the maximum size of grains in the upper layers of the disk for a model with $\dot{M}$=10^{-8} $M_\odot$ yr^{-1}, ϵ=0.01, and i=60°. We show disk models with a_{max}=0.05 μm (dark blue), 0.25 μm (magenta), 1 μm (dark green), 5 μm (red), 10 μm (light green), and 100 μm (cyan) in the wall (broken lines) and the disk (solid lines). The broken line corresponds to the stellar photosphere.

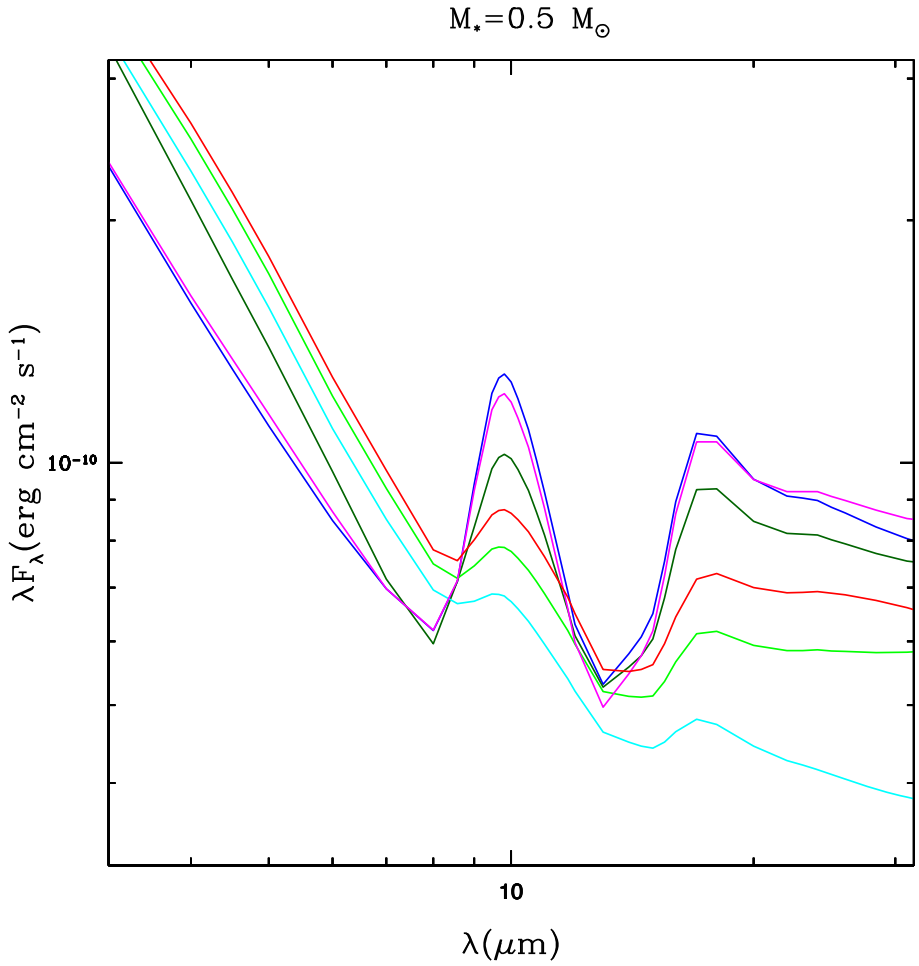

Figure 2.37 Dependence of silicate emission on grain size for a disk model of M_*=0.5 $M_\odot$ with olivine silicates. Here we vary the maximum size of grains in the upper layers of the disk for a model with $\dot{M}$=10^{-8} $M_\odot$ yr^{-1}, ϵ=0.01, and i=60°. We show disk models with a_{max}=0.05 μm (dark blue), 0.25 μm (magenta), 1 μm (dark green), 5 μm (red), 10 μm (light green), and 100 μm (cyan) in the wall (broken lines) and the disk (solid lines).

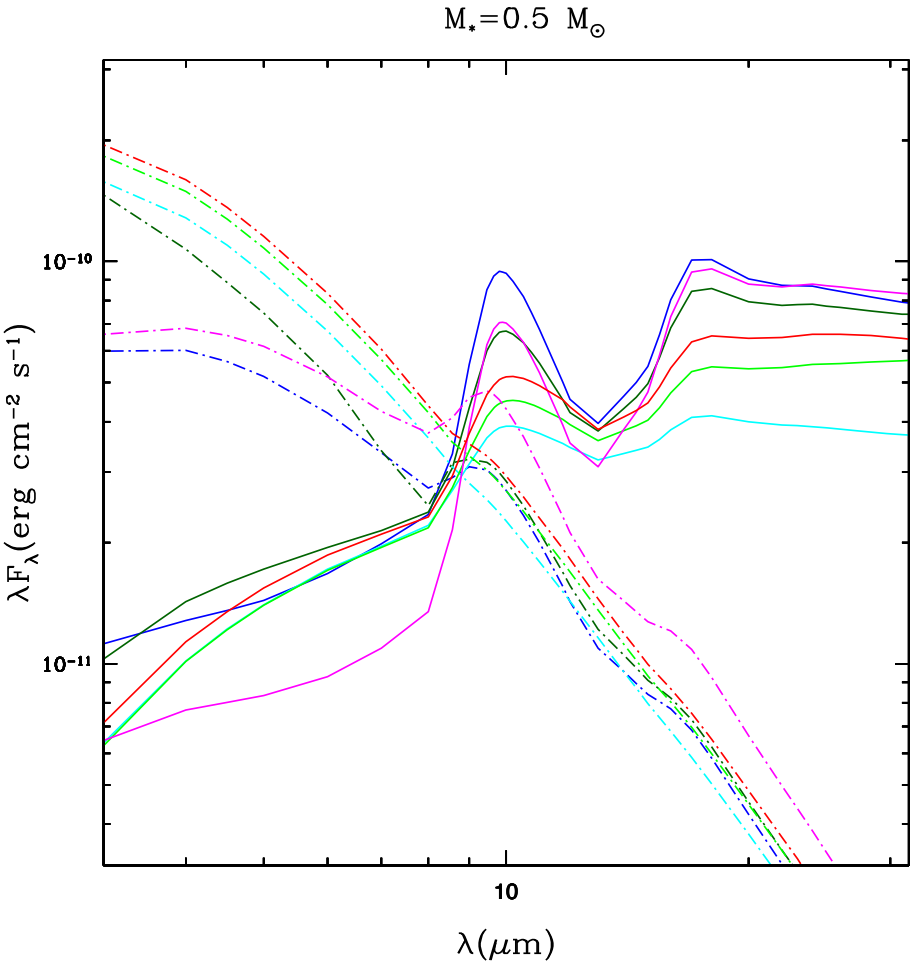

Figure 2.38 Dependence of of wall (broken lines) and outer disk (solid lines) emission on grain size for a disk model of M_*=0.5 $M_\odot$ with olivine silicates. Here we vary the maximum size of grains in the upper layers of the disk for a model with $\dot{M}$=10^{-8} $M_\odot$ yr^{-1}, ϵ=0.01, and i=60°. We show disk models with a_{max}=0.05 μm (dark blue), 0.25 μm (magenta), 1 μm (dark green), 5 μm (red), 10 μm (light green), and 100 μm (cyan) in the wall (broken lines) and the disk (solid lines).

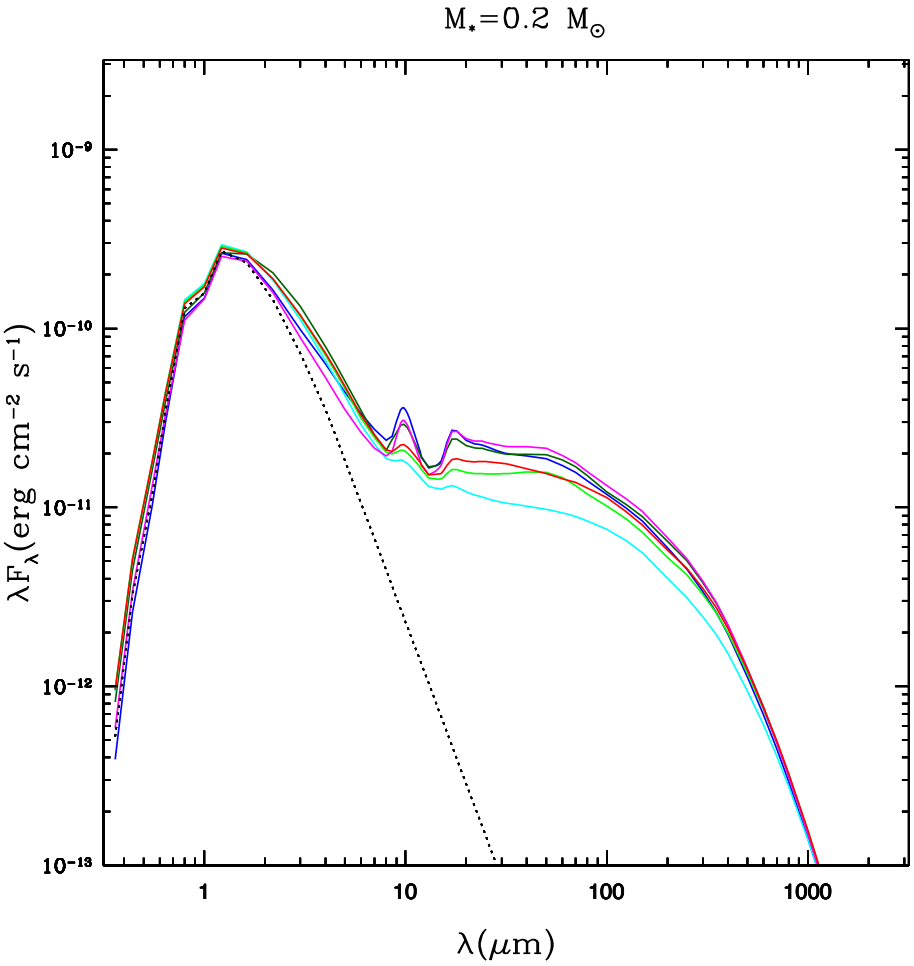

Figure 2.39 Dependence of disk emission on grain size for a disk model of M_*=0.2 $M_\odot$ with olivine silicates. Here we vary the maximum size of grains in the upper layers of the disk for a model with $\dot{M}$=10^{-8} $M_\odot$ yr^{-1}, ϵ=0.01, and i=60°. We show disk models with a_{max}=0.05 μm (dark blue), 0.25 μm (magenta), 1 μm (dark green), 5 μm (red), 10 μm (light green), and 100 μm (cyan) in the wall (broken lines) and the disk (solid lines). The broken line corresponds to the stellar photosphere.

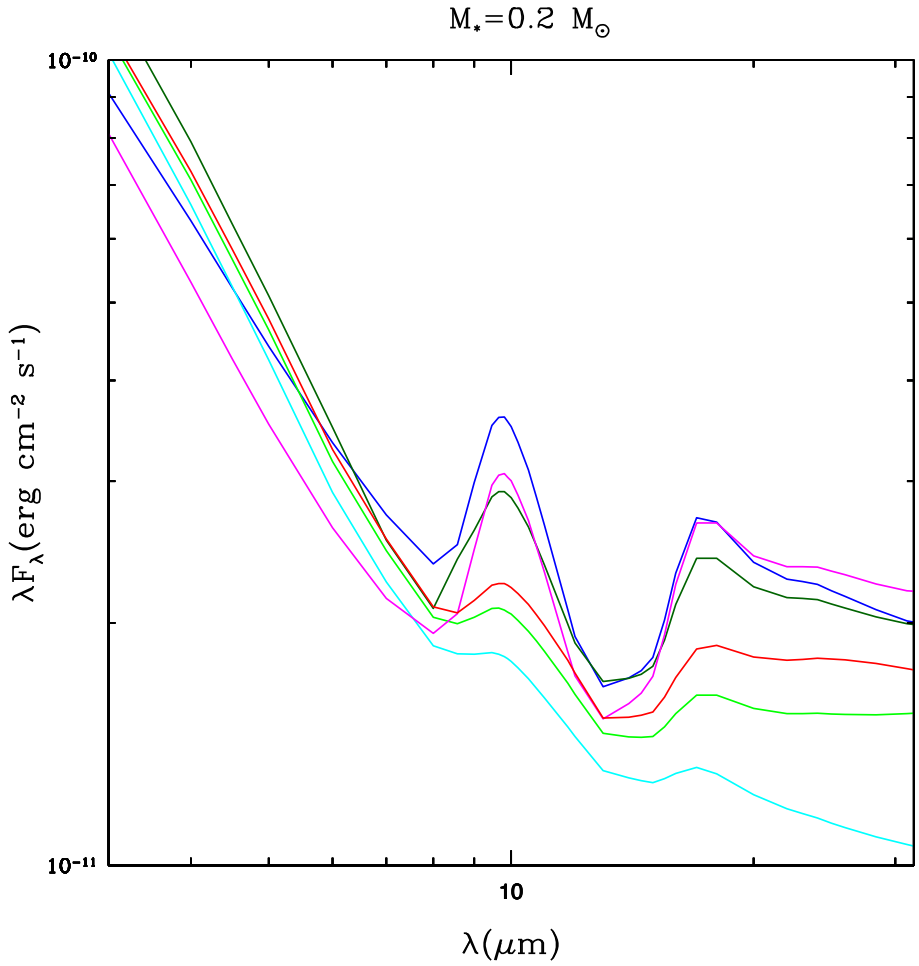

Figure 2.40 Dependence of silicate emission on grain size for a disk model of M_*=0.2 $M_\odot$ with olivine silicates. Here we vary the maximum size of grains in the upper layers of the disk for a model with $\dot{M}$=10^{-8} $M_\odot$ yr^{-1}, ϵ=0.01, and i=60°. We show disk models with a_{max}=0.05 μm (dark blue), 0.25 μm (magenta), 1 μm (dark green), 5 μm (red), 10 μm (light green), and 100 μm (cyan) in the wall (broken lines) and the disk (solid lines).

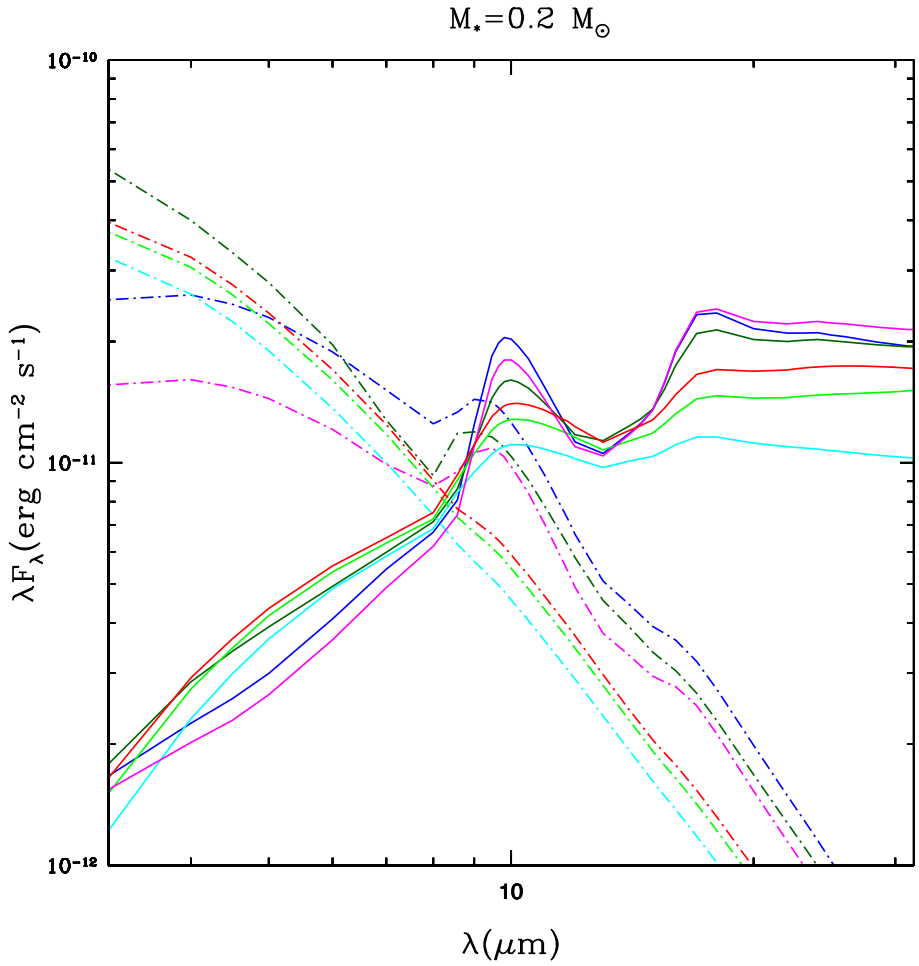

Figure 2.41 Dependence of wall (broken lines) and outer disk (solid lines) emission on grain size for a disk model of M_*=0.2 $M_\odot$ with olivine silicates. Here we vary the maximum size of grains in the upper layers of the disk for a model with $\dot{M}$=10^{-8} $M_\odot$ yr^{-1}, ϵ=0.01, and i=60°. We show disk models with a_{max}=0.05 μm (dark blue), 0.25 μm (magenta), 1 μm (dark green), 5 μm (red), 10 μm (light green), and 100 μm (cyan) in the wall (broken lines) and the disk (solid lines).

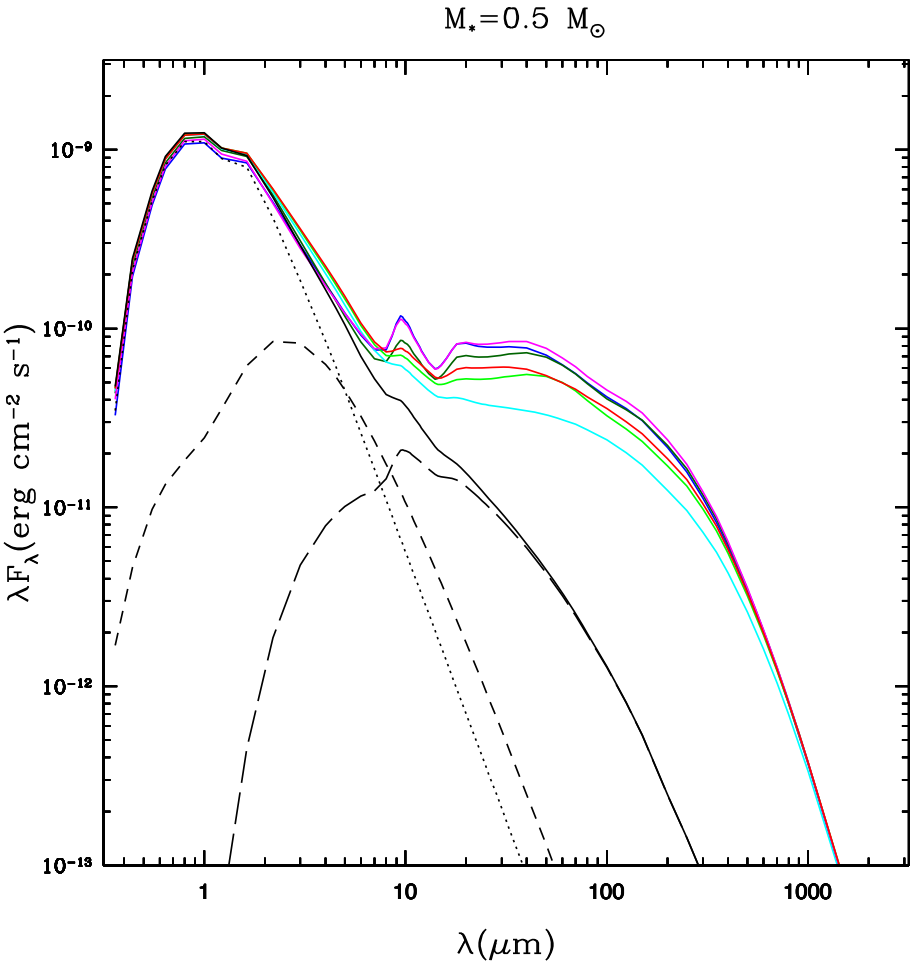

Figure 2.42 Emission for a disk with large grains and a low mass accretion rate around a 0.5 $M_\odot$ star. Here we use astronomical silicates, an a_{max} of 10 μm, ϵ of 0.001, and a mass accretion rate of 10^{-10} $M_\odot$ yr^{-1} (solid black line). Broken lines correspond to the stellar photosphere (dotted), the wall (short dashed), and the outer disk (long dashed). Colored solid lines correspond to models shown in Figure 2.26 and are shown for reference.

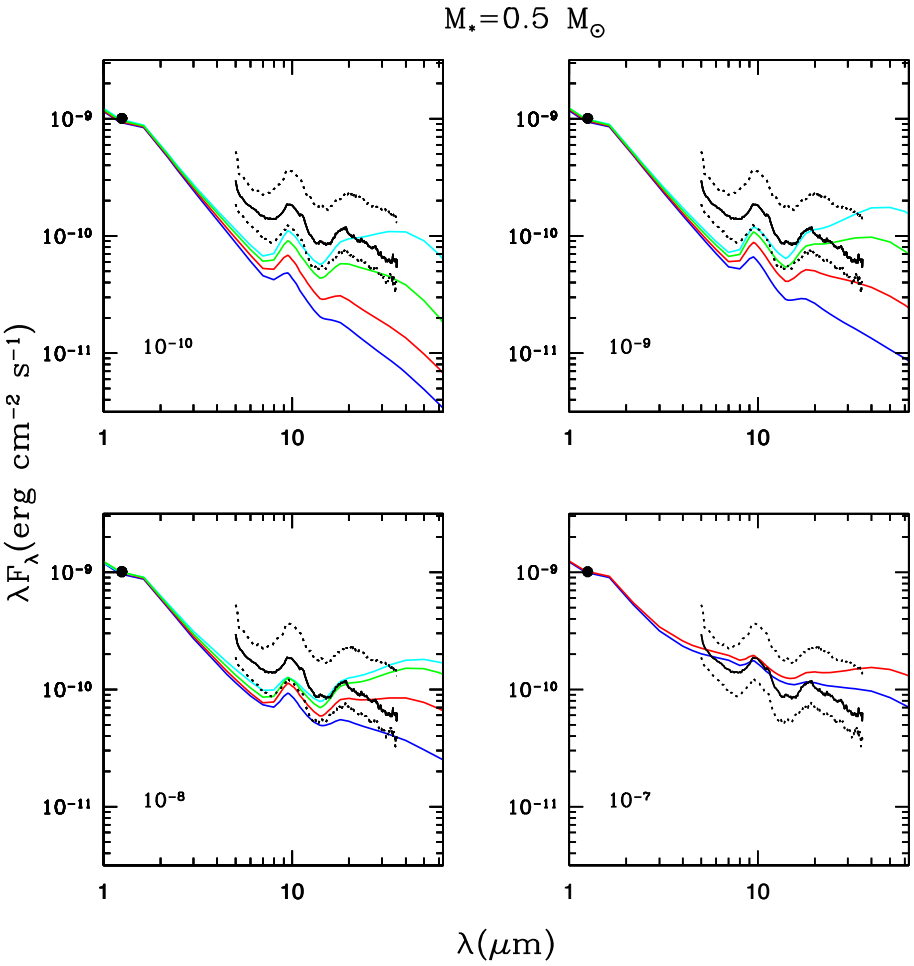

Figure 2.43 Median SED of Taurus compared to disk models with M_*=0.5 $M_\odot$ and astronomical silicates. The solid black line corresponds to the Taurus median SED for K5–M2 stars and broken lines delimit the region within which 50% of the observations lie. The observed SEDs are scaled to the models at J-band (filled black circle). The models have mass accretion rates between 10^{-7}–10^{-10} $M_\odot$ yr^{-1} and ϵ = 0.001 (dark blue), 0.01 (red), 0.1 (green), and 1.0 (cyan) at an inclination of 60° (see Figure 2.22 for an expanded wavelength range). Since the observed SEDs have been corrected for extinction here we do not include extinction of the star by the disk. Taurus data are from Furlan et al. (submitted).

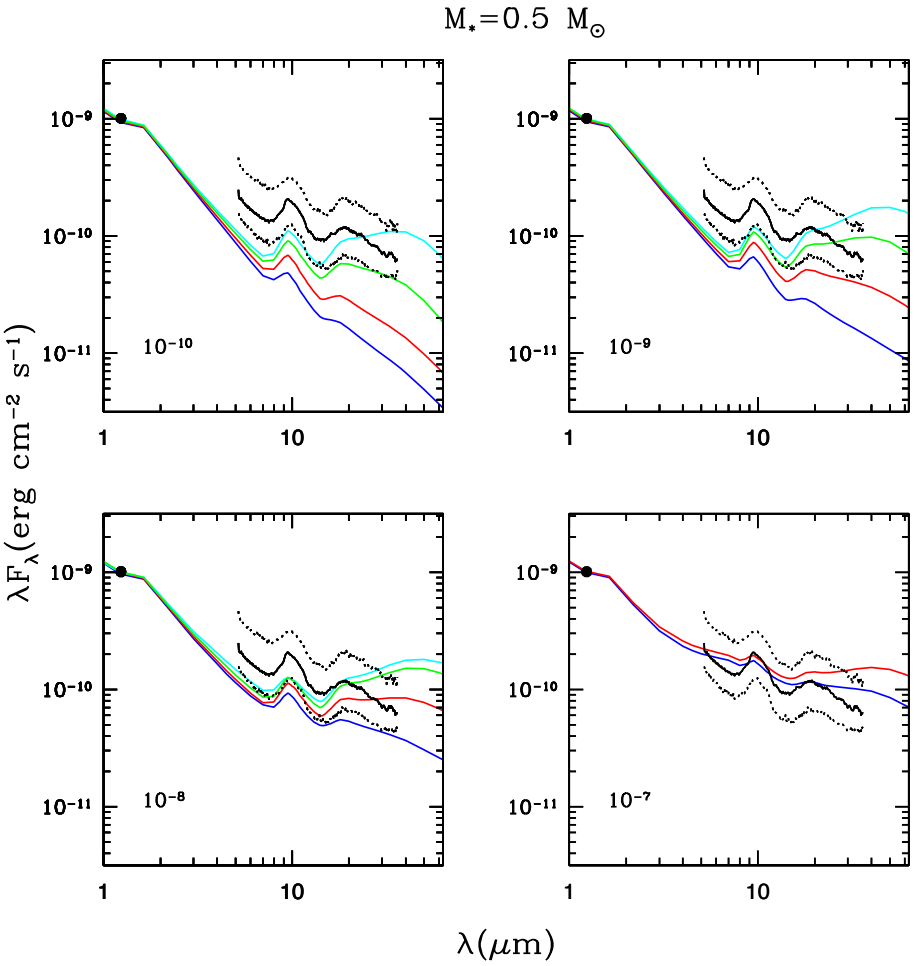

Figure 2.44 Median SED of Chamaeleon K5–M2 stars compared to disk models with M_*=0.5 $M_\odot$ and astronomical silicates. The solid black line corresponds to the Chamaeleon median SED and broken lines delimit the region within which 50% of the observations lie. The observed SEDs are scaled to the models at J-band (filled black circle). The models have mass accretion rates between 10^{-7}–10^{-10} $M_\odot$ yr^{-1} and ϵ = 0.001 (dark blue), 0.01 (red), 0.1 (green), and 1.0 (cyan) at an inclination of 60° (see Figure 2.22 for an expanded wavelength range). Since the observed SEDs have been corrected for extinction here we do not include extinction of the star by the disk. Chamaeleon data are from Puravankara et al. (in preparation).

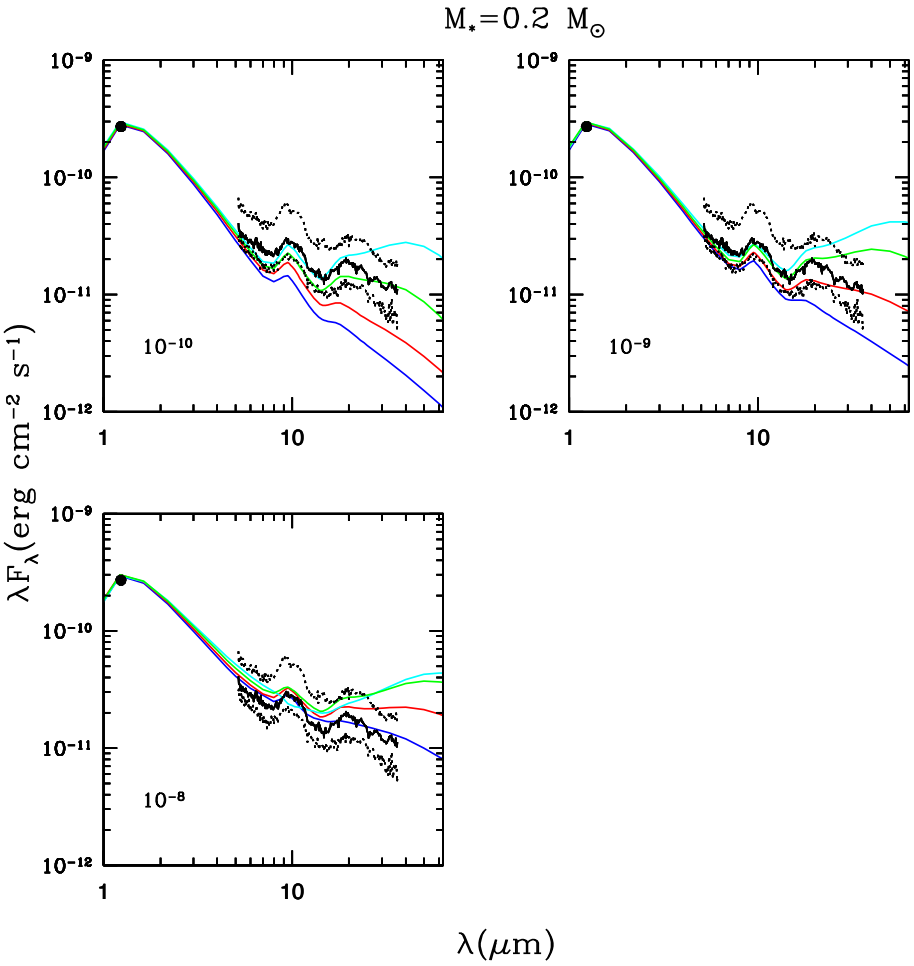

Figure 2.45 Median SED of Chamaeleon M3–M8 stars compared to disk models with M_*=0.2 $M_\odot$ and astronomical silicates. The solid black line corresponds to the Chamaeleon median SED and broken lines delimit the region within which 50% of the observations lie. The observed SEDs are scaled to the models at J-band (filled black circle). The models have mass accretion rates between 10^{-8}–10^{-10} $M_\odot$ yr^{-1} and ϵ = 0.001 (dark blue), 0.01 (red), 0.1 (green), and 1.0 (cyan) at an inclination of 60° (see Figure 2.23 for an expanded wavelength range). Since the observed SEDs have been corrected for extinction here we do not include extinction of the star by the disk. Chamaeleon data are from Puravankara et al. (in preparation).

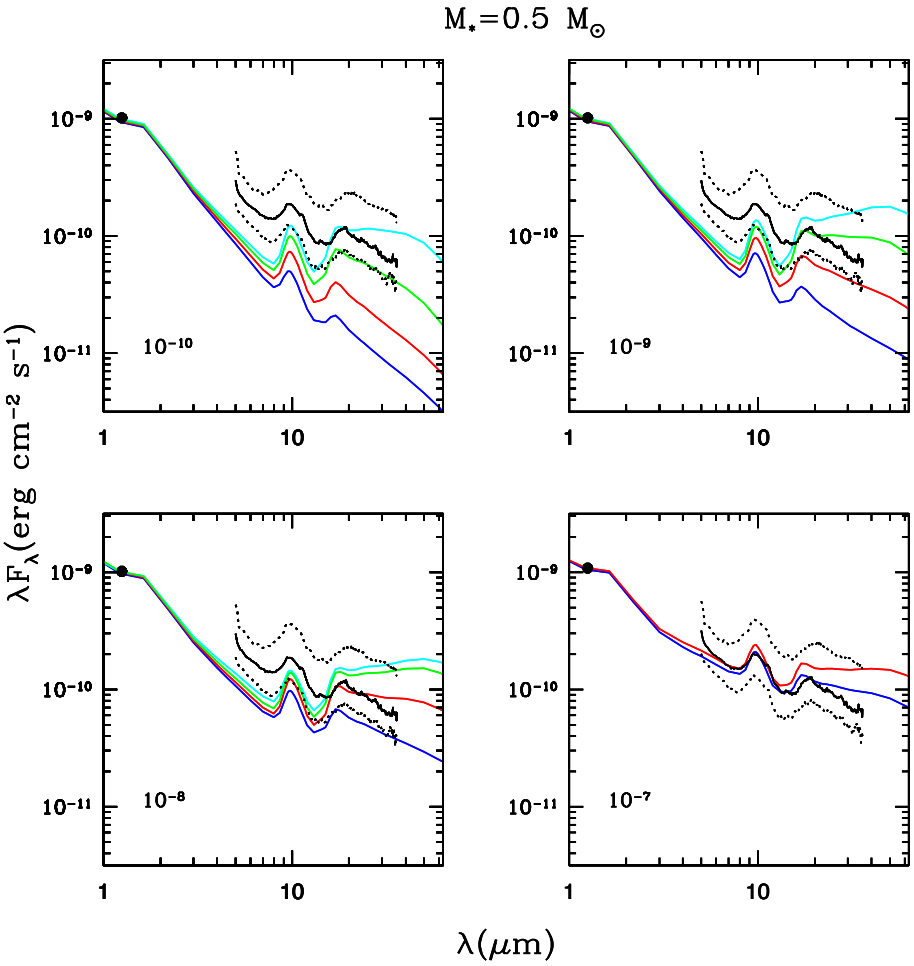

Figure 2.46 Median SED of Taurus compared to disk models with M_*=0.5 $M_\odot$ and olivine silicates. The solid black line corresponds to the Taurus median SED and broken lines delimit the region within which 50% of the observations lie. The observed SEDs are scaled to the models at J-band (filled black circle). The models have mass accretion rates between 10^{-7}–10^{-10} $M_\odot$ yr^{-1} and $\epsilon = 0.001$ (dark blue), 0.01 (red), 0.1 (green), and 1.0 (cyan) at an inclination of 60° (see Figure 2.34 for an expanded wavelength range). Since the observed SEDs have been corrected for extinction here we do not include extinction of the star by the disk. Taurus data are from Furlan et al. (submitted).

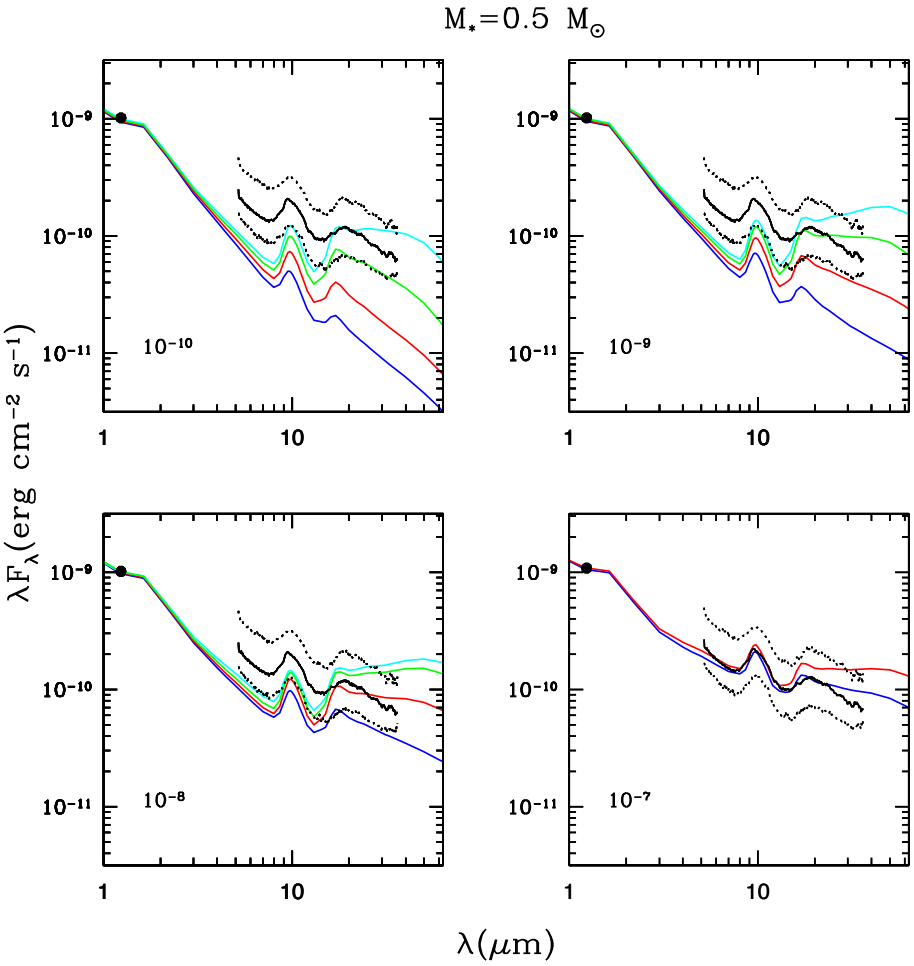

Figure 2.47 Median SED of Chamaeleon K5–M2 stars compared to disk models with M_*=0.5 $M_\odot$ and olivine silicates. The solid black line corresponds to the Chamaeleon median SED and broken lines delimit the region within which 50% of the observations lie. The observed SEDs are scaled to the models at J-band (filled black circle). The models have mass accretion rates between 10^{-7}–10^{-10} $M_\odot$ yr^{-1} and $\epsilon = 0.001$ (dark blue), 0.01 (red), 0.1 (green), and 1.0 (cyan) at an inclination of 60° (see Figure 2.34 for an expanded wavelength range). Since the observed SEDs have been corrected for extinction here we do not include extinction of the star by the disk. Chamaeleon data are from Puravankara et al. (in preparation).

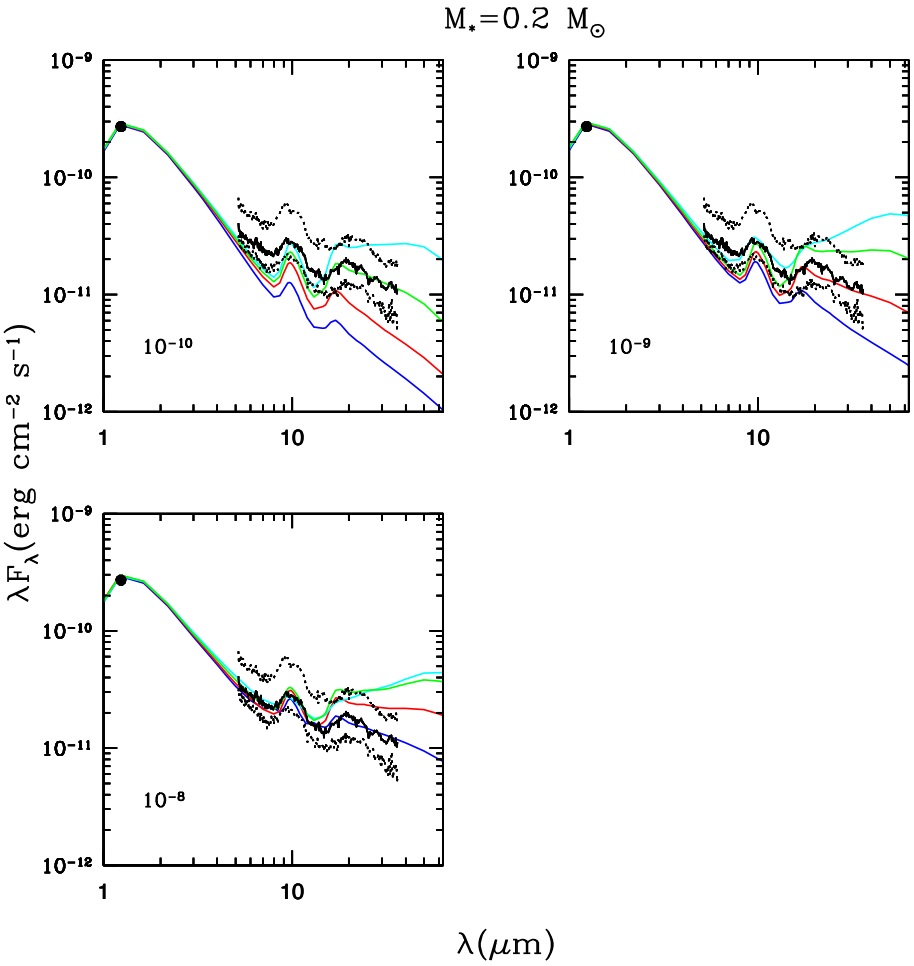

Figure 2.48 Median SED of Chamaeleon M3–M8 stars compared to disk models with M_*=0.2 $M_\odot$ and olivine silicates. The solid black line corresponds to the Chamaeleon median SED and broken lines delimit the region within which 50% of the observations lie. The observed SEDs are scaled to the models at J-band (filled black circle). The models have mass accretion rates between 10^{-8}–10^{-10} $M_\odot$ yr^{-1} and $\epsilon = 0.001$ (dark blue), 0.01 (red), 0.1 (green), and 1.0 (cyan) at an inclination of 60° (see Figure 2.35 for an expanded wavelength range). Since the observed SEDs have been corrected for extinction here we do not include extinction of the star by the disk. Chamaeleon data are from Puravankara et al. (in preparation).

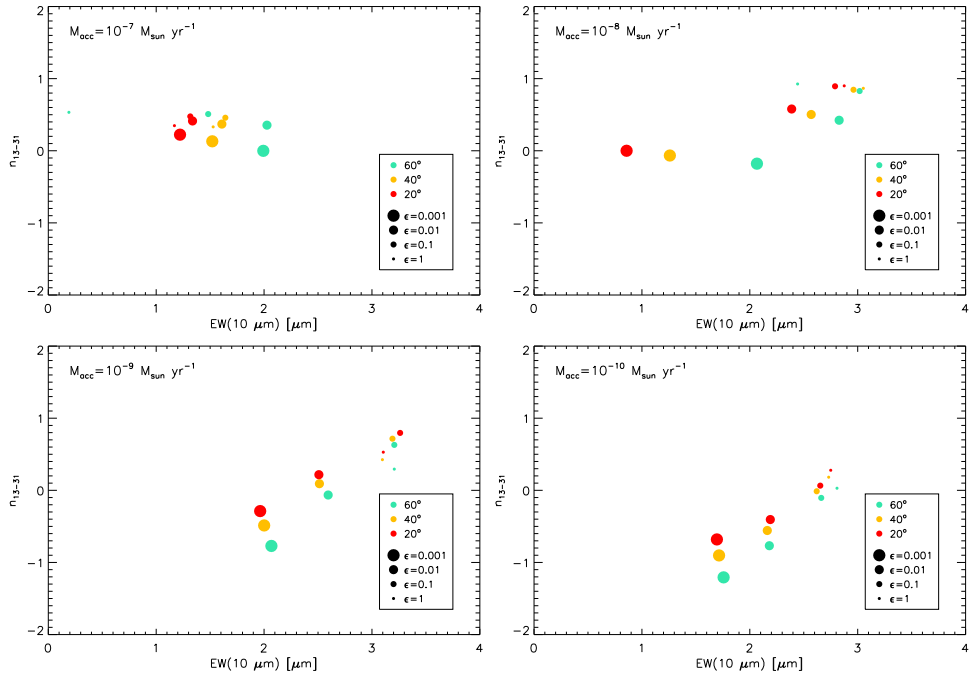

Figure 2.49 Slope of SED between 13 and 31 μm versus the equivalent width of the 10 μm silicate emission feature for disk models with M=0.5 $M_{\odot}$. ϵ are labeled according to the size of the circles and inclinations angles are labeled by color. Refer to key at bottom right of panels. Figure from Furlan et al. (submitted).

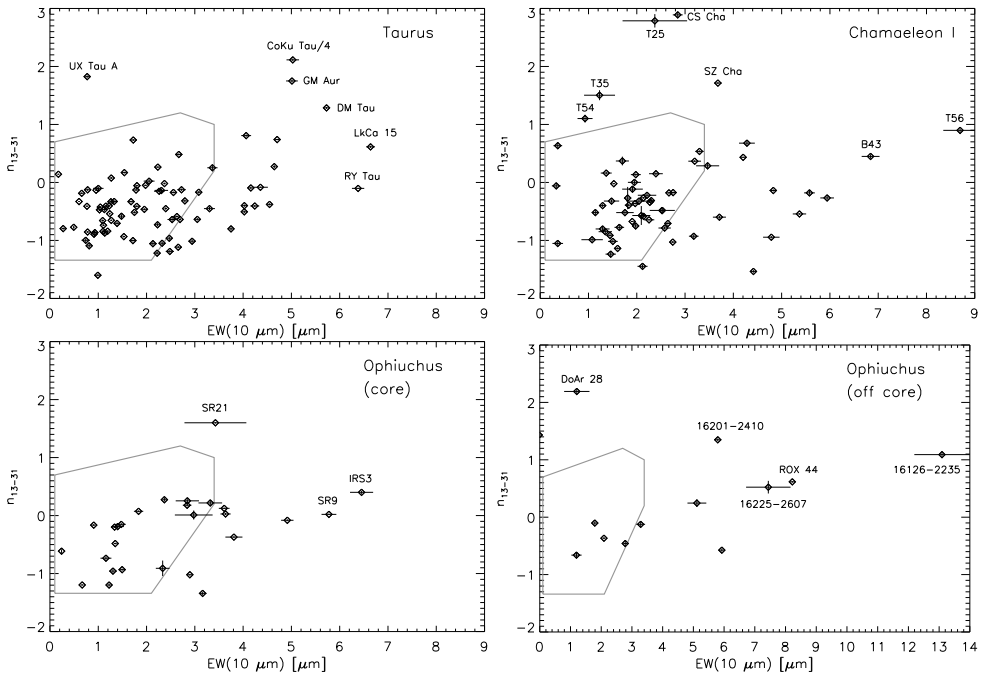

Figure 2.50 Spectral indices of targets in Taurus, Chamaeleon, and Ophiuchus compared with disk models. We show the slope of the SED between 13 μm and 31 μm versus the equivalent width of the 10 μm silicate feature. The disks which can be explained by typical "full" disk models lie within the polygon. Transitional disks and the pre-transitional disks LkCa 15 and UX Tau A are labeled. There are some disks which cannot be explained with the full disk model (i.e. the unlabeled symbols which lie outside the polygon). These "outliers" have more silicate emission than predicted by full disk models. Figure taken from Furlan et al. (submitted).

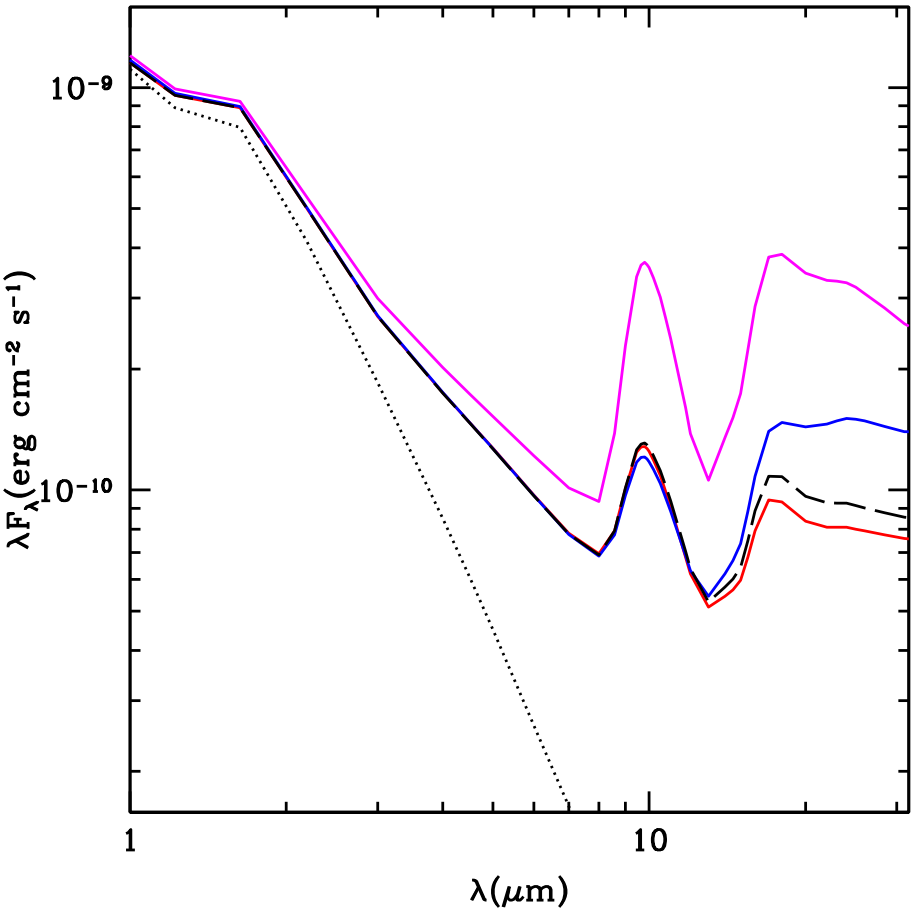

Figure 2.51 Simulations of gapped disks compared to a typical full disk model. Models correspond to a disk around a 0.5 $M_\odot$ star with olivine silicates, a mass accretion rate of 10^{-8} $M_\odot$ yr^{-1}, an ϵ of 0.01, and an inclination of 60°. The dotted line corresponds to the stellar photosphere. A disk with a gap extending from 5 AU to 10 AU in the disk (red line) is almost indistinguishable from a full disk (dashed line). Here we assume that the wall of the outer disk is shadowed by the inner disk and does not contribute to the emission. As the inner disk accretes onto the star and becomes smaller, one would expect that a fraction of the outer disk's wall will become illuminated. Therefore, one will begin to see departures from a full disk beyond 20 μm (dark blue). Note that in this simulation the gap ranges from 2 – 10 AU in the disk. Once the gap spans 0.2 – 10 AU (magenta) in the disk, significant differences from a full disk are evident in the SED, particularly in the strength of the 10 μm silicate feature. As is seen in the pre-transitional disk of LkCa 15, we assumed that the outer wall is fully illuminated and that there is $\sim 10^{-10}$ $M_\odot$ of optically thin dust within the gap.

Chapter 3

Probing the Dust and Gas in the Transitional Disk of CS Cha with *Spitzer*

Abstract: Here we present the *Spitzer* IRS spectrum of CS Cha, a member of the ∼2 Myr old Chamaeleon star–forming region, which reveals an optically thick circumstellar disk truncated at ∼43 AU, the largest hole modeled in a transitional disk to date. Within this inner hole, $\sim 5 \times 10^{-5}$ lunar masses of dust are located in a small optically thin inner region which extends from 0.1 to 1 AU. In addition, the disk of CS Cha has bigger grain sizes and more settling than the previously modeled transitional disks DM Tau, GM Aur, and CoKu Tau/4, suggesting that CS Cha is in a more advanced state of dust evolution. The *Spitzer* IRS spectrum also shows [Ne II] 12.81 μm fine-structure emission with a luminosity of 1.3×10^{29} ergs s^{-1}, indicating that optically thin gas is present in this ∼43 AU hole, in agreement with H_α measurements and a UV excess which indicate that CS Cha is still accreting 1.2×10^{-8} $M_\odot$ yr^{-1}. We do not find a correlation of the [Ne II] flux with L_X, however, there is a possible correlation with $\dot{M}$, which if confirmed would suggest that EUV fluxes due to accretion are the main agent for formation of the [Ne II] line.

3.1 Introduction

The *Spitzer Space Telescope* (Werner et al., 2004) has dramatically improved the ability to study the dust in disks by giving us detailed spectral energy distributions (SEDs) in the mid-infrared, where the dust dominates the emission. *Spitzer* Infrared Spectrograph (Houck et al., 2004) observations of T Tauri stars have provided strong evidence of dust evolution, particularly in the well surveyed ∼1-2 Myr old Taurus-Auriga star–forming region (Furlan et al., 2006). The most notable evidence of dust evolution lies in the observations of transitional disks. These disks have characteristics that fall between those objects that have clear evidence for disks and those objects with no disk material; the SEDs point to inner holes in the disk. All transitional disks have a significant deficit of flux in the near-IR which has been explained by modeling the disks with truncated optically thick disks (Uchida et al., 2004; Calvet et al., 2005b; D'Alessio et al., 2005).

CoKu Tau/4 is one of these transitional disks in Taurus (Forrest et al., 2004; D'Alessio et al., 2005). The SED of this object is photospheric below 8 μm and rises at longer wavelengths, showing weak silicate emission at 10 μm; this can be explained by the emission of the frontally illuminated edge or "wall" of an outer disk truncated at 10 AU from the star (D'Alessio et al., 2005) and the weak silicate emission arises in the atmosphere of the wall. There are no small grains in the inner disk, in agreement with CoKu Tau/4's classification as a non-accreting, weak T Tauri star. Hydrodynamical simulations indicate that this hole may be due to the formation of a planet (Quillen et al., 2004). Other studies point to photoevaporation of the disk by the star (Alexander & Armitage, 2007). However, the clearing in the

inner disk of CoKu Tau/4 is most likely due to clearing by its companion (Ireland & Kraus, 2008). Similar to CoKu Tau/4, DM Tau has been modeled with an inner disk region free of small dust and a truncated optically thick disk at 3 AU (Calvet et al., 2005b). However, this star is still accreting, indicating that gas should still remain in the inner disk region. GM Aur, which is also accreting, was modeled by Calvet et al. (2005b) with an optically thick disk truncated at 24 AU and a small amount of dust in the inner disk which leads to its observed near-IR excess. This disk hole could also be due to a planet (Rice et al., 2003). TW Hya, a transitional disk in the ∼10 Myr old TW Hya association (Jayawardhana et al., 1999; Webb et al., 1999), has an outer optically thick disk with a 4 AU hole filled with an inner optically thin region populated by a small amount of dust (Calvet et al., 2002; Uchida et al., 2004).

Not only has *Spitzer* been a powerful tool in exploring the dust evolution in circumstellar disks, it also has the potential to access new probes of the gas evolution in these disks, an area of study which is still in its infancy and largely uncertain. High-resolution molecular spectroscopy has permitted us to access abundant molecular tracers within the inner disk such as H_2 and CO (Bergin et al., 2004; Najita et al., 2007b). A new gas diagnostic has emerged in the mid-infrared with the detection of [Ne II] emission with *Spitzer*. [Ne II] emission at 12.81 μm has been detected from a few T Tauri stars that were observed as part of the FEPS *Spitzer* Legacy program (Pascucci et al., 2007) as well as in the transitional disks CS Cha, DM Tau, and TW Hya (Espaillat et al., 2007a).

We will present and analyze *Spitzer* IRS data of CS Cha, a transitional disk in the ∼2 Myr old Chamaeleon star–forming region (Luhman, 2004).

3.2 Observations

CS Cha was observed by the *Spitzer* IRS instrument on 11 July 2005 in Staring Mode (AOR ID: 12695808). We used the short- and long-wavelength, low-resolution (SL, LL) modules of IRS at a resolving power of $\lambda/\delta\lambda = 60 - 100$. The total exposure time was 28 and 12 seconds for SL and LL respectively. We reduced the data with the SMART package (Higdon et al., 2004). We follow the same reduction procedure as Calvet et al. (2005b). The 12.81 μm [Ne II] line is not extended and is consistent with the CS Cha point source.

The photometry at 24 and 70 μm was extracted from the MIPS post-BCD mosaicked images (AOR ID: 3962112) using the aperture photometry routine in the Astronomical Point Source Extraction (APEX) software package developed by the SSC (Makovoz & Marleau, 2005). An aperture of radius 14.″94, with a sky annulus between 29.″88and 42.″33, was used at 24 μm while an aperture of radius 29.″55, with a sky annulus between 39.″40 and 68.″95, was used at 70 μm. Both fluxes were aperture corrected by factors of 1.143 at 24 μm and 1.298 at 70 μm, as calculated by Su et al. (2006). No color correction was applied.

3.3 Analysis

3.3.1 Dust Properties

Figure 3.1 shows the SED of CS Cha consisting of optical (Gauvin & Strom, 1992), 2MASS, L-band (Luhman, 2004), *Spitzer* IRS, IRAS (Gauvin & Strom, 1992), MIPS, and millimeter (Henning et al., 1993) data. We also show the median SED of Taurus (D'Alessio et al., 1999; Furlan et al., 2006) which emphasizes the stark deficit of flux

in the near infrared, an indicator of an inner disk hole, which is characteristic of transitional disks.

A distance of 160 pc to Chamaeleon I (Whittet et al., 1997) and a spectral type of K6 from Luhman (2004) are adopted. The extinction is calculated by fitting the observed photospheric colors to the photosphere calibrated by a standard K6 star with an effective temperature of 4205 K (Kenyon & Hartmann, 1995). Data are then dereddened with an A_V of 0.8 and the Mathis (1990) reddening law. Stellar parameters (M_*, R_*, L_*) are listed in Table 3.1; the mass was derived from the Siess et al. evolutionary tracks (Siess et al., 2000). An inclination angle of 60° to the line of sight is adopted.

The SED suggests a UV excess which is thought to be formed in the accretion shock on the stellar surface (Calvet & Gullbring, 1998). This is supported by H_α equivalent widths of 20 Å (Luhman, 2004) and 65 Å (Hartigan, 1993), which indicate CS Cha is accreting (White & Basri, 2003). We calculate a mass accretion rate of 1.2×10^{-8} $M_\odot$ yr^{-1} from this U-band excess following Gullbring et al. (1998), with a typical uncertainty of a factor of 2 or 3 (Calvet et al., 2004).

We model CS Cha as a truncated optically thick disk with a frontally illuminated vertical wall and an inner optically thin region. The black solid line in Figure 3.2 is the best fit model to the observations; different model components are represented by the broken lines. We use a grain-size distribution that follows a power-law of the form $a^{-3.5}$, where a is the grain radius, with a_{min} of 0.005 μm and a_{max} of 5 μm. The structure and emission of the optically thick disk (Figure 3.2) is calculated with models including dust settling following D'Alessio et al. (2006), where we use

millimeter fluxes (Henning et al., 1993; Lommen et al., 2007) and MIPS to constrain the outer disk properties. Input parameters are the stellar properties and the mass accretion rate of the disk ($\dot{M}$), the viscosity parameter (α), the dust composition, and the settling parameter $\epsilon = \zeta_{up}/\zeta_{st}$, i.e. the mass fraction of the small grains in the upper layers relative to the standard dust-to-gas mass ratio (D'Alessio et al., 2006). Table 3.1 shows all relevant values. The disk mass, 0.04 $M_\odot$, is determined by the mass surface density which is proportional to $\dot{M}/\alpha$ and the assumed disk radius. This result is not inconsistent with the disk mass of 0.021 $M_\odot$ derived by Henning et al. (1993) from 1.3 mm fluxes.

The optically thick disk has an edge or "wall" directly exposed to stellar radiation (Figure 3.2). The radiative transfer in the wall atmosphere is calculated following D'Alessio et al. (2005) with the following inputs: stellar mass (M_*), stellar radius (R_*), $\dot{M}$, stellar effective temperature (T_*), maximum and minimum grains sizes, temperature of the optically thin wall atmosphere (T_{wall}). See Table 3.1 for the wall's location (R_{wall}), maximum grain size (a_{max}), and other parameters.

The emission at 10 μm comes from the optically thin inner region (Calvet et al., 2005b) which extends up to 1 AU from the star and has a minimum grain size of 1.9 μm and a maximum grain size of 2.1 μm (Figure 3.2). The total emission is scaled to the vertical optical depth at 10 μm, $\tau_0 \sim 0.009$. This region is populated by $\sim 10^{-12}$ $M_\odot$ or $\sim 5\times10^{-5}$ M_{moon} of uniformly distributed dust. This small amount of dust leads to the slight 5 – 8 μm excess above the photosphere (most easily seen in Figure 3.3). The dust in this region is composed of 88% amorphous silicates, 5% of amorphous carbon, 5% organics, 1% troilite and less than 1% of enstatite and

forsterite.

Figure 3.3 illustrates the necessity of larger grains in both the wall and optically thin inner region to fit the observations. The solid line corresponds to the model of the wall and optically thin region with the larger grain sizes which we adopted above. The dotted line corresponds to models with the smaller, ISM-like grains, as are found in the Taurus transitional disks CoKu Tau/4, DM Tau, and GM Aur. Figure 3.3 shows that larger grains have better agreement with the slope of the SED beyond 15 μm and are necessary to produce the slight near-infrared excess, the shape of the 10 μm feature, and the >20 μm IRS emission in CS Cha.

3.3.2 Gas Properties

We detect [Ne II] fine-structure emission at 12.81 μm ($^2P_{1/2} \rightarrow ^2 P_{3/2}$) in CS Cha (see Figure 3.3). Using the IRAF tool *SPLOT*, we find the integrated line flux, $\int F_\lambda d\lambda$, to be 4.3$\pm$0.6 $\times$ 10^{-14} ergs cm^{-2} s^{-1} or 1.3 $\times$ 10^{29} ergs s^{-1}.

Glassgold et al. (2007) have recently suggested that circumstellar disks exposed to stellar X-rays would produce [Ne II] fine-structure emission at a level that would be detectable with *Spitzer* in nearby star–forming regions. In the Glassgold et al. (2007) model, the disk surface is both ionized and heated by stellar X-rays. Ne ions (primarily Ne^+ and Ne^{2+}) are produced through X-ray ionization and destroyed by charge exchange with atomic hydrogen and radiative recombination. Alternatively, (Gorti & Hollenbach, 2009) propose that EUV photons from the stellar chromosphere and/or stellar accretion can create an ionized HII-region-like layer at the disk surface that can also produce significant [Ne II] emission.

3.4 Discussion & Conclusions

CS Cha shows clear evidence of advanced dust evolution in relation to other transitional disks: it has significant grain growth and substantial settling in its outer disk. The dust in the wall of the outer disk in CS Cha has grown to much larger sizes (5 μm) than the dust in the transitional disks CoKu Tau/4, DM Tau, GM Aur, and TW Hya, all of which have maximum grain sizes in the outer wall of 0.25 μm (D'Alessio et al., 2005; Calvet et al., 2005b, 2002; Uchida et al., 2004), and CS Cha has large grains in the inner optically thin region as well, similar to TW Hya (Sargent et al., 2006). CS Cha also needs more settling in the outer disk ($\epsilon = 0.01$) to fit the far-infrared and millimeter data, indicating much higher dust depletion in the upper layers than found in GM Aur and DM Tau, which were modeled with $\epsilon = 0.1$ and 0.5, respectively (Calvet et al., 2005b; Hughes et al., 2009) . In addition, CS Cha further stands out due to its large hole size, having the largest modeled to date at $\sim$ 43 AU. This large inner hole serves to decrease the mid-infrared dust continuum and hence increase the line to continuum ratio, facilitating the detection of [Ne II] fine-structure emission.

The luminosity of the [Ne II] 12.81 μm line in CS Cha is strong compared to other [Ne II] detections in disks. The luminosity seen in DM Tau is 1.3×10^{28} ergs s^{-1} and for GM Aur the 5 σ upper limit is 7.4×10^{28} ergs s^{-1} (measured from spectra in Calvet et al., 2005b). TW Hya shows [Ne II] emission at 12.81 μm with a luminosity of 3.9×10^{28} ergs s^{-1} (measured from Uchida et al., 2004). In addition, the luminosities seen in four CTTS that were observed in the FEPS survey are $\sim 10^{28}$ ergs s^{-1} (Pascucci et al., 2007).

To gain insight into the origin of the Neon emission we compare $L_{[NeII]}$ to L_X and $\dot{M}$ in Figure 3.4. We see no apparent correlation between $L_{[NeII]}$ and L_X as was reported by Pascucci et al. (2007) and as would be expected from the X-ray heating model of Glassgold et al. (2007), which suggests that other processes like viscous heating, jets, and UV heating are involved (Glassgold et al., 2007). We find a possible correlation between $L_{[NeII]}$ and $\dot{M}$ which suggests that accretion related heating may play a substantial role in producing [Ne II] emission. Accretion related processes that affect the disk heating are viscous dissipation and irradiation by UV emission from the accretion shock region. Calvet et al. (2004) show that FUV fluxes scale with L_{acc}, and a similar scaling is expected for the EUV; in turn, Gorti & Hollenbach (2009) show that EUV heating and ionization can result in significant [Ne II] emission.

Nevertheless, both the X-ray and EUV heating models under-predict the $L_{[NeII]}$ seen in CS Cha (Glassgold et al., 2007; Pascucci et al., 2007). We note that the optically thin inner region of CS Cha is populated by large grains, which would favor UV flux penetration of the gas (Aikawa & Nomura, 2006) and possibly lead to enhanced $L_{[NeII]}$. Further exploration of the gas and dust in other transitional disks is necessary to test any link between these components. Similarly, jets and outflows, which are also characteristic of sources with higher accretion rates, may contribute to a positive trend. High resolution spectroscopy of CS Cha can explore this contribution from the jet (Takami et al., 2003).

Table 3.1. Stellar and Model Properties of CS Cha

Stellar Parameters	
M_* ($M_\odot$).....	0.91
R_* ($R_\odot$).....	2.3
T_* (K).....	4205
L_* ($L_\odot$).....	1.5
$\dot{M}$ ($M_\odot$ yr^{-1}).....	1.2×10^{-8}
Distance (pc).....	160
A_V.....	0.8
Wall Parameters	
R_{wall} (AU).....	42.7
a_{min} (μm).....	0.005
a_{max} (μm).....	5
T_{wall} (K).....	90
z_{wall} (AU)[1].....	5
Optically Thick Outer Disk Parameters	
$R_{d,out}$ (AU).....	300
ϵ.....	0.01
α.....	0.005
M_d ($M_\odot$).....	0.04
Optically Thin Inner Region Parameters	
$R_{in,thin}$ (AU).....	0.1
$R_{out,thin}$ (AU).....	1
$a_{min,thin}$ (μm).....	1.9
$a_{max,thin}$ (μm).....	2.1
$M_{d,thin}$ ($M_\odot$).....	1.7×10^{-12}

[1] z_{wall} is the height above the disk midplane

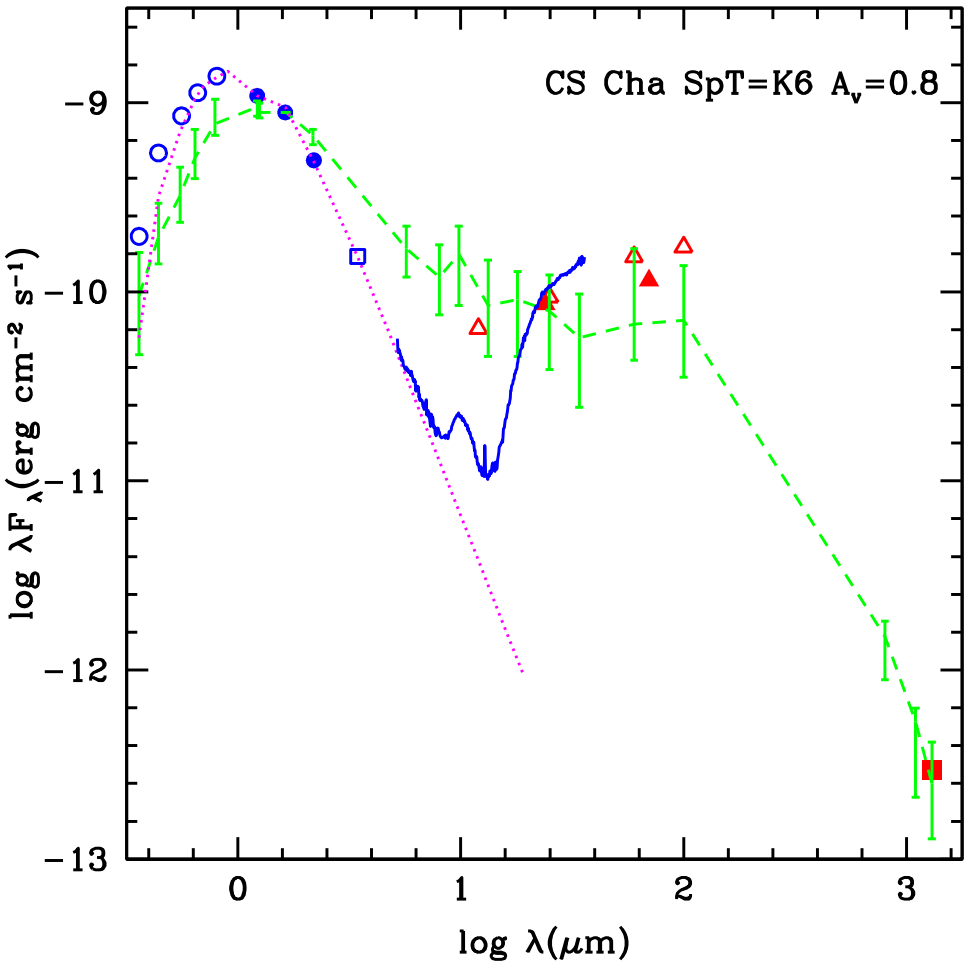

Figure 3.1 SED of CS Cha. Optical (open circles), J,H,K (filled circles), L-band (open square), *Spitzer* IRS data (blue solid line), IRAS (open triangles), MIPS (closed triangles) and sub-mm (closed square) are shown. Red corresponds to observed magnitudes and blue symbols are dereddened magnitudes. The short-dashed green line with quartiles is the median SED of Taurus and the dotted magenta line is the stellar photosphere.

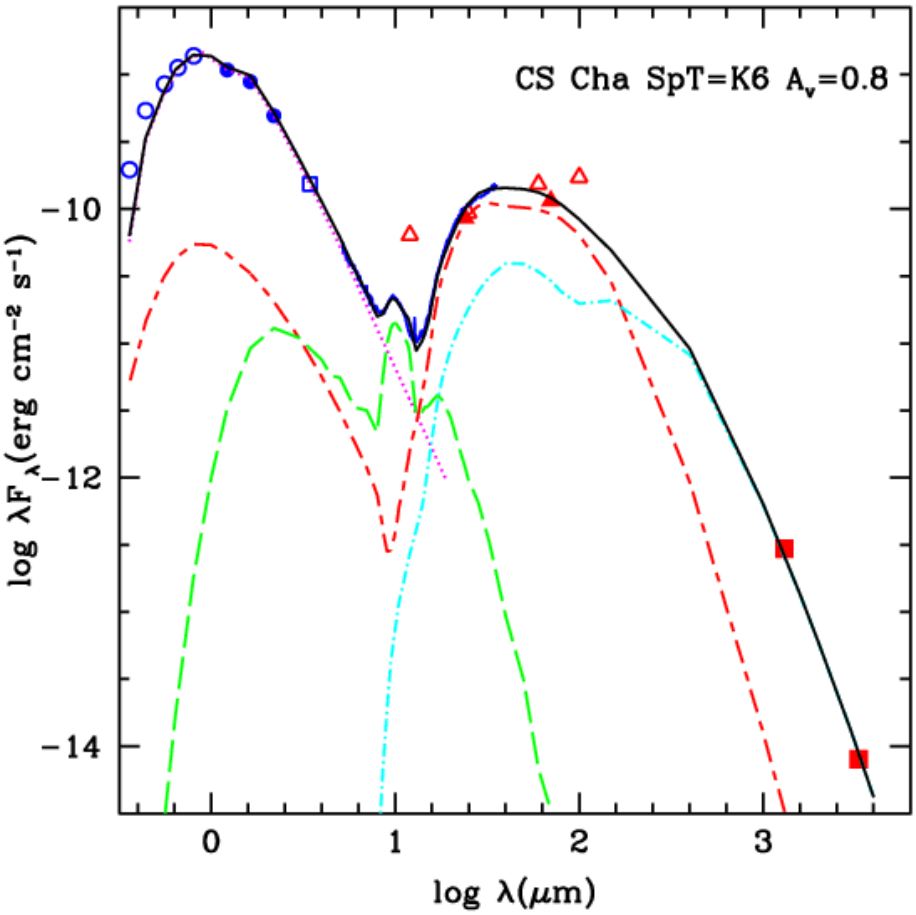

Figure 3.2 SED and transitional disk model of CS Cha. The solid black line is the best fit model with parameters from Table 3.1. Separate model components are also shown: wall (scattered and thermal emission; red short-long-dash line), optically thick disk (blue dot-dash), optically thin inner region (green long-dashed), stellar photosphere (magenta dotted line). Note that the model does not fit the IRAS points. IRAS has a larger field of view than *Spitzer* which could overreport the flux, especially at 100 μm. However, the model agrees with the MIPS data, which has a smaller field of view than IRAS. We also include ATCA 3.3 mm data (Lommen et al., 2007).

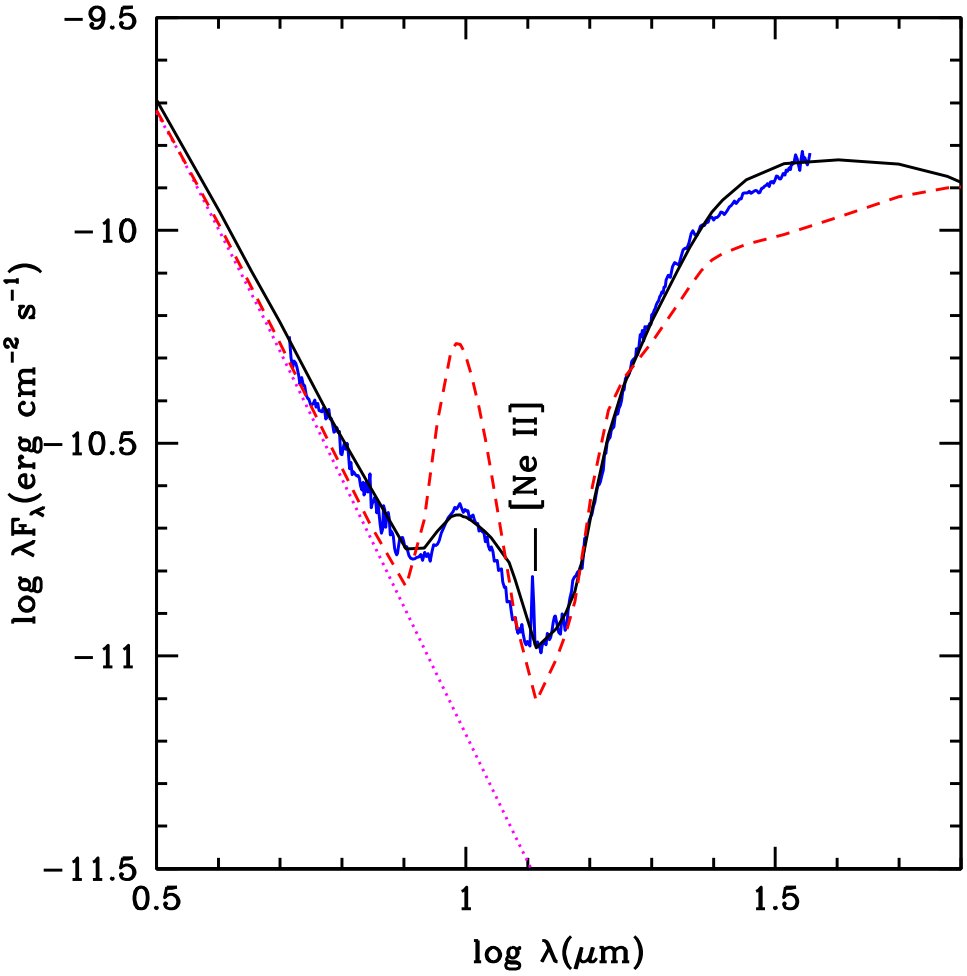

Figure 3.3 Models of CS Cha with big grains versus small grains. The solid black line corresponds to the model that uses big grains and it is the best-fit disk model shown in Figure 3.2 and Table 3.1. The red dashed line is the model that uses small grains; the wall has a_{max}=0.25 μm and the optically thin region has a_{min}=0.005 μm and a_{max}=0.25 μm.

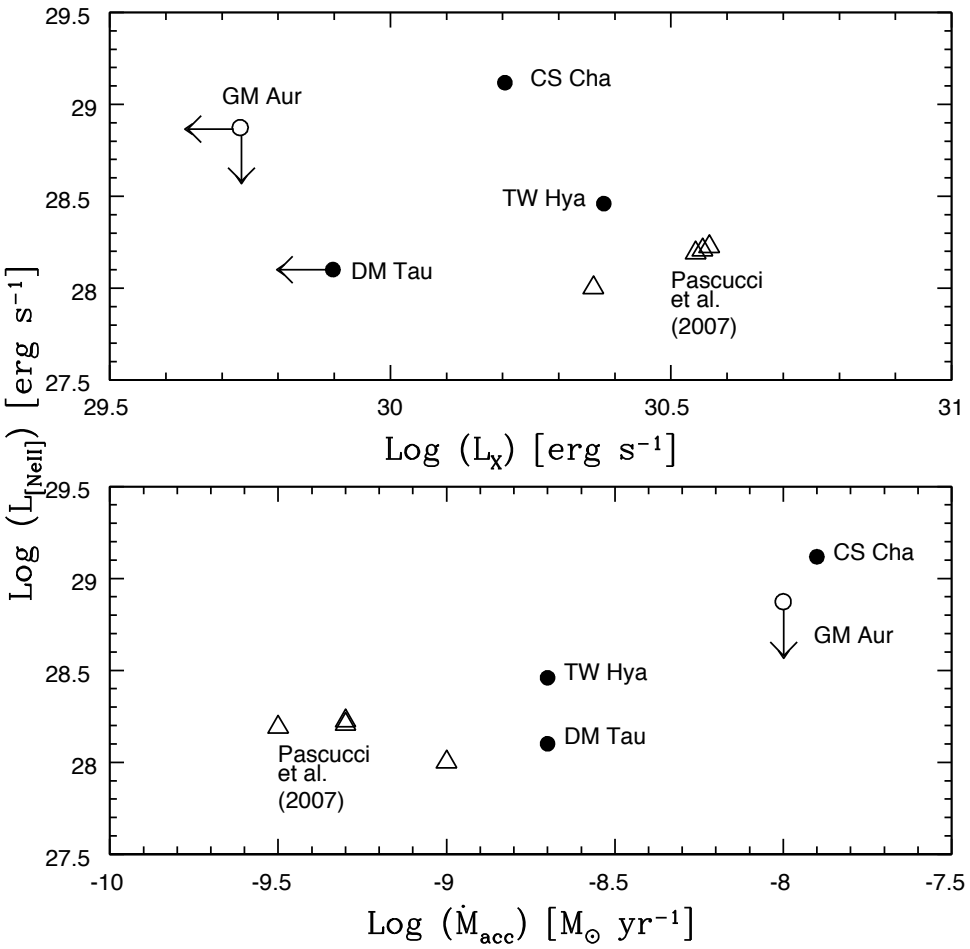

Figure 3.4 Comparison of $L_{[NeII]}$ with L_X and $\dot{M}$ for TTS. Top: $L_{[NeII]}$ vs. L_X. There is no obvious correlation. Triangles are from Pascucci et al. (2007), circles correspond to [Ne II] luminosities derived in this chapter. The L_X for CS Cha and TW Hya are from Feigelson et al. (1993) and Kastner et al. (1999), scaled to 160 and 55 pc, respectively. We show upper limits for the $L_{[NeII]}$ of GM Aur and the L_X of GM Aur and DM Tau (Neuhaeuser et al., 1995). All L_X are from ROSAT and vary by a factor of $\sim$2. Bottom: $L_{[NeII]}$ vs. $\dot{M}$. There is a possible positive correlation. The $\dot{M}$ for CS Cha is derived here and $\dot{M}$ for GM Aur and DM Tau are from Calvet et al. (2005b). TW Hya's $\dot{M}$ is from veiling measurements but varies between 0.4×10^{-9} to 10^{-8} $M_\odot$ yr^{-1} (Alencar & Batalha, 2002; Muzerolle et al., 2000).

Chapter 4

CVSO 224: A Slowly Accreting ∼10 Myr Old Transitional Disk in Orion OB1a

Abstract: Here we present the *Spitzer* IRS spectrum of CVSO 224, the sole transitional disk located within the ∼10 Myr old 25 Orionis group in Orion OB1a. A model fit to the spectral energy distribution of this object indicates a ∼7 AU inner disk hole that contains a small amount of optically thin dust. In previous studies, CVSO 224 had been classified as a weak-line T Tauri star based on its Hα equivalent width, but here we find an accretion rate of 7×10^{-11} $M_\odot$ yr^{-1} based on high-resolution Hectochelle observations of the Hα profile. CVSO 224's low $\dot{M}$ is in line with photoevaporative clearing theories. However, the *Spitzer* IRS spectrum of CVSO 224 has a substantial mid-infrared excess beyond 20 μm which indicates that it is surrounded by a massive outer disk. Millimeter measurements are necessary to constrain the mass of the outer disk around CVSO 224 in order to confirm that photoevaporation is not the mechanism behind creating its inner disk hole.

4.1 Introduction

Stars surrounded by transitional disks have characteristics that fall between objects that have clear evidence for disks and stars with no disk material. They have deficits of infrared flux at $\lambda < 8$ μm but show strong excesses at longer wavelengths, indicating

that the innermost regions have undergone significant clearing of small dust grains (Strom et al., 1989; Skrutskie et al., 1990).

The *Spitzer Space Telescope* has greatly improved our resolution in the infrared and has recently provoked extensive modeling studies of several transitional disks around T Tauri stars e.g TW Hya (Uchida et al., 2004), GM Aur, DM Tau (Calvet et al., 2005b), CS Cha (Espaillat et al., 2007a), HD 98800B (Furlan et al., 2007), and Hen 3-600 (Uchida et al., 2004). These objects have been explained as inwardly truncated disks which are optically thick to the stellar radiation, with most of the mid-infrared emission originating in the inner edge or "wall" of the outer disk. Spectral energy distributions (SEDs) point to holes in these disks of less than ∼46 AU. The inner holes of the transitional disks around DM Tau and CoKu Tau/4 are cleared of small dust grains (D'Alessio et al., 2005; Calvet et al., 2005b) while the transitional disks GM Aur, TW Hya, CS Cha, HD 98800B, and Hen 3-600 have a small yet detectable near-infrared excess produced by some submicron and micron sized optically thin dust remaining in the inner disk hole (Calvet et al., 2005b, 2002; Espaillat et al., 2007a; Furlan et al., 2007; Uchida et al., 2004). In addition to these disks with holes (i.e. large reductions of small dust grains from the star out to an outer optically thick wall), the "pre-transitional disk" class has recently been identified (Espaillat et al., 2007b). These objects, exemplified by UX Tau A and LkCa 15, have an inner optically thick disk separated from an outer optically thick disk by an optically thin gap (Espaillat et al., 2007b, 2008a). See Section 1.2.2 for more details on possible clearing mechanisms for these gaps and holes.

While most transitional disk studies have focused on objects located in 1–2 Myr

old star–forming regions with relatively isolated star formation, here we present detailed modeling of CVSO 224, the only transitional disk located in the ∼10 Myr old 25 Orionis group (Briceño et al., 2007) in the Orion OB1a subassociation (Briceño et al., 2005).

4.2 Observations & Data Reduction

We present the SED of CVSO 224, which is also known as 1a_1200 (Hernández et al., 2007) and 05254675+0143303 (2MASS), in Figure 4.1. B- and R-band photometry were taken from the USNO database. V- and I-band photometry (Briceño et al., 2007) as well as J-, H-, and K-band (2MASS) are shown. IRAC and MIPS data were taken from Hernández et al. (2007).

A value of the extinction, A_V, of 0.21 for CVSO 224 is derived from fitting an M3 photosphere (Kenyon & Hartmann, 1995) to the observations (scaled at J-band), and the data are dereddened with the Mathis (1990) reddening law. The derived A_V is consistent with a mean extinction of 0.5 mag found toward Orion OB1a by Calvet et al. (2005a). Stellar parameters (M_*, R_*; Table 4.1) are derived from the HR diagram and the Siess et al. evolutionary tracks (Siess et al., 2000) using a T_* of 3470 K (Kenyon & Hartmann, 1995) for an M3 star (Briceño et al., 2007). The distance to 25 Orionis is 330 pc (Briceño et al., 2007).

CVSO 224 was observed by the *Spitzer* IRS instrument on March 8, 2006 (AOR ID: 16264960) with the short-wavelength, low-resolution (SL) module of IRS and the long-wavelength, low-resolution (LL) module, covering ∼5 to 40 μm, at a resolving power of $\lambda/\delta\lambda = 60 - 100$. The observation was carried out in IRS Staring Mode.

We used the Spectral Modeling, Analysis, and Reduction Tool (SMART) software package developed by the IRS instrument team (Higdon et al., 2004) to extract and calibrate the spectrum. Furlan et al. (2006) can be consulted for further data-reduction details.

In Figure 4.2 we show the high-resolution (R∼34,000) spectrum of CVSO 224 centered on the Hα 6563Å line. It was obtained with the Hectochelle multifiber instrument (Szentgyorgyi et al. 1998) mounted on the 6.5m MMT at Mt. Hopkins, Arizona for the dataset presented in Briceño et al. (2007). We refer the reader to that article for details on the observations and data reduction.

4.3 Analysis

4.3.1 Accretion Properties

According to theories of magnetospheric accretion, the inner disk is truncated by the stellar magnetic field and material is channeled onto the star via accretion columns (Figure 1.2). This leads to strong, broad Hα emission profiles due to the high temperatures and velocities of the accreting material (Muzerolle et al., 2001). White & Basri (2003) showed that a star is accreting if EW(Hα) $\geq$ 20 Å for M3 stars. According to this criterion, CVSO 224, a M3 star (Briceño et al., 2007) with EW(Hα) of $\leq$ 20 Å, can be classified as a weakly accreting T Tauri star (WTTS) (Briceño et al., 2007). However, some stars which lie just below this EW(Hα) limit could be slow accretors (Barrado y Navascués & Martín, 2003). When analyzing the high-resolution spectrum of CVSO 224 taken with Hectochelle (Figure 4.2) we find that the width of the Hα profile at 10% is larger than 200 km/s indicating that this star

is accreting (White & Basri, 2003).

We estimated the accretion rate using the magnetospheric accretion models of Muzerolle et al. (2001). See that paper for the details of the fitting procedure. In short, we calculated models using the mass, radius, and effective temperature of the star as fixed inputs. The gas temperature, density (calculated from $\dot{M}$), and inclination were then varied to find the best fit to the observed line profile. The profile of CVSO 224 has a central self-reversal as seen in WTTS (e.g. Figure 1 of Muzerolle et al. 2000), but also has broad wings and redshifted absorption. This suggests that we are seeing signatures of both the stellar chromosphere and the accreting material traveling in the magnetospheric field lines. Since the line core is dominated by chromospheric emission, which is not included in the models, only the line wings were considered in the fit. The resultant best-fit model parameters are i=30°, T_{max}=12,000 K, $\dot{M}$=7×10^{-11} $M_{\odot}$yr^{-1}. The inclination angle derived here is constrained to about 15° of the nominal value of 30° since the actual geometry is likely much more complicated (Muzerolle et al., 2001). We adopt this value for CVSO 224 since there is no other estimate for the inclination angle.

4.3.2 Disk Properties

When we compare CVSO 224 to the median SED of Taurus (Figure 4.1; D'Alessio et al., 1999; Furlan et al., 2006) which has been shown to be representative of a full disk (D'Alessio et al., 1999, 2006), it is apparent that there is a strong infrared deficit, indicating that CVSO 224 is surrounded by a transitional disk. We follow D'Alessio et al. (2005) to calculate the structure and emission of the optically thick

disk's inner edge or "wall," assumed to be vertical and axisymmetric. The radiative transfer in the wall atmosphere is calculated with M_*, R_*, T_*, distance, inclination, and $\dot{M}$ as well as minimum and maximum grain sizes (Table 4.1). We use a grain-size distribution that follows a power-law of $a^{-3.5}$, where a is the grain radius. We assume ISM sized grains and adopt a_{min}=0.005 μm and a_{max}=0.25 μm (Draine & Lee, 1984). The wall has a radial gradient of temperature and we use its outermost temperature, T_{wall}, as a free parameter in fitting the SED. This temperature, combined with the dust composition, determines the wall radius (D'Alessio et al., 2005). The best fit to the SED is shown in Figure 4.3 and corresponds to T_{wall}=120 K and R_{wall}=7 AU. The wall height, z_{wall} (1 AU), is also a free parameter which is dependent on the best-fit to the SED. Varying the inclination angle within 15° of 30° does not change the size of the inner hole.

CVSO 224 has a near-infrared excess; the ratio of its observed to photospheric emission at 5.8 μm is 1.6. The low value of T_{wall} implies that the wall can account for neither the 10 μm silicate-feature emission nor the small near-IR excess. While a wall with a higher T_{wall} produces more 10 μm emission, it cannot account for the excess beyond 20 μm. As is seen in previous studies (Calvet et al., 2005b; Espaillat et al., 2007a), a small amount of optically thin dust can account for the 10 μm emission and the near-IR excess. Following Calvet et al. (2002), the spectrum for the optically thin region is calculated as the sum of the emergent flux from optically thin annuli where the dust in each annulus is heated by stellar radiation. We hold the inner radius fixed at the dust destruction radius (0.04 AU) and the outer radius is determined by the best fit (1 AU). The silicate feature is well fit with a_{max}=4 μm

and probes temperatures of ∼190–1110 K. About 4×10^{-12} $M_\odot$ of dust exists in the optically thin region which in the models is composed of ∼80% amorphous silicates, ∼14% organics, ∼3% amorphous carbon, ∼2.6% troilite, and less than 1% enstatite and forsterite. The total emission of this optically thin region is scaled to the vertical optical depth at 10 μm, $\tau_0 \sim 0.025$.

Since there are no far-infrared or millimeter measurements for CVSO 224, we cannot constrain the contribution to the SED from the outer disk. However, previous papers have shown that the wall and optically thin dust region dominate the mid-infrared flux (Calvet et al., 2005b; Espaillat et al., 2007a,b) and so in this first approximation we neglect the outer disk.

4.4 Discussion & Conclusions

CVSO 224 is ∼10 Myr old, making it one of the oldest transitional disks around a classical T Tauri star. TW Hya is another ∼10 Myr old transitional disk that has been studied in detail. In both objects, there is an inner hole of ≤10 AU that contains optically thin dust that is larger than ISM-sized grains (Calvet et al., 2002). The ∼2 Myr old CS Cha also has larger grains in its optically thin region (Espaillat et al., 2007a). In contrast, LkCa 15 and GM Aur in Taurus (∼1 Myr old) have small ISM-sized grains in their optically thin regions (Espaillat et al., 2007b; Calvet et al., 2005b). These optically thin disks are possibly the result of the inward drift of small dust grains from the outer disk (Rice et al., 2006). Larger dust grains in the optically thin regions of older transitional disks may imply that there is some correlation between the process that creates the optically thin dust and dust evolution

over time. Like GM Aur and LkCa 15, CVSO 224 and TW Hya have no obvious signs of a substantial amount of crystalline silicates in their disks. This is hard to explain given that one would expect 10 Myr of processing to result in crystalline silicates. This lack of crystallization is in contrast to several young full disks in Taurus which show high degrees of dust processing (Watson et al., 2009).

CVSO 224 is an ideal target to test the role of photoevaporation in transitional disks. Photoevaporation will create an inner hole in disks with masses < 0.005 $M_\odot$ and mass accretion rates below the photoevaporative wind rate of $\sim 10^{-10}$ $M_\odot$ yr^{-1} (Alexander & Armitage, 2007). CVSO 224's $\dot{M}$ is below the photoevaporative wind rate; however, we are detecting a robust mid-infrared excess beyond 20 μm from the disk's wall. This excess agrees with the median SED of Taurus' T Tauri disks (Figure 4.1) and is similar to what is observed in other massive ($M_{disk} > 0.05$ $M_\odot$) transitional disks (e.g. DM Tau, GM Aur Calvet et al., 2005b), indicating that CVSO 224 still has a substantial outer disk. This indication of a massive outer disk is evidence against photoevaporation being the main cause of clearing behind the hole we observe in CVSO 224. Additionally, Alexander & Armitage (2007) show that the size of the inner hole should reach tens of AU within 0.1 Myr of the onset of photoevaporation. Excluding the unlikely possibility that we are catching CVSO 224 immediately after photoevaporation has switched on, one would expect the inner hole to be larger and the outer disk to be mostly gone. Millimeter observations of CVSO 224 are necessary to confirm that it has a massive disk in order to eliminate the possibility that photoevaporation is creating the disk hole around CVSO 224.

If CVSO 224 does have a massive disk and is not being photoevaporated, one can

speculate that the $\dot{M}$ of the outer disk, $\dot{M}_{disk}$, is actually higher than the observed accretion rate onto the star, $\dot{M}_{star}$. One way to create a situation where $\dot{M}_{star}$ is less than $\dot{M}_{disk}$ is with planet formation. If a planet is forming in the disk, the mass coming from the outer disk is shared by the planet and the inner disk (Lubow & D'Angelo, 2006; Najita et al., 2007a; Alexander & Armitage, 2007). Lubow & D'Angelo (2006) show that the mass accretion rate past a planet and into the inner disk is 10–25 % of the mass accretion rate outside the planet's orbit. Alternatively, the low mass accretion rate of CVSO 224 could also be due to a stellar companion. Hen 3-600 is another weakly accreting ∼10 Myr old transitional disk (5×10^{-11} $M_{\odot}$ yr^{-1}; Muzerolle et al. 2000) whose hole is most likely due to dynamical clearing by its companion (Uchida et al., 2004). Its low $\dot{M}$ also indicates that photoevaporation should be clearing this disk, however, Hen 3-600 has a small hole (∼1 AU; Uchida et al. 2004) and its infrared excess (Low et al., 2005) indicates a substantial outer disk. Hen 3-600's $\dot{M}_{star}$ could be limited by binary tidal forces (Artymowicz & Lubow, 1996) and not be reflective of $\dot{M}_{disk}$.

CVSO 224 presents an opportune test of photoevaporation and planet formation in older disks and further observations of this object will help clarify the role of photoevaporation in disk clearing. Millimeter studies of CVSO 224 are necessary to derive the mass of its outer disk. If a massive disk is present, its low $\dot{M}$ could be due to a planetary or stellar companion and more study will be needed to distinguish between these two scenarios.

Table 4.1. Stellar and Model Properties of CVSO 224

Stellar Properties	
$M_*(M_\odot)$	0.3
R_* ($R_\odot$)	0.9
T_* (K)	3470
L_* ($L_\odot$)	0.1
Distance (pc)	330
$\dot{M}$ ($M_\odot yr^{-1}$)	7×10^{-11}
Inclination (°)	30
A_V	0.21
Spectral Type	M3
Optically Thick Outer Wall	
a_{min} (μm)	0.005
a_{max}(μm)	0.25
T_{wall} (K)	120
z_{wall} (AU)	1
R_{wall} (AU)	7
Optically Thin Inner Region	
$R_{in,thin}$ (AU)	0.04
$R_{out,thin}$ (AU)	1
$a_{min,thin}$ (μm)	0.005
$a_{max,thin}$ (μm)	4
$M_{dust,thin}$ ($M_\odot$)	4×10^{-12}

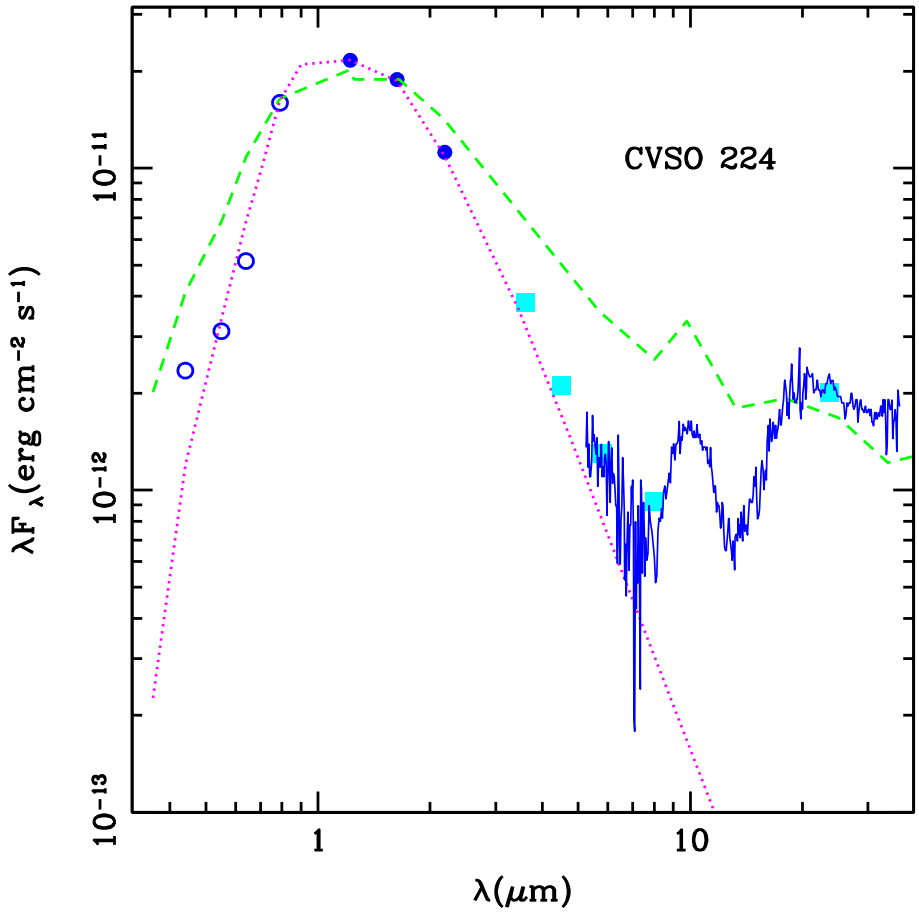

Figure 4.1 SED of CVSO 224. We show dereddened ground-based optical (open circles), J,H,K (filled circles), *Spitzer* IRAC and MIPS (closed squares), and *Spitzer* IRS (solid line) data. We also show the median SED of Taurus (D'Alessio et al., 1999; Furlan et al., 2006, short-dashed line), which represents a full disk, and an M3 photosphere (Kenyon & Hartmann, 1995, dotted line).

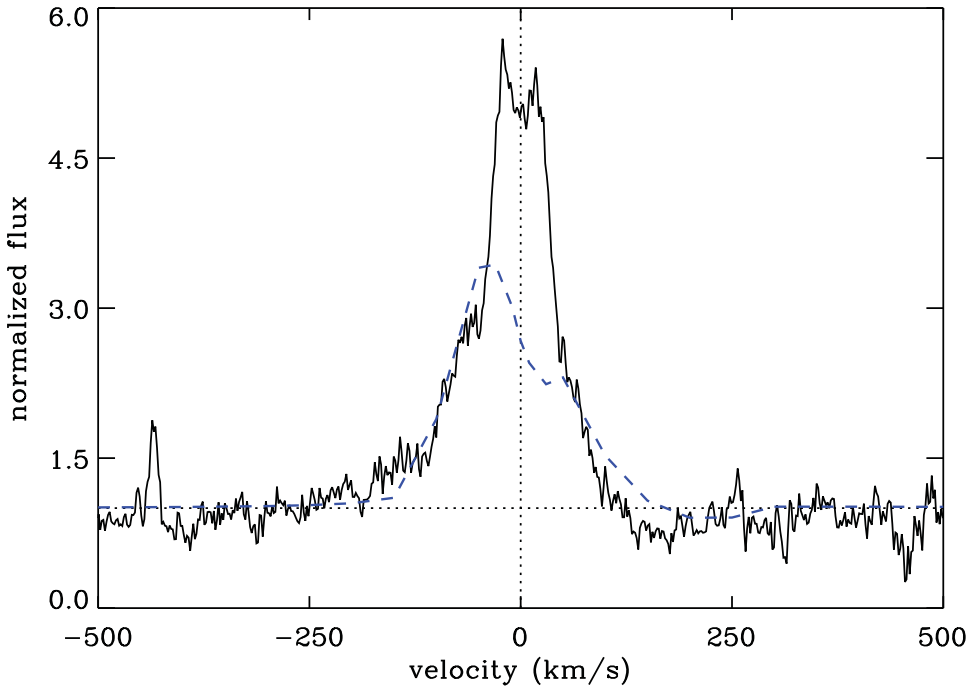

Figure 4.2 Hectochelle spectrum of CVSO 224 (solid line) with the best-fit accretion model (dashed line). We estimate an accretion rate of $7{\times}10^{-11}$ $M_{\odot}yr^{-1}$. The Hα emission profile of CVSO 224 has a chromospheric component (i.e. central self-reversal) as well as accretion signatures such as broad wings and redshifted absorption.

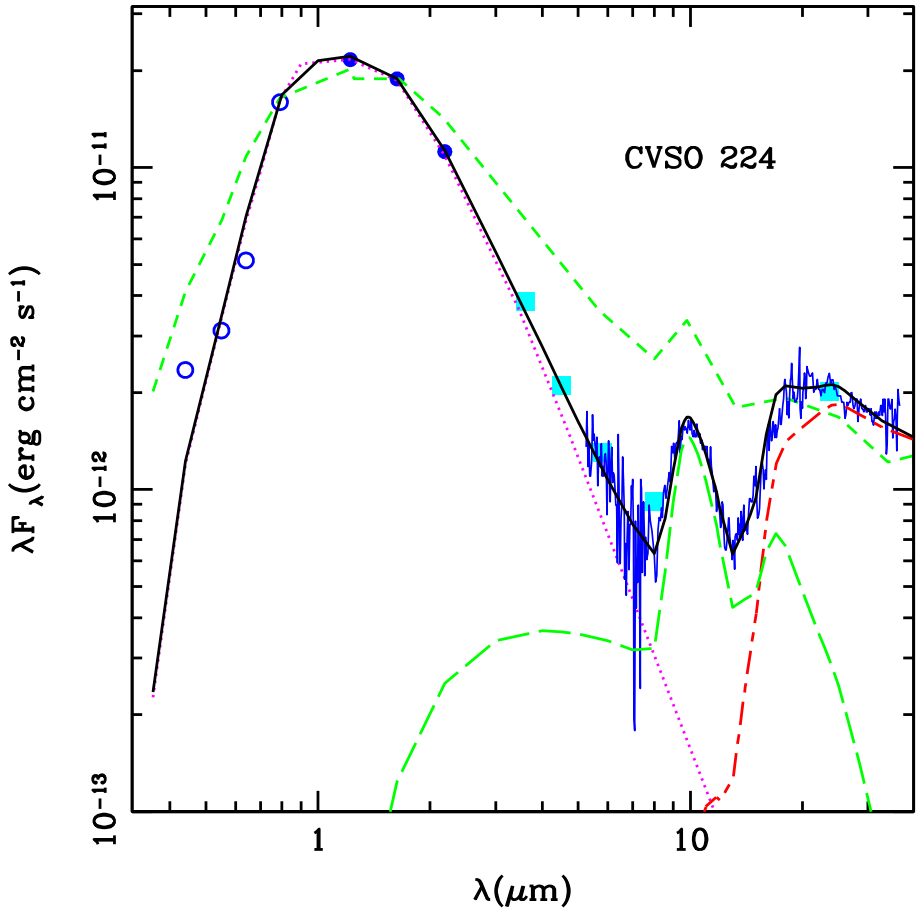

Figure 4.3 SED and transitional disk model of CVSO 224. Symbols are the same as in Figure 4.1. The best-fit model (heavy solid line) corresponds to an inner disk hole of 7 AU that has $\sim 4 \times 10^{-12}$ $M_\odot$ of optically thin dust located between the dust destruction radius and 1 AU; the disk is relatively devoid of small dust grains between 1 and 7 AU. Model components are as follows: stellar photosphere (dotted line), optically thin dust region (long-dash), outer wall (dot-short-dash).

Chapter 5

On the Diversity of the Taurus Transitional Disks: UX Tau A & Lk Ca 15

Abstract: The recently recognized class of "transitional disk" systems consists of young stars with optically-thick outer disks but inner disks which are mostly devoid of small dust. Here we introduce a further class of "pre-transitional disks" with significant near-infrared excesses which indicate the presence of an optically thick inner disk separated from an optically thick outer disk; thus, the spectral energy distributions of pre-transitional disks suggest the incipient development of disk gaps rather than inner holes. In UX Tau A, our analysis of the *Spitzer* IRS spectrum finds that the near-infrared excess is produced by an inner optically thick disk and a gap of ∼56 AU is present. The *Spitzer* IRS spectrum of LkCa 15 is suggestive of a gap of ∼46 AU, confirming previous millimeter imaging. In addition, UX Tau A contains crystalline silicates in its disk at radii $\gtrsim$ 56 AU which poses a challenge to our understanding of the production of this crystalline material. In contrast, LkCa 15's silicates are amorphous and pristine. UX Tau A and LkCa 15 increase our knowledge of the diversity of dust clearing in low-mass star formation.

5.1 Introduction

Previous studies have revealed stars with inner disks that are mostly devoid of small dust, and these "transitional disks" have been proposed as the bridge between Class II objects, young stars surrounded by full disks accreting material onto the central star, and Class III objects, stars where the protoplanetary disk is mostly dissipated and accretion has stopped (Strom et al., 1989; Skrutskie et al., 1990; Stassun et al., 2001).

New spectra from the *Spitzer Space Telescope* which greatly improve our resolution in the infrared have been used to define the class of "transitional disks" as those with spectral energy distributions (SEDs) characterized by a significant deficit of flux in the near-infrared relative to optically thick full disks, and a substantial infrared excess in the mid- and far-infrared. Extensive modeling studies of several transitional disks around T Tauri stars (D'Alessio et al., 2005; Uchida et al., 2004; Calvet et al., 2005b; Espaillat et al., 2007a) and F-G stars (Brown et al., 2007) have been presented. In particular, the SEDs of the transitional disks of the T Tauri stars CoKu Tau/4 (D'Alessio et al., 2005), TW Hya (Calvet et al., 2002; Uchida et al., 2004), GM Aur, DM Tau (Calvet et al., 2005b), and CS Cha (Espaillat et al., 2007a) have been explained by modeling the transitional disks with truncated optically thick disks with most of the mid-infrared emission originating in the inner edge or "wall" of the truncated disk. In all these cases, except in CoKu Tau/4, material is accreting onto the star, so gas remains inside the truncated disk, but with a small or negligible amount of small dust, making these regions optically thin.

Here we present models of UX Tau A and LkCa 15, low-mass pre-main sequence

stars in the young, ∼1 Myr old Taurus star–forming region which have been previously reported as transitional disks (Furlan et al., 2006; Bergin et al., 2004). We present evidence for gaps in optically thick disks, as opposed to "inner holes," that is, large reductions of small dust from the star out to an outer optically thick wall.

5.2 Observations & Data Reduction

Figures 5.1 and 5.2 are plots of the spectral energy distributions for UX Tau A and LkCa 15 respectively. For Lk Ca 15, the reduction of the *Spitzer* Infrared Array Camera (IRAC) images (Program 37) was done with SSC pipeline S14.0 and the post-BCD (Basic Calibrated Data) MOPEX v030106 (Makovoz et al., 2006). We extracted the photometry of this object using the apphot package in IRAF, with an aperture radius of 10 pixels and a background annulus from 10 to 20 pixels. Fluxes at 3.6, 4.5, 5.8, and 8.0 μm are 7.55, 7.35, 7.24, 6.41 mag (1 σ=0.05 mag). The Submillimeter Array (SMA) observations of LkCa 15 were made on September 6th, 2003 using the Compact Configuration of six of the 6 meter diameter antennas at 345 GHz with full correlator bandwidth of 2 GHz. Calibration of the visibility phases and amplitudes was achieved with observations of the quasar 0423-013 and 0530+135, typically at intervals of 20 minutes. Observations of Uranus provided the absolute scale for the flux density calibration and the uncertainties in the flux scale are estimated to be 20%. The data were calibrated using the MIR software package (http://www.cfa.harvard.edu/∼cqi/mircook.html). Fluxes at 216.5, 226.5, 345.2, and 355.2 GHz are 121.4±4.3, 152.8±5.2, 416.8±37.6, and 453.1±48.1 mJy respectively.

5.3 Analysis

5.3.1 Model Parameters

We follow D'Alessio et al. (2006, 2005) to calculate the structure and emission of the optically thick disk and the wall. Input parameters for the optically thick disk are the stellar properties, the mass accretion rate of the disk ($\dot{M}$), the viscosity parameter (α), and the settling parameter $\epsilon = \zeta_{up}/\zeta_{st}$, i.e. the mass fraction of the small grains in the upper layers relative to the standard dust-to-gas mass ratio (D'Alessio et al., 2006). We use a grain-size distribution that follows a power-law of the form $a^{-3.5}$, where a is the grain radius, with a minimum grain size of 0.005 μm. In the upper, optically thin layer of the disk, the maximum grain size is 0.25 μm. In the midplane of the disk, the maximum grain size is 1 mm. The radiative transfer in the wall atmosphere is calculated with the stellar properties, $\dot{M}$, the maximum and minimum grain sizes, and the temperature of the optically thin wall atmosphere (T_{wall}). Table 5.1 lists the maximum grain sizes of the walls and other relevant parameters. We use the same dust composition as Espaillat et al. (2007a) unless otherwise noted.

In each case we use a distance of 140 pc to Taurus (Kenyon et al., 1994). We assume an outer disk radius of 300 AU. Spectral types and stellar temperatures are adopted from Kenyon & Hartmann (1995). Data are dereddened with the Mathis (1990) reddening law and extinctions are derived from fitting a standard stellar photosphere (Kenyon & Hartmann, 1995) to the data. Stellar parameters (M_*, R_*, L_*) are derived from the HR diagram and the Siess et al. evolutionary tracks (Siess

et al., 2000). Mass accretion rates are estimated from the U-band excess following Gullbring et al. (1998) with a typical uncertainty of a factor of 3 (Calvet et al., 2004).

5.3.2 UX Tau A

The sharp flux increase in the SED of UX Tau A (Figure 5.1) can be modeled by an optically thick outer disk truncated at ∼56 AU. The wall of the outer disk dominates the flux in the mid- and far-infrared while the outer optically thick disk contributes to most of the flux in the millimeter. We note that UX Tau A is in a multiple system (Furlan et al., 2006), with the closest component at $2\farcs6 \sim 360$ AU in projection; thus, the outer disk may have a smaller $R_{disk,out}$ than assumed here, which may decrease the disk mass but not the derived wall properties a_{max}, T_{wall}, and z_{wall} which are constrained by the best fit to the mid-infrared. In modeling the outer disk, we hold $\dot{M}$ fixed and vary α; this is equivalent to finding the best-fit disk mass since $M_d \propto \dot{M}/\alpha$.

When compared to the median SED of Taurus (Figure 5.1; D'Alessio et al., 1999; Furlan et al., 2006) which has been shown to be representative of an optically thick continuous disk (D'Alessio et al., 1999, 2006), UX Tau A's relatively strong mid-infrared deficit makes it apparent that its disk is not continuous i.e. it is not a "full disk." However, in contrast with the other transitional disks found around TTS, the near-infrared portion of UX Tau A's SED agrees with the median SED of TTS in Taurus; this indicates that optically thick material remains in the innermost part of the disk in contrast to all other transitional disks modeled so far. Since the inner disk is optically thick, it must have a sharp gas-dust transition at the dust destruction

radius as "full disks" in CTTS (Muzerolle et al., 2003; D'Alessio et al., 2006). In Figure 5.1 we show the contribution from the wall of an optically thick inner disk located at the dust destruction radius at 0.16 AU, assuming T_{wall}=1400 K. The best fit is obtained with large grains, in agreement with the lack of a 10 μm silicate feature. The flux deficit in the SED around 10 μm puts an upper limit to the extent of the inner optically thick disk to <0.18 AU.

5.3.3 Lk Ca 15

Our analysis of a model fit to LkCa 15 shows an optically thick disk truncated at ∼46 AU, as delineated by millimeter interferometric imaging (Piétu et al., 2006). The outer optically thick disk contributes to most of the flux in the millimeter and the wall of the outer disk contributes much of the flux in the mid- and far-infrared (Figure 5.2).

The near-infrared portion of the SED of LkCa 15 lies below the median SED of Taurus, so the case for an optically thick inner disk is not as clear cut as in UX Tau A. However, the near-IR excess above the photosphere in Lk Ca 15 is substantially higher than is seen in GM Aur (Calvet et al., 2005b), TW Hya (Calvet et al., 2002; Uchida et al., 2004), or CS Cha (Espaillat et al., 2007a), where the optically thin inner disk contains a small amount of dust. Our analysis suggests that an optically thick inner disk wall at the dust destruction radius (0.12 AU) can account for the significant near-infrared excess in Lk Ca 15 (Figure 5.2), and that the optically thick component cannot extend beyond 0.15 AU. We also require 4×10^{-11} $M_{\odot}$ of optically thin dust between 0.15 and 5 AU to produce the 10 μm silicate feature. This optically thin dust

mixture is composed of 85% amorphous silicates, 6.8% organics, 1.3% troilite, 6.8% amorphous carbon, and less than 1% enstatite and forsterite. The total emission of this optically thin region is scaled to the vertical optical depth at 10 μm, $\tau_0 \sim 0.012$. We follow Calvet et al. (2002) in calculating the optically thin dust region and note that the dust composition and τ_0 are free parameters constrained by the best fit to the SED.

In Figure 5.3 we present an alternative structure for LkCa 15's inner disk. It is possible to fit LkCa 15's SED with only optically thin dust within the inner hole. In this model, the near-infrared excess and 10 μm emission would originate in 5×10^{-11} $M_\odot$ of optically thin dust located between 0.12 to 4 AU. This optically thin dust mixture would be composed of 61% amorphous silicates, 7% organics, 1% troilite, 30% amorphous carbon, and less than 1% enstatite and forsterite. The total emission of this optically thin region is scaled to the vertical optical depth at 10 μm, $\tau_0 \sim$ 0.018. This model (Figure 5.4, bottom) does not fit the slope of the near-side of the IRS spectrum ($<7\mu$m) or the IRAC data as well as the previously discussed model (Figure 5.4, top). The optical depth in the near-infrared is $\sim$0.01, about 5 times greater than that of the previous model, mainly due to the difference in the amorphous carbon fraction.

While an optically thin region is necessary in both scenarios, we can exclude a model where the optically thin region extends further than $\sim$ 5 AU since the contribution at 20 μm then becomes too strong.

5.4 Discussion & Conclusions

Here we introduce the "pre-transitional disk" class where we see the incipient development of disk gaps in optically thick protoplanetary disks as evidenced by significant near-infrared excesses when compared to the Taurus median SED and previously studied transitional disks (D'Alessio et al., 2005; Calvet et al., 2002; Uchida et al., 2004; Calvet et al., 2005b; Espaillat et al., 2007a). The pre-transitional disk of UX Tau A has a ∼56 AU gap as opposed to an inner hole. It is also possible to fit LkCa 15's SED with a ∼46 AU gap that contains some optically thin dust; a model that has a hole rather than a gap also fits its SED and future near-infrared interferometry may be able to discriminate between these models. However, the truncation of LkCa 15's outer disk at ∼46 AU is consistent with resolved millimeter interferometric observations (Piétu et al., 2006) which makes it one of three inner disk holes imaged in the millimeter (TW Hya: Hughes et al. (2007); GM Aur: Hughes et al. (2009)). In addition to our sample, the disks around F-G stars studied by Brown et al. (2007) also belong to the pre-transitional disk category. The large gaps that are being detected in pre-transitional disks are most likely due to observational bias since larger gaps will create larger mid-infrared deficits in the SED. Smaller gaps will most likely have less apparent dips in their SEDS and be more difficult to identify, however, if their gaps contain some optically thin material the silicate emission in these objects should be much stronger than can be explained by a full disk model.

The existence of an inner optically thick disk may be an indicator of the first stages of disk clearing that will eventually lead to the the inner holes that have been seen in previously reported transitional disks; this has important implications on

disk evolution theories since only planet-formation can account for this structure. Hydrodynamical simulations have shown that a newly formed planet could accrete and sweep out the material around it through tidal disturbances (Quillen et al., 2004), even maintaining substantial accretion rates (Varnière et al., 2006). Moreover, Najita et al. (2007a) have found that the intrinsic properties of transitional disks may favor planet formation. Another proposed formation mechanism for the holes in transitional disks is photoevaporation, in which a photoevaporative wind halts mass accretion towards the inner disk and material in this inner disk is rapidly evacuated creating an inner hole (Clarke et al., 2001); the hole then increases in size as the edge continues photoevaporating (Alexander & Armitage, 2007). Neither this model nor the inside-out evacuation induced by the MRI (Chiang & Murray-Clay, 2007) would explain how an optically thick inner disk accreting at a sizable accretion rate (see Table 5.1) would remain inside the hole. Rapid dust growth and settling has also been proposed to explain the holes in disks (Dullemond & Dominik, 2004, 2005). Again, this does not account for the presence of optically thick inner disk material given that theory suggests grain growth should be fastest in the inner disk, not at some intermediate radius (Dullemond & Dominik, 2004, 2005; Weidenschilling et al., 1997).

Our sample also has interesting dust compositions (Watson et al., 2009). LkCa 15 has an amorphous silicate feature indicating little if any processing leading to the crystallization seen in other young stars. Amorphous silicates are also seen in CoKu Tau/4, DM Tau, and GM Aur (Sargent et al., 2006). In contrast, UX Tau A is different from all the other transitional disks because it has crystalline silicate

emission features in addition to amorphous silicate emission features (Figure 5.1 inset). The wall at ∼56 AU is the main contributor to the crystalline silicate emission since it dominates the flux in the mid- and far-infrared. This raises the question of whether crystalline silicates are created close to the star or if they can be created in situ at ∼56 AU. If the former, it challenges current radial-mixing theories, none of which can get significant amounts of crystalline silicates out to this distance (Gail, 2001; Bockelée-Morvan et al., 2002; Keller & Gail, 2004). One possibility for *in situ* processing may be collisions of larger bodies, which might produce small grains heated sufficiently to create crystals (S. Kenyon, private communication).

Pre-transitional disks offer further insight into the diversity of the "transitional disk" class and future studies of these disks will greatly advance our understanding of disk evolution and planet formation.

Table 5.1. Stellar and Model Properties of UX Tau A and LkCa 15

Stellar Properties		
	UX Tau A	LkCa 15
M_* ($M_\odot$)	1.5	1.1
R_* ($R_\odot$)	2	1.7
T_* (K)	4900	4350
L_* ($L_\odot$)	2.18	.96
$\dot{M}$ ($M_\odot$ yr^{-1})	9.6×10^{-9}	2.4×10^{-9}
Inclination (°)	60	42[1]
A_V	1.3	1.2
Spectral Type	K2	K5
Optically Thick Inner Wall		
a_{max} (μm)[2]	10	1
T_{wall} (K)	1400	1400
z_{wall} (AU)[2,3]	0.01	0.01
R_{wall} (AU)	0.16	0.12
Optically Thick Inner Disk[4]		
$R_{disk,out}$ (AU)[2]	<0.18	<0.15
$M_{disk,inner}$ ($M_\odot$)	$<8\times10^{-6}$	$<5\times10^{-5}$
Optically Thick Outer Wall		
a_{max} (μm)	0.25	0.25
T_{wall} (K)[2]	110	95
z_{wall} (AU)[2]	6	4
R_{wall} (AU)	56	46
Optically Thick Outer Disk		
ϵ[2]	.01	.001
α[2]	.015	.0006
M_{disk} ($M_\odot$)[2]	.01	.1
Optically Thin Inner Region		
$R_{in,thin}$ (AU)	-	0.15 (0.12)[5]
$R_{out,thin}$ (AU)[2]	-	5 (4)
$a_{min,thin}$ (μm)	-	0.005
$a_{max,thin}$ (μm)	-	0.25
$M_{dust,thin}$ ($M_\odot$)	-	$4(5)\times10^{-11}$

[1]Simon et al. (2000)

[2]These are free parameters which are constrained by the best fit to the SED.

[3]z_{wall} is the height of the wall above the midplane

[4]We assume the same ϵ and α as the outer disk.

[5]For LkCa 15, values in parenthesis refer to parameters in the case that there is no optically thick inner wall.

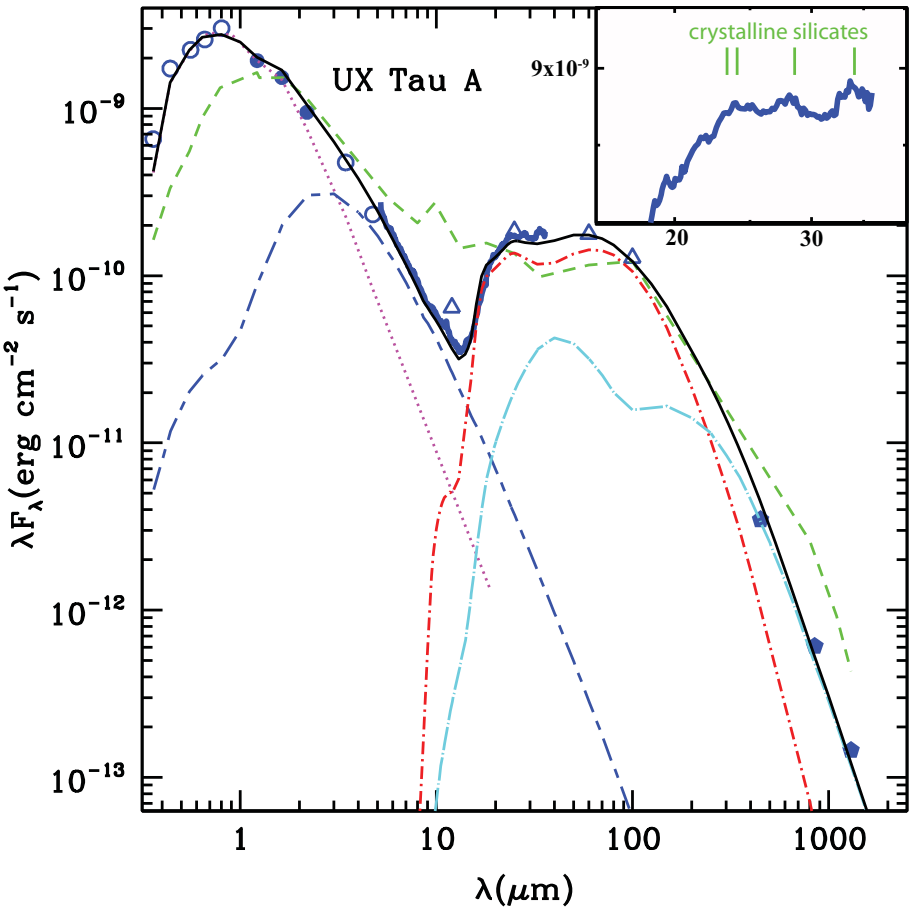

Figure 5.1 SED and pre-transitional disk model of UX Tau A. We show ground-based optical, L- and M-band photometry, (open circles; Kenyon & Hartmann, 1995), J,H,K (2MASS; filled circles), *Spitzer* IRS (blue solid line; Furlan et al., 2006), IRAS (open triangles; Weaver & Jones, 1992), and millimeter (filled pentagons; Andrews & Williams, 2005) data. The solid black line is the best fit model with a disk gap of ∼56 AU (see Table 5.1 for model parameters). Separate model components are as follows: stellar photosphere (magenta dotted line), inner wall (blue short-long-dash), outer wall (red dot-short-dash), and outer disk (cyan dot-long-dash). We also show the median SED of Taurus (green short-dashed line). The insert is a close-up of the *Spitzer* IRS spectrum longwards of ∼16 μm and indicates the crystalline silicate emission features in addition to underlying features from amorphous silicates (Watson et al., 2009).

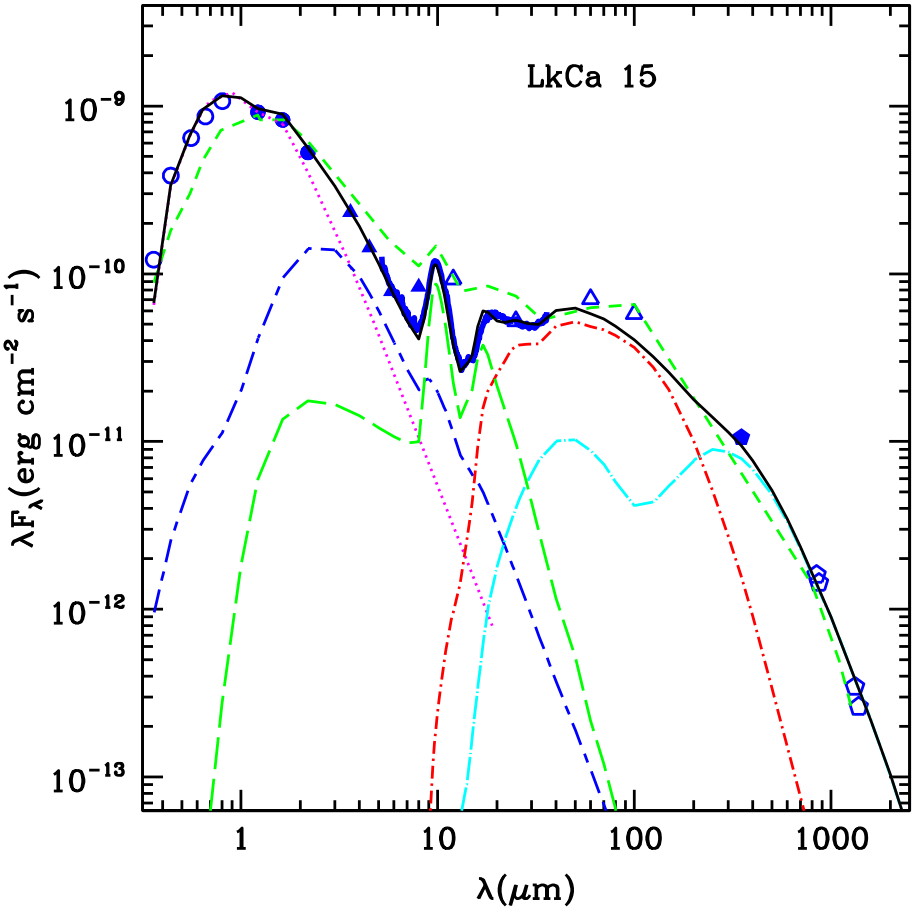

Figure 5.2 SED and pre-transitional disk model of Lk Ca 15. Symbols and lines are the same as listed in Figure 5.1's caption. The green long-dash line is the optically thin inner region. Open pentagons come from this work. LkCa 15 has an outer disk that is truncated at an inner radius of ∼46 AU which is consistent with millimeter results (Piétu et al., 2006). We can fit the SED with an inner optically thick wall and a small amount of optically thin dust in the gap.

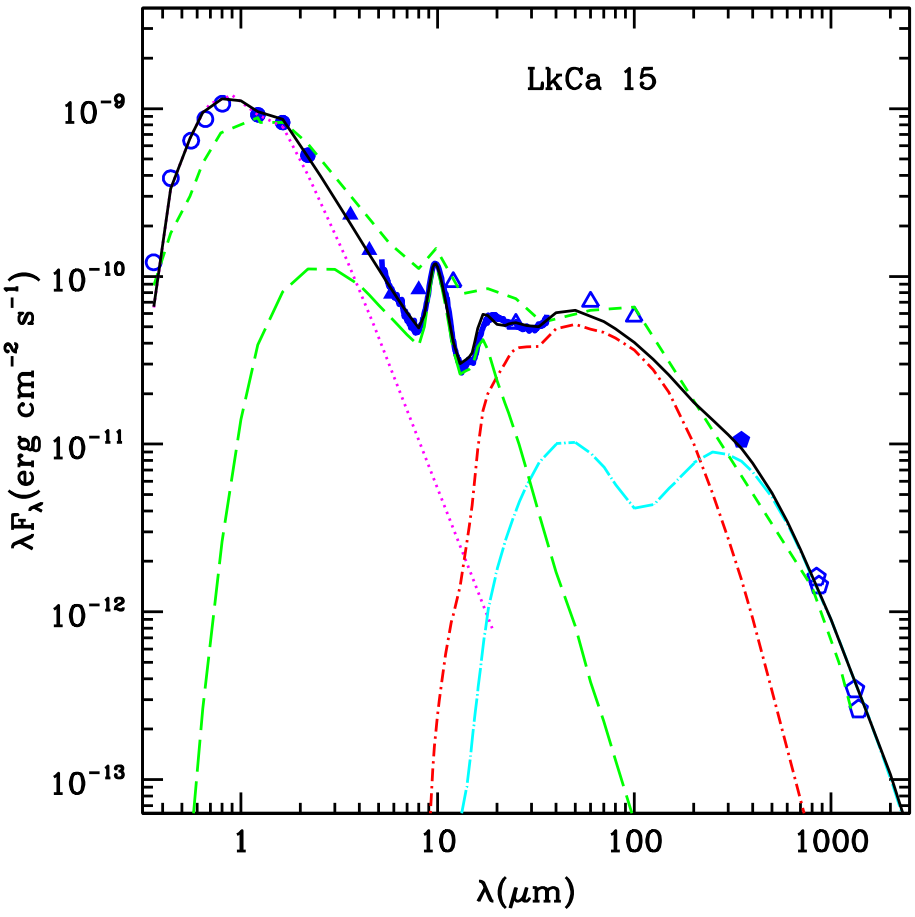

Figure 5.3 SED and transitional disk model of Lk Ca 15. Symbols and lines are the same as listed in Figure 5.3's caption. Here we show a disk model of Lk Ca 15 without an optically thick inner wall. Model parameters are listed in Table 5.1.

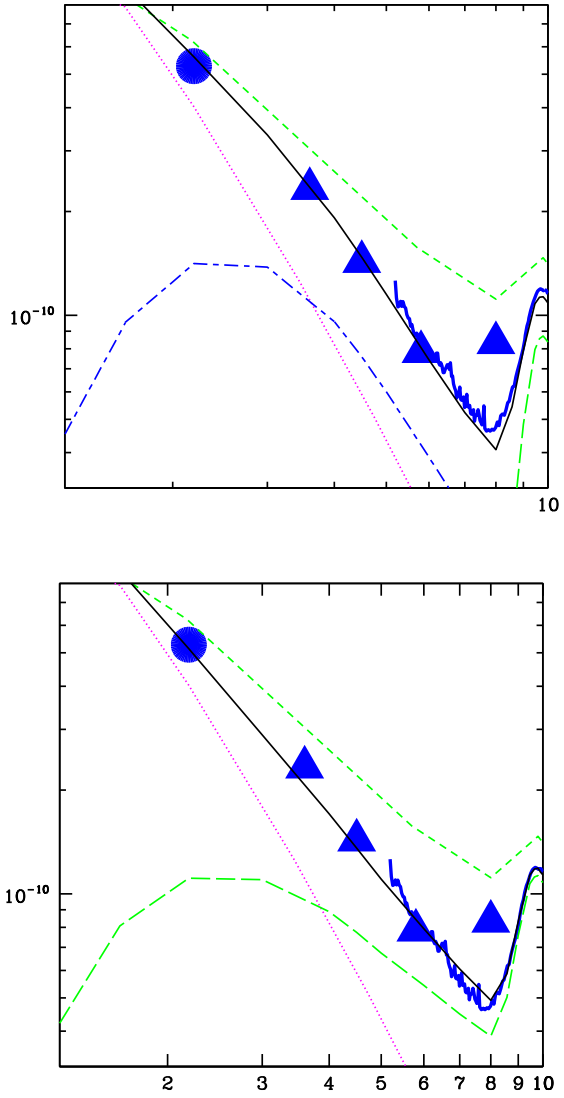

Figure 5.4 Comparison of pre-transitional and transitional disk model fits to the near-infrared emission of Lk Ca 15. Here we provide close-ups of the SED and models presented in Figures 5.2 (top) and 5.3 (bottom) between 3 to $\sim$10 μm.

Chapter 6

Confirmation of a Gapped Primordial Disk Around LkCa 15

Abstract: Recently, analysis of near-infrared broad-band photometry and *Spitzer* IRS spectra has led to the identification of a new "pre-transitional disk" class whose members have an inner optically thick disk separated from an outer optically thick disk by an optically thin gap. This is in contrast to the "transitional disks" which have inner disk holes (i.e. large reductions of small dust from the star out to an outer optically thick wall). In LkCa 15, one of these proposed pre-transitional disks, detailed modeling showed that although the near-infrared fluxes could be understood in terms of optically thick material at the dust sublimation radius, an alternative model of emission from optically thin dust over a wide range of radii could explain the observations as well. To unveil the true nature of LkCa 15's inner disk we obtained a medium-resolution near-infrared spectrum spanning the wavelength range 2-5 μm using SpeX at the NASA Infrared Telescope Facility. We report that the excess near-infrared emission above the photosphere of LkCa 15 is a black-body continuum which can only be due to optically thick material in an inner disk around the star. When this confirmation of a primordial inner disk is combined with earlier observations of an inner edge to LkCa 15's outer disk it reveals a gapped structure. Forming planets

emerge as the most likely mechanism for clearing the gap we detect in this evolving disk.

6.1 Introduction

The origin of a star and its planets is intricately tied to the evolution of the system's primordial accretion disk. These disks are composed of gas and dust and are formed in the collapse of the star's natal, molecular cloud (Terebey et al., 1984). As time passes, the dust grains in these primordial disks evolve: they collide and stick, eventually growing in size and perhaps forming planetary systems much like our own (Weidenschilling et al., 1997). The finer details of how the disk material evolves from an initially well-mixed distribution of gas and dust to a system composed mostly of large solids like our own solar system is not well understood.

In recent years a growing number of primordial disks with signatures of dust evolution hinting to the early stages of planet formation have been identified. Most of these cases, dubbed "transitional disks," (Strom et al., 1989) consist of stars with inner holes in their disks that are mostly devoid of material. Within the past few years, observations at mid-infrared wavelengths by the *Spitzer Space Telescope* have led us to define transitional disks as those objects with small or negligible near-infrared flux excesses over photospheric fluxes but with a substantial excess in the mid-infrared and beyond. This flux deficit at near-infrared wavelengths relative to full disks accreting material onto the star has been explained by modeling transitional disks as optically thick disks with inner cleared regions; the mid-infrared emission originates in the inner edge or "wall" of the truncated disk which is frontally illuminated by the

star (Calvet et al., 2005b). A small number of these transitional disks with detailed *Spitzer* IRS spectra have been analyzed to date. The estimated truncation radii of these disks cover a wide range, from ∼4 AU in DM Tau (Calvet et al., 2005b) to 46 AU in CS Cha (Espaillat et al., 2007a). Transitional disks have been found in all ages where protoplanetary disks have been identified, from the ∼1–2 yr old Taurus population (Calvet et al., 2005b) to the 10 Myr old TW Hya association (Calvet et al., 2002) and 25 Ori (Espaillat et al., 2008b). In each case, the disk is accreting mass onto the star so we can conclude that gas is being transported through the inner cleared disk. In addition, in some cases a small amount of micron or sub-micron dust coexists with the gas in this region, giving rise to an excess over photospheric fluxes detected in the near infrared. Details of the distribution of this optically thin dust are largely unknown, although near-infrared interferometric observations suggest that this material is highly structured (Ratzka et al., 2007).

A new class of evolving disks has been identified very recently. Disks in this class have inwardly truncated outer disks, as the transitional disks. However, their significantly larger near-infrared excess, comparable to that of full disks, points to the existence of a remaining optically thick disk separated by a gap from the outer disk. A handful of these disks have been analyzed to date, including four around intermediate mass stars (Brown et al., 2007) and two around classical T Tauri stars (Espaillat et al., 2007b). In two of these cases, LkCa 15 and LkHα 330, millimeter interferometry has confirmed the truncation of the outer disk (Piétu et al., 2006; Brown et al., 2008) in agreement with the SED modeling (Espaillat et al., 2007b; Brown et al., 2007). However, the substantial near-infrared excess of LkCa 15 could be explained by either

optically thick material or by 5×10^{-11} $M_\odot$ of optically thin dust mixed with the gas in the inner disk (Espaillat et al., 2007b). These contradictory hypotheses cannot not be properly tested with the existing near-infrared data, which consists of 2MASS and *Spitzer* broad-band photometry.

Here, we present detailed spectroscopic data that allows us to unambiguously search for optically thick material in the inner disk of LkCa 15, a CTTS in the Taurus cloud, in which an outer disk truncated at 46 AU has been imaged in the millimeter (Piétu et al., 2006). We confirm that LkCa 15 belongs to the new class of disks around young stellar objects, the "pre-transitional disks," (Espaillat et al., 2007b) where a gap is opening within the disk around a low mass pre-main sequence star.

6.2 Observations & Data Reduction

We obtained a 2–5 μm spectrum of LkCa 15 with SpeX at the NASA Infrared Telescope Facility (IRTF) (Rayner et al., 2003) on December 3, 2007. The spectrum was reduced with Spextool (Cushing et al., 2004) and dereddened with the Mathis dereddening law (Mathis, 1990) and an A_V of 1.2 (Espaillat et al., 2007b). For our template spectrum we use HD36003 (K5 V) which corresponds to the spectral type of LkCa 15 (Kenyon & Hartmann, 1995) and was obtained from the IRTF Spectral Library.[1] In Figure 6.1 we present the medium resolution near-infrared spectra of LkCa 15 and the K5 dwarf template.

[1]http://irtfweb.ifa.hawaii.edu/~spex/IRTF_Spectral_Library/

6.3 Analysis

LkCa 15's spectrum has absorption lines that are weaker than those seen in the spectrum of a standard star of the same spectral type (Figure 6.2). This "veiling" of the absorption lines is due to an excess continuum that adds to the intrinsic photospheric flux, decreasing the depths of the absorption lines (Hartigan et al., 1989). We see this veiling phenomenon in similar spectra of full primordial disks (Muzerolle et al., 2003) in which it is due to blackbody emission from the inner disk's optically thick wall located at the radius where dust sublimates. We derived the veiling (r=F_{excess}/F_*; Hartigan et al., 1989) by adding an artificial excess continuum to the template spectrum until the photospheric line depths matched those seen in LkCa 15's spectrum in the K-band. We measure a veiling of 0.3 at $\sim$2.3 μm, which is consistent with the excess above the photosphere inferred from broadband photometry (Espaillat et al., 2007b). The veiling seen in LkCa 15 cannot be produced by a low-mass companion because such an object would cause the spectral lines in the composite spectrum of the system to be stronger than the lines expected from the optical spectral type, rather than weaker as observed.

To extract the spectrum of the excess emission (Figure 6.3), we follow Muzerolle et al. (2003) and scale the entire LkCa 15 spectrum according to the above K-band veiling estimate (Figure 6.1) and subtract the original template spectrum from it. The near-infrared excess emission above the photospheric flux that is seen in LkCa 15 is well-matched by a single-temperature blackbody of 1600 K (Figure 6.3), which lies within the range of dust sublimation temperatures found for a large sample of classical T Tauri stars and Herbig Ae/Be stars (Monnier & Millan-Gabet, 2002).

From this we conclude that the near-infrared excess of LkCa 15 originates from the wall of an optically thick inner disk located at the dust destruction radius. When these results are interpreted with previous *Spitzer* IRS and millimeter observations, we can firmly state that this object has a gapped disk structure (Figure 6.4), making LkCa 15 a member of the pre-transitional disk class.

6.4 Discussion & Conclusions

Unseen planets (Quillen et al., 2004; Rice et al., 2003) have been proposed to clear out the large cavities within the primordial disks around GM Aur (Calvet et al., 2005b), DM Tau (Calvet et al., 2005b), TW Hya (Calvet et al., 2002; Uchida et al., 2004; Hughes et al., 2007), and CoKu Tau/4 (D'Alessio et al., 2005). However, several other explanations are also possible. The inner disk holes in most of these "transitional disks" can be explained by inside-out evacuation mechanisms like the magneto-rotational instability (MRI; Chiang & Murray-Clay, 2007). In addition, a stellar companion can inwardly truncate the outer disk as is most likely the cause of the inner hole of CoKu Tau/4 (Ireland & Kraus, 2008).

Alexander & Armitage (2007) found that the accretion rates and disk masses of GM Aur, DM Tau, and TW Hya suggest planet formation in these systems. This still does not discount that the MRI is the main clearing agent in the inner disk given that this mechanism is still viable in the presence of a planet. Consequently, inner disk holes are not conclusive signatures of planet formation.

The origin of the gap in LkCa 15 can be evaluated against different mechanisms that have been proposed to clear the inner disk, namely the MRI, photoevaporation,

stellar companions, and planet formation. The MRI operates on the ionized, frontally illuminated wall of the inner disk and allows material to accrete onto the star leading to inside-out clearing (Chiang & Murray-Clay, 2007); the MRI cannot account for a remnant optically thick inner disk. In the photoevaporation model, a stellar wind creates a small gap and halts the inward accretion of mass. Without replenishment the inner disk quickly accretes onto the central star and only then can the hole grow outward (Clarke et al., 2001). When the hole is about 46 AU, as is seen in LkCa 15, no inner disk remains (Alexander & Armitage, 2007) so LkCa 15's gap cannot be due to photoevaporation. A companion star would have to be located at about 18 – 26 AU (Artymowicz & Lubow, 1994) in order to truncate the outer disk at 46 AU and studies of LkCa 15 have revealed no stellar mass companion down to about 4 AU (Leinert et al., 1993; Ireland & Kraus, 2008). Planet formation emerges as the most likely explanation since a planet can create a gap about its orbit (Paardekooper & Mellema, 2004; Varnière et al., 2006). The large gap of LkCa 15, which encompasses the orbits of Mercury (.4 AU) and Neptune (30 AU), raises the interesting possibility that we are seeing clearing due to multiple planets which would suggest that LkCa 15 may be an early analog of our own Solar system.

In conclusion, our observations confirm the presence of an inner optically thick disk in LkCa 15. The existence of optically thick material inside a truncated disk provides significant insight into the models presented to date to explain the transitional disks and calls for more detailed studies of this new class of disk.

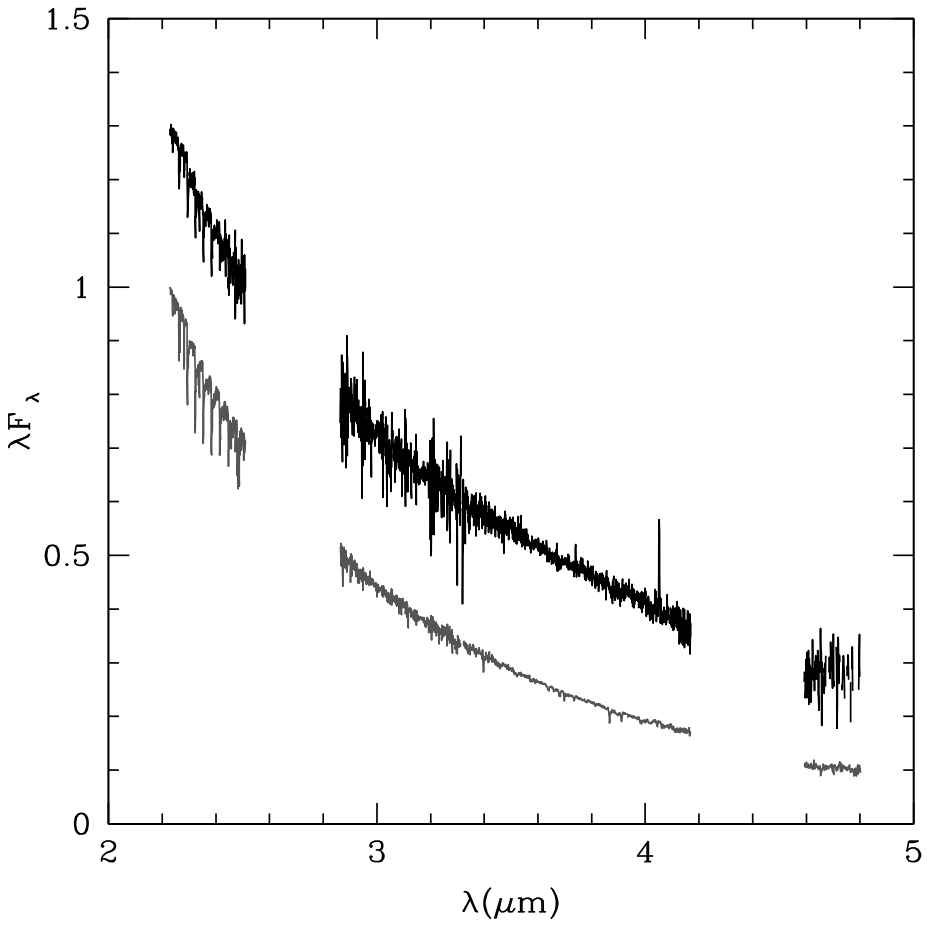

Figure 6.1 Near-infrared SpeX spectra of LkCa 15. LkCa 15's spectrum (upper dark line) is scaled relative to the K5 dwarf template (lower light line) by the derived veiling value of 0.3. Telluric absorption is too strong at 2.5–2.8 μm and 4.2–4.6 μm for useful measurements at these wavelengths. Fluxes are in units of the template's flux at $\sim$2.2 μm.

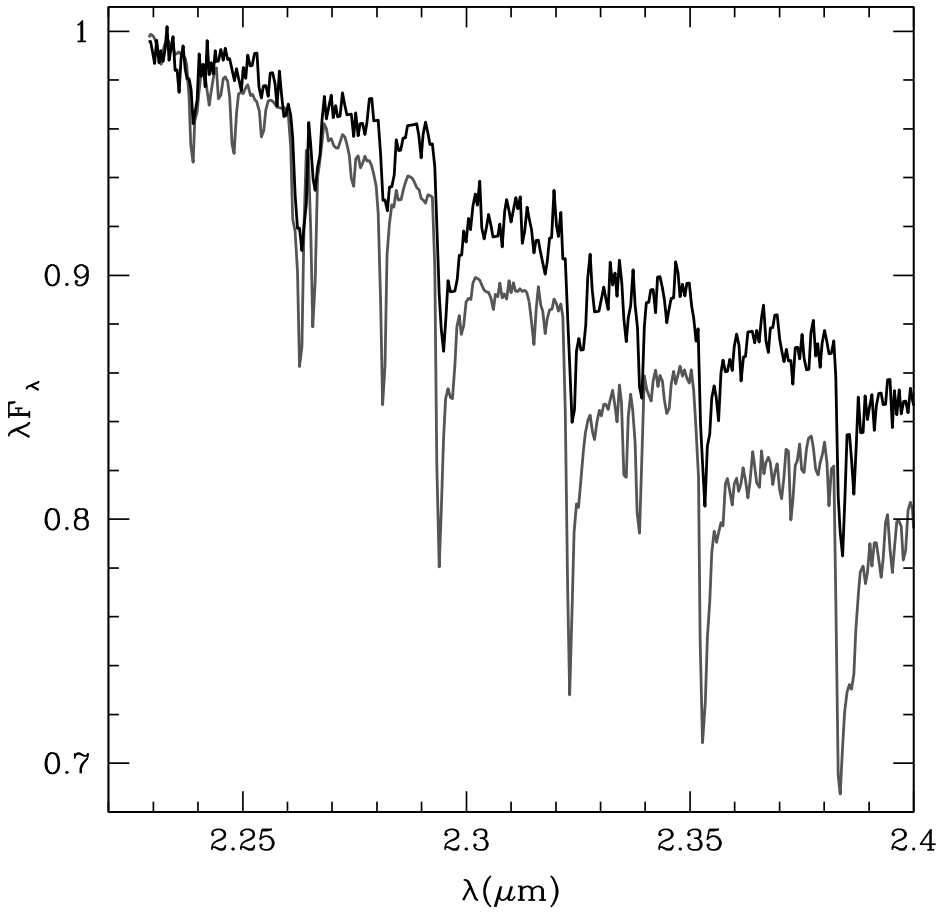

Figure 6.2 Veiling of LkCa 15. We show the K-band portion of the spectra in Figure 6.1. The LkCa 15 spectrum (upper dark line) has been scaled down to the template's flux at ∼2.2 μm in order to more clearly show the veiled absorption lines of LkCa 15 relative to the K5 dwarf template (lower light line).

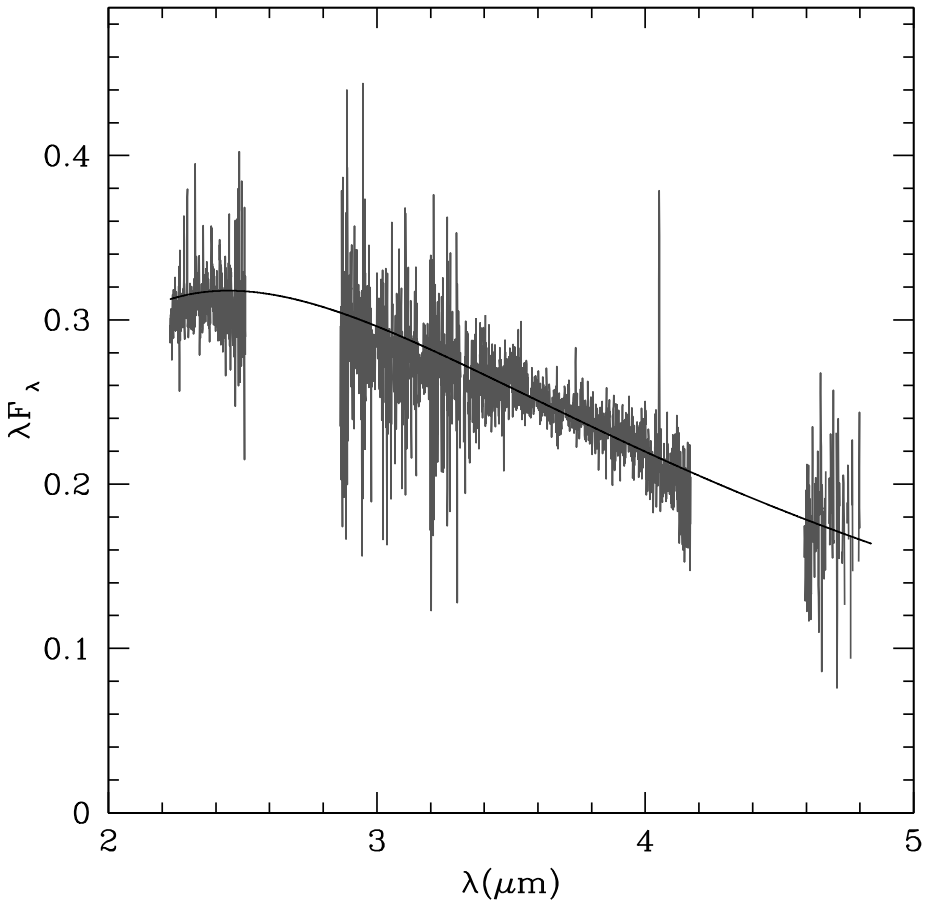

Figure 6.3 Near-infrared excess spectrum of LkCa 15. The near-infrared excess of LkCa 15 (light line) is fit with a 1600 K blackbody (dark line). Fluxes are in the same units as Figure 6.1. The excess was obtained by subtracting the original template spectrum from the veiling-scaled LkCa 15 spectrum which are both shown in Figure 6.1.

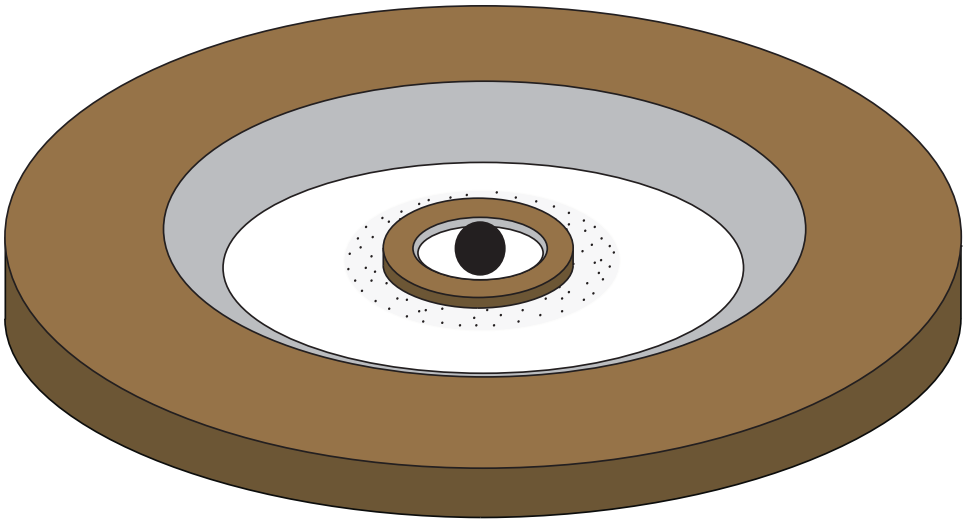

Figure 6.4 Schematic of pre-transitional disk structure. The central circle is the star. Progressing outward the components of the disk consist of the following: the inner wall at the dust destruction radius (light gray), the inner disk (brown), a disk gap (white) with a small amount of optically thin dust (dots), the outer disk wall (light gray), and the outer disk (brown). Based on Piétu et al. (2006) and Espaillat et al. (2007b), LkCa 15's optically thick inner disk is located between 0.12 AU and 0.15 AU and the optically thin dust extends out to 5 AU. Between 5 and 46 AU the disk is relatively clear of small dust grains and the outer disk is inwardly truncated at 46 AU. The spectrum of LkCa 15 shown in Figure 6.1 arises from both the star and the inner wall of this schematic; the near-infrared excess emission (Figure 6.3) originates only from the inner wall.

Chapter 7

Unveiling the Innermost Regions of Disks with Gaps and Holes

Abstract: In the past few years several disks with inner holes that are relatively empty of small dust grains have been detected and are known as transitional disks. Recently, *Spitzer* has identified a new class of "pre-transitional disks" which have an optically thick inner disk separated from an optically thick outer disk by an optically thin disk gap. Near-infrared spectra with SpeX provided the first confirmation of a gap in the pre-transitional disk of LkCa 15 by verifying that the near-infrared excess emission in this object was due to an optically thick inner disk. In this chapter, we present similar data for UX Tau A and demonstrate it has a pre-transitional disk as well. We also present SpeX spectra of the transitional disks DM Tau and GM Aur, and illustrate the differences between the inner disks of pre-transitional and transitional disks.

7.1 Introduction

Several disks which have nearly photospheric near-infrared emission but substantial excesses above the stellar photosphere at wavelengths beyond $\sim$20 μm have been observed and are referred to as "transitional disks" (Strom et al., 1989). Using data from the *Spitzer* Infrared Spectrograph (Houck et al., 2004), detailed modeling has

demonstrated that this flux deficit at near-infrared wavelengths relative to full disks can be explained by optically thick disks with inner holes of < 40 AU (e.g. Calvet et al., 2005b; Espaillat et al., 2007a, 2008b). In most cases these inner holes are not completely devoid of material (e.g. GM Aur, TW Hya, CS Cha, CVSO 224); a small amount of micron or submicron optically thin dust exists within the hole, giving rise to a small infrared excess over photospheric fluxes as well as silicate emission (Calvet et al., 2005b; Espaillat et al., 2007a, 2008b). Gas has also been detected within the inner holes of transitional disks (e.g. Bergin et al., 2004; Salyk et al., 2007)

Recently, *Spitzer* identified a new class of "pre-transitional disks" around LkCa 15 and UX Tau A (Espaillat et al., 2007b). These disks have deficits of mid-infrared flux (5 μm – 20 μm) and substantial excesses at longer wavelengths, as is seen in the transitional disks. However, in contrast to the small near-infrared (2 μm – 5 μm) excesses exhibited by some transitional disks, pre-transitional disks have significant near-infrared excesses relative to their stellar photospheres, comparable to the median spectral energy distribution of disks in Taurus (D'Alessio et al., 1999). The distinctive shapes of these SEDs indicate that pre-transitional disks have an inner disk separated from an outer disk and that we may be seeing the development of gaps within protoplanetary disks. As a result, observations of these pre-transitional disks provide a unique insight into the process of dust clearing since their structure is most likely due to planet formation and not to other inside-out clearing mechanisms such as photoevaporation (Clarke et al., 2001), the magnetorotational instability (Chiang & Murray-Clay, 2007), or grain growth (Dullemond & Dominik, 2005) which have been proposed to explain the inner holes of transitional disks.

While LkCa 15's outer disk truncation at 46 AU has been imaged in the millimeter (Piétu et al., 2006), Espaillat et al. (2007b) showed that the substantial near-infrared excess of LkCa 15 could be explained by either optically thick material or by $\sim 10^{-11}$ $M_{\odot}$ of optically thin dust mixed with the gas in the inner disk. In order to resolve this issue, Espaillat et al. (2008a) obtained a medium resolution near-infrared SpeX spectrum spanning the wavelength range 2 – 5 μm. This near-infrared spectrum had absorption lines that were weaker relative to the spectrum of a standard star of the same spectral type. This phenomena, called "veiling," is also observed in similar spectra of full disks and is explained by emission from dust located at the dust sublimation radius (Muzerolle et al., 2003). Espaillat et al. (2008a) measured a veiling factor (r_K; Hartigan et al., 1989) of 0.3±0.1 for LkCa 15 at ∼2.3 μm and fit the near-infrared excess from 2 – 5 μm with a single-temperature blackbody of 1600 K. These SpeX data confirmed that LkCa 15 had an inner optically thick disk, making this observation the first independent verification of a gap in a protoplanetary disk.

Espaillat et al. (2007b)'s identification of UX Tau A as a pre-transitional disk was based on analysis of broad-band 2MASS and *Spitzer* IRAC photometry. In order to further assess the nature of its inner disk, we present a near-infrared SpeX spectrum of UX Tau A and confirm its gapped disk structure. To explore the differences between the inner disks of pre-transitional and transitional disks we present similar data for DM Tau and GM Aur. We present the spectrum of the weak T Tauri star LkCa 14 and use this diskless star to test our measurement methods. We also determine spectral types for our targets based on FAST optical spectra.

7.2 Observations & Data Reduction

Spectra for LkCa 14, DM Tau, GM Aur, and UX Tau A were obtained at the NASA Infrared Telescope Facility facility using SpeX (Rayner et al., 2003). The dates of the observations, the exposure times, and the signal-to-noise ratios for each target are given in Table 7.1. We used the Long XD2.1 grating, covering 2.1 to 5.0 μm, with a slit of $0\farcs5\times15''$ for a resolution ($\lambda/\delta\lambda$) of 1500. We extracted the data with Spextool (Cushing et al., 2004) and corrected for telluric absorption using the *xtellcor* routine (Vacca et al., 2003). Our telluric standards for LkCa 14, DM Tau, GM Aur, and UX Tau A were HD25175, HD27761, HD27777, and HD30739, respectively. Bad pixels and regions of high telluric noise (2.5–2.9 μm and 4.2–4.6 μm) were manually removed from the spectra.

Low-dispersion optical spectra for our sample were obtained in 1995 and 1996 using the 1.5 m telescope of the Whipple Observatory with the FAst Spectrograph for the Tillinghast Telescope (FAST) spectrograph (Fabricant et al., 1998), equipped with the Loral 512×2688 CCD. The spectrograph was set up in the standard configuration used for FAST COMBO projects, a 300 groove mm^{-1} grating and a $300''$ wide slit. This combination offers 3400 Å of spectral coverage centered at 5500 Å, with a resolution of $\sim$6 Å. The spectra were reduced at the Harvard-Smithsonian Center for Astrophysics using software developed specifically for FAST COMBO observations. All individual spectra were wavelength-calibrated and combined using standard IRAF routines.

7.3 Analysis

Classical T Tauri stars tend to have observed photospheric absorption lines which are weaker than those of non-accreting stars. This "veiling" (Hartigan et al., 1989) is due to an excess continuum which adds to the star's emission and "fills in" stellar absorption lines, making them appear weaker. In the optical and shorter wavelengths, this is primarily due to the hot continuum which arises from the accretion shock onto the star (Calvet & Gullbring, 1998). In the near-infrared, for stars which are not strong accretors, veiling of photospheric absorption lines is mainly due to dust in the disk (Muzerolle et al., 2003).

Here we extract the excess continuum due to dust by measuring the amount of veiling of the target in the K-band. We estimated veiling by comparing the line strengths in the target to those of a standard star of the same spectral type. Spectra of standard stars were obtained from the IRTF Spectral Library (Rayner, J. T., Cushing, M. C., Vacca, W. D. 2009, in preparation; Cushing et al., 2005).[1] To measure the veiling present in each target, we artificially veiled the standard spectra by adding a continuum of $F_{excess} = r \times F_{standard}$ where r is the veiling factor ($=F_{excess}/F_*$). The standard spectra were veiled until the depths of the absorption lines matched those of the target spectrum in the region from 2.20 – 2.28 μm. We then scaled the target by $1 + r_K$ and subtracted the standard spectrum to measure the shape of near-infrared excess emission. In order to measure the effect of adopting different spectral types on the derived r_K and excess emission, we compare the targets to a range of standards based on spectral types derived previously in the literature and in this work.

[1] http://irtfweb.ifa.hawaii.edu/~spex/IRTF_Spectral_Library/

Veiling measurements are dependent on the spectral types which are adopted. In order to obtain a more accurate estimate on the veiling, we derived spectral types for LkCa 14, DM Tau, GM Aur, and UX Tau A using FAST optical spectra. Spectral types were obtained using the SPTCLASS tool,[2] an IRAF/IDL code based on the methods described in Hernández et al. (2004). For LkCa 14 we find a spectral type of K5.5±1.0; for UX Tau A we find G6.0±1.0; DM Tau has a spectral type of M1.5±1.0 and we find GM Aur has a spectral type of K5.5±1.0 (Table 7.2). In Figures 7.1 and 7.2 we illustrate the accuracy of the fitting procedure in the cases of UX Tau A and GM Aur, respectively. In G-type stars, the metallic lines play an important role in classifying the spectrum and in later type stars the molecular bands become more important. The features used to classify UX Tau A are the Ca I, G-band (CH), Na I, and Fe I lines. For GM Aur, the molecular bands TiO and CaH were used.

7.3.1 LkCa 14

In order to test our method of measuring the veiling and excess emission of TTS, we analyzed the spectrum of LkCa 14, a single (White & Ghez, 2001), non-accreting diskless T Tauri star in Taurus (Kenyon & Hartmann, 1995). The expectation is that this object should have no K-band veiling since it does not exhibit excess emission at near- and mid-IR wavelengths in its SED. We measure the veiling in LkCa 14 by comparing its K-band spectrum to that of spectral standards. To explore the effect of using different standards on our analysis, we adopted standards with spectral types which agreed with that found by Herbig et al. (1986, M0) as well as those that fall

[2]http://www.astro.lsa.umich.edu/∼hernandj/SPTclass/sptclass.html

within the spectral classification errors from the previous section (K5.5±1.0). We use standards with spectral types of M0 V (HD19305), K5 V (HD36003), and K7 V (HD237903) and note that the IRTF library does not have spectra for K4 V or K6 V. In Figure 7.3, LkCa 14 is compared to each of the adopted standards and we find that LkCa 14 has no veiling (r_K=0±0.1) relative to each.

In order to extract the excess emission from 2–5 μm, if present, we first deredden the spectra. The standards from the IRTF library have already been corrected for reddening. We dereddened the spectrum of LkCa 14 using the visual extinction derived from comparing B-, V- (Høg et al., 2000), R-band (Norton et al., 2007), and 2MASS photometry to stellar photospheres from Kenyon & Hartmann (1995). Assuming spectral types of M0, K5, and K7 for LkCa 14, we derive A_V=0 in each case. After scaling LkCa 14 to match the standard's flux at 2.2 μm and subtracting the standard (Figure 7.4), we find that there is no excess emission. When LkCa 14 is compared to a K5 standard (top, Figure 7.4) there is a small excess between $\sim$ 3.5 and 4.2 μm which is most likely due to errors in the spectral slopes of the objects. We conclude that, as expected, LkCa 14 has no veiling and no excess emission.

7.3.2 UX Tau A

UX Tau A is a single star (White & Ghez, 2001, A. Kraus, private communication) which is surrounded by a pre-transitional disk (Espaillat et al., 2007b). Its outer wall is located at $\sim$56 AU and its gap is devoid of small dust grains. Earlier in this chapter, we find a spectral type of G6.0±1.0 for UX Tau A. Here we compare UX Tau A to spectral types of G6.5 V (HD115617) and G8 V (HD101501) which fall

within our measurement error; the IRTF library does not have main sequence G6 or G7 stars. We also compare UX Tau A to a K2 star (HD3765) since this was the spectral type reported by Herbig (1977) and adopted by Espaillat et al. (2007b). The absorption lines in the K-band spectrum of UX Tau A are weaker than those in the spectra of the standard dwarfs, as shown in Figure 7.5. Similar veiling has been observed in similar spectra of full disks (Muzerolle et al., 2003). We measure veiling factors (r_K) of 0.3 (G6.5), 0.4 (G8), and 1.0 (K2).

Assuming UX Tau A is a G6.5, G8, or K2 star, we derive A_V = 1.8, 1.7, and 1.3, respectively, by comparing U, B, V, R, I, J, H, and K photometry (Kenyon & Hartmann, 1995, 2MASS) to standard photospheres (Kenyon & Hartmann, 1995); we use these values to deredden the spectra of UX Tau A with the Mathis dereddening law (Mathis, 1990). After extracting the near-infrared excess of UX Tau, we find that it can be fit by a single-temperature blackbody at the dust destruction temperature for each spectral type. Assuming a spectral type of G6.5 the temperature of the best-fit blackbody is ∼1350 K, for G8 it is ∼1500 K, and for K2 it is 1800 K. (Figures 7.6, 7.7, and 7.8). While adopting different spectral types will lead to a difference in the temperature of the extracted excess emission, these temperatures are all within the range of dust sublimation temperatures found for a much larger sample of CTTS and Herbig Ae/Be stars by (Monnier & Millan-Gabet, 2002).

7.3.3 DM Tau

DM Tau is a single star (White & Ghez, 2001, A. Kraus, private communication) surrounded by a transitional disk with a ∼3 AU hole that is empty of small dust

grains (Calvet et al., 2005b). Spectral types of M1 (Herbig, 1977) and M1.5±1.0 (Section 7.3) have been measured for this object and so here we compare DM Tau to standard stars with spectral types of M0 V (HD19305), M1V (HD42581), M2 V (HD95735), and M3 V (Gl338). The absorption lines of DM Tau are not veiled relative to any of the standards (Figure 7.9).

Comparing U, B, V, R, I, J, H, and K photometry from Kenyon & Hartmann (1995) and 2MASS to the stellar photospheres for an M0, M2, M3, and M4 star (Kenyon & Hartmann, 1995) we find extinctions (A_V) of 0.9, 0.6, 0.4, and 0.0 respectively. The DM Tau spectrum is dereddened with the Mathis dereddening law (Mathis, 1990) and these derived extinctions. We find that for each spectral type DM Tau has no significant near-IR excess emission at 3 – 5 μm (Figure 7.10), in agreement with the fact that DM Tau has no small dust within its hole as inferred from its lack of any excess emission above the photosphere in the K-band up to $\sim$ 8 μm (Figure 1.11; Calvet et al., 2005b). As in the case of LkCa 14, DM Tau shows a small excess when compared to some of the standards, which may be an indication of a spectral slope errors.

7.3.4 GM Aur

The transitional disk around the single star GM Aur (White & Ghez, 2001, A. Kraus, private communication) has an inner hole of $\sim$ 20 AU (Hughes et al., 2009) which contains some submicron-sized optically thin dust (Calvet et al., 2005b). This object has measured spectral types of K3 (Herbig, 1977) and K5.5±1.0 (Section 7.3). We compare GM Aur to a K5 star (HD36003) from the IRTF library as well as a K3 star

(HD219134) since this is commonly adopted in the literature. We note that the IRTF library does not have suitable K4 V or K6 V standards. We derive extinctions (A_V) for GM Aur of 1.2 (K3) and 0.8 (K5) using U, B, V, R, I, J, H, and K photometry from Kenyon & Hartmann (1995) and 2MASS and correct the spectrum with these values and the Mathis dereddening law (Mathis, 1990).

As seen in LkCa 14 and DM Tau, GM Aur's K-band absorption lines are not veiled when compared to the K3 or K5 standards (Figure 7.11), but GM Aur does show an excess at 3– 5 μm when compared to each of the standard stars (Figures 7.12 and 7.13). The excess seen in GM Aur's SpeX spectrum could arise from the small dust within the hole of GM Aur which contributes to the excess emission above the photosphere seen in its SED from $\sim$ 3 – 8 μm (Figure 1.11; Calvet et al., 2005b). Calvet et al. (2005b) showed that this emission comes from optically thin submicron-sized dust located within the inner 5 AU of GM Aur's 20 AU hole. In the case of adopting a K3 or K5 spectral type we can fit the excess with blackbodies of $\sim$600 and 700 K respectively (Figures 7.12 and 7.13). These temperatures lie outside those typically assumed for the dust destruction temperature and may suggest there is some structure to the optically thin dust within GM Aur's hole, which is typically assumed to be uniform.

Alternatively, it is possible to fit GM Aur's excess with a single-temperature blackbody at a temperature corresponding to the dust destruction radius if we take $r_K = 0.1$. We note that GM Aur's SpeX spectrum (Figure 7.11) does not display the systematic veiling seen in UX Tau A (Figure 7.5) or LkCa 15 (Espaillat et al., 2007b). However, the typical errors for veiling measurements of this kind are $\pm$0.1

and so we explore the possibility that GM Aur has $r_K = 0.1$ in Figure 7.14. In this case, we can fit the excess with a blackbody of ∼1350 K which suggests that GM Aur has optically thick material located at the dust destruction radius, and that it could be a pre-transitional disk. However, we caution that a result from such a small veiling measurement is not conclusive.

7.4 Discussion & Conclusions

We presented veiling and near-infrared excess measurements for a diskless WTTS, transitional disks, and pre-transitional disks (Table 7.2). To date, the inner optically thick disks of both of the proposed pre-transitional disks of LkCa 15 and UX Tau A have been confirmed. We can fit their continua between 2–5 μm with single temperature blackbodies of 1600 K and 1350 K respectively. These blackbody temperatures indicate there is optically thick material located at the dust destruction radius in these disks. Muzerolle et al. (2003) fit the near-infrared excesses of nine classical T Tauri stars with blackbodies of temperatures ranging from 1200 to 1400 K. With a blackbody fit of 1350 K, UX Tau A falls within this range of temperatures. The blackbody fit to the excess of the pre-transitional disk LkCa 15 (1600 K) has a temperature higher than that found for the CTTS analyzed by Muzerolle et al. (2003), however, this temperature falls within the range of dust sublimation temperatures (1000–2000 K) found for a much larger sample of CTTS and Herbig Ae/Be stars by Monnier & Milan-Gabet (2002).

Here we also present spectra from 2–5 μm for the transitional disks DM Tau and GM Aur. DM Tau has an inner hole of 3 AU (Calvet et al., 2005b) which is relatively

cleared of small dust as indicated by the lack of near-infrared emission in its *Spitzer* IRS spectrum. However, it is still accreting and so we can infer that gas is located within the hole. In our SpeX spectra, we detect Pfγ and Brα emission which confirms accretion is still occurring in DM Tau (Muzerolle et al., 2001). In this object, we find no veiling in the K-band as well as no excess near-infrared emission, resembling what is seen in the diskless WTTS LkCa 14, indicating that the inner disk is relatively devoid of dust.

GM Aur has a 20 AU hole (Calvet et al., 2005b; Hughes et al., 2009) as well as a small excess above the photosphere in the near-infrared, as measured in its *Spitzer* IRS spectrum, which has been interpreted as originating in optically thin dust located within the disk hole (Calvet et al., 2005b). GM Aur is also accreting as can be seen from its strong Pfγ and Brα emission in our SpeX spectrum. Here we measure a veiling factor of 0$\pm$0.1 for GM Aur. Previously, Folha & Emerson (1999) measured a veiling of 0.3$\pm$0.2 for GM Aur in the K-band with a spectral standard of K7. Taking into account that absorption lines tend to be deeper in later spectral types, this is likely to be an overestimate of the veiling. With our measured r_K of 0, GM Aur has a small near-infrared excess that can be fit by a blackbody of $\sim$700 K. This does not fall within the range of typical dust destruction temperatures and suggests GM Aur's optically thin region may have some structure within it. If we adopt an r_K of 0.1 for GM Aur, which is within the veiling measurement errors, we can fit its near-infrared emission with a blackbody of $\sim$1350 K. This may open the possibility that GM Aur is actually a pre-transitional disk, resembling that of LkCa 15, however, the lack of systematic veiling in the K-band supports that there is no

veiling in GM Aur. Veiling derived from higher resolution spectra using appropriate spectral standards are necessary to ascertain if there is actually veiling in GM Aur in the K-band.

In conclusion, we confirm that the inner disk of UX Tau A is optically thick and that it is a pre-transitional disk. Its near-infrared emission differs significantly from that of the transitional disk of DM Tau which resembles the diskless star LkCa 14 in the near-IR. Our results call the nature of GM Aur into question and high-resolution spectra are needed to settle this issue.

Table 7.1. Log of SpeX Observations

Target	K_s[1]	Date	Exposure (s)	SNR[2]
LkCa 14	8.6	2009 Feb 18	1800	270
DM Tau	9.5	2009 Feb 16	2400	170
GM Aur	8.3	2009 Feb 14	1800	100
UX Tau A	7.6	2009 Feb 14	1800	230

[1]2MASS Point Source Catalog

[2]Measured at $\sim$2.2μm.

Table 7.2. Characteristics of SpeX Sample

Target	Spectral Type	A_V	r_K	Blackbody Temperature of Excess Emission(K)
LkCa 14	K5.5	0	0	...
DM Tau	M1.5	0.4	0	...
GM Aur	K5.5	0.8	0	700
LkCa 15	K5[1]	1.2[2]	0.3[3]	1600[3]
UX Tau A	G6	1.8	0.3	1350

[1]LkCa 15 has a spectral type of K5$\pm$1.0 as measured by both Herbig (1977) and this work.

[2]Value from Espaillat et al. (2007b).

[3]Value Espaillat et al. (2008a).

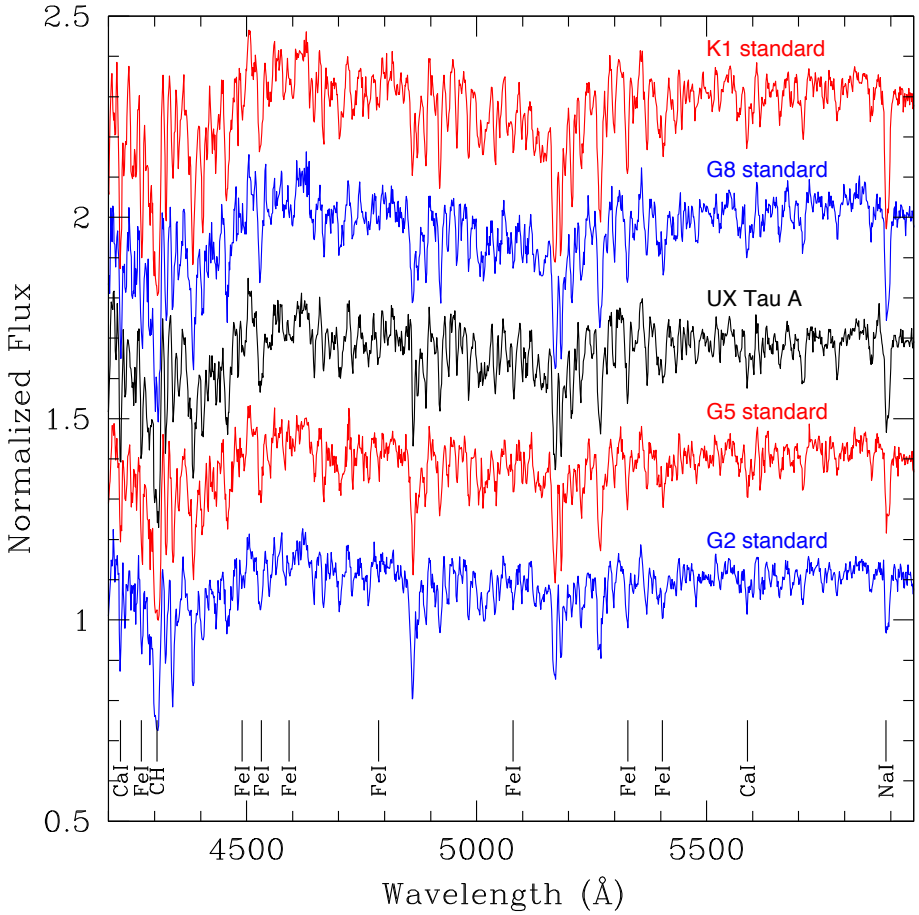

Figure 7.1 FAST spectrum of UX Tau A compared to spectral type standards. Based on these data, we measure a spectral type of G6.5±1 for UX Tau A. Some of the features used for spectral classification are marked.

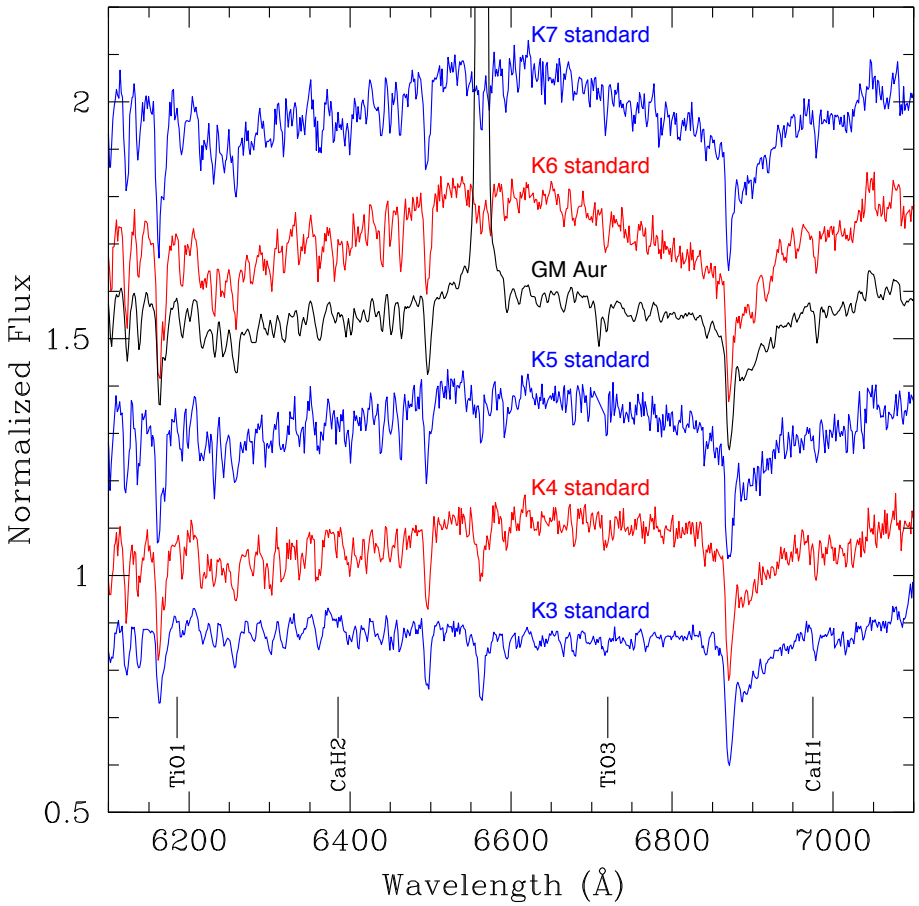

Figure 7.2 FAST spectrum of GM Aur compared to spectral type standards. Based on these spectra, we measure a spectral type of K5.5±1 for GM Aur. Some of the features used for spectral classification are marked.

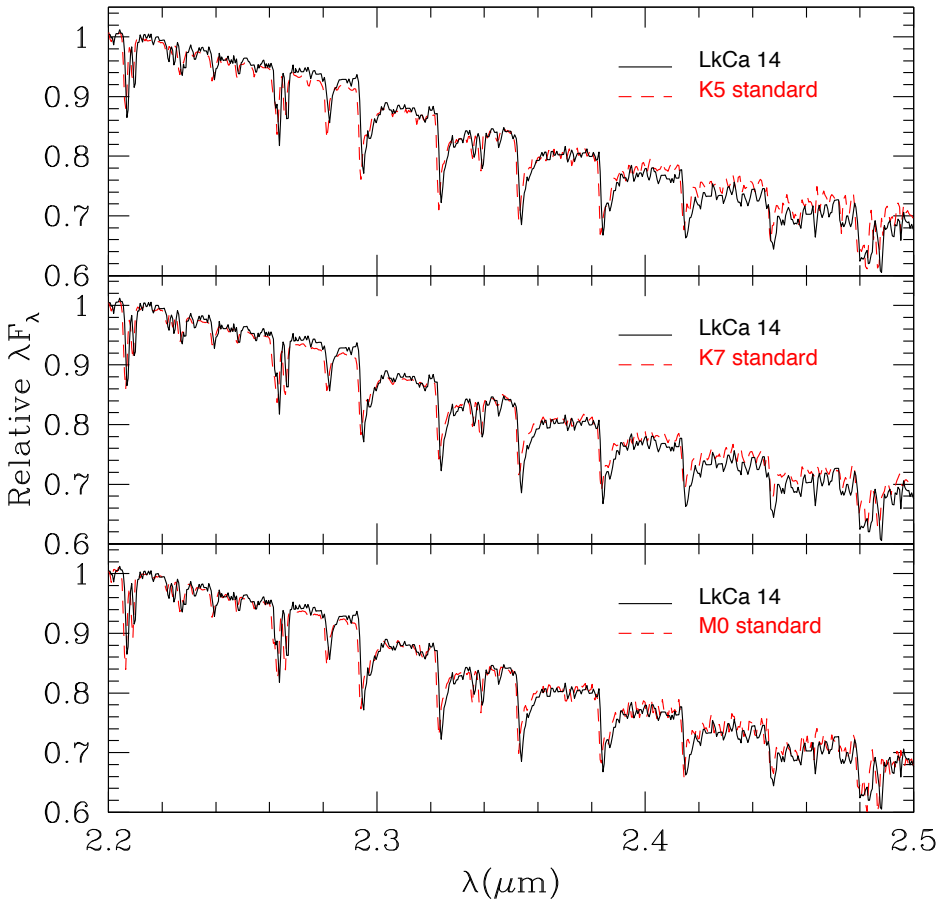

Figure 7.3 K-band SpeX spectrum of the diskless T Tauri star LkCa 14 compared to dwarf standard stars. We compare the spectrum of LkCa 14 (solid line) to standards with spectral types of K5, K7, and M0 (broken lines). LkCa 14 has absorption lines that are not substantially veiled relative to the standard stars and in each case we derive a veiling value (r_K) of 0 for LkCa 14. This indicates that K-band spectra of dwarfs are good templates for the photospheres of young stars with spectral types of late K to early M.

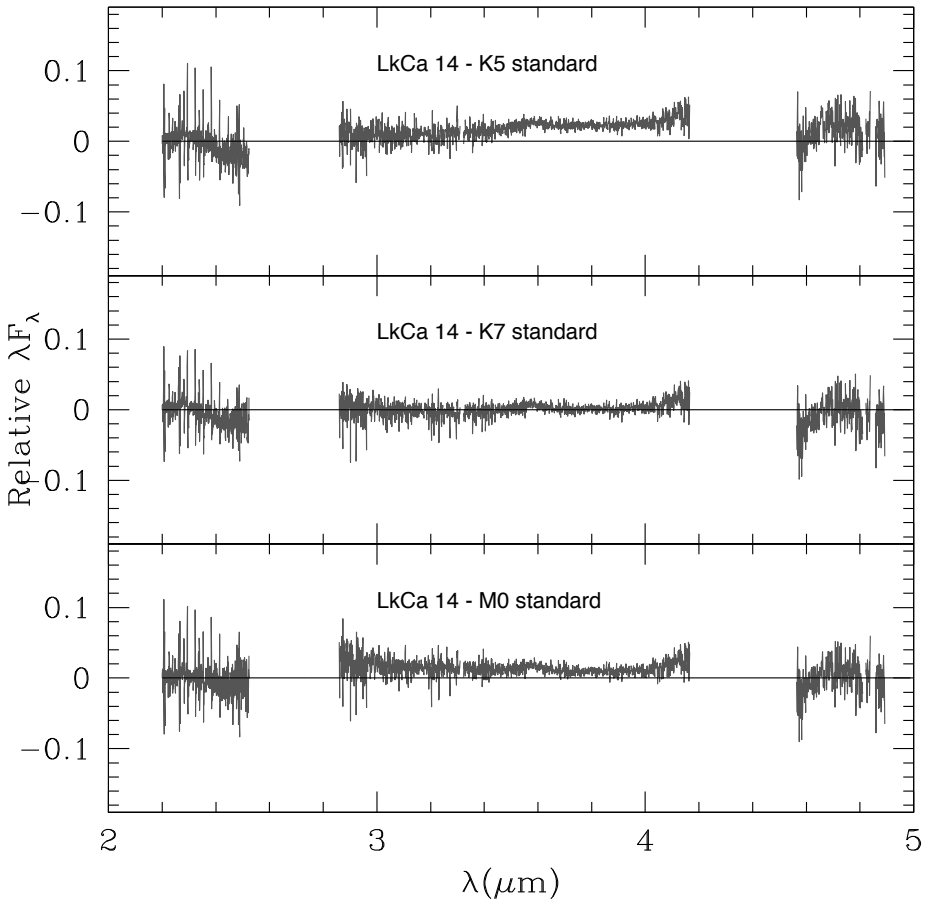

Figure 7.4 Near-infrared excess emission of LkCa 14 relative to standard stars. After scaling the target spectrum by $1 + r_K$ and subtracting the standard stars at K5, K7, and M0, we find that there is no excess emission above the photosphere of LkCa 14 (gray). The heavy line in each panel corresponds to zero excess. The small excess between ~ 3.5 and 4.2 μm in the top panel is likely due to spectral slope errors.

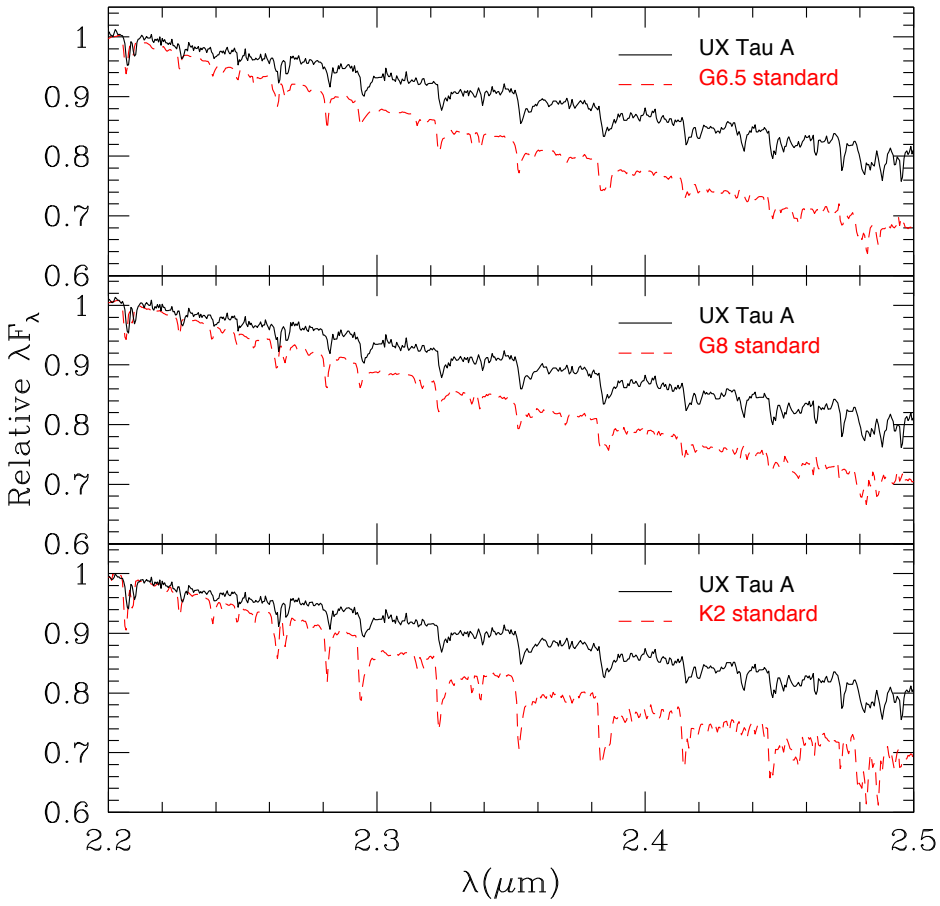

Figure 7.5 K-band SpeX spectrum of UX Tau A compared to dwarf standard stars. We compare the spectrum of UX Tau A (solid line) to standards with spectral types of G6.5, G8, and K2 (broken lines) after scaling the target to the standard at 2.2μm. The spectrum of UX Tau A has absorption lines that are weaker relative to the spectrum of the standard stars and we derive r_K=0.3 (G6.5), r_K=0.4 (G8), and r_K=1.0 (K2) at $\sim$ 2.2 μm.

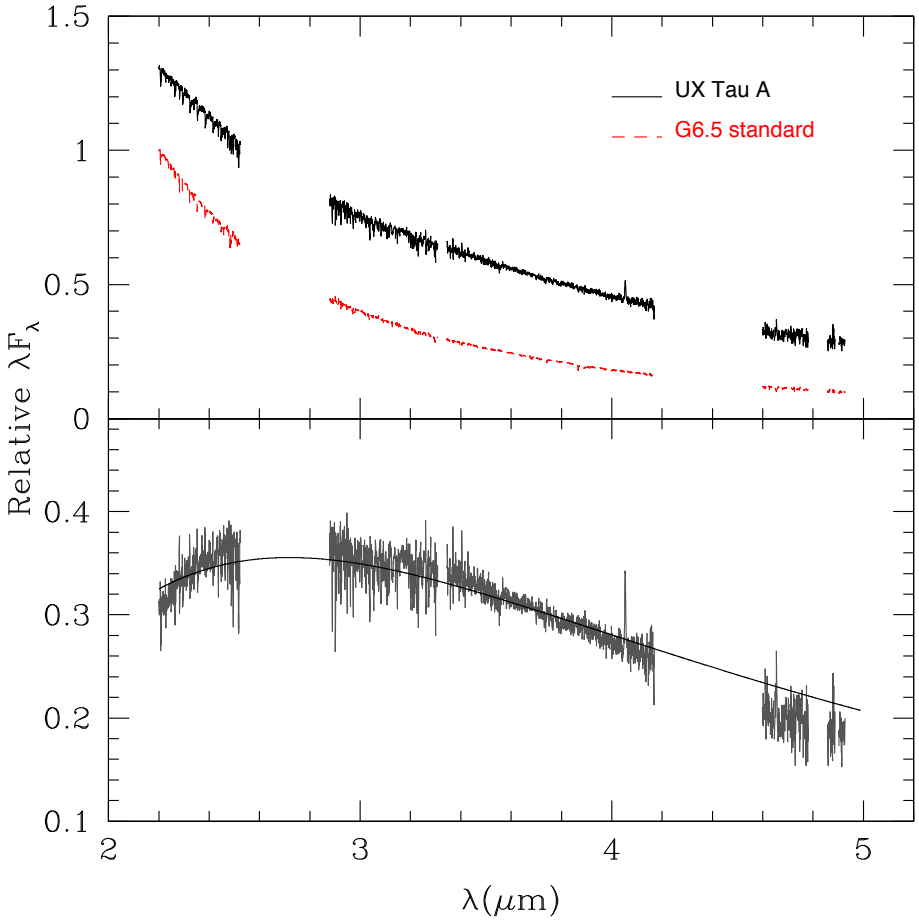

Figure 7.6 Near-infrared excess emission of UX Tau A relative to a G6.5 standard. After normalizing the target to the standard star's flux at 2.2 μm and then scaling the target by $1 + r_K$, we subtracted the standard star (top, light line) from the veiling-scaled (r_K=0.3) target spectrum (top, black line) to extract the shape of the excess emission above the photosphere (bottom, gray). The near-infrared excess of UX Tau A can be fit by a single-temperature blackbody of ∼1350 K (bottom, solid black line). The emission feature at $\sim$ 4 μm is Brα.

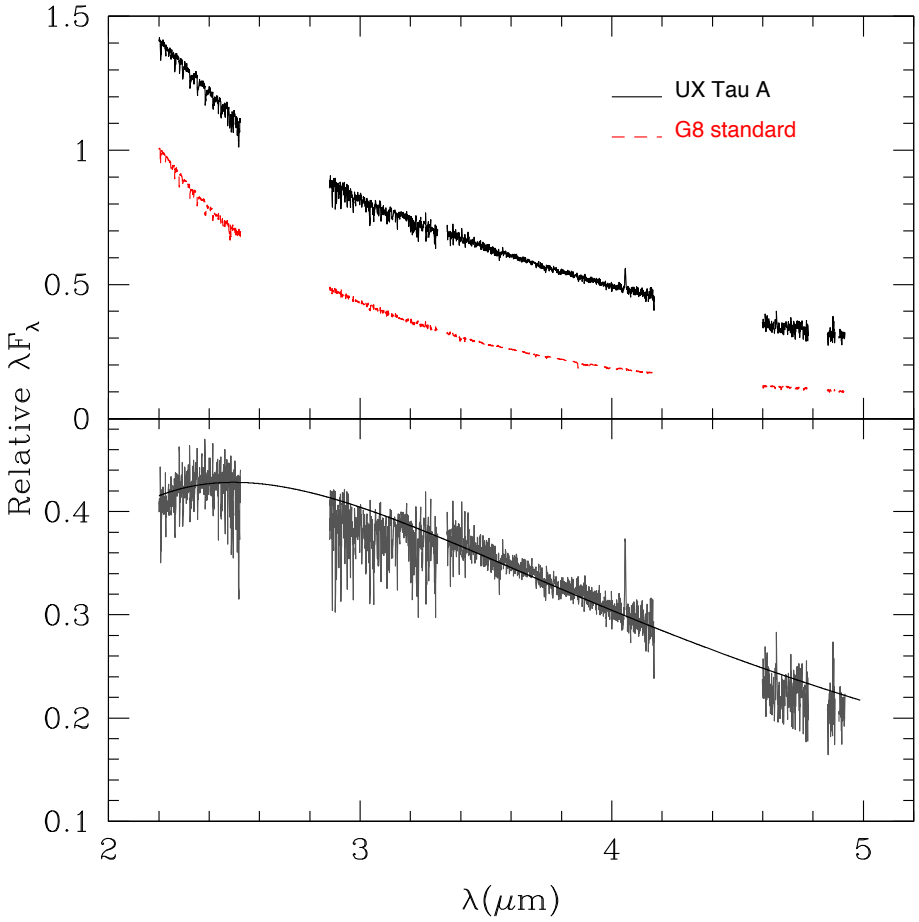

Figure 7.7 Near-infrared excess emission of UX Tau A relative to a G8 standard. We subtracted the standard star (top, light line) from the veiling-scaled (r_K=0.4) target spectrum (top, black line) to extract the shape of the excess emission above the photosphere (bottom, gray). The near-infrared excess of UX Tau A can be fit by a single-temperature blackbody of ∼1500 K (bottom, solid black line). The emission feature at ~ 4 μm is Brα.

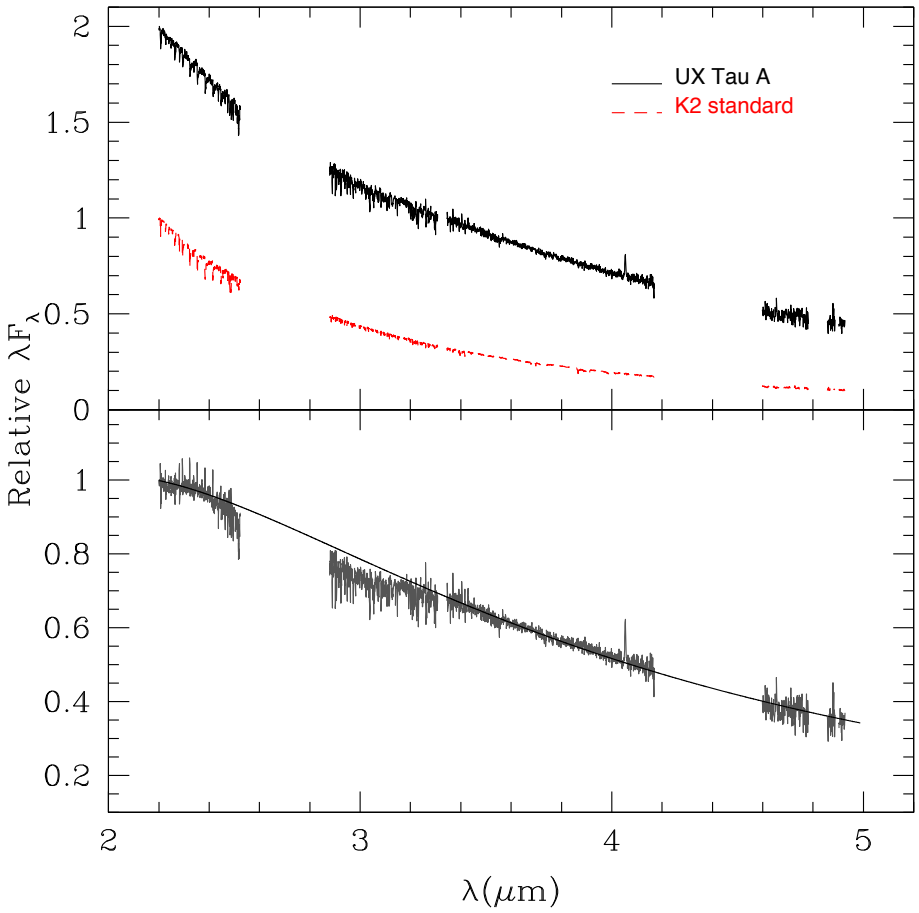

Figure 7.8 Near-infrared excess emission of UX Tau A relative to a K2 standard. We subtracted the standard star (top, light line) from the veiling-scaled (r_K=1.0) target spectrum (top, black line) to extract the shape of the excess emission above the photosphere (bottom, gray). The near-infrared excess of UX Tau A can be fit by a single-temperature blackbody of 1800 K (bottom, solid black line). The emission feature at ~ 4 μm is Brα.

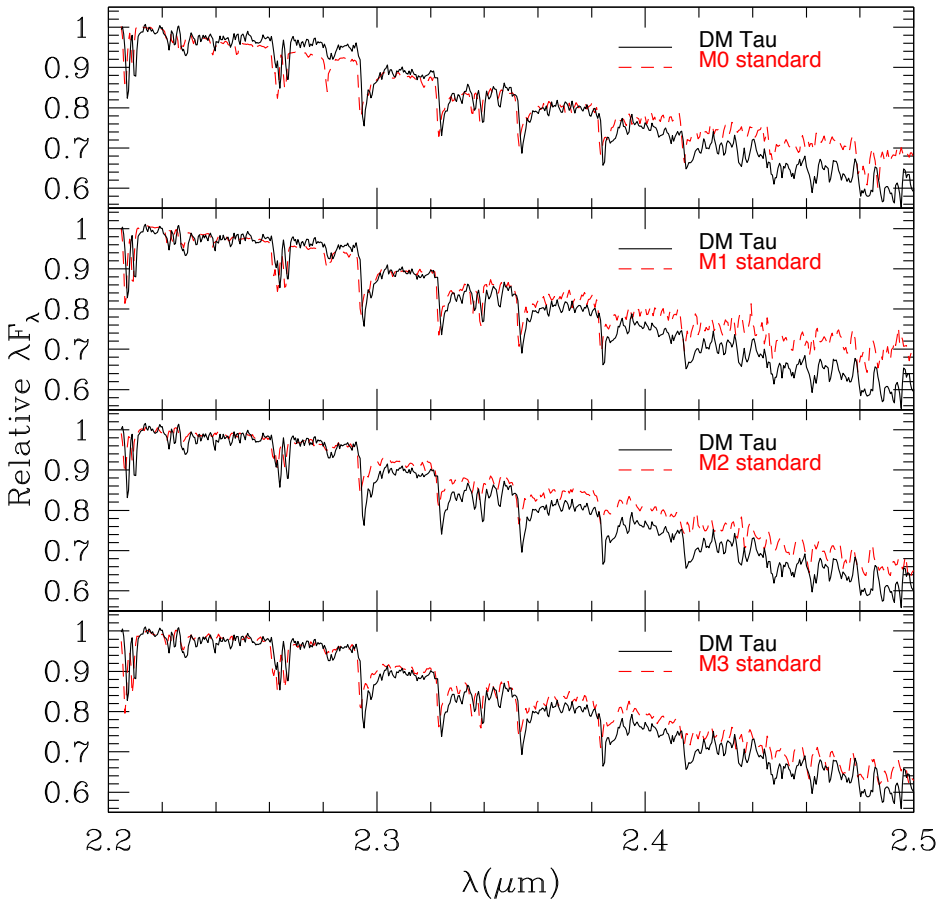

Figure 7.9 K-band SpeX spectrum of the DM Tau compared to dwarf standard stars. We compare the spectrum of DM Tau (solid line) to standards with spectral types of M0, M1, M2, and M3 (broken lines) after scaling the target to the standard at 2.2μm. DM Tau has absorption lines that are not veiled relative to the standard stars and in each case we derive r_K=0 for DM Tau.

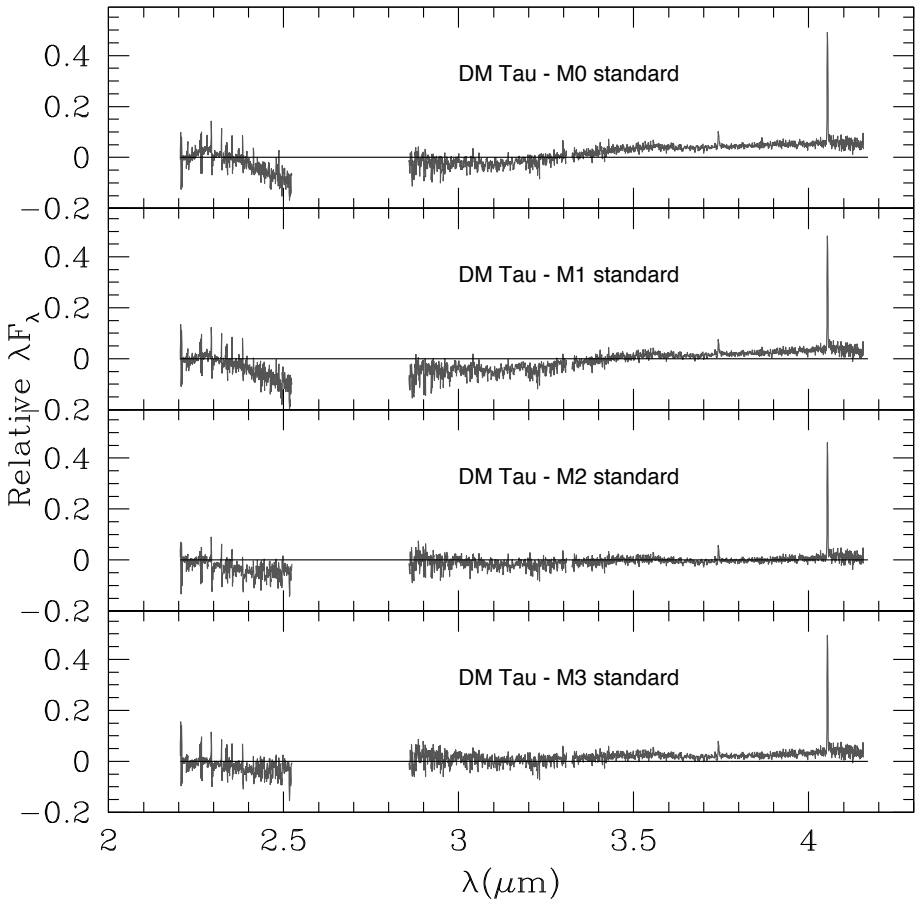

Figure 7.10 Near-infrared excess emission of DM Tau relative to standard stars. After normalizing the target to the standard star's flux at 2.2 μm and then scaling the target by $1 + r_K$, we extracted the excess emission above the photosphere of DM Tau (gray), by subtracting standard stars with spectral types of M0, M1, M2, and M3 from the veiling-scaled target spectrum. Note that DM Tau was too faint to extract any data at wavelengths greater than ~ 4.2 μm. The heavy lines correspond to zero excess. The emission features at ~ 3.8 μm and ~ 4 μm are Pfγ and Brα respectively.

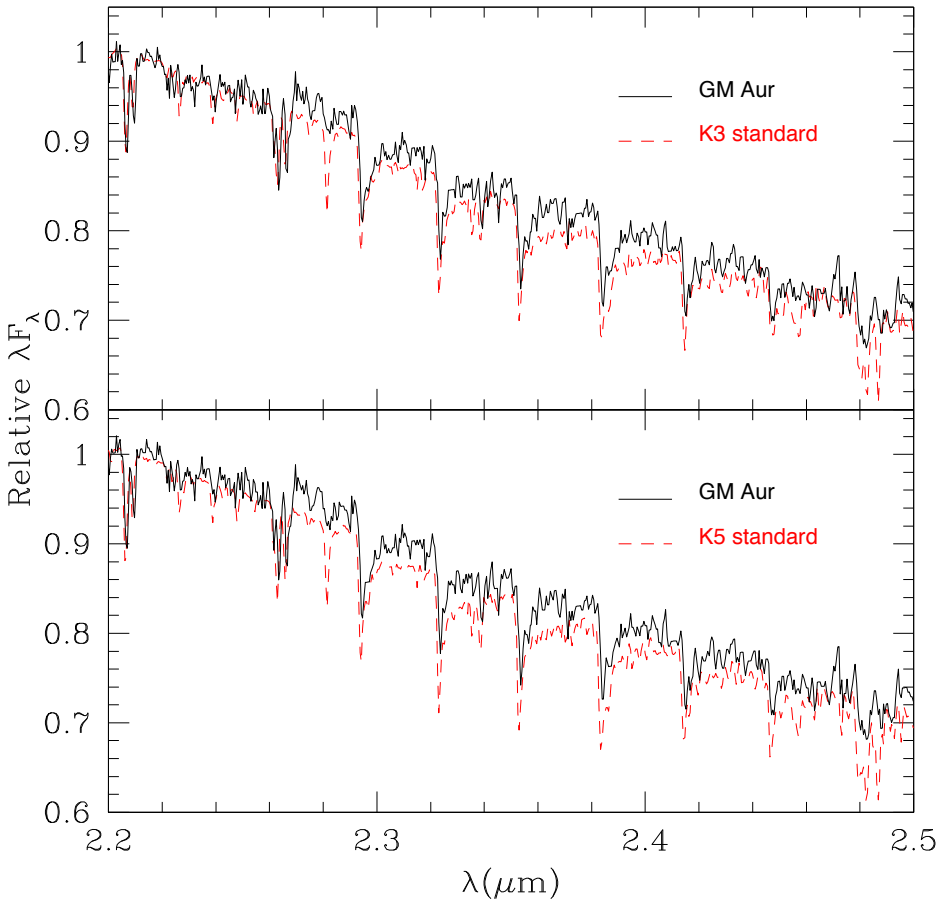

Figure 7.11 K-band SpeX spectrum of GM Aur compared to dwarf standard stars. We compare the spectrum of GM Aur (solid line) to standards with spectral types of K3 and K5 (broken lines) after scaling the target to the standard at 2.2μm. GM Aur has absorption lines that are not substantially veiled relative to the standards (r_K=0.0).

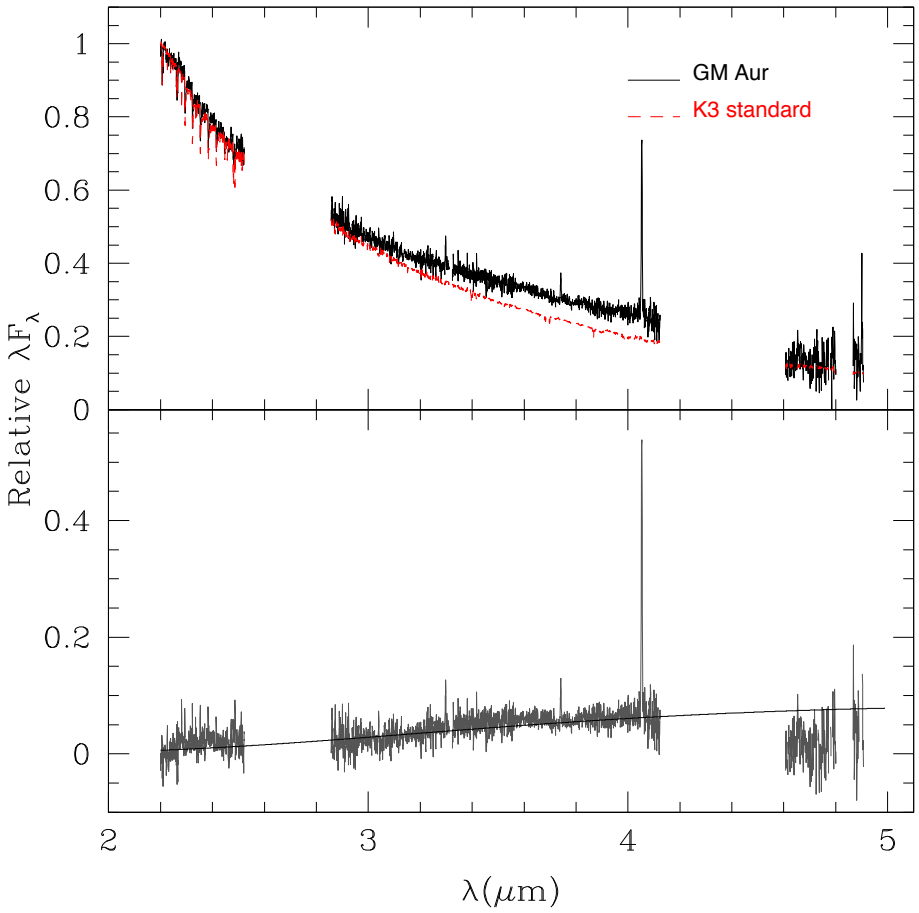

Figure 7.12 Near-infrared excess emission of GM Aur relative to a K3 standard. After normalizing the target to the standard star's flux at 2.2 μm and then scaling the target by $1+r_K$, we subtracted the standard star (top, light line) from the veiling-scaled target spectrum (top, black line) and find that there is an excess above the photosphere (bottom, gray) which can be fit by a ∼600 K blackbody (bottom, heavy line). The emission features at $\sim$ 3.8 μm and $\sim$ 4 μm are Pfγ and Brα respectively.

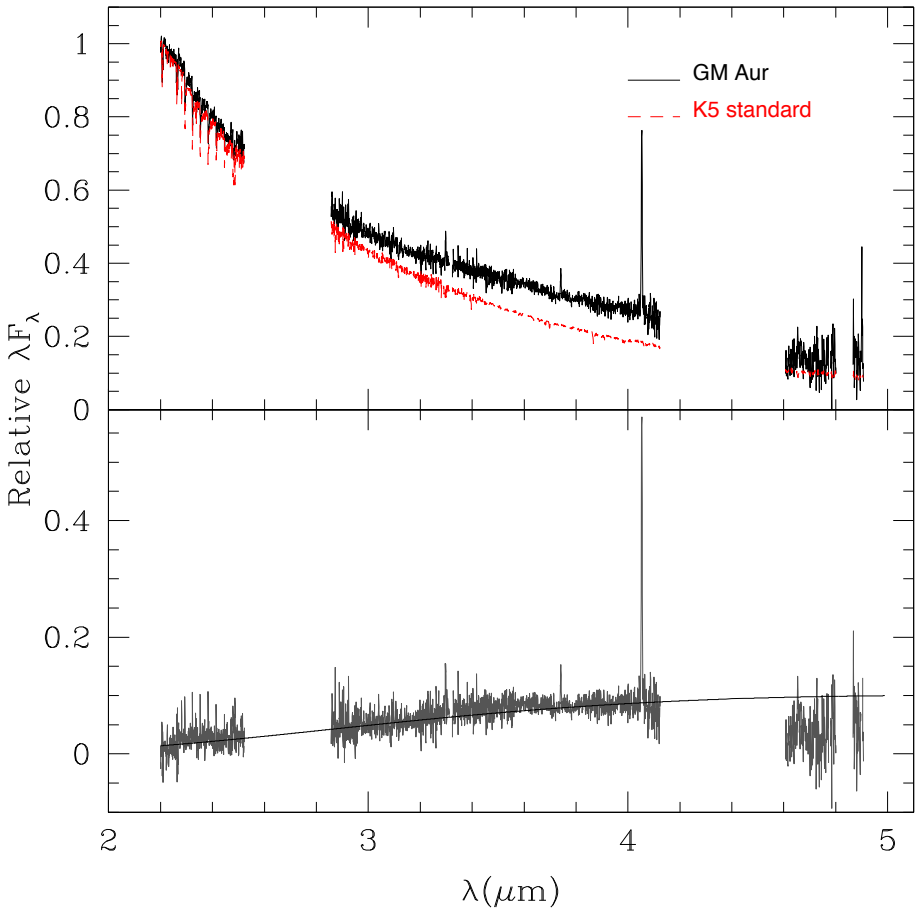

Figure 7.13 Near-infrared excess emission of GM Aur relative to a K5 standard with r_K=0. We subtracted the standard star (top, light line) from the veiling-scaled target spectrum (top, black line) and find that there is an excess above the photosphere (bottom, gray). The heavy line (bottom) corresponds to a blackbody of ∼700 K. The emission features at $\sim$ 3.8 μm and $\sim$ 4 μm are Pfγ and Brα respectively.

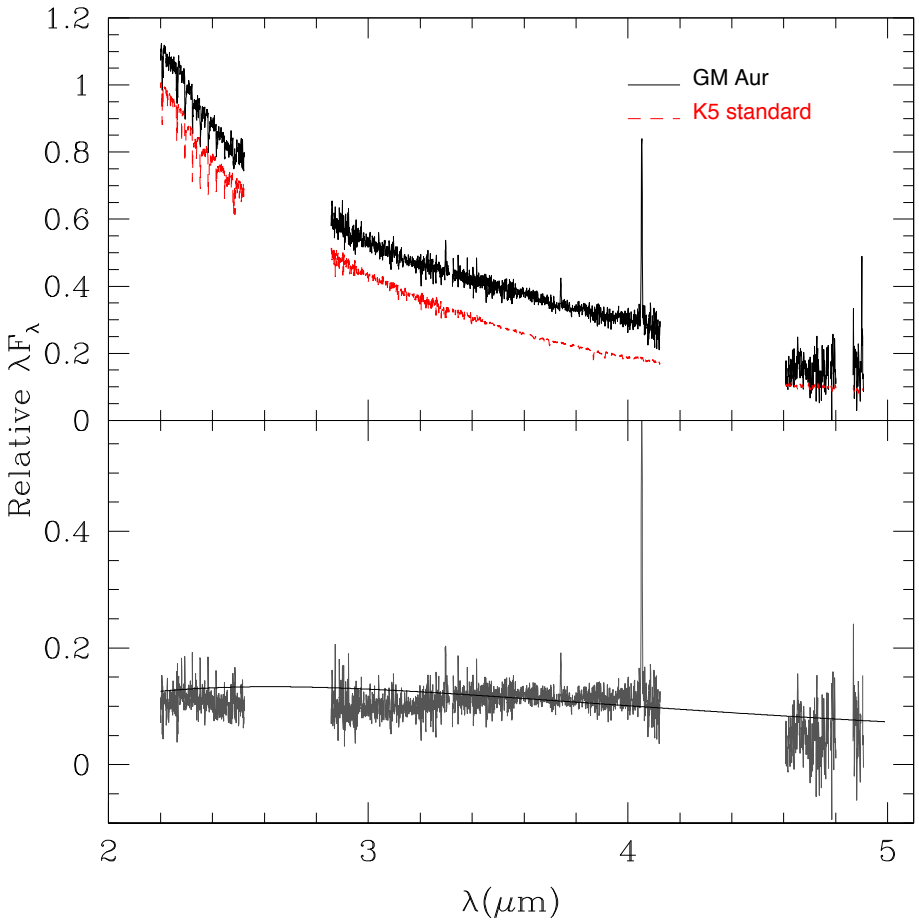

Figure 7.14 Near-infrared excess emission of GM Aur relative to a K5 standard with r_K=0.1. We subtracted the standard star (top, light line) from the veiling-scaled target spectrum (top, black line) and find that there is an excess above the photosphere (bottom, gray). The heavy line (bottom) corresponds to a blackbody of ∼1350 K. The emission features at ∼ 3.8 μm and ∼ 4 μm are Pfγ and Brα respectively.

Chapter 8

Summary & Conclusions

In this thesis we showed that most disks in Taurus, Chamaeleon, and Ophiuchus can be explained by full disk models. However, there a few disks which have gaps and holes in their dust distributions and here we modeled the disk structure of a handful of these pre-transitional disks and transitional disks. We also found that some disks cannot be explained by the full disk models and are not known to be transitional or pre-transitional disks. We proposed that these objects are pre-transitional disks with smaller gaps than previously observed and are in the early stages of gap opening. Our findings indicate that an extensive and detailed modeling survey of disks around young stars would be fruitful and is needed to provide significant constraints on grain growth, settling, and clearing in young disks to aid in theoretical models of dust evolution and planet formation.

8.1 The Transitional Disks

With *Spitzer* IRS spectra, we have been able to study in great detail several "transitional disks" which have nearly photospheric near-infrared emission but substantial excesses at mid-infrared wavelengths and beyond as is seen in full disks. Sophisticated disk models have shown that this flux deficit at near-infrared wavelengths

can be explained by optically thick disks with an inner hole (Calvet et al., 2005b; D'Alessio et al., 2005; Espaillat et al., 2007a, 2008b). Most of these inner holes are not completely empty and contain a small amount of small optically thin dust (e.g. GM Aur, TW Hya, CS Cha, CVSO 224).

In Chapter 3, we modeled the disk of the ∼2 Myr old CS Cha with an inner hole of ∼46 AU which contained small optically thin dust (Espaillat et al., 2007a). We found that this optically thin dust has grown to much larger sizes (2μm) than the ISM-sized dust within the inner holes of the younger ∼1 Myr old transitional disks in Taurus. However, larger grains are also seen in the holes of the 10 Myr old TW Hya (Calvet et al., 2002) and CVSO 224 (Espaillat et al., 2008b) and so there may be a correlation between the process that creates the optically thin dust found within inner disk holes and dust evolution. CS Cha also needs a more settled outer disk to fit its far-infrared and millimeter data.

We also detected the slowest accreting transitional disk found to date, CVSO 224 in the ∼10 Myr old 25 Orionis group in Orion OB1a (Chapter 4; Espaillat et al., 2008b). CVSO 224 provides a unique opportunity to explore the role of photoevaporation in transitional disks. While hydrodynamical simulations have shown that a newly formed planet could accrete and sweep out the material around it through tidal disturbances (Rice et al., 2006), photoevaporation has been proposed as an alternate formation mechanism for the holes observed in transitional disks. A photoevaporative wind can halt mass accretion towards the inner disk allowing material in this inner disk to be rapidly evacuated creating an inner hole (Clarke et al., 2001); the hole then increases in size as the edge continues photoevaporating (Alexander &

Armitage, 2007). However, the mass accretion rates and disk masses of GM Aur, DM Tau, CS Cha, and TW Hya are too high for photoevaporation to occur. CVSO 224's low $\dot{M}$ is in line with photoevaporative clearing theories (Alexander & Armitage, 2007). However, CVSO 224 exhibits substantial emission between $\sim$20 – 40 μm in its *Spitzer* IRS spectrum. This is evidence for a substantial outer disk in this object, indicating that the disk is not being photoevaporated. This discrepancy could be explained if the mass accretion rate of the outer disk is actually higher than what we are measuring at the star which is possible if a planet is within CVSO 224's hole and is sharing the mass accretion flow with the star (Lubow & D'Angelo, 2006). Follow-up millimeter studies are needed to confirm that the outer disk of CVSO 224 is massive in order to further support this idea.

8.2 The Pre-Transitional Disks

We have recently identified a new class of "pre-transitional disks" around the stars UX Tau A and LkCa 15 in the Taurus cloud (Chapter 5; Espaillat et al., 2007b). These pre-transitional disks have a deficit of mid-infrared flux (5 – 20 μm) and substantial emission beyond 20 μm as is seen in the transitional disks, however, in contrast to the small near-infrared excess exhibited by some transitional disks, pre-transitional disks have significant near-infrared excesses (2 – 5 μm). These excesses are comparable to the median SED of T Tauri disks in Taurus which is representative of an optically thick full disk (D'Alessio et al., 1999). This indicates that the pre-transitional disks have an optically thick inner disk and that we are seeing the development of gaps within protoplanetary disks. UX Tau A has a 56 AU gap that is relatively empty of

small grains while LkCa 15's 46 AU gap has a small amount of optically thin dust within the inner 5 AU of the gap. The existence of an inner optically thick disk may be an indicator of the first stages of disk clearing that will eventually lead to the the inner holes that are seen in transitional disks.

We presented the first independent confirmation of a gap in a protoplanetary disk (Chapter 6; Espaillat et al., 2008a). We obtained a medium resolution near-infrared SpeX spectrum spanning the wavelength range 2-5 μm (Espaillat et al., 2008b) and fit the near-IR excess of LkCa 15 with a single-temperature blackbody of 1600 K, such as is seen in full disks (Muzerolle et al., 2003), indicating that the near-infrared excess of LkCa 15 originates from the wall of an optically thick inner disk at the dust destruction radius. In addition, we confirmed the gap in the pre-transitional disk of UX Tau A (Chapter 7). Its near-infrared excess between 2–5 μm could be fit with a single-temperature blackbody of 1500 K.

The gaps detected in UX Tau A and LkCa 15 are large ($\sim$46–56 AU) and pre-transitional disks with smaller gaps have not yet been detected. In Chapter 2, we presented a first attempt at describing the overall qualities of disks in Taurus (Furlan et al. submitted), Chamaeleon (Manoj et al. in prep), and Ophiuchus (McClure et al. in prep) by creating a grid of $\sim$240 disks with the models of D'Alessio et al. (2006). This grid was calculated for stellar masses of 0.2 $M_\odot$ and 0.5 $M_\odot$, mass accretion rates of 10^{-7} – 10^{-10} $M_\odot$ yr^{-1}, inclinations spanning $\sim$ 0 to $\sim$90°, an α parameter of 0.01, settling parameters of 1, 0.1, 0.01, and 0.001, different dust compositions, and various maximum grain sizes in the upper disk layers. Individual fits to SEDs were not done. We used the grid to measure the slope of the SED between 13 μm

and 31 μm versus the equivalent width of the 10 μm silicate feature. Aside from the well-known transitional and pre-transitional disks, most of the disks can be explained by typical "full" disk models. However, there is a subset of $\sim$30 disks which show stronger silicate emission than can be explained by the full disk models. We show that this extra emission cannot be accounted for with smaller grains in the upper disk layers or a different dust composition. We propose that these objects are pre-transitional disks with small gaps (<20 AU) where the extra silicate emission comes from optically thin small dust located within these disk gaps. Detailed modeling and millimeter imaging is needed to explore this possibility.

8.3 Neon Gas in the Planet-Forming Regions of T Tauri Disks

Significant gas must be present for giant planets to form and the lifetime of the gas in the inner disk places an upper limit on the timescale for giant planet formation. A new gas diagnostic has emerged in the mid-infrared with the detection of [Ne II] emission with *Spitzer*. [Ne II] emission has been detected from a few disks that were observed as part of the FEPS Legacy program (Pascucci et al., 2007) and the C2D program (Lahuis et al., 2007) as well as in the transitional disks CS Cha, DM Tau, and TW Hya in our GTO IRS Disks program (Espaillat et al., 2007a).

In Espaillat et al. (2007a), we found that there was no apparent correlation between $L_{[NeII]}$ and L_X as would be expected from the X-ray heating model of Glassgold et al. (2007) which has been proposed to explain this [Ne II] emission. However, these measurements were based on non-simultaneous data and X-ray emission is known to

be variable (Feigelson et al., 2007; Güdel et al., 2007). Therefore, a correlation between $L_{[NeII]}$ and L_X may have been missed. We did find a possible correlation between $L_{[NeII]}$ and $\dot{M}$ which suggests that accretion related EUV heating may play a substantial role in producing [Ne II] emission. Measurements of $L_{[NeII]}$, L_X, and L_{acc} in a larger sample of disks are required to test these proposed correlations.

8.4 Comparing Pre-Transitional and Transitional Disk Observations with Planet Formation Theories

There are two leading theories of planet formation: the core nucleated accretion model and the gas instability model. According to the core nucleated accretion model (Pollack et al., 1996; Bodenheimer et al., 2000), dust grains will grow into planetesimals which will accrete other planetesimals and then form solid cores. These cores can become terrestrial planets or, if the cores are massive enough, gas giant cores which can accrete the surrounding gas in the disk (Pollack et al., 1996; Bodenheimer et al., 2000). The core accretion model can account for both terrestrial planets and gas giants. For several years it was thought that the formation time for Jupiter-mass planets via core accretion was longer than the lifetime of disks. However, Hubickyj et al. (2005) show that by adopting low dust opacities the core's envelope is smaller and can therefore accrete faster. A Jupiter-mass planet with a core of 10 Earth-masses can form at 5 AU in 1 Myr and in 5 Myr with a core of 5 Earth-masses (Hubickyj et al., 2005), about half the time predicted by models using higher dust opacities (for a review see Lissauer & Stevenson, 2007). In the gas instability model (Boss, 2000; Mayer et al., 2002; Durisen et al., 2007), fragmentation due to gravita-

tional instabilities in the dense dust midplane (Goldreich & Ward, 1973) can form Jupiter-mass clumps in the outer disk (Boss, 2000; Mayer et al., 2002). The gas instability model can create Jupiter-mass gas giants within a few hundred years (Boss, 2000), but this model cannot explain the formation of lower mass ice giants like Neptune or terrestrial planets. Since the core nucleated accretion model can account for low–mass planets, it is currently the favored planet formation mechanism; however, hybrid scenarios incorporating core accretion and gas instability are possible.

To date, over one hundred Jupiter-mass planets have been detected (Butler et al., 2006). About eleven Neptune-mass planets have also been discovered (Santos et al., 2004; McArthur et al., 2004; Butler et al., 2004; Vogt et al., 2005; Rivera et al., 2005; Bonfils et al., 2005; Udry et al., 2006; Sousa et al., 2008; Bonfils et al., 2007; Melo et al., 2007; Endl et al., 2008) and as the precision of radial velocity measurements improves, this number is expected to increase. Neptune-mass planets may be the result of failed core accretion, when the gas in the disk dissipated before the core could accrete enough gas to form a Jupiter-mass planet. Such a situation is plausible given that observational results find that disks begin to dissipate as early as 1 Myr (Hernández et al., 2007), but core accretion requires 1–5 Myr to form Jupiter mass planets.

The detection of transitional and pre-transitional disks in young star–forming regions seems to support the core accretion model. To clear out the relatively large gaps and holes that have been detected, it is likely that more than one planet is present in the inner disks of these objects. Since Jupiter-mass planets form within 1–5 Myr, it is plausible that the transitional and pre-transitional disks detected

in the ∼1–3 Myr old Taurus cloud (Hartmann, 2003) contain Jupiter-mass planets. However, a typical disk will have a Jupiter mass (10^{-3} $M_{\odot}$) at 6 AU and a Saturn mass at 3 AU (see Figure 2.3). Therefore, it is unlikely that there would be several Jupiter-mass planets clearing the gaps and holes we have detected. Instead, these disks could also contain sub-Jupiter mass planets. The vast majority of transitional and pre-transitional disks are still accreting material onto the star (see Table 1.1), indicating that gas is still present within the inner disk. As a result, planets within gaps and holes can still be accreting gas and growing in mass (Artymowicz & Lubow, 1996). Therefore, most transitional and pre-transitional disks have enough mass within their cleared regions to have formed multiple planets *in situ* and planet formation may still be underway.

If the transitional and pre-transitional disks are a result of core accretion, then this implies that we have yet to detect the smaller gaps which would indicate that planet formation has just begun. In Chapter 2, we presented evidence based on *Spitzer* IRS spectra for pre-transitional disks with small gaps that were filled with optically thin dust. These disks could be the missing link in the evolution of planet formation.

8.5 Directions for the Future

Given the importance of dust in disks and that dust is more easily observed than gas at most wavelengths, the fact that so many questions remain regarding how dust initially evolves into a planet and the planet's ensuing effect on the dust calls for a detailed study of dust evolution in young disks. The best targets on which to

undertake such a study are the disks around the low–mass pre–main sequence stars in the star–forming clouds of Taurus, Chamaeleon, and Ophiuchus.

As we reviewed in Section 1.1, the first steps in making a planet are the growth of grains and subsequent settling to the midplane. However, theory predicts that grains with sizes up to 100 μm will be severely depleted within 10^4 years (Dullemond & Dominik, 2004, 2005) which is in stark contrast to *Spitzer* observations which reveal substantial infrared excesses and ubiquitous silicate emission from 1 Myr old disks (Furlan et al., 2006). One should explore why almost none of the predicted SEDs match the actual observations by taking a closer look at the amount of grain growth and settling in these star–forming regions. In this thesis we find a range of grain sizes and settling parameters amongst transitional disks. These results are promising and call for larger, more detailed studies. We are developing the next generation of the D'Alessio model, which will relax the assumption that the degree of depletion throughout the disk is constant in order to explore how dust settling varies throughout disks. A self-consistent analysis of SEDs and spatial brightness distributions with these models can provide a direct quantification of the degree of grain growth and the radial and vertical distribution of dust throughout the disk, providing essential constraints to dust evolution models.

Currently, we have only detected large gaps of $\sim$50 AU (Espaillat et al., 2007b) and the smaller gaps expected during the initial stages of planet formation have yet to be found. However, there exists an unstudied subset of disks which we propose are pre-transitional disks with small gaps (<10 AU; Section 2.5). These disks have more silicate emission than a full disk, pointing to the existence of gaps in the optically

thick disks of these "outliers" that are filled will small optically thin dust from which the extra emission arises. Using the D'Alessio model in conjunction with SEDs and spatial brightness distributions obtained with the *SMA* and *ALMA*, one can constrain the grain growth and settling of these pre-transitional disks as well as the sizes of their gaps. The dust evolution in pre-transitional disks can then be compared to that of full disks. If planets are clearing these gaps, then the dust evolution in pre-transitional disks should be more advanced relative to the full disks since significant dust evolution is needed to create planets.

Systematic, semi-empirical evidence will provide needed insight and constraints to aid in theoretical modeling of dust evolution and planet formation, bringing us a few steps closer to understanding the origin of our own solar system.

References

Aikawa, Y., & Nomura, H. 2006, *ApJ*, 642, 1152

Alencar, S. H. P., & Batalha, C. 2002, *ApJ*, 571, 378

Alexander, R. D., & Armitage, P. J. 2007, *MNRAS*, 375, 500

Andrews, S. M., & Williams, J. P. 2005, *ApJ*, 631, 1134

Artymowicz, P., & Lubow, S. H. 1994, *ApJ*, 421, 651

—. 1996, *ApJ*, 467, L77+

Baraffe, I., Chabrier, G., Allard, F., & Hauschildt, P. H. 2002, *A&A*, 382, 563

Barrado y Navascués, D., & Martín, E. L. 2003, *AJ*, 126, 2997

Batalha, C., Batalha, N. M., Alencar, S. H. P., Lopes, D. F., & Duarte, E. S. 2002, *ApJ*, 580, 343

Bergin, E., Calvet, N., Sitko, M. L., Abgrall, H., D'Alessio, P., Herczeg, G. J., Roueff, E., Qi, C., Lynch, D. K., Russell, R. W., Brafford, S. M., & Perry, R. B. 2004, *ApJ*, 614, L133

Bockelée-Morvan, D., Gautier, D., Hersant, F., Huré, J.-M., & Robert, F. 2002, *A&A*, 384, 1107

Bodenheimer, P., Hubickyj, O., & Lissauer, J. J. 2000, Icarus, 143, 2

Bonfils, X., Forveille, T., Delfosse, X., Udry, S., Mayor, M., Perrier, C., Bouchy, F., Pepe, F., Queloz, D., & Bertaux, J.-L. 2005, *A&A*, 443, L15

Bonfils, X., Mayor, M., Delfosse, X., Forveille, T., Gillon, M., Perrier, C., Udry, S., Bouchy, F., Lovis, C., Pepe, F., Queloz, D., Santos, N. C., & Bertaux, J.-L. 2007, *A&A*, 474, 293

Bontemps, S., André, P., Kaas, A. A., Nordh, L., Olofsson, G., Huldtgren, M., Abergel, A., Blommaert, J., Boulanger, F., Burgdorf, M., Cesarsky, C. J., Ce-

sarsky, D., Copet, E., Davies, J., Falgarone, E., Lagache, G., Montmerle, T., Pérault, M., Persi, P., Prusti, T., Puget, J. L., & Sibille, F. 2001, *A&A*, 372, 173

Boss, A. P. 2000, *ApJ*, 536, L101

Briceño, C., Calvet, N., Hernández, J., Vivas, A. K., Hartmann, L., Downes, J. J., & Berlind, P. 2005, *AJ*, 129, 907

Briceño, C., Hartmann, L., Hernández, J., Calvet, N., Vivas, A. K., Furesz, G., & Szentgyorgyi, A. 2007, *ApJ*, 661, 1119

Brown, J. M., Blake, G. A., Dullemond, C. P., Merín, B., Augereau, J. C., Boogert, A. C. A., Evans, II, N. J., Geers, V. C., Lahuis, F., Kessler-Silacci, J. E., Pontoppidan, K. M., & van Dishoeck, E. F. 2007, *ApJ*, 664, L107

Brown, J. M., Blake, G. A., Qi, C., Dullemond, C. P., & Wilner, D. J. 2008, *ApJ*, 675, L109

Butler, R. P., Vogt, S. S., Marcy, G. W., Fischer, D. A., Wright, J. T., Henry, G. W., Laughlin, G., & Lissauer, J. J. 2004, *ApJ*, 617, 580

Butler, R. P., Wright, J. T., Marcy, G. W., Fischer, D. A., Vogt, S. S., Tinney, C. G., Jones, H. R. A., Carter, B. D., Johnson, J. A., McCarthy, C., & Penny, A. J. 2006, *ApJ*, 646, 505

Calvet, N., Briceño, C., Hernández, J., Hoyer, S., Hartmann, L., Sicilia-Aguilar, A., Megeath, S. T., & D'Alessio, P. 2005a, *AJ*, 129, 935

Calvet, N., D'Alessio, P., Hartmann, L., Wilner, D., Walsh, A., & Sitko, M. 2002, *ApJ*, 568, 1008

Calvet, N., D'Alessio, P., Watson, D. M., Franco-Hernández, R., Furlan, E., Green, J., Sutter, P. M., Forrest, W. J., Hartmann, L., Uchida, K. I., Keller, L. D., Sargent, B., Najita, J., Herter, T. L., Barry, D. J., & Hall, P. 2005b, *ApJ*, 630, L185

Calvet, N., & Gullbring, E. 1998, *ApJ*, 509, 802

Calvet, N., & Hartmann, L. 1992, *ApJ*, 386, 239

Calvet, N., Magris, G. C., Patino, A., & D'Alessio, P. 1992, Revista Mexicana de Astronomia y Astrofisica, 24, 27

Calvet, N., Muzerolle, J., Briceño, C., Hernández, J., Hartmann, L., Saucedo, J. L., & Gordon, K. D. 2004, *AJ*, 128, 1294

Calvet, N., Patino, A., Magris, G. C., & D'Alessio, P. 1991, *ApJ*, 380, 617

Carmona, A., van den Ancker, M. E., Henning, T., Goto, M., Fedele, D., & Stecklum, B. 2007, *A&A*, 476, 853

Carpenter, J. M., Mamajek, E. E., Hillenbrand, L. A., & Meyer, M. R. 2006, *ApJ*, 651, L49

Chiang, E., & Murray-Clay, R. 2007, Nature Physics, 3, 604

Chiang, E. I., & Goldreich, P. 1997, *ApJ*, 490, 368

Clarke, C. J., Gendrin, A., & Sotomayor, M. 2001, *MNRAS*, 328, 485

Cushing, M. C., Rayner, J. T., & Vacca, W. D. 2005, *ApJ*, 623, 1115

Cushing, M. C., Vacca, W. D., & Rayner, J. T. 2004, *PASP*, 116, 362

D'Alessio, P., Calvet, N., & Hartmann, L. 2001, *ApJ*, 553, 321

D'Alessio, P., Calvet, N., Hartmann, L., Franco-Hernández, R., & Servín, H. 2006, *ApJ*, 638, 314

D'Alessio, P., Calvet, N., Hartmann, L., Lizano, S., & Cantó, J. 1999, *ApJ*, 527, 893

D'Alessio, P., Canto, J., Calvet, N., & Lizano, S. 1998, *ApJ*, 500, 411

D'Alessio, P., Hartmann, L., Calvet, N., Franco-Hernández, R., Forrest, W. J., Sargent, B., Furlan, E., Uchida, K., Green, J. D., Watson, D. M., Chen, C. H., Kemper, F., Sloan, G. C., & Najita, J. 2005, *ApJ*, 621, 461

Dorschner, J., Begemann, B., Henning, T., Jaeger, C., & Mutschke, H. 1995, *A&A*, 300, 503

Draine, B. T., & Lee, H. M. 1984, *ApJ*, 285, 89

Dullemond, C. P., & Dominik, C. 2004, *A&A*, 421, 1075

—. 2005, *A&A*, 434, 971

Durisen, R. H., Boss, A. P., Mayer, L., Nelson, A. F., Quinn, T., & Rice, W. K. M. 2007, in Protostars and Planets V, ed. B. Reipurth, D. Jewitt, & K. Keil, 607–622

Edwards, S., Fischer, W., Hillenbrand, L., & Kwan, J. 2006, *ApJ*, 646, 319

Endl, M., Cochran, W. D., Wittenmyer, R. A., & Boss, A. P. 2008, *ApJ*, 673, 1165

Espaillat, C., Calvet, N., D'Alessio, P., Bergin, E., Hartmann, L., Watson, D., Furlan, E., Najita, J., Forrest, W., McClure, M., Sargent, B., Bohac, C., & Harrold, S. T. 2007a, *ApJ*, 664, L111

Espaillat, C., Calvet, N., D'Alessio, P., Hernández, J., Qi, C., Hartmann, L., Furlan, E., & Watson, D. M. 2007b, *ApJ*, 670, L135

Espaillat, C., Calvet, N., Luhman, K. L., Muzerolle, J., & D'Alessio, P. 2008a, *ApJ*, 682, L125

Espaillat, C., Muzerolle, J., Hernández, J., Briceño, C., Calvet, N., D'Alessio, P., McClure, M., Watson, D. M., Hartmann, L., & Sargent, B. 2008b, *ApJ*, 689, L145

Fabricant, D., Cheimets, P., Caldwell, N., & Geary, J. 1998, *PASP*, 110, 79

Feigelson, E., Townsley, L., Güdel, M., & Stassun, K. 2007, in Protostars and Planets V, ed. B. Reipurth, D. Jewitt, & K. Keil, 313–328

Feigelson, E. D., Casanova, S., Montmerle, T., & Guibert, J. 1993, *ApJ*, 416, 623

Folha, D. F. M., & Emerson, J. P. 1999, *A&A*, 352, 517

Forrest, W. J., Sargent, B., Furlan, E., D'Alessio, P., Calvet, N., Hartmann, L., Uchida, K. I., Green, J. D., Watson, D. M., Chen, C. H., Kemper, F., Keller, L. D., Sloan, G. C., Herter, T. L., Brandl, B. R., Houck, J. R., Barry, D. J., Hall, P., Morris, P. W., Najita, J., & Myers, P. C. 2004, *ApJS*, 154, 443

Furlan, E., Hartmann, L., Calvet, N., D'Alessio, P., Franco-Hernández, R., Forrest, W. J., Watson, D. M., Uchida, K. I., Sargent, B., Green, J. D., Keller, L. D., & Herter, T. L. 2006, *ApJS*, 165, 568

Furlan, E., Sargent, B., Calvet, N., Forrest, W. J., D'Alessio, P., Hartmann, L., Watson, D. M., Green, J. D., Najita, J., & Chen, C. H. 2007, *ApJ*, 664, 1176

Gail, H.-P. 2001, *A&A*, 378, 192

Gauvin, L. S., & Strom, K. M. 1992, *ApJ*, 385, 217

Genzel, R., & Stutzki, J. 1989, *ARA&A*, 27, 41

Glassgold, A. E., Najita, J., & Igea, J. 2004, *ApJ*, 615, 972

Glassgold, A. E., Najita, J. R., & Igea, J. 2007, *ApJ*, 656, 515

Goldreich, P., & Tremaine, S. 1980, *ApJ*, 241, 425

Goldreich, P., & Ward, W. R. 1973, *ApJ*, 183, 1051

Gómez, M., & Kenyon, S. J. 2001, *AJ*, 121, 974

Gorti, U., & Hollenbach, D. 2009, *ApJ*, 690, 1539

Güdel, M., Padgett, D. L., & Dougados, C. 2007, in Protostars and Planets V, ed. B. Reipurth, D. Jewitt, & K. Keil, 329–344

Guenther, E. W., Esposito, M., Mundt, R., Covino, E., Alcalá, J. M., Cusano, F., & Stecklum, B. 2007, *A&A*, 467, 1147

Gullbring, E., Hartmann, L., Briceno, C., & Calvet, N. 1998, *ApJ*, 492, 323

Gutermuth, R. A., Megeath, S. T., Muzerolle, J., Allen, L. E., Pipher, J. L., Myers, P. C., & Fazio, G. G. 2004, *ApJS*, 154, 374

Haisch, Jr., K. E., Lada, E. A., & Lada, C. J. 2001, *ApJ*, 553, L153

Hartigan, P. 1993, *AJ*, 105, 1511

Hartigan, P., Hartmann, L., Kenyon, S., Hewett, R., & Stauffer, J. 1989, *ApJS*, 70, 899

Hartmann, L. 2003, *ApJ*, 585, 398

—. 2009, Cambridge Astrophysics Series, 47

Hartmann, L., Calvet, N., Gullbring, E., & D'Alessio, P. 1998, *ApJ*, 495, 385

Hartmann, L., Hewett, R., & Calvet, N. 1994, *ApJ*, 426, 669

Hartmann, L., Megeath, S. T., Allen, L., Luhman, K., Calvet, N., D'Alessio, P., Franco-Hernandez, R., & Fazio, G. 2005, *ApJ*, 629, 881

Henning, T., Pfau, W., Zinnecker, H., & Prusti, T. 1993, *A&A*, 276, 129

Herbig, G. H. 1977, *ApJ*, 214, 747

Herbig, G. H., Vrba, F. J., & Rydgren, A. E. 1986, *AJ*, 91, 575

Hernández, J., Calvet, N., Briceño, C., Hartmann, L., & Berlind, P. 2004, *AJ*, 127, 1682

Hernández, J., Calvet, N., Briceño, C., Hartmann, L., Vivas, A. K., Muzerolle, J., Downes, J., Allen, L., & Gutermuth, R. 2007, *ApJ*, 671, 1784

Hernández, J., Calvet, N., Hartmann, L., Briceño, C., Sicilia-Aguilar, A., & Berlind, P. 2005, *AJ*, 129, 856

Higdon, S. J. U., Devost, D., Higdon, J. L., Brandl, B. R., Houck, J. R., Hall, P., Barry, D., Charmandaris, V., Smith, J. D. T., Sloan, G. C., & Green, J. 2004, *PASP*, 116, 975

Høg, E., Fabricius, C., Makarov, V. V., Urban, S., Corbin, T., Wycoff, G., Bastian, U., Schwekendiek, P., & Wicenec, A. 2000, *A&A*, 355, L27

Hollenbach, D., Johnstone, D., Lizano, S., & Shu, F. 1994, *ApJ*, 428, 654

Houck, J. R., Roellig, T. L., van Cleve, J., Forrest, W. J., Herter, T., Lawrence, C. R., Matthews, K., Reitsema, H. J., Soifer, B. T., Watson, D. M., Weedman, D., Huisjen, M., Troeltzsch, J., Barry, D. J., Bernard-Salas, J., Blacken, C. E., Brandl, B. R., Charmandaris, V., Devost, D., Gull, G. E., Hall, P., Henderson, C. P., Higdon, S. J. U., Pirger, B. E., Schoenwald, J., Sloan, G. C., Uchida, K. I., Appleton, P. N., Armus, L., Burgdorf, M. J., Fajardo-Acosta, S. B., Grillmair, C. J., Ingalls, J. G., Morris, P. W., & Teplitz, H. I. 2004, *ApJS*, 154, 18

Hubickyj, O., Bodenheimer, P., & Lissauer, J. J. 2005, Icarus, 179, 415

Hughes, A. M., Andrews, S. M., Espaillat, C., Wilner, D. J., Calvet, N., D'Alessio, P., Qi, C., Williams, J. P., & Hogerheijde, M. R. 2009, *ApJ*, 698, 131

Hughes, A. M., Wilner, D. J., Calvet, N., D'Alessio, P., Claussen, M. J., & Hogerheijde, M. R. 2007, *ApJ*, 664, 536

Ireland, M. J., & Kraus, A. L. 2008, *ApJ*, 678, L59

Jayawardhana, R., Hartmann, L., Fazio, G., Fisher, R. S., Telesco, C. M., & Piña, R. K. 1999, *ApJ*, 521, L129

Kastner, J. H., Huenemoerder, D. P., Schulz, N. S., & Weintraub, D. A. 1999, *ApJ*, 525, 837

Keller, C., & Gail, H.-P. 2004, *A&A*, 415, 1177

Kenyon, S. J., Dobrzycka, D., & Hartmann, L. 1994, *AJ*, 108, 1872

Kenyon, S. J., & Hartmann, L. 1987, *ApJ*, 323, 714

—. 1995, *ApJS*, 101, 117

Lada, C. J. 1987, in IAU Symposium, Vol. 115, Star Forming Regions, ed. M. Peimbert & J. Jugaku, 1–17

Lada, C. J., Muench, A. A., Luhman, K. L., Allen, L., Hartmann, L., Megeath, T., Myers, P., Fazio, G., Wood, K., Muzerolle, J., Rieke, G., Siegler, N., & Young, E. 2006, *AJ*, 131, 1574

Lahuis, F., van Dishoeck, E. F., Blake, G. A., Evans, II, N. J., Kessler-Silacci, J. E., & Pontoppidan, K. M. 2007, *ApJ*, 665, 492

Leinert, C., Zinnecker, H., Weitzel, N., Christou, J., Ridgway, S. T., Jameson, R., Haas, M., & Lenzen, R. 1993, *A&A*, 278, 129

Lissauer, J. J., & Stevenson, D. J. 2007, in Protostars and Planets V, ed. B. Reipurth, D. Jewitt, & K. Keil, 591–606

Lommen, D., Wright, C. M., Maddison, S. T., Jørgensen, J. K., Bourke, T. L., van Dishoeck, E. F., Hughes, A., Wilner, D. J., Burton, M., & van Langevelde, H. J. 2007, *A&A*, 462, 211

Low, F. J., Smith, P. S., Werner, M., Chen, C., Krause, V., Jura, M., & Hines, D. C. 2005, *ApJ*, 631, 1170

Lubow, S. H., & D'Angelo, G. 2006, *ApJ*, 641, 526

Luhman, K. L. 2004, *ApJ*, 602, 816

—. 2007, *ApJS*, 173, 104

Luhman, K. L., & Rieke, G. H. 1999, *ApJ*, 525, 440

Makovoz, D., Khan, I., & Masci, F. 2006, in Society of Photo-Optical Instrumentation Engineers (SPIE) Conference Series, Vol. 6065, Society of Photo-Optical Instrumentation Engineers (SPIE) Conference Series, ed. C. A. Bouman, E. L. Miller, & I. Pollak, 330–341

Makovoz, D., & Marleau, F. R. 2005, *PASP*, 117, 1113

Malbet, F., & Bertout, C. 1991, *ApJ*, 383, 814

Mathieu, R. D., Adams, F. C., & Latham, D. W. 1991, *AJ*, 101, 2184

Mathis, J. S. 1990, *ARA&A*, 28, 37

Mathis, J. S., Rumpl, W., & Nordsieck, K. H. 1977, *ApJ*, 217, 425

Mayer, L., Quinn, T., Wadsley, J., & Stadel, J. 2002, Science, 298, 1756

McArthur, B. E., Endl, M., Cochran, W. D., Benedict, G. F., Fischer, D. A., Marcy, G. W., Butler, R. P., Naef, D., Mayor, M., Queloz, D., Udry, S., & Harrison, T. E. 2004, *ApJ*, 614, L81

Megeath, S. T., Hartmann, L., Luhman, K. L., & Fazio, G. G. 2005, *ApJ*, 634, L113

Melo, C., Santos, N. C., Gieren, W., Pietrzynski, G., Ruiz, M. T., Sousa, S. G., Bouchy, F., Lovis, C., Mayor, M., Pepe, F., Queloz, D., da Silva, R., & Udry, S. 2007, *A&A*, 467, 721

Monnier, J. D., & Millan-Gabet, R. 2002, *ApJ*, 579, 694

Muzerolle, J., Calvet, N., Briceño, C., Hartmann, L., & Hillenbrand, L. 2000, *ApJ*, 535, L47

Muzerolle, J., Calvet, N., & Hartmann, L. 1998, *ApJ*, 492, 743

—. 2001, *ApJ*, 550, 944

Muzerolle, J., Calvet, N., Hartmann, L., & D'Alessio, P. 2003, *ApJ*, 597, L149

Najita, J. R., Carr, J. S., Glassgold, A. E., & Valenti, J. A. 2007a, in Protostars and Planets V, ed. B. Reipurth, D. Jewitt, & K. Keil, 507–522

Najita, J. R., Strom, S. E., & Muzerolle, J. 2007b, *MNRAS*, 378, 369

Natta, A., Prusti, T., Neri, R., Wooden, D., Grinin, V. P., & Mannings, V. 2001, *A&A*, 371, 186

Neuhaeuser, R., Sterzik, M. F., Schmitt, J. H. M. M., Wichmann, R., & Krautter, J. 1995, *A&A*, 297, 391

Norton, A. J., Wheatley, P. J., West, R. G., Haswell, C. A., Street, R. A., Collier Cameron, A., Christian, D. J., Clarkson, W. I., Enoch, B., Gallaway, M., Hellier, C., Horne, K., Irwin, J., Kane, S. R., Lister, T. A., Nicholas, J. P., Parley, N., Pollacco, D., Ryans, R., Skillen, I., & Wilson, D. M. 2007, *A&A*, 467, 785

Paardekooper, S.-J., & Mellema, G. 2004, *A&A*, 425, L9

Pascucci, I., Gorti, U., Hollenbach, D., Najita, J., Meyer, M. R., Carpenter, J. M., Hillenbrand, L. A., Herczeg, G. J., Padgett, D. L., Mamajek, E. E., Silverstone,

M. D., Schlingman, W. M., Kim, J. S., Stobie, E. B., Bouwman, J., Wolf, S., Rodmann, J., Hines, D. C., Lunine, J., & Malhotra, R. 2006, *ApJ*, 651, 1177

Pascucci, I., Hollenbach, D., Najita, J., Muzerolle, J., Gorti, U., Herczeg, G. J., Hillenbrand, L. A., Kim, J. S., Carpenter, J. M., Meyer, M. R., Mamajek, E. E., & Bouwman, J. 2007, *ApJ*, 663, 383

Piétu, V., Dutrey, A., Guilloteau, S., Chapillon, E., & Pety, J. 2006, *A&A*, 460, L43

Pollack, J. B., Hollenbach, D., Beckwith, S., Simonelli, D. P., Roush, T., & Fong, W. 1994, *ApJ*, 421, 615

Pollack, J. B., Hubickyj, O., Bodenheimer, P., Lissauer, J. J., Podolak, M., & Greenzweig, Y. 1996, Icarus, 124, 62

Quillen, A. C., Blackman, E. G., Frank, A., & Varnière, P. 2004, *ApJ*, 612, L137

Ratzka, T., Leinert, C., Henning, T., Bouwman, J., Dullemond, C. P., & Jaffe, W. 2007, *A&A*, 471, 173

Rayner, J. T., Toomey, D. W., Onaka, P. M., Denault, A. J., Stahlberger, W. E., Vacca, W. D., Cushing, M. C., & Wang, S. 2003, *PASP*, 115, 362

Rice, W. K. M., Armitage, P. J., Wood, K., & Lodato, G. 2006, *MNRAS*, 373, 1619

Rice, W. K. M., Wood, K., Armitage, P. J., Whitney, B. A., & Bjorkman, J. E. 2003, *MNRAS*, 342, 79

Rivera, E. J., Lissauer, J. J., Butler, R. P., Marcy, G. W., Vogt, S. S., Fischer, D. A., Brown, T. M., Laughlin, G., & Henry, G. W. 2005, *ApJ*, 634, 625

Salyk, C., Blake, G. A., Boogert, A. C. A., & Brown, J. M. 2007, *ApJ*, 655, L105

Santos, N. C., Israelian, G., & Mayor, M. 2004, *A&A*, 415, 1153

Sargent, B., Forrest, W. J., D'Alessio, P., Li, A., Najita, J., Watson, D. M., Calvet, N., Furlan, E., Green, J. D., Kim, K. H., Sloan, G. C., Chen, C. H., Hartmann, L., & Houck, J. R. 2006, *ApJ*, 645, 395

Shakura, N. I., & Syunyaev, R. A. 1973, *A&A*, 24, 337

Shu, F. H., Adams, F. C., & Lizano, S. 1987, *ARA&A*, 25, 23

Sicilia-Aguilar, A., Hartmann, L., Calvet, N., Megeath, S. T., Muzerolle, J., Allen, L., D'Alessio, P., Merín, B., Stauffer, J., Young, E., & Lada, C. 2006, *ApJ*, 638,

897

Siess, L., Dufour, E., & Forestini, M. 2000, *A&A*, 358, 593

Simon, M., Dutrey, A., & Guilloteau, S. 2000, *ApJ*, 545, 1034

Skrutskie, M. F., Dutkevitch, D., Strom, S. E., Edwards, S., Strom, K. M., & Shure, M. A. 1990, *AJ*, 99, 1187

Sousa, S. G., Santos, N. C., Mayor, M., Udry, S., Casagrande, L., Israelian, G., Pepe, F., Queloz, D., & Monteiro, M. J. P. F. G. 2008, *A&A*, 487, 373

Stassun, K. G., Mathieu, R. D., Vrba, F. J., Mazeh, T., & Henden, A. 2001, *AJ*, 121, 1003

Strom, K. M., Strom, S. E., Edwards, S., Cabrit, S., & Skrutskie, M. F. 1989, *AJ*, 97, 1451

Strom, S. E. 1972, *PASP*, 84, 745

Su, K. Y. L., Rieke, G. H., Stansberry, J. A., Bryden, G., Stapelfeldt, K. R., Trilling, D. E., Muzerolle, J., Beichman, C. A., Moro-Martin, A., Hines, D. C., & Werner, M. W. 2006, *ApJ*, 653, 675

Takami, M., Bailey, J., & Chrysostomou, A. 2003, *A&A*, 397, 675

Terebey, S., Shu, F. H., & Cassen, P. 1984, *ApJ*, 286, 529

Uchida, K. I., Calvet, N., Hartmann, L., Kemper, F., Forrest, W. J., Watson, D. M., D'Alessio, P., Chen, C. H., Furlan, E., Sargent, B., Brandl, B. R., Herter, T. L., Morris, P., Myers, P. C., Najita, J., Sloan, G. C., Barry, D. J., Green, J., Keller, L. D., & Hall, P. 2004, *ApJS*, 154, 439

Udry, S., Mayor, M., Benz, W., Bertaux, J.-L., Bouchy, F., Lovis, C., Mordasini, C., Pepe, F., Queloz, D., & Sivan, J.-P. 2006, *A&A*, 447, 361

Vacca, W. D., Cushing, M. C., & Rayner, J. T. 2003, *PASP*, 115, 389

Varnière, P., Blackman, E. G., Frank, A., & Quillen, A. C. 2006, *ApJ*, 640, 1110

Vogt, S. S., Butler, R. P., Marcy, G. W., Fischer, D. A., Henry, G. W., Laughlin, G., Wright, J. T., & Johnson, J. A. 2005, *ApJ*, 632, 638

Ward, W. R. 1988, Icarus, 73, 330

Watson, D. M., Leisenring, J. M., Furlan, E., Bohac, C. J., Sargent, B., Forrest, W. J., Calvet, N., Hartmann, L., Nordhaus, J. T., Green, J. D., Kim, K. H., Sloan, G. C., Chen, C. H., Keller, L. D., d'Alessio, P., Najita, J., Uchida, K. I., & Houck, J. R. 2009, *ApJS*, 180, 84

Weaver, W. B., & Jones, G. 1992, *ApJS*, 78, 239

Webb, R. A., Zuckerman, B., Platais, I., Patience, J., White, R. J., Schwartz, M. J., & McCarthy, C. 1999, *ApJ*, 512, L63

Weidenschilling, S. J., Spaute, D., Davis, D. R., Marzari, F., & Ohtsuki, K. 1997, Icarus, 128, 429

Werner, M. W., Roellig, T. L., Low, F. J., Rieke, G. H., Rieke, M., Hoffmann, W. F., Young, E., Houck, J. R., Brandl, B., Fazio, G. G., Hora, J. L., Gehrz, R. D., Helou, G., Soifer, B. T., Stauffer, J., Keene, J., Eisenhardt, P., Gallagher, D., Gautier, T. N., Irace, W., Lawrence, C. R., Simmons, L., Van Cleve, J. E., Jura, M., Wright, E. L., & Cruikshank, D. P. 2004, *ApJS*, 154, 1

White, R. J., & Basri, G. 2003, *ApJ*, 582, 1109

White, R. J., & Ghez, A. M. 2001, *ApJ*, 556, 265

White, R. J., & Hillenbrand, L. A. 2004, *ApJ*, 616, 998

Whittet, D. C. B., Prusti, T., Franco, G. A. P., Gerakines, P. A., Kilkenny, D., Larson, K. A., & Wesselius, P. R. 1997, *A&A*, 327, 1194

Wilking, B. A., Meyer, M. R., Robinson, J. G., & Greene, T. P. 2005, *AJ*, 130, 1733